PHOTOPHYSICAL INVESTIGATION OF IRIDIUM-CARBON SIGMA BONDED COMPLEXES

FRED OMEGA GARCES

Fred Ω Garces

8.A.89

UNIVERSITY OF CALIFORNIA

SANTA BARBARA

STRUCTURAL CHARACTERIZATION AND PHOTOPHYSICAL INVESTIGATION OF IRIDIUM-CARBON SIGMA BONDED COMPLEXES

A Dissertation submitted in partial satisfaction

of the requirements for the degree of

Doctor of Philosophy

in

Chemistry

by

Fred Omega Garces

Committee in charge:

Professor Peter C. Ford

Professor Henry W. Offen

Professor Galen D. Stucky

Professor Richard J. Watts
(Committee Chair)

November 1988

The Dissertation of

Fred Omega Garces

is approved:

Professor Peter C. Ford

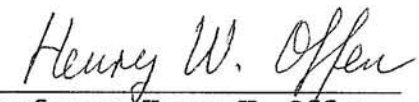

Professor Henry W. Offen

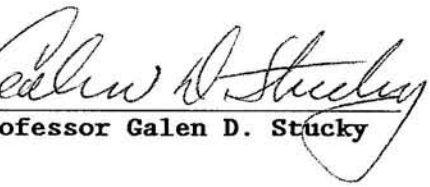

Professor Galen D. Stucky

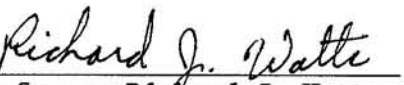

Professor Richard J. Watts
(Committee Chair)

November 1988

DISRT ME

November 30, 1988

I would like to dedicate my dissertation
to the ones I love most,
my family.

To mom and dad (Nieves and Joe),
thank you for the support—
spiritual, emotional and financial.
thank you for never letting me doubt myself
and my abilities.
most of all thank you for being my parents.
To Noel, Lelian and Grace,
thank you for always being patience with me
and challenging me always to do better.
And especially to Will,
thank you for always putting our needs
in front of your own.
your example of hard work and determination has
always been an inspiration to me.

Most of all, thank you all for always being there for me.

Of all the people in the world, I am lucky because a few precious individuals have some how manage to cross their lives path with mine. I am very grateful to have Dr. Kevin A. King as a wonderful inspiration in chemistry. Dr. Peter J. Spellane, for introducing me to the magical world of NMR spectroscopy. Dr. Carl A. Craig, for making research at the WIW a rock-roll experience (we-b-jamin'). Ashley P. Wilde, for slowing me down (you've save my sanity). To the rest of the WIW past and present: Peter Djurovich, Christine Miller, Greg Carlson, Ken Dedian, Hector Torres and Kazuhiko Mizuno. It was my pleasure working with all of you. I also want to thank the undergraduates I've had the pleasure of working with: Selmira Tellechea, Maryann Torres and Mae Libunao (GRMP), Joe Escobar and Debbie Rashe (SARI). To Ty Chin-Choy, Dr. Mike Eddy, Dr. Bill Harrison and Delphine Davis, thanks for being collaborators. I would especially like to thank Dr. Nancy Keder. I'm truly fortunate to have the privilege of work with you (thank you for always being patient with me).

Finally I am grateful to Professor Watts for teaching me much about chemistry and life. Thanks for never losing patience with me. Since I've entered your group four years ago I've become a better person and scientist. As I've read some where, "...you have given me many things which I will treasure for a lifetime, and the most important thing of all is the gift of your friendship...."

VITAE

February 26, 1960——Born——Ormoc City, Philippines

April 30, 1971——U.S. Citizenship, Agana, Guam

May 18, 1982——B. S., San Diego State University
San Diego, CA 92182

November 30, 1988——Ph. D., University of California
Santa Barbara, CA 93117

PUBLICATIONS

"Photoproperties of Ortho-metalated Ir (III) and Rh (III) Complexes"; K.A. King, F. O. Garces, R. J. Watts; Proceedings of the Seventh International Symposium on the Photochemistry and Photophysics of Coordination Compounds; H. Yersin and A. Vogler, Ed., Springer Verlag, Berlin, in press

"Synthesis and Photophysical Studies of Ortho-Metalated Pd(II) Complexes Including Two Novel Pd(II)/Rh(III) Dimers"; C.A. Craig, F.O. Garces, R.J. Watts; Ibid.,

"Synthesis, Structure, ElectroChemistry and Photophysics of Methyl-Substituted Phenylpyridine Ortho-metalated Ir(III) Complexes"; Fred O. Garces, K.A. King, R.J. Watts, Inorganic Chemistry 1988, 27 3464.

"A New Ortho-Metalated Dichloro-Bridged Complex of Ir(III) with 2,2'-bipyridine: $[Ir(bpy\text{-}C^3,N')(bpy\text{-}N,N')Cl]_2Cl_2$"; Fred O. Garces, Richard J. Watts, Inorganic Chemistry, In Press.

INVITED SEMINARS

6/85 "Preliminary Results on the Characterization of Substituted Phenylpyridine Dichloro-bridge Iridium (III) Dimers"; Southern California Photochemistry Conference, USC-Catalina, California.

6/86 "Methyl-Substituted Phenylpyridine Iridium (III) Complexes: A Better Photoreducing Agent"; Southern California Photochemistry Conference, UCLA-Lake Arrowhead, California.

4/87 "The Role of Ortho-metalating Complexes in the Photoreduction of Carbon Dioxide"; Graduate Research Mentorship Program Conference, University of California, Santa Barbara, California.

7/87 "Structural and Photophysical Properties of Methyl-Substituted Phenylpyridine Ortho-Metalating Ir(III) Complexes"; Southern California Inorganic Photochemical Conference, Caltech-Capra Ranch, California.

10/87 "Structural Studies of Methyl Substituted Phenylpyridine Iridium (III) Complexes"; Pacific Conference on Chemistry and Spectroscopy, Irvine, California.

7/88 "Structural and Photophysical Evidence for a new Ortho-Metalated Complex of 2,2'-bipyridine with Iridium (III)"; Southern California Inorganic Photochemical Conference, UCSB-Lake Cachuma, California.

7/88 "$[Ir(bpy\text{-}C^3,N')(bpy\text{-}N,N')Cl]_2Cl_2$, the first dichloro-bridged dimer of a bipyridine complex of Ir(III)"; Southern California Inorganic Photochemical Conference, Lake Cachuma, University of California, Santa Barbara, California.

CONTRIBUTED PAPERS/POSTER

"Photoproperties of Ortho-metalated Ir(III) and Rh(III) Complexes", K.A.King, F.O.Garces, S.Sprouse, and R.J.Watts, Seventh International Symposium on the Photochemistry and Photophysics of Coordination Compounds, Elmau, FRG, March 29 - April 2, 1987.

"Synthesis and Photophysical Studies of Ortho-metalated Pd(II) Complexes Including Two Novel Pd(II)/Rh(III) Dimers" C.A.Craig, F.O.Garces and R.J.Watts, Seventh International Symposium on the Photochemistry and Photophysics of Coordination Compounds, Elmau, FRG, March 29 - April 2, 1987.

"Photophysical Properties of Ortho-metalated Pd(II) and Pd(II) / Rh(III) Complexes"; C.A. Craig, F. O. Garces, R.J. Watts; 193rd ACS National Conference, Denver, Colorado, April 5-10, 1987.

"Structural Characterization and Photophysical Properties of Methyl-Substituted Phenylpyridine Iridium (III) Complexes"; F.O. Garces, K.A. King, C.A. Craig, P.J. Spellane, R.J. Watts; 193rd ACS National Conference, Denver, Colorado, April 5-10, 1987.

"Energy Transfer in Excited States of Ortho-metalated Ir(III) and Rh(III) Complexes"; K.A. King, F. Garces, S. Sprouse, R.J. Watts; 193rd ACS National Conference, Denver, Colorado, April 5-10, 1987.

"Energy Transformation in Organometallic Complexes" K.A.King, F.O.Garces, C.Craig, A.Wilde, K.Ichimura, T. Kobayashi, and R.J.Watts, Eleventh DOE Solar Photochemistry Research Conference, Lake Tahoe, California, June 8-11, 1987.

"Characterization of Methyl-Substituted Ir(III) Ortho-metalated Complexes"; F.O. Garces; A scholarly paper submitted to the Dean's Prize Competition; UCSB, Santa Barbara, CA March 1987.

"Photophysical Investigation of Palladium (II) Ortho-Metalates"; Carl A. Craig, Fred O. Garces, Richard J. Watts, Pacific Conference on Chemistry and Spectroscopy, Irvine, CA., October 28-30, 1987.

"Excited State Characterization of Chemically-Modified Ortho-metalating complexes"; F.O. Garces, M. Libunao, M. Torres, S. Tellechea, and R.J. Watts, SACNAS Conference, El-Paso, Texas, October 29-31, 1987.

"Analysis of the ^{1}H and ^{13}C NMR spectra of $[Ir(bpy\text{-}C^{3},N')(bpy\text{-}N,N')Cl]_2^{2+}$: Evidence for a Carbon Bonded Structure"; Fred O. Garces, P.J. Spellane, R.J. Watts, NMR Dedication Ceremony, Santa Barbara, CA., January 7, 1987.

"Proton, Carbon, and Fluorine NMR 'Assignments of 3,3-Difluoroandrostan-17-ol Acetate by Homo- and Heteronuclear Correlation Spectroscopy' "; Delphine Davis, Fred Garces, R.J. Watts, J.T. Gerig, NMR Dedication Ceremony, Santa Barbara, CA., January 7, 1987.

"Photophysical Properties of Ortho-metalated Complexes of Palladium (II)"; C.A.Craig, F.O.Garces, R. J. Watts, Southwestern Regional ACS conference, Las Vegas, Nv., March 9, 1987.

"Ground and Excited State Properties of Cyclo-Metalated Iridium (III) Complexes: A Potential Photocatalyst"; Fred O. Garces, R.J. Watts, Southwestern Regional ACS conference, Las Vegas, Nv., March 9, 1987.

"Structural and Photophysical Studies of Metal-Carbon Sigma-Bonded Species: New Ortho-Metalated Complexes of 2,2'Bipyridine, R.J. Watts, F.O. Garces, A.P.Wilde, C. Miller, Twelfth DOE Solar Photochemistry Research Conference, Washington D.C., May 23, 1988.

"^{1}H and ^{13}C NMR Analysis of $[Ir(bpy\text{-}C^{3},N')(bpy\text{-}N,N')Cl]_2$2: Evidence for an Ortho-Metalated Dimer Structure"; Fred O. Garces, P.J. Spellane, R.J. Watts, 195th ACS National Conference, Toronto, Canada, June 5-10, 1988.

"Photophysics of Ortho-metalated Palladium(II) and Rhodium(III) Complexes, C.A.Craig, F.O.Garces, R.J. Watts, 195th ACS National Conference, Toronto, Canada, June 5-10, 1988.

"Temperature and Solvent Dependence of Absorption and Emission of Ortho-metalated Complexes of Ir(III)"; A.P. Wilde, K. A. King, C. Miller, F. O. Garces, R. J. Watts, XII IUPAC Symposium on Photochemistry, Bologna, Italy, July 17, 22, 1988.

"Structural and Photophysical Investigation of $[Ir(bpy\text{-}N,N')(bpy\text{-}C^{3},N')Cl]_2^{2+}$: A Dichloro-bridged Ortho-metalated Dimer"; F.O.Garces, P.J. Spellane, R.J.Watts, XII IUPAC Symposium on Photochemistry, Bologna, Italy, July 17, 22, 1988.

INTRAMURAL GRANTS

1/87 "Ortho-metalating Ir(III) Complexes as a Photocatalyst in the Photoreduction of Carbon Dioxide"; F.O. Garces, R.J. Watts; Graduate Research Mentorship Program, UCSB, Santa Barbara, CA 3400.00$

10/87 Society for the Advancement of Chicanos and Native Americans in Science / Graduate Research Mentorship Program, (Travel Funds). "Excited State Characterization of Chemically-Modified Ortho-metalating Complexes" 1000.00$

5/88 "The Synthesis of Modified Ortho-metalated Ir(III) Complexes: A Potentially better Photocatalyst"; F.O.Garces, R.J. Watts; Summer Academic Research Internship Program (SARI), UCSB, Santa Barbara, CA 4000.00$

ABSTRACT

STRUCTURAL CHARACTERIZATION AND PHOTOPHYSICAL INVESTIGATION OF IRIDIUM-CARBON SIGMA BONDED COMPLEXES

by

Fred Omega Garces

The purpose of the work in Part I was to explore the enhancement of the already-high photoreducing potential of ortho-metalated complexes such as $[Ir(ppy)_2Cl]_2$ and $[Ir(ppy)_2bpy]^+$ by introducing functional groups onto the ppy ligand. The ligands 3-methyl-2-phenylpyridine (mppy) and 2(p-tolyl)pyridine (ptpy), which contain methyl groups donating electron density to either the phenyl ring (ptpy) or the pyridyl ring (mppy) were used for this purpose. In the course of this investigation, structural characterizations by NMR techniques and crystallographic analysis indicated that these complexes possess mutually cis Ir-C bonds; the dimers are D_2 symmetric and the monomers are C_2 symmetric. ^1H and ^{13}C resonances were completely assigned in the NMR spectra.

Electrochemical and photophysical investigations suggest that the electron density about the iridium metal of these complexes are enhanced by the modification of ppy ligands. Our results show that

these methyl-substituted ortho-metalated iridium complexes are much stronger photoreducing agents than their non-substituted counterparts.

Preparation and characterization of four novel iridium bipyridyl complexes are discussed in Part 2 of this dissertation. Iridium (IV) seems to be a key ingredient in the preparation of these complexes. Structural characterizations suggest that the first of these bpy complexes is an ortho-metalated dichloro-bridged bpy dimer, $[Ir(bpy\text{-}C^3,N')(bpy\text{-}N,N')Cl]_2^{2+}$, I. Characterizations of I include, ^1H and ^{13}C NMR spectroscopic; mass spectroscopic; electrochemical; photophysical (including acid / base measurements) techniques.

The second complex exists as a $[Ir(Hbpy\text{-}C^3,N')(bpy\text{-}N,N')Cl_2]^+$ cation and an $[IrCl_4(bpy)]^-$ anion in an ion pair arrangement as shown by crystallographic techniques, II. NMR and mass spectroscopy provide good evidence for ortho-metalated bpy ligands in the cationic moiety.

Our spectroscopic and elemental analysis evidence for the third complex suggest an Ir(IV), cis- $[Ir^{IV}(bpy\text{-}N,N')_2Cl_2]^{+2}$ species, III. And finally the fourth complex isolated has been identified as the trans-$[Ir(bpy)_2Cl_2]^+$, IV.

The last chapter describes other ortho-metalated iridium (III) complexes similar to those described in Part I. NMR spectroscopic and photophysical results are presented.

TABLE OF CONTENT

LIST OF FIGURES

LIST OF TABLES

FORWARD

This dissertation covers two major area of research. The first is ortho-metalated iridium 2-phenylpyridine complexes in which the ppy ligand has been structurally modified by a methyl group either in the phenyl ring (ptpy) or pyridyl ring (mppy). Structural and photophysical characterization of these complexes is described in Part I, Chapters 2, 3 and 4.

The second major area of research is one I have been involved with for just this past year. It involves iridium bipyridyl complexes. Using Ir(IV) in the synthetic procedure results in four novel complexes. Our results show that two of these are ortho-metalated bpy complexes. The emphasis in Part 2, Chapters 5 and 6, is the structural characterization of these four bpy complexes.

A general overview of photochemistry is described in Chapter 1. This chapter is intended to give a simplified view of how the measurements in the thesis relates to photoconversion system.

Chapter 7 presents some ortho-metalated iridium complexes which I prepared or characterized during my tenure here.

The appendix is a package of experimental procedures. NMR is discussed in great length because of its significant in my research. Also in the appendix is an extension of the acknowledgement page found in page iii.

The following are structural representations of all the iridium complexes discussed in this dissertation.

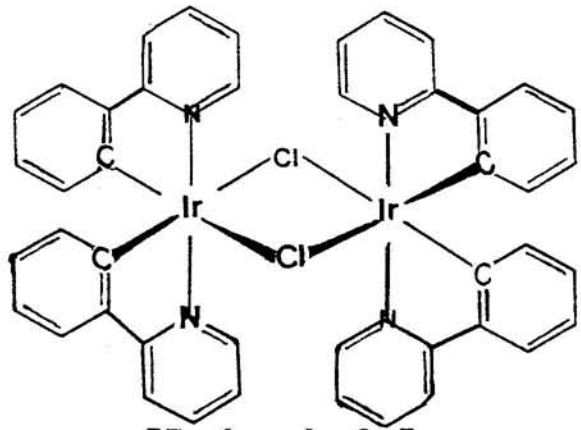

$[Ir(ppy)_2Cl]_2$

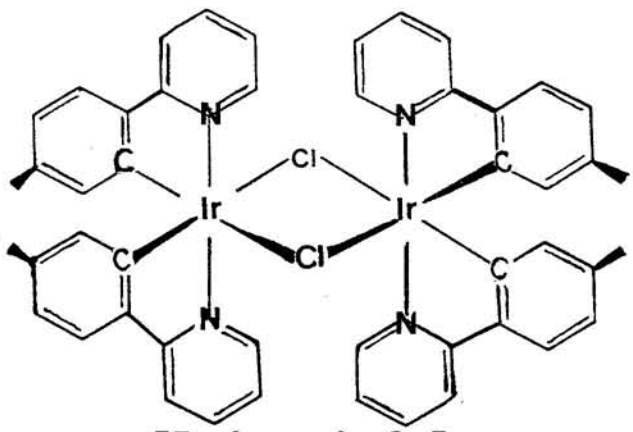

$[Ir(ptpy)_2Cl]_2$

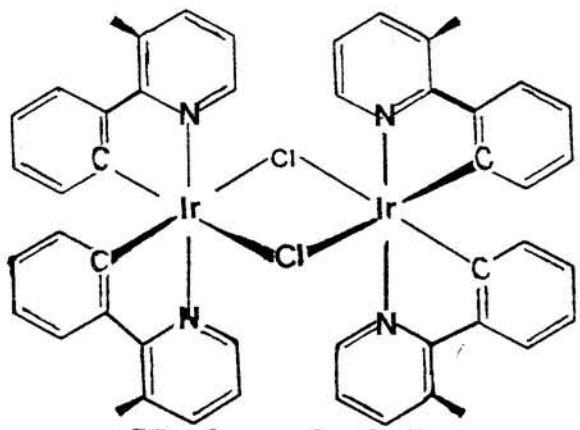

$[Ir(mppy)_2Cl]_2$

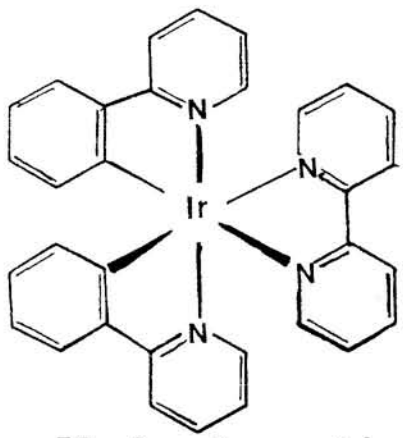

$[Ir(ppy)_2bpy]^+$

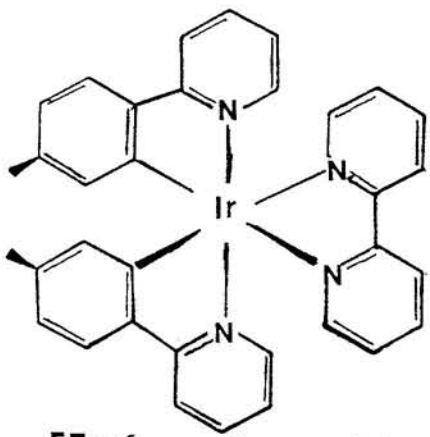

$[Ir(ptpy)_2bpy]^+$

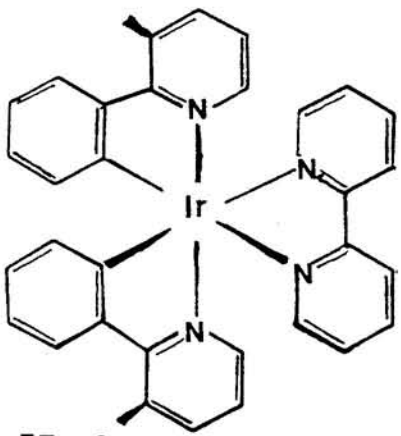

$[Ir(mppy)_2bpy]^+$

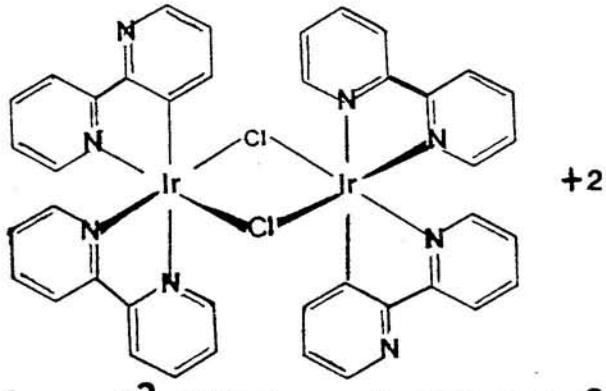

$[Ir(bpy\text{-}C^3,N')(bpy\text{-}N,N')Cl]_2^{2+}$

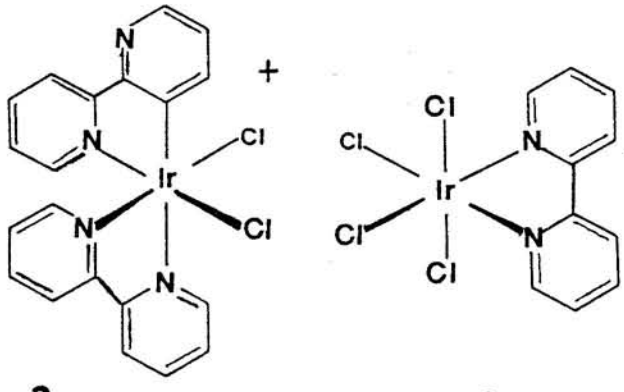

$[Ir(Hbpy\text{-}C^3,N')(bpy\text{-}N,N')Cl_2]^+ \ [IrCl_4(bpy)]^-$

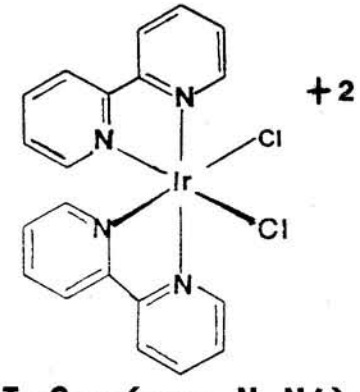

$[IrCl_2(bpy\text{-}N,N')_2]^{2+}$

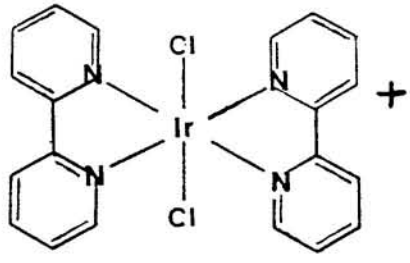

TRANS-$[Ir(bpy)_2Cl_2]^+$

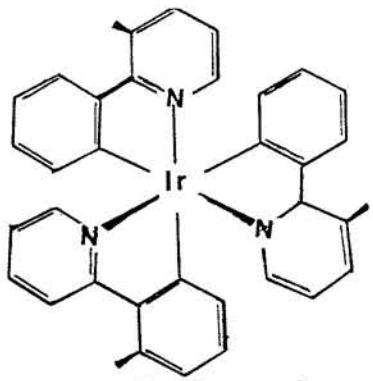

FAC-IR(MPPY)$_3$

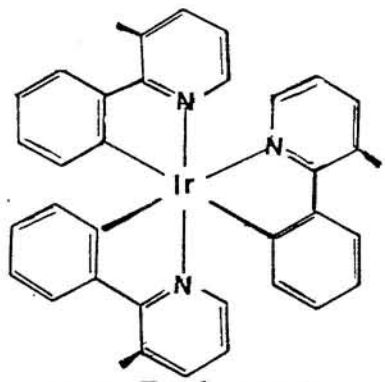

MER-IR(MPPY)$_3$

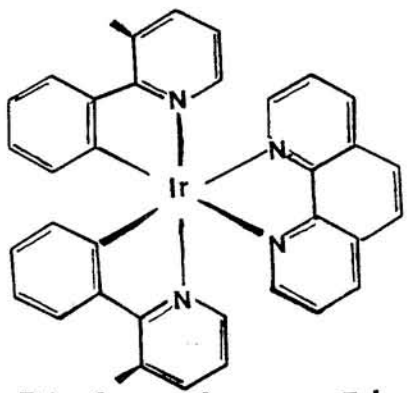

[IR(MPPY)$_2$PHEN]$^+$

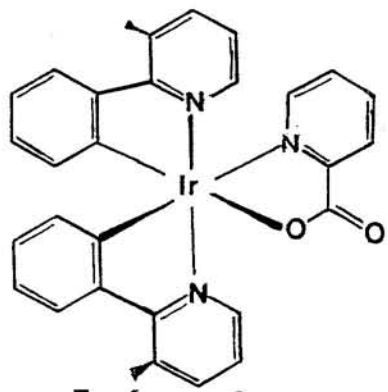

IR(MPPY)$_2$PIC

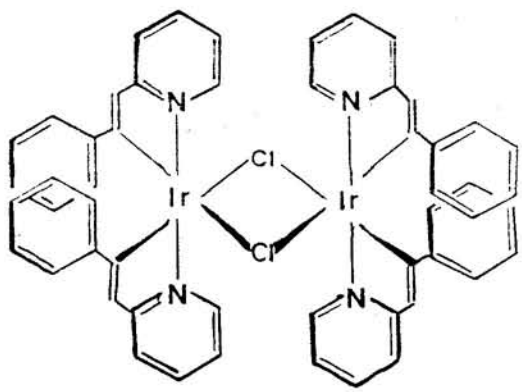

[IR(STPY)$_2$CL]$_2$

CHAPTER 1

ORTHO-METALATED COMPLEXES AND STORAGE OF SOLAR ENERGY: A GENERAL OVERVIEW.

The whole of science is nothing more
than a refinement of everyday thinking.

- Albert Einstein

Our group started research in ortho-metalated complexes when Professor Watts first discovered an isomer of $Ir(bpy)_3^{3+}$.[1,2] The structure of this isomer, $[Ir(bpy\text{-}C^3,N)(bpy\text{-}N,N')_2]^{2+}$, was the center of numerous debates, which were finally settled by crystallographic analysis.[3,4] The crystal structure showed that the product in question possesses two normal chelating bpy ligands while the third was bound to the iridium center via metalation; through the N' atom from one pyridyl ring and the C^3 atom of the other pyridyl ring, Figure 1.1. Later Watts et al. showed that the structure of this isomer in solution is similar to that in the solid state.[5] NMR analysis included two dimensional shift correlation spectroscopy (COSY) to assist in the assignment of all the proton resonances in the ^1H NMR spectrum and to provide insight on the electronic

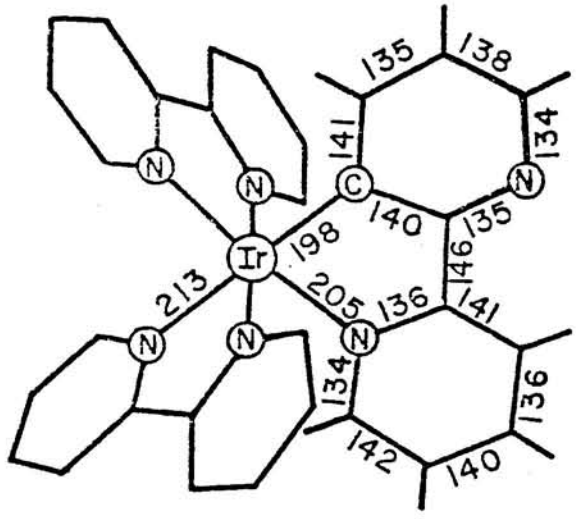

FIGURE 1.1

Structure of $[Ir(bpy\text{-}C^3,N)(bpy\text{-}N,N')_2]^{2+}$. [3]

properties of the complex. It was this pioneering work with $[Ir(bpy\text{-}C^3,N')(bpy\text{-}N,N')_2]^{+2}$ which led our research group to the study of ortho-metalated complexes and to rely on NMR techniques for the elucidation of molecular structures.

The topics of research presented in this dissertation involve the structural characterization and photophysical investigation of iridium-carbon σ-bonded complexes which are capable of photosensitizing chemical reactions for solar storage via fuel generation. The experimental arsenal covers (1) synthetic schemes to prepare targeted complexes, (2) NMR techniques and X-ray crystallography to elucidate structures, (3) cyclic voltammetry to determine potentials of the ground state, (4) absorption, emission and excited state absorption measurements to characterize the excited state, (5) laser spectroscopy, Stern-Volmer quenching and

quantum yield measurements to monitor lifetimes and understand electron and energy transfer processes. Furthermore, investigation on the dependence of temperature, solvent, excitation and pH were used to elucidate electronic transitions in some of these complexes. Ultimately, results from these experiments will enable us to determine the viability of these complexes as photoreagents.

The development of solar-driven artificial processes (photoconversion systems) that convert abundant resources into chemical fuels, e.g., $2H_2O + h\nu \longrightarrow 2H_2 + O_2$ is important if only to sustain current energy requirements for the near future. Photoconversion mechanisms in photobiology, photoelectrochemistry, photovoltaics and photochemistry provide systems capable of harnessing the sun's energy cleanly and efficiently.[6] More recently, Jean-Marie Lehn suggests the development of supramolecular devices for this purpose.[7] The main component fundamental to the photoconversion system is the photosensitizer. Characterization of complexes capable of photosensitizing chemical reactions is the focus of research in Professor Watts' laboratory.

Kutal[8] describes the main components of a photoconversion system, Figure 1.2, in which solar irradiation drives a photochemical reaction in a thermodynamically unfavorable direction, $\Delta G > 0$, to form products (chemical fuel). Photosensitizers are used to absorb the incident light because in most instances the reactant(s) do not absorb solar irradiation. Reversal of the cycle by application of heat or catalyst, liberates the stored energy.

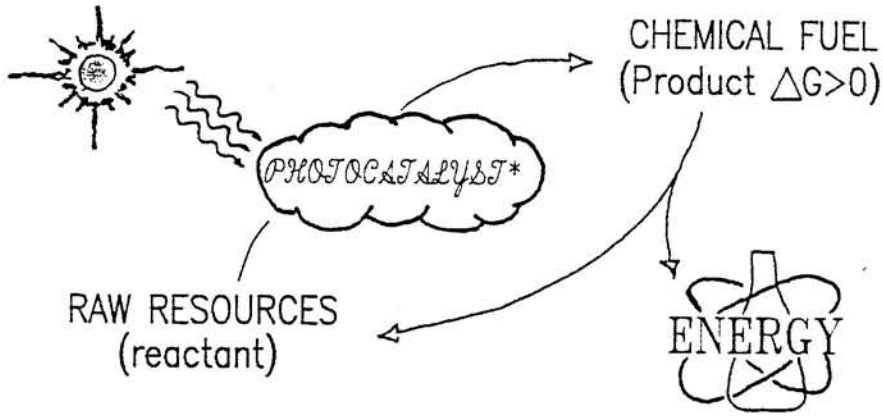

FIGURE 1.2

Fundamental components of an abiotic photoconversion system.[8]

This system will most likely require electron relays and redox catalysts in addition to the ones already mentioned. Nevertheless, as mentioned, the gist of a photoconversion system is the photosensitizer and its ability to absorb electromagnetic radiation, preferably at wavelengths utilizing the solar spectral range and then, through its excited state, activate inert substrates such as H_2O and CO_2 in order to transform optical energy to chemical potential energy stored in bonds. The photo-generation of excited state precursors (substrate bound to the metal catalyst) having sufficient redox potentials leads to substrate reduction or oxidation via multi-electron transfer processes which are necessary for product formation.

Kutal,[8] Bolton[9] and Balzani[10] discuss several criteria fundamental for a viable photoconversion energy storage cycle. These criteria are: (1) The reactions in the photochemical cycles should be capable of operating over a wide band width of the visible and ultraviolet portion of the solar spectrum with a threshold wavelength well into the red or near infrared. In other words, the photosensitizer should absorb visible light. (2) The photochemical reaction must be endergonic, $\Delta G > 0$. That is, upon absorption of electromagnetic radiation the system must proceed in the thermodynamically unfavorable direction. (3) The endergonic photoreactions must be cyclic with only raw materials and solar irradiation being consumed. That is, the photosensitizer must be regenerated after each cycle. (4) The quantum yield should be near unity. The efficiency of converting absorbed photons to chemical energy must be high. (5) For long term storage of the products, the back reaction must be extremely slow under ambient conditions. Furthermore, upon heating or addition of catalyst, the back reaction should proceed controllably, rapidly and specifically. (6) To ensure maximum efficiency, side reactions leading toward the depletion of photosensitizers, reactants, products and/or catalysts must be at a minimum. (7) Finally, reagents and other necessary components of the photoconversion system should be available, manageable, inexpensive and nontoxic.

There are inherent limitations in photoconversion processes aside these stringent requirements which limit the overall

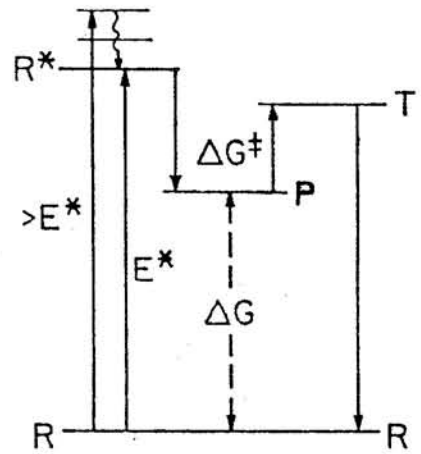

$$\text{ENERGY STORAGE: } R \xrightarrow{h\nu} P$$

$$\text{ENERGY RELEASE: } P \xrightarrow[\text{catalyst}]{\text{heat}} R$$

FIGURE 1.3

Energy diagram for photoconversion storage cycle.[8]

efficiency of converting solar energy to chemical fuel.[8,11] Figure 1.3 illustrates an energy diagram for a photoconversion process. The diagram shows that only photons with energies corresponding to E^* will be absorbed by the reactant R, without significant waste. Photons having energies less than the threshold value E^*, will not be absorbed. Furthermore, absorption of photons having energies greater than E^* results in the population of vibrationally excited levels of R^*; internal conversion results in the lowest vibrational level of R^* to be populated and any energy in excess of E^* is lost to the surroundings. In addition to absorption losses, the conversion of raw materials to useful fuels will require free energy from the system to prevent the back reaction. As such, the available energy corresponds to ΔG and not E^*; the system will in effect lose energy due to storage.

Ross and Hsiao et al.[12], calculated the maximum thermodynamic efficiency for an abiotic solar conversion system to be 32% at 840 nm, taking into consideration the fraction of solar power available at the bandgap energy. If losses due to an activation barrier ($\Delta G^{\ddagger}$) are figured into the calculation, the gross efficiency drops to 9.2 $\pm$ 0.8%. This, however, is still comparable to the 5.6 $\pm$ 1.2% efficiency for photosynthesis.[13]

TABLE 1.1

Endergonic fuel-generation reactions

Reaction	ΔG (KJ/mol)	n (mol)	E (V)
$H_2O(l) + h\nu \longrightarrow H_2(g) + 1/2\ O_2(g)$:	237	2	1.23
$CO_2(g) + 2H_2O(l) + h\nu \longrightarrow CH_3OH(l) + 3/2\ O_2(g)$:	703	6	1.21
$CO_2(g) + 2H_2O(l) + h\nu \longrightarrow CH_4(g) + 2O_2(g)$:	818	8	1.06
$N_2(g) + 3H_2O(l) + h\nu \longrightarrow 2NH_3(g) + 3/2\ O_2(g)$:	678	6	1.17

Raw materials for photoconversion processes are readily available from our environment. Economical, ecological and energetic considerations indicate that water, carbon dioxide and dinitrogen are the most attractive raw materials for photoconversion

processes. Table 1.1 shows some of the thermodynamic parameters of some endergonic fuel generation reactions[9].

All the reactions shown in Table 1.1 involve multi-electron changes. Herein lies the problem; photoredox reactions of transition metal complexes generally occur with the transfer of only one electron per absorbed photon. How can a one-electron redox process satisfy a multi-electron reaction in such a way as to avoid formation of high energy radicals that retard the efficiency of the photoconversion process? The answer lies in charge-storage catalyst whose role is to mediate multi-electron changes by accumulating the proper number of electrons for delivery to the reactants and furthermore stabilizing any intermediates that form.

Traditional photosensitizers charge-storage catalyst such as $Ru(bpy)_3^{2+}$ operate in aqueous media. However, recent emphasis has been toward the development of complexes capable of operating in both aqueous and nonaqueous media and possessing multiple functionality as photosensitizer / relay / catalyst. Functions of metal complexes may be classified as: (1) electron relays in order act as intermediate electron storage devices, (2) redox catalysts to enhance the rate of the redox processes, and (3) redox substrates to regenerate the photosensitizer or catalyst. The ability of a metal complex to play multiple roles in photoconversion systems is contingent on its excited state (as well as ground state) properties.

The excited states of metal complexes are useful in photochemical conversion because they participate in rapid outer sphere electron transfer, sustain long lifetimes, possess favorable redox potentials and are accessible by absorption of visible light. Balzani[10] points out that an excited state induced in a molecule by absorption of light becomes virtually a new species with its own chemical and physical properties distinct from those corresponding to the ground state molecule. In the excited state, the molecule has a higher electron affinity and a lower ionization potential. This asset makes the excited state a better oxidant and a better reductant than that of the ground state.

The Latimer diagram of $Ru(bpy)_3^{2+}$, Figure 1.4, shows that the excited state is both a moderately strong oxidant (-0.86 V vs. NHE) and a very strong reductant (+0.84 V) compared to the ground state

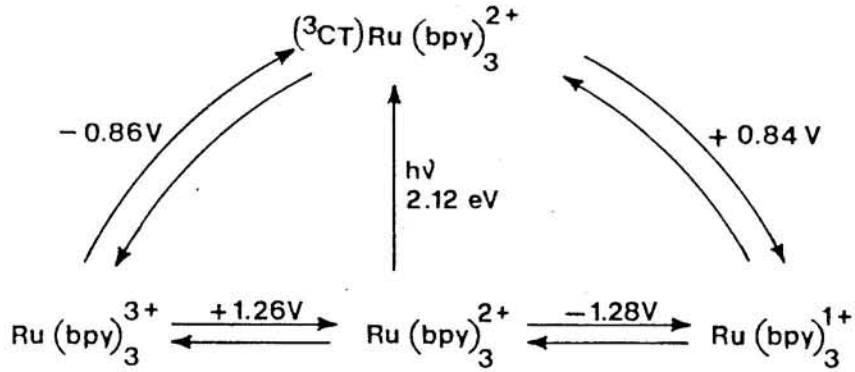

FIGURE 1.4

Latimer diagram for $Ru(bpy)_3^{2+}$ (vs. NHE).[10]

which has an oxidation and reduction potential of +1.26 and -1.28 V, respectively. Moreover, the excited state redox potential of metal complexes such as $Ru(bpy)_3^{2+}$, may be altered ("tuned") by several types of structural modifications. Modifications include: (1) changing the central metal, (2) replacing some or all of the ligands with other suitable ligands i.e., 2-phenylpyridine (**ppy**), (3) modifying the ligands by adding suitable functional groups, and (4) using mixed bimetallic complexes to access, within a single chemical moiety, redox properties associated with each monomeric complex.

Changing the metal in $Ru(bpy)_3^{2+}$ to Ir(III) for example, produces a complex, $Ir(bpy)_3^{3+}$, with excellent photo-oxidizing power (~2 V vs. NHE).[14] On the other hand, replacing bpy in $Ir(bpy)_3^{3+}$ with ppy produces a very strong photo-reductant, $Ir(ppy)_3$.[15] Species containing both bpy and ppy coordinated to a common metal ion center such as in $[Ir(ppy)_2bpy]^+$, have intermediate photoredox capabilities and can operate as either photo-oxidants or photo-reductants.[16] Thus, the optimization of photoredox properties of metal complexes can be provided by the combination of ortho-metalating ligands such as ppy and its derivatives with coordinating ligands such as bpy.

The metal-carbon bond in ortho-metalated complexes can be described as a 2-electron, 2-center covalent σ-bond with bonding density along the metal–carbon internuclear axis. The intriguing properties manifested from the metal carbon σ-bond make ortho-metalated complexes viable for many photosensitizer applications.

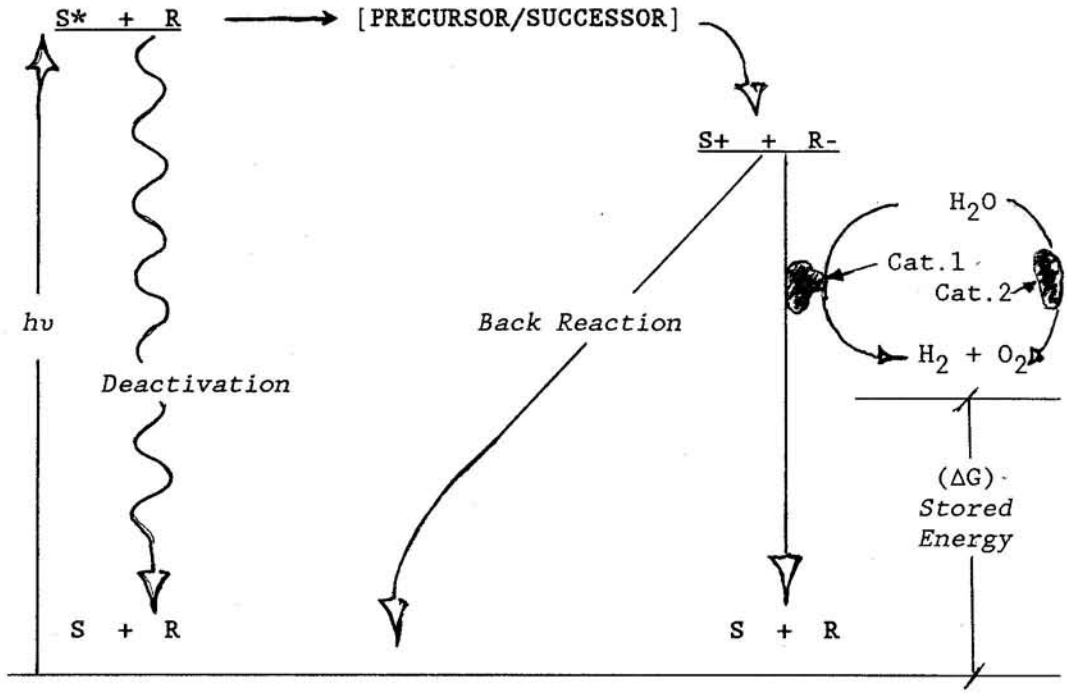

FIGURE 1.5

Energy reaction coordinate diagram for substrate (S) and reactant (R) undergoing electron transfer processes.[19]

Favorable properties imparted through ortho-metalation include:[17,18] 1) An enhancement of the excited state redox potential to drive endergonic chemical reactions as a consequence of the increase of the energy of metal-localized states because of the greater ligand field strength of ppy over bpy. 2) The availability of low-lying MLCT states from the enhancement of electron density about the metal center from the strong σ-donor ability of the metal-carbon bond. 3) Cathodic shift in the oxidation potential of the metal center in

ortho-metalated complexes giving rise to very strong photoreductants but relatively weak photooxidants.

Gratzel[19] discusses three examples of suitable light-harvesting units which utilize metal complexes to capture photons and convert their energy to storable chemical fuel. The first two units consist of colloidal semiconductors and are more efficient than the third unit. The third, and most fundamental unit, comprises the sensitizer/relay pair. This unit, however, has poor efficiency because the area in which light induced charge separation and redox catalysis occurs, is not confined in a concentrated area.

In its most basic form, the unit consist of a sensitizer (S) and a relay (R), Figure 1.5. The illustration shows no spontaneous electron transfer occurring between the two species, S and R in the ground state. Upon excitation however, the sensitizer becomes virtually a new molecule with respect to the corresponding ground state thus exhibits different chemical properties. The sensitizer can then diffuse to an electron relay forming the precursor S*•••R. During this encounter, electron transfer may occur forming the successor $[S^{+}\bullet\bullet\bullet R^{-}]$; at this stage a majority of the photon energy absorbed by S can be converted into chemical potential through the product ions S^{+} and R^{-}, see equation 1.1. These ions can then convert raw materials into chemical fuel, as shown in Figure 1.5.

(1.1) $S + R + h\nu \rightarrow S^{*} + R \rightleftharpoons \underset{\text{Precursor}}{S^{*}\bullet\bullet\bullet R} \rightleftharpoons \underset{\text{Successor}}{[S^{+}\bullet\bullet\bullet R^{-}]} \rightarrow \underset{\text{Redox product}}{S^{+} + R^{-}}$

The electron transfer within the precursor, $[S^{+}\cdots R^{-}]$ is governed by the Franck-Condon principle in which the nuclear positions and nuclear velocities remain essentially unchanged during the electronic transition.[20-22] The potential energy diagram, Figure 1.6, shows that there is an energy state where the precursor and successor have identical energies. At this point in the precursor/successor encounter, electron transfer occurs without violating the Franck-Condon principle. Upon electron transfer, the inner vibration coordinates of the molecules and the outer solvation sphere adjust to a nonequilibrium position. Consequently there is an expenditure of free energy of reorganization ΔG^{*}_{λ} in the system. ΔG^{*}_{λ} may be related to the rate constant of the electron transfer event by the equation 1.2.

(1.2) $$K_t = \gamma_N K_{el} \text{ EXP } \{-\Delta G^{*}_{\lambda} / RT\}$$

In this equation, γ_N is the effective vibration frequency, K_{el} is the electronic transmission coefficient, R is the universal gas constant and T is the temperature in Kelvins.

Furthermore, ΔG^{*}_{λ}, a kinetic parameter, can be related to the free energy, $\Delta G°$, a thermodynamic parameter, for electronic transfer, by the Marcus-Hush equation 1.3.

(1.3) $$\Delta G^{*}_{\lambda} = \Delta G^{*}_{\lambda}(o) \; [1 + \{\Delta G^{o}/4 \; \Delta G^{*}_{\lambda}(o)\}]^{2}$$

Here, $\Delta G^{*}_{\lambda}(o)$ is the free energy of reorganization. The Marcus equation implies that the free-energy of activation is expected to

decrease (meaning the reaction rate increases) when the reaction is thermodynamically favored. There is a point, however, in which the rate decreases at even higher thermodynamic driving force; this is called the Marcus inverted region.[20]

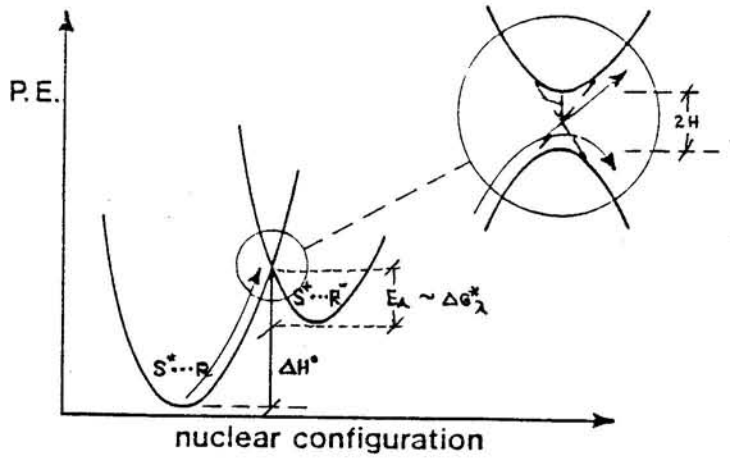

Figure 1.6

Classical model for electron-transfer process.[6,19]

Electron transfer rates can be measured by Stern-Volmer quenching.[23,24] Compounds which accept electrons are referred to as oxidative quenchers, and compounds which donate electrons are referred to as reductive quenchers. Table 1.2 lists some quenchers along with their redox potentials.[25-28] By lifetime or emission intensity measurements of the excited state complex as it undergoes electron transfer with these quencher compounds, rates of electron

transfer can be calculated. For lifetime quenching the rate constant of electron transfer, kq, may be determined from equation 1.4. A plot of $[1/\tau o - 1/\tau n]$ verses [Qn] leads to kq.

(1.4) $$[\ 1/\tau o - 1/\tau n\ ] = kq\ [Qn]$$

where, τo, is the lifetime of the complex with no quencher
τn, is the lifetime of the complex for a given concentration of quencher [Qn]
kq, is the rate constant of electron transfer
[Qn], is the quencher concentration

The excited state photoreducing and photo-oxidizing power ($*Er^o$ and $*Eox^o$) of the complex may be estimated by plotting kq against the redox potential, E^o, of the quencher. A quencher with small E^o values (quenchers which easily donate or accept electrons) will have kq values in the order of $\sim 10^9$. A kq with this magnitude, is usually referred to as diffusion controlled; diffusion of the quencher to the excited state governs the rate of electron transfer. As the E^o potential increases the electron transfer begins to be sluggish and the kq drops below diffusion control. In other words, each encounters does not lead to electron transfer and a graph of E^o vs. log kq deviates from a straight line (with slope zero) and starts to break downward (as you will see in Figure 3.4.11). The E^o potential at which the graph breaks is estimated to be the excited state redox potential.[29] The curvature of this graph also provide insights into the degree of structural distortion of the excited state.

TABLE 1.2

Redox Potentials of Oxidative and Reductive Quenchers (vs. NHE)

Oxidative Quenchers	-E°	Reductive Quenchers	E°.
pDNB p-dinitrobenzene	0.69	Pt phenothiazine	0.53
mDNB m-dinitrobenze	0.90	DMA N,N-dimethylaniline	0.81
NBA m-nitrobenzaldehyde	1.02	DPA diphenylamine	0.83
CNB p-chloronitrobenzene	1.06	AN aniline	0.98
NB nitrobenzene	1.15	TMB 1,2,4 trimethoxybenzene	1.12
MNB p-methylnitrobenzene	1.20	DMB 1,4 Dimethoxybenzene	1.34
pAN p-aminonitrobenzene	1.34	mTMB 1,3,5-trimethoxybenzene	1.49

In the past five years our group has synthesized and identified ortho-metalated complexes for use in photoconversion schemes. To this end, Dr. Kevin A. King was responsible for pioneering the work in ortho-metalated complexes.[30] During his tenure in the group, he prepared and characterized iridium dimers such as $[Ir(NC)_2Cl]_2$ where NC = 2-phenylpyridine (**ppy**), or 7,8-benzoquinoline (**bzq**). From these dimers, he prepared complexes of the type $[Ir(NC)_nNN_{3-n}]^{3-n}$ where NN is 2,2'-bipyridine, or 1,10-phenanthroline. He also

isolated the first Ir(III) ppy triply ortho-metalated complex, fac-$Ir(ppy)_3$. Ashley P. Wilde studied the excited state behavior of some of these iridium complexes.[31] Dr. Steven Sprouse synthesized Rh analogues,[32] while Dr. Carl A. Craig prepared the Pd and Pt analogues[33] with other ligands such as 2,(2-thienyl)pyridine, 2-phenylpyrimidine and ethylenediamine among those already mentioned. Craig also developed the synthetic scheme to couple mixed metal, mixed valence ortho-metalating complexes of the type $[M(NC)Cl_2(NC)_2M']$ where M is Pt, or Pd, NC is ppy or bzq, and M' is Rh(III). Dr. Peter Spellane prepared Re analogues, but his greatest asset to the group was his pioneering work in NMR spectroscopy to characterize the Ir, Ru, and Rh complexes of King and Sprouse.[34] The collaborative efforts by these individual have afforded fundamental understanding on the utility of ortho-metalated complexes as photosensitizer.

LITERATURE CITED:

1. Watts, R.J.; Harrington, J.S.; Van Houten, J. J. Am. Chem. Soc. **1977** 99 2179.

2. Watts, R.J.; Harrington, J.S.; Van Houten, J. J. Adv. Chem. Ser. **1978** 168 157.

3. Wickramashinghe, W.A.; Bird, P.H.; Serpone, N. J. Chem. Soc. Chem. Commun. **1981** 1284.

4. Nord, G.; Hazell, A.; Hazell, E.; Wernberg, O. Inorg. Chem. **1983** 22 3429.

5. Spellane, P.J.; Watts, R.J.; Curtis, C.J. Inorg. Chem. **1983** 22 4060.

6. "Photochemical Conversion and Storage of Solar Energy"; Connolly,J.S. ed., Academic Press: New York, N.Y., 1981.

7. Lehn,J-M. Angew. Chem. Init. Ed. **1988** 27:1 89.

8. Kutal,C. J. Chem. Ed. **1983** 60:10 882.

9. Bolton,J.R. Science **1978** 202 705.

10. Balzani,V.; Moggi,L.; Manfrin,M.F.; Bolletta,F.; Gleria,M. Science **1975** 189 852.

11. Adamson,A.W.; Namnath,J.; Shastry,V.J.; Slawson,V. J. Chem. Ed. **1984** 61:3 221.

12. Ross,R.T.; Hsiao,T.L. J. Appl. Phys. **1977** 48 4783.

13. Zelitch,I. Photosynthesis, Photorespiration and Plant Productivity; Academic Press: New York, 1971; p 131.

14. Bergeron,S.F.; Watts,R.J. J.Am.Chem.Soc. **1979** 101 3151.

15. King,K.A.; Spellane,P.J.; Watts,R.J. J.Am.Chem.Soc. **1985** 107 1431.

16. King,K.A.; Watts,R.J. J.Am.Chem.Soc. **1987** 109 1589.

17. Sprouse, S.; King, K.A.; Spellane, P.J.; Watts, R.J. J. Am. Chem. Soc. **1984** 106 6647.

18. King, K.A.; Spellane, P.J.; Watts, R.J. J. Am. Chem. Soc. 1984 107 1431.

19. "Energy Resources through Photochemistry and Catalysis"; Gratzel, M. ed., Academic Press: New York, N.Y., 1983.

20. Scandola, F.; Balzani, V. J. Chem. Ed. 1983 60:10 814.

21. Sutin, N.; Creutz, C. Ibid.

22. Balzani, V.; Bolletta, F.; Gandolfi, M.T. Topics Curr. Chem. 1978 75 1

23. Stern, O.; Volmer, M. Physik. Z. 1919 20 183.

24. "Creation and Detection of the Excited States"; Wagner,P.J. ed., Vol. I Part A, Marcel Dekker: New York, N.Y., 1971.

25. Balzani, V.; Moggi, L.; Manfrin, M.F.; Bolletta, F. Coord. Chem. Rev. 1975 15 321.

26. Gafney, H.D.; Adamson, A.W. J. Am. Chem. Soc. 1972 94 8238.

27. Brock, C.R.; Meyer, T.J.; Whittern, D.G. J. Am. Chem. Soc. 1974 97 2909.

28. Marshall, J.L.; Stobart, S.R.; Gray, H.B. J. Am. Chem. Soc. 1984 106 3027.

29. King, K.A.; Finlayson M.F.; Spellane,P.J.; Watts R.J. Sci. Pap. Ins. Phys. Chem. Res. 1984 78 97 and reference therein.

30. King,K.A. "Ph.D.Thesis"; University of California, Santa Barbara, 1986

31. Wilde, A.P. "M.S. Thesis"; University of California, Santa Barbara, 1988

32. Sprouse,S.D. "Ph.D.Thesis"; University of California, Santa Barbara, 1984

33. Craig,C.A. "Ph.D.Thesis"; University of California, Santa Barbara, 1988

34. Spellane,P.J. "Ph.D.Thesis" University of California, Santa Barbara, 1985

PART I

METHYL-SUBSTITUTED PHENYLPYRIDINE ORTHO-METALATED Ir (III) COMPLEXES

Transition metal complexes containing ligands with extended π-systems (e.g., pyridine, bipyridine), have generated tremendous interest because of their potential to participate as photocatalysts in solar-driven artificial photoconversion processes.[1-10] The classic example of a molecule used as a photocatalyst in photoconversion systems is $Ru(bpy)_3^{2+}$.[3,4,5,11-15] The excited state redox potentials of metal complexes such as $Ru(bpy)_3^{2+}$ may be altered by several types of structural modifications as mentioned in Chapter 1. I have already described the advantage of using ortho-metalating **ppy** ligands over chelating **bpy** ligands in order to optimize the photoredox properties of metal complexes. In addition, ortho-metalation reactions of the type used in preparation of ppy complexes, allude to in Chapter 1, are common in the literature and many of the products have been well-characterized.[16-25] For example, the major complex produced in reactions of Iridium(III) chloride salts with **ppy** is an ortho-metalated dimer, $[Ir(ppy)_2Cl]_2$,

which like the triply ortho-metalated **ppy** monomer, $Ir(ppy)_3$,[26] is also a powerful photoreducing agent. The enhanced photoreducing potential of these ortho-metalated complexes is attributed to the increase of electron density about the metal due to the strong σ-donor character of the coordinating carbon which facilitates electrochemical oxidation at the metal center as evidenced in electrochemical measurements.[27] Furthermore, low energy metal-to-ligand charge-transfer (MLCT) transitions result when both σ-metalating ligands such as **ppy** and good π-accepting ligands such as **bpy** are present in the coordination sphere of a central metal ion as in $[Ir(ppy)_2bpy]^+$.[27-29]

The purpose of the work in Part I in this dissertation, was to explore the enhancement of the already-high photoreducing potential of ortho-metalated complexes such as $[Ir(ppy)_2Cl]_2$ and $[Ir(ppy)_2bpy]^+$ by introducing functional groups onto the **ppy** ligand. Two ortho-metalating ligands employed for this purpose were 3-methyl-2-phenylpyridine **(mppy)** and 2(p-tolyl)pyridine **(ptpy)**, Figure 2.1.1. These ligands contain activating methyl groups which donate electron density to either the phenyl ring (**ptpy**) or the pyridyl ring (**mppy**). The result of a study of Ir (III) complexes containing methyl-substituted ortho-metalating ligands include extensive structural characterization by NMR techniques and crystallographic analysis, complete electrochemical measurements, and exhaustive photophysical investigation.

CHAPTER 2

CHARACTERIZATION OF ORTHO-METALATED DICHLORO-BRIDGED IRIDIUM DIMERS

Generally the theories we believe we call facts,
and the facts we disbelieve we call theories.

-Felix Cohen.

This chapter describes the characterization of $[Ir(ptpy)_2Cl]_2$ and $[Ir(mppy)_2Cl]_2$ dimers. Structural characterization by ^1H, ^{13}C, APT, SFORD, and selective decoupling NMR techniques suggest a D_2 symmetric (point group) complexes. Proton and carbon-13 resonances were assigned by COSY and CSCM techniques, respectively. The ultraviolet visible absorption spectra show low energy charge transfer bands ranging from 484 to 400 nm. Emission spectra at room temperature show a broad emission band at 515 nm but structured emissions with band maxima at 494 and 526 nm in 77 K glasses. Emission lifetimes are 5 μs at 77 K and range between 32 - 148 ns under ambient conditions. Quantum yields are less than 1% for both dimers. Finally, CV's indicate cathodic shifts in the half-wave potentials up to 100 mV for these dimers compared to the nonsubstituted ppy dimer, $[Ir(ppy)_2Cl]_2$.

I. SYNTHESES

1. Tetrakis (2-(p-Tolyl)pyridine-C^2,N')-μ-Dichlorodiiridium. $[Ir(ptpy)_2Cl]_2$

Iridium trichloride hydrate (0.3557g, 1.0mmol) was combined with 2-(p-tolyl)pyridine (0.70ml, 4.4mmol) in 2-ethoxyethanol (30ml, distilled and dried over $MgSO_4$) and water (10ml). The preparation and purification of this complex was carried out analogously to the $[Ir(ppy)_2Cl]_2$ synthesis[16,25,29]. The resulting dark yellow crystals and the yellow amorphous powder were collected on a glass frit and dried to yield the product (0.148g, 26.22%).

Calculated for $Ir_2C_{48}H_{40}N_4Cl_2 \cdot 3/4(C_7H_8)$:

Analysis: C,53.42%; H,3.87%; N,4.68%; Cl,5.92%.

Found: C,53.29%; H,3.90%; N,4.52%.

2. Tetrakis (3-Methyl-2-phenylpyridine-C^2,N')-μ-Dichlorodiiridium. $[Ir(mppy)_2Cl]_2$

The synthesis and work up of this product, using iridium trichloride hydrate (0.3527g, 1.0mmol) and 3-methyl-2-phenylpyridine (0.70ml, 4.4mmol), was carried out analogously to the $[Ir(ptpy)_2Cl]_2$ synthesis to give $[Ir(mppy)_2Cl]_2$ as a bright yellow amorphous powder (0.2829g, 50.16%).

Calculated for $Ir_2C_{48}H_{40}N_4Cl_2$:

Analysis: C,51.10%; H,3.57%; N,4.97%; Cl,5.74%.

Found: C,50.78%; H,3.66%; N,4.62%.

II. MEASUREMENTS

1. NMR

The ^{1}H, ^{13}C, attached proton test (APT), 2D homo- (COSY) and 2D heteronuclear (CSCM) correlation spectroscopy spectra were obtained from a GN-500 FT-NMR General Electric spectrometer. Single frequency off-resonance decoupled (SFORD) spectra and selective decoupling experiments were obtained from a Nicolet NT-300 FT-NMR spectrometer. Samples were dissolved in 99.9 atom % dichloromethane-d_2 for analysis. Details of the NMR measurements are described in Appendix A.

2. Cyclic Voltammetry

An IBM EC-225 voltammetric analyzer was used to obtain cyclic voltammogram (CV) measurements. Ambient temperature CVs with tetraethylammonium hexafluorophosphate (TEAH) supporting electrolyte were obtained in dichloromethane (distilled and dried over $CaCl_2$). Details of the CV measurements may be found in Appendix B.

3. Absorption

Absorption spectra were obtained from a Cary 15 spectrophotometer. Dimer samples were dissolved in dichloromethane with concentration ranging from 10^{-4} to 10^{-6} M. Further details of the absorption measurements are given in Appendix C.

4. Luminescence

Emission spectra were obtained from either a Perkin-Elmer MPF-3 spectrophotofluorimeter or a Spex Fluorolog 2 series spectrophotometer. Temperature emission studies utilized an Oxford Instrument Cryocal PR-100, operated by a TRI Research T-2000 Cryocontroller. Three dimensional emission-excitation-intensity (EEI) stack plots were automatically accumulated from the Spex Datamate with the excitation-emission matrix program supplied by Spex Industries. Lifetimes were measured with an AVCO-Everett C-950 nitrogen laser with 337 nm pulses. Dichloromethane (DCM) solvent was used for ambient temperature emission measurements and ethanol-methanol-dichloromethane (EtOH-MeOH-DCM 4:1:1 v/v/v) was used for low temperature (77 K) measurements. Quantum yields were measured using optically dilute methods; fluorescein in 0.1 N NaOH was used as the standard with dimer samples dissolved in DCM for analysis. Experimental details are described in Appendix C.

III. RESULTS

1. ^{1}H and ^{13}C NMR

Labeling schemes for 2-(p-tolyl)pyridine and 3-methyl-2-phenylpyridine, Figure 2.1.1 may be helpful for this discussion. The representative spacial structures of $[Ir(ptpy)_2Cl]_2$ and $[Ir(mppy)_2Cl]_2$, Figure 2.1.2, may also be helpful in understanding the shielding and deshielding affects for the protons and carbons in these dimers.

The ^{1}H NMR spectra of $[Ir(ptpy)_2Cl]_2$ and $[Ir(mppy)_2Cl]_2$, Figures 2.1.3a and 2.1.4a respectively, show proton resonances between 10 - 0 ppm. The intense aliphatic singlet at 1.97 ppm represents the protons in the methyl group. The aromatic region of the spectra, Figures 2.1.3b and 2.1.4b, integrates for seven resonances (excluding DCM-d_2 solvent, chemical shift (δ) = 5.32 and residual toluene, δ = 7.20), indicative of four equivalent **ptpy** (or mppy) ligands per molecule; each ligand containing seven distinct aromatic protons.

Proton resonances in the "A" and "B" spin system of the ligand for $[Ir(ptpy)_2Cl]_2$ and $[Ir(mppy)_2Cl]_2$ were assigned by COSY J-correlation connective analysis, Figures 2.1.5 and 2.1.6 respectively. Since selective decoupling spectra for $[Ir(ptpy)_2Cl]_2$ and $[Ir(mppy)_2Cl]_2$ gave similar results, its analysis will not be discussed here (a discussion on selective decoupling may be found in Appendix A). Proton assignments for the dimers are compiled in

Table 2.1 and Appendix A. These results are consistent with proton assignments for the nonsubstituted $[Ir(ppy)_2Cl]_2$ dimer.[16,25,29]

The ^{13}C NMR spectra for $[Ir(ptpy)_2Cl]_2$ and $[Ir(mppy)_2Cl]_2$, Figures 2.1.7 and 2.1.8 respectively, show all twelve carbon resonances. The intensities of these signals are consistent with one aliphatic (δ ~ 22), four nonprotonated and seven protonated carbons. The ^{13}C APT spectra for $[Ir(ptpy)_2Cl]_2$ and $[Ir(mppy)_2Cl]_2$, Figure 2.1.9 and 2.1.10 respectively, are supportive of this observation showing protonated carbon resonances as negative signals and the nonprotonated carbon as positive signals. The CSCM contour spectra for $[Ir(ptpy)_2Cl]_2$ and $[Ir(mppy)_2Cl]_2$, Figures 2.1.11 and 2.1.12, respectively, show the ^{1}H, ^{13}C and APT spectra on the projections with the contours mapped to their assigned nuclei. The seven contours in each spectrum are assigned to their proton/carbon resonances by ^{J}C-H connectivity from the ^{1}H projection to the ^{13}C projection; assignments are compiled in Table 2.1 and Appendix A.

TABLE 2.1

^{1}H and ^{13}C NMR Assignments for $[Ir(ptpy)_2Cl]_2$ and $[Ir(mppy)_2Cl]_2$ in dichloromethane-d_2 (vs. TMS)

Position	$[IR(PTPY)_2CL]_2$	$[IR(MPPY)_2CL]_2$
A_1	- /145.4	- /147.4
A_2	- /141.8	- /146.6
A_3	5.68/131.5	5.84/131.0
A_4	- /139.6	6.54/128.4
A_5	6.67/122.7	6.80/121.4
A_6	7.44/123.9	7.85/128.2
B_2	- /168.4	- /166.4
B_3	7.87/118.6	- /132.1
B_4	7.76/136.8	7.61/141.3
B_5	6.79/122.4	6.70/122.6
B_6	9.21/151.8	9.29/151.0
Me	1.97/21.7	2.87/23.8

FIGURE 2.1.1:

Ortho-metalating ligands (a.) 2-(p-tolyl)pyridine (ptpy) (b.) 3-methyl-2-phenylpyridine (mppy) (c.) 2,2′ bipyridine (bpy).

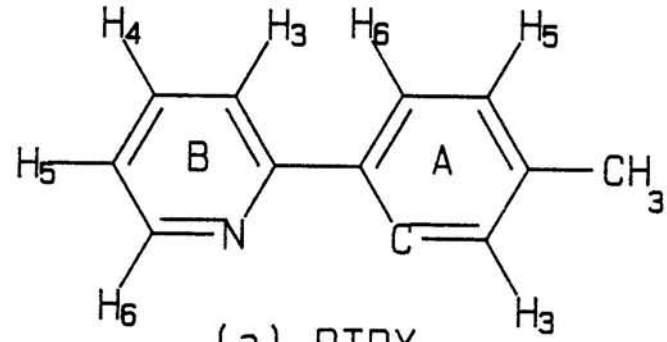

(a) PTPY

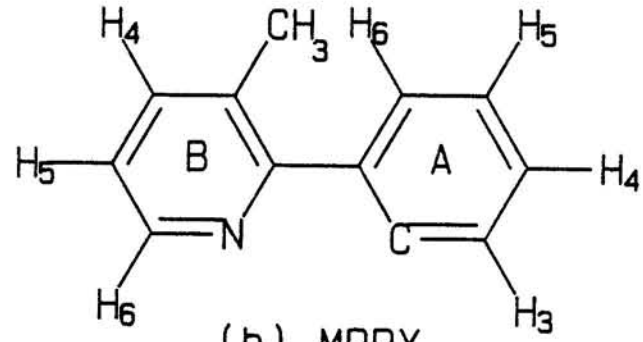

(b) MPPY

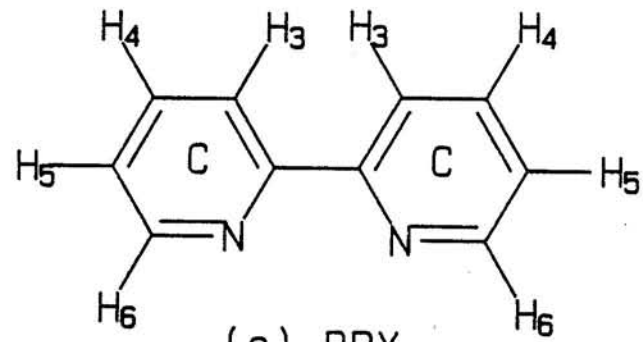

(c) BPY

FIGURE 2.1.2:

CHEM-X representative structures of (a.) $[Ir(ptpy)_2Cl]_2$ and (b.) $[Ir(mppy)_2Cl]_2$.

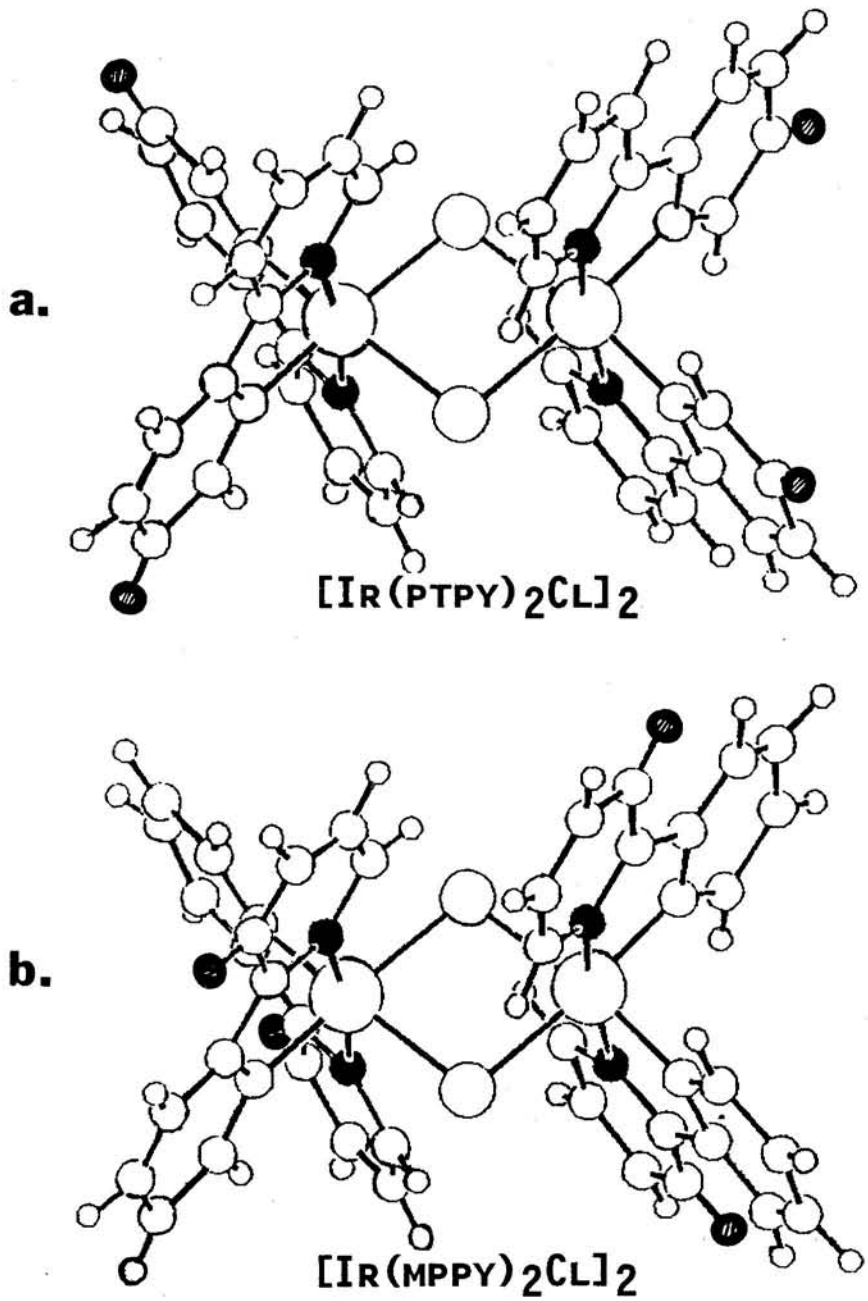

FIGURE 2.1.3:

^1H NMR spectra for $[Ir(ptpy)_2Cl]_2$ in dichloromethane-d_2 (a). 10 - 0 ppm and (b.) 10 - 5 ppm.

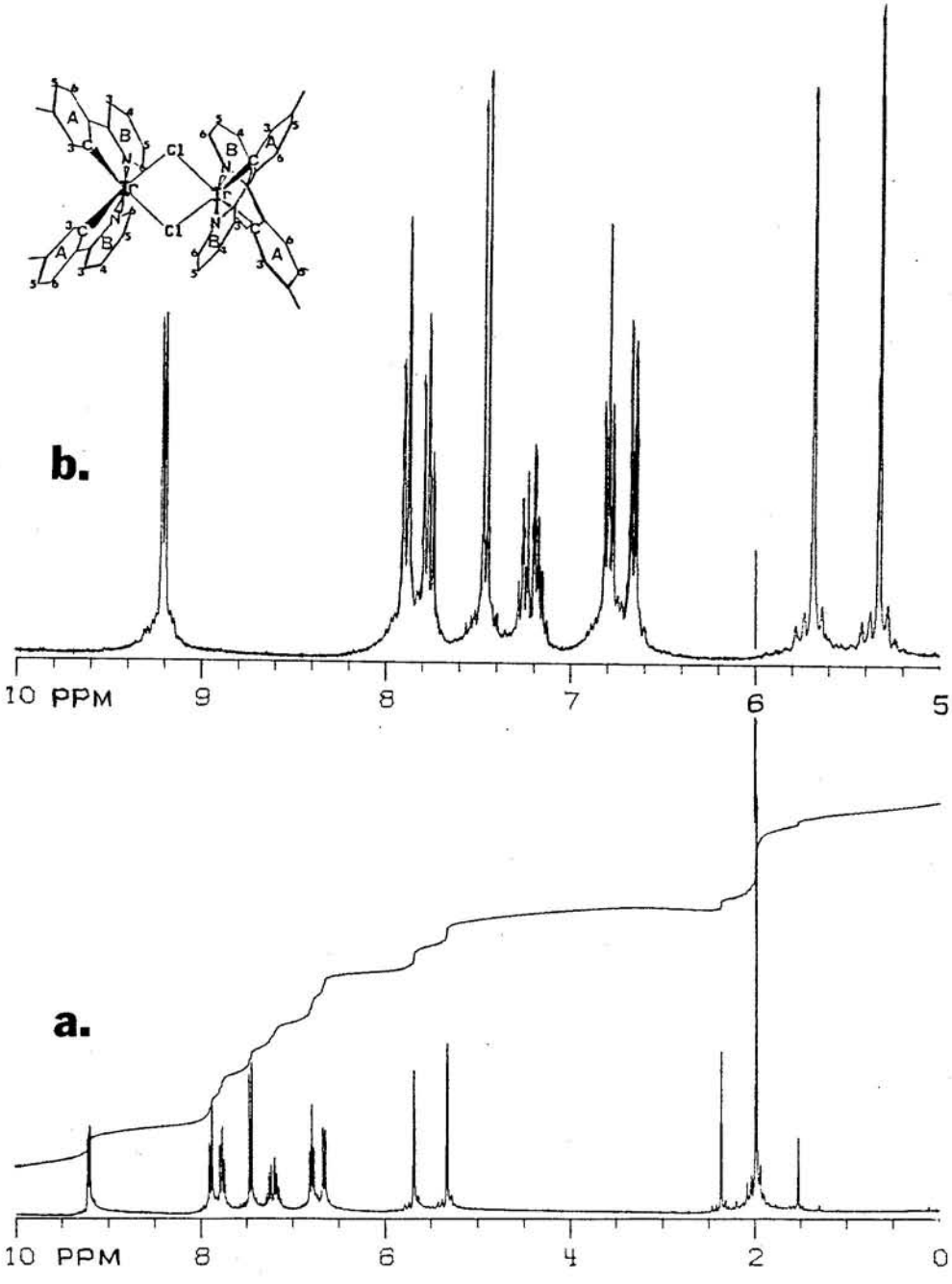

FIGURE 2.1.4:

^{1}H NMR spectra for $[Ir(mppy)_2Cl]_2$ in dichloromethane-d_2 (a). 10 - 0 ppm and (b.) 10 - 5 ppm.

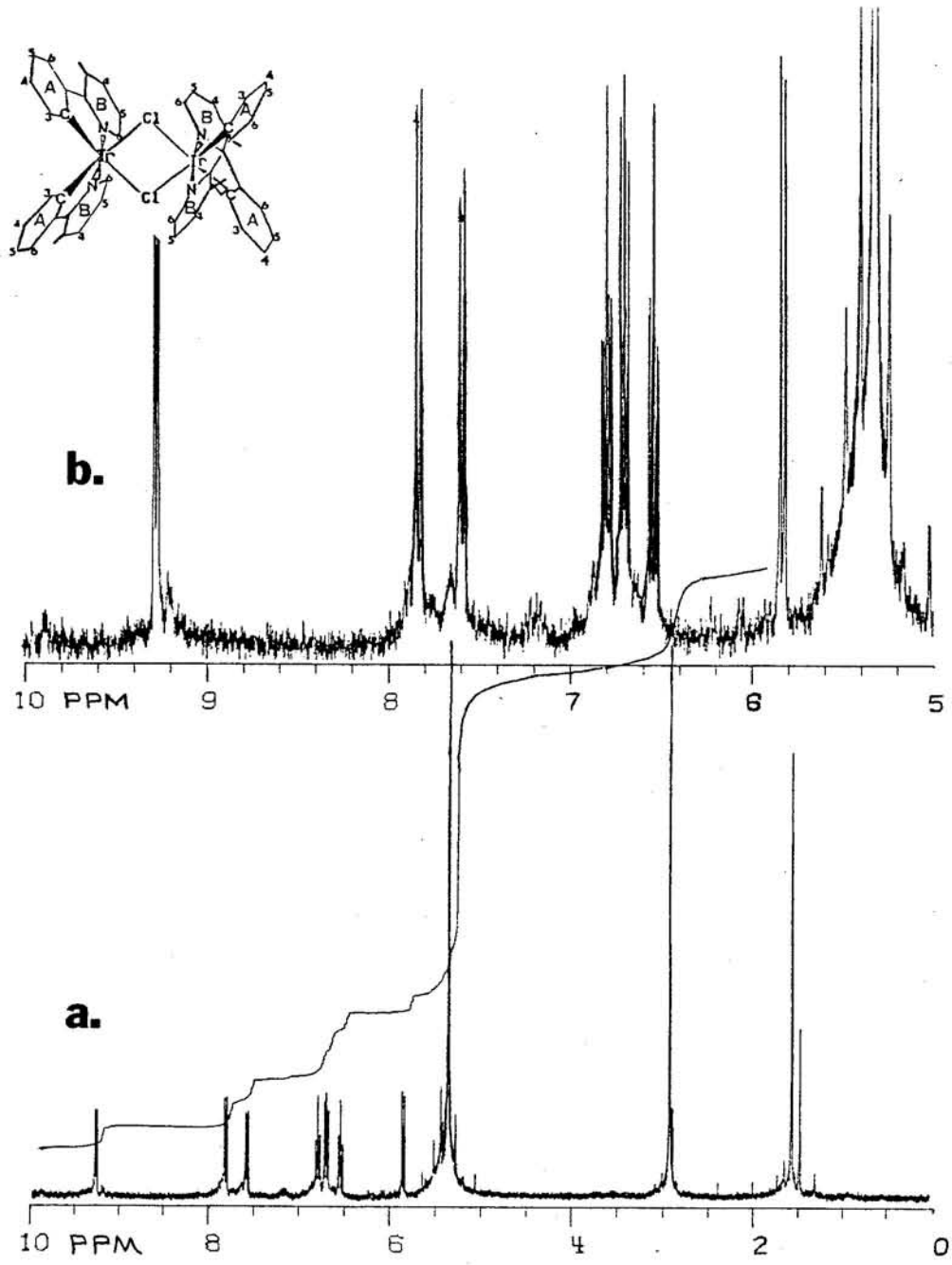

FIGURE 2.1.5:

^{1}H 2D-Correlation Spectroscopy (COSY) spectrum for $[Ir(ptpy)_2Cl]_2$ in dichloromethane-d_2.

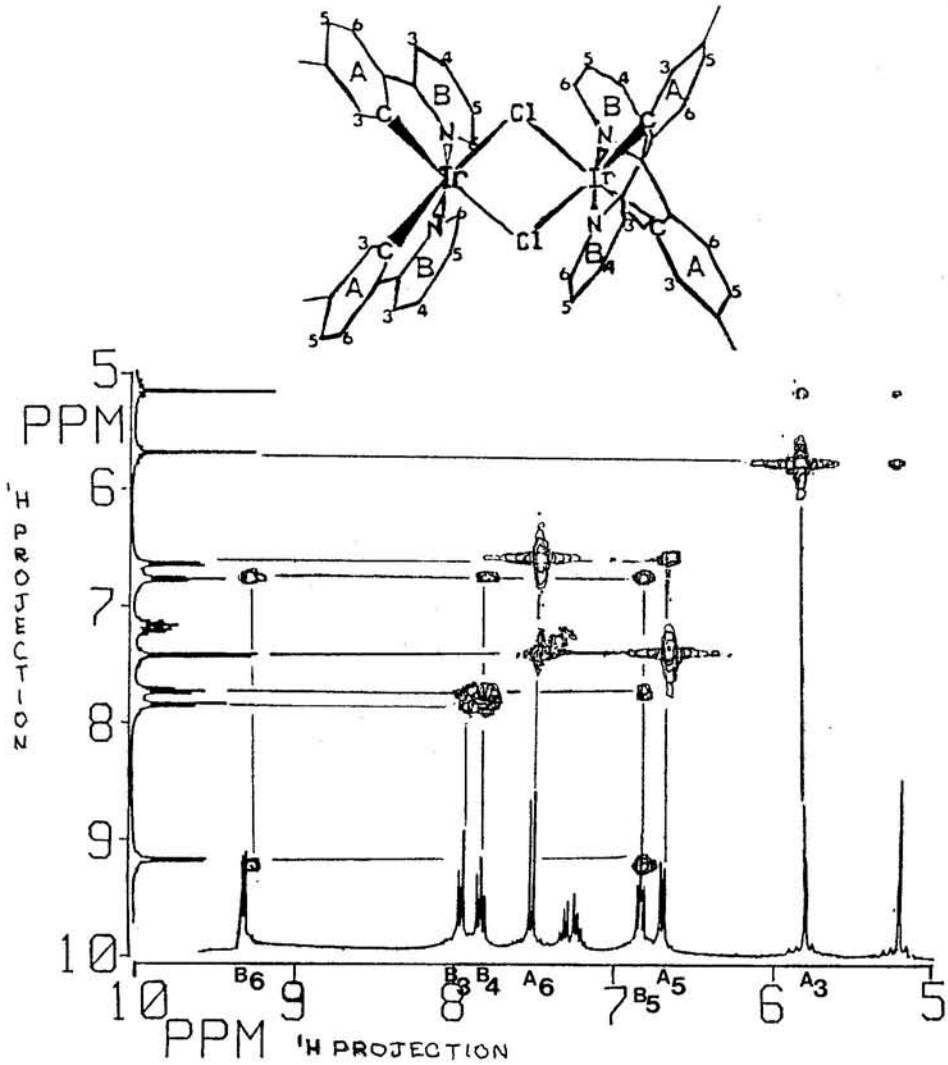

FIGURE 2.1.6:

^{1}H 2D-Correlation Spectroscopy (COSY) spectrum for $[Ir(mppy)_2Cl]_2$ in dichloromethane-d_2.

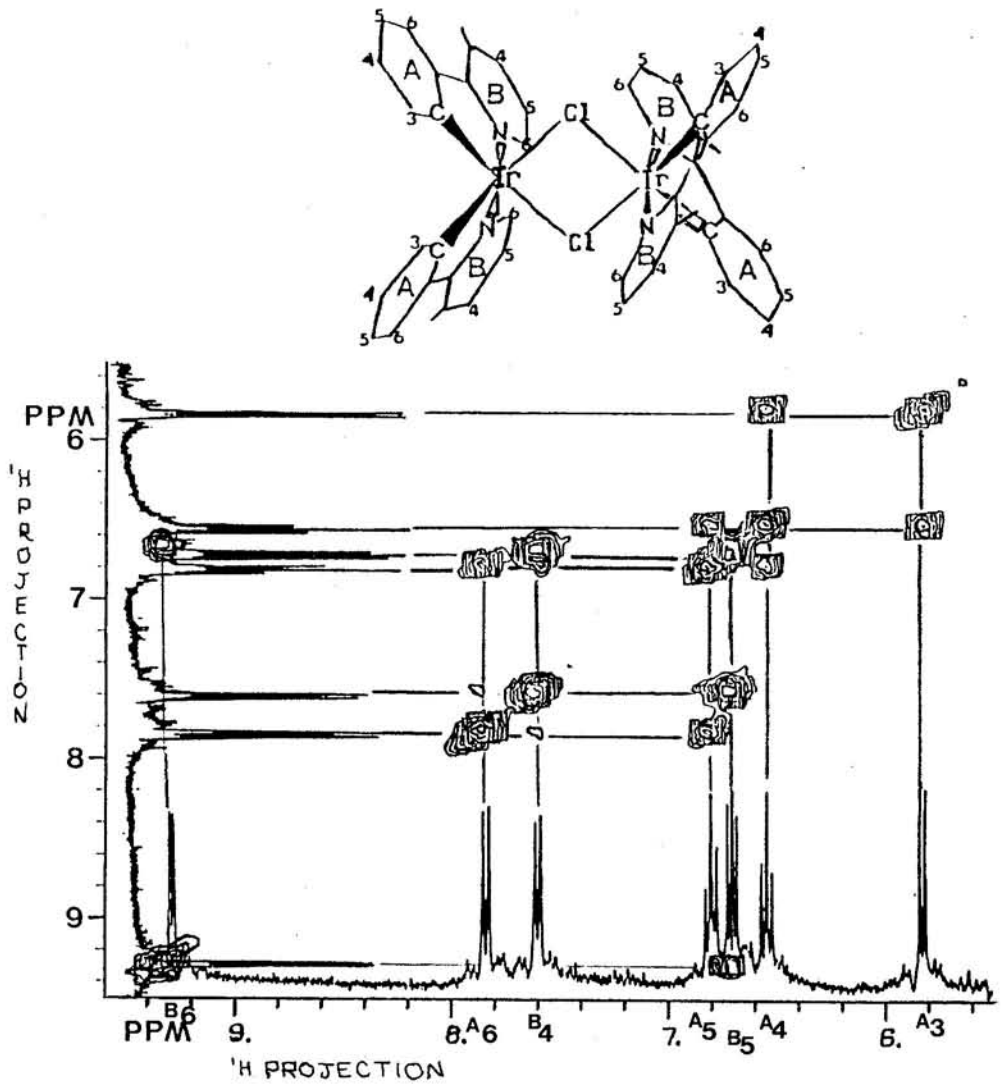

FIGURE 2.1.7:

^{13}C NMR spectrum for $[Ir(ptpy)_2Cl]_2$, (200 - 0 ppm) in DCM-d_2.

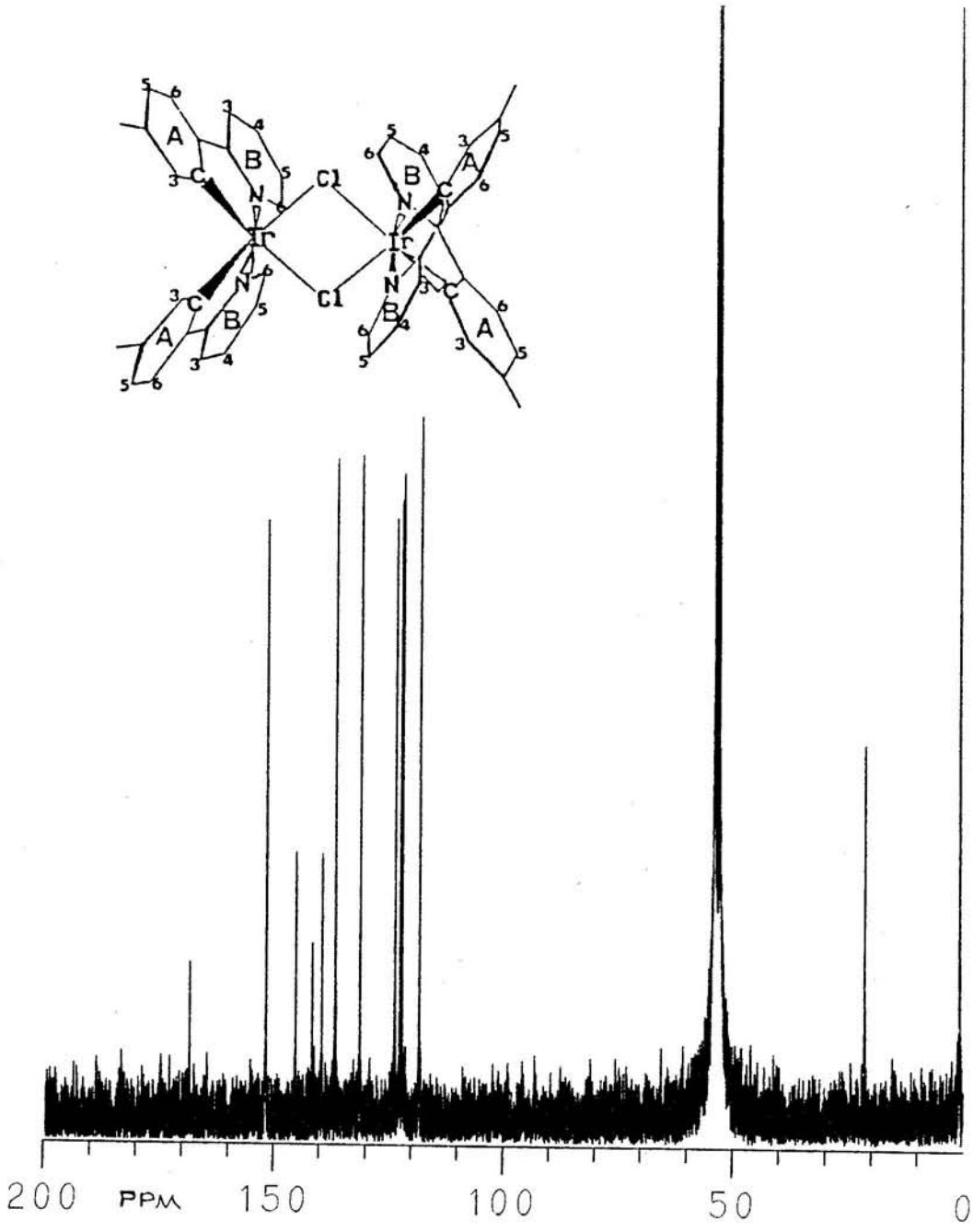

FIGURE 2.1.8:

^{13}C NMR spectrum for $[Ir(mppy)_2Cl]_2$, (200 - 0 ppm) in DCM-d_2.

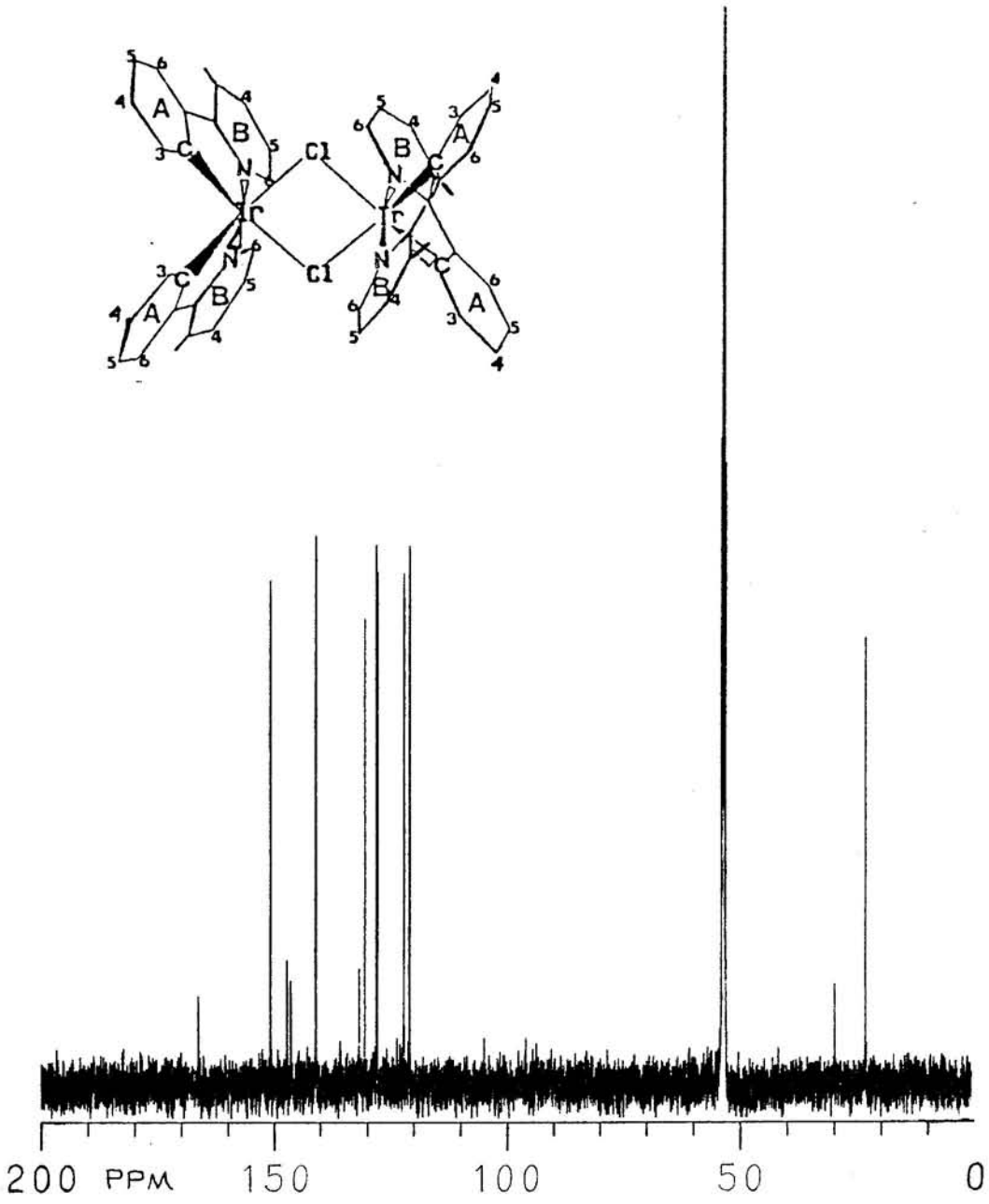

FIGURE 2.1.9:

^{13}C NMR spectra for $[Ir(ptpy)_2Cl]_2$, (170 - 110 ppm) in DCM-d_2.
(a.) ^{13}C NMR spectrum and (b.) Attached Proton Test (APT) Spectrum.

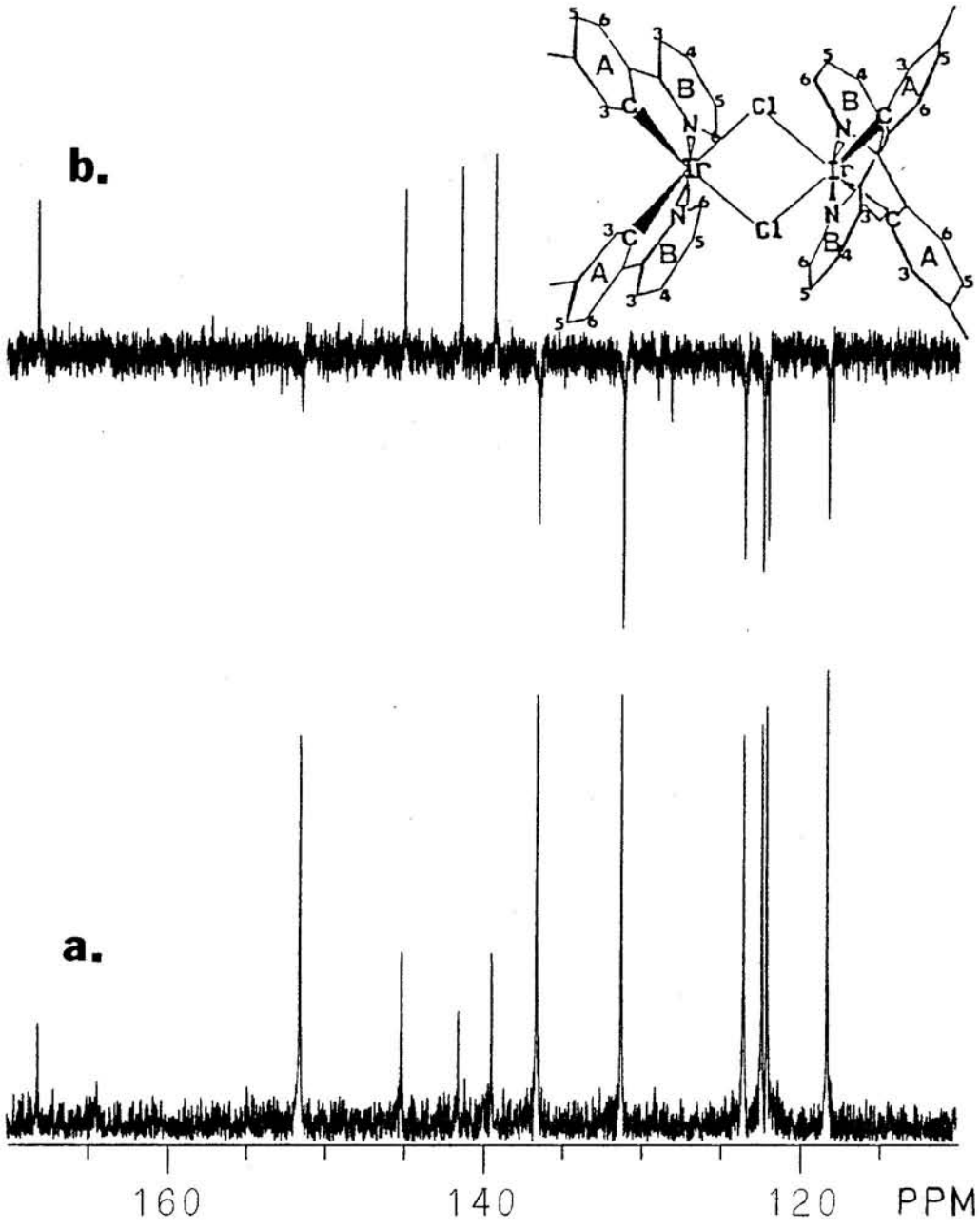

FIGURE 2.1.10:

^{13}C NMR spectra for $[Ir(mppy)_2Cl]_2$, (170 - 120 ppm) in DCM-d_2.
(a.) ^{13}C NMR spectrum and (b.) Attached Proton Test (APT) Spectrum.

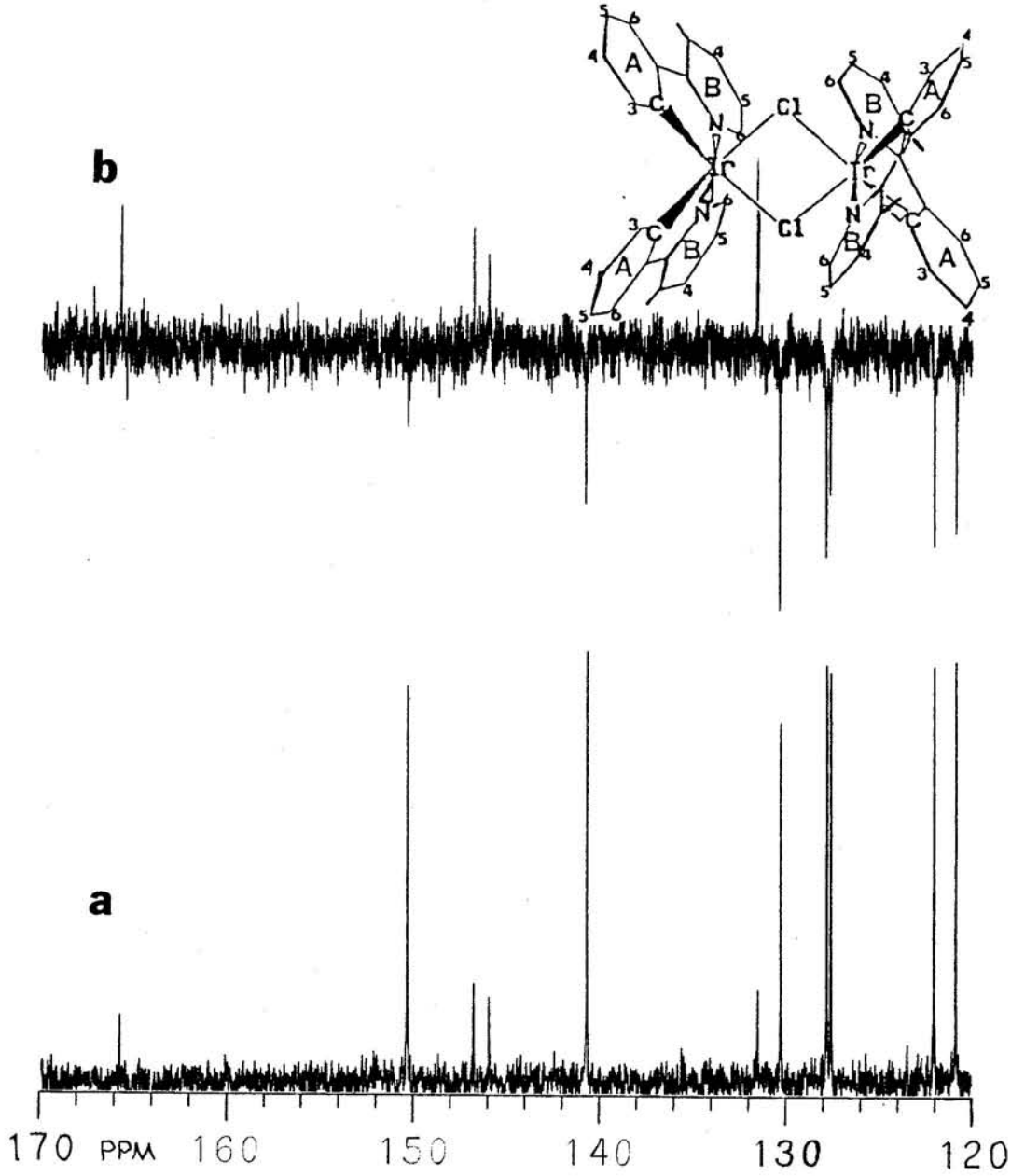

FIGURE 2.1.11:

^{1}H-^{13}C Heteronuclear Correlation Spectroscopy (CSCM) spectrum for $[Ir(ptpy)_2Cl]_2$ in dichloromethane-d_2.

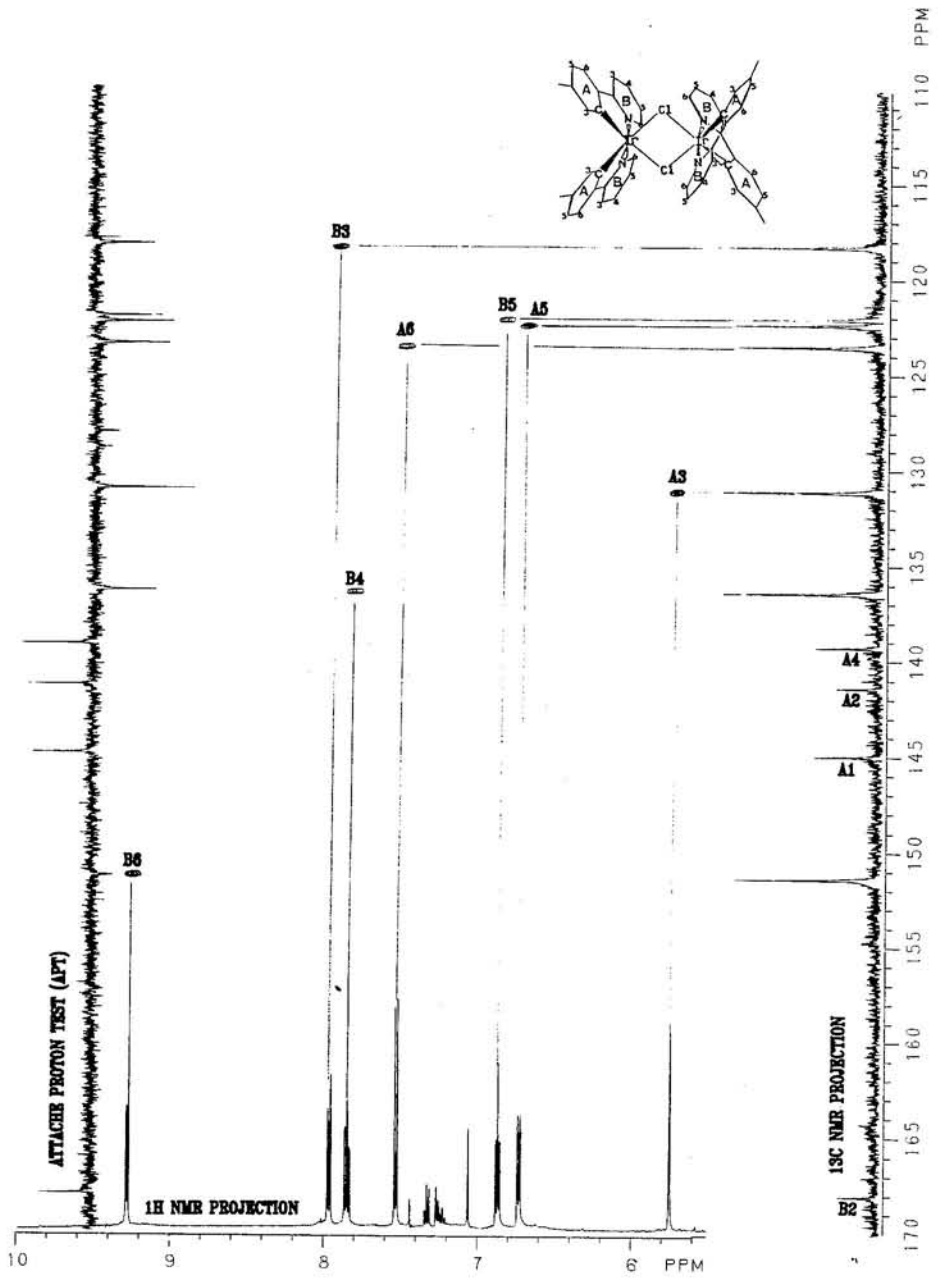

FIGURE 2.1.12:

^{1}H-^{13}C Heteronuclear Correlation Spectroscopy (CSCM) spectrum for $[Ir(mppy)_2Cl]_2$ in dichloromethane-d_2.

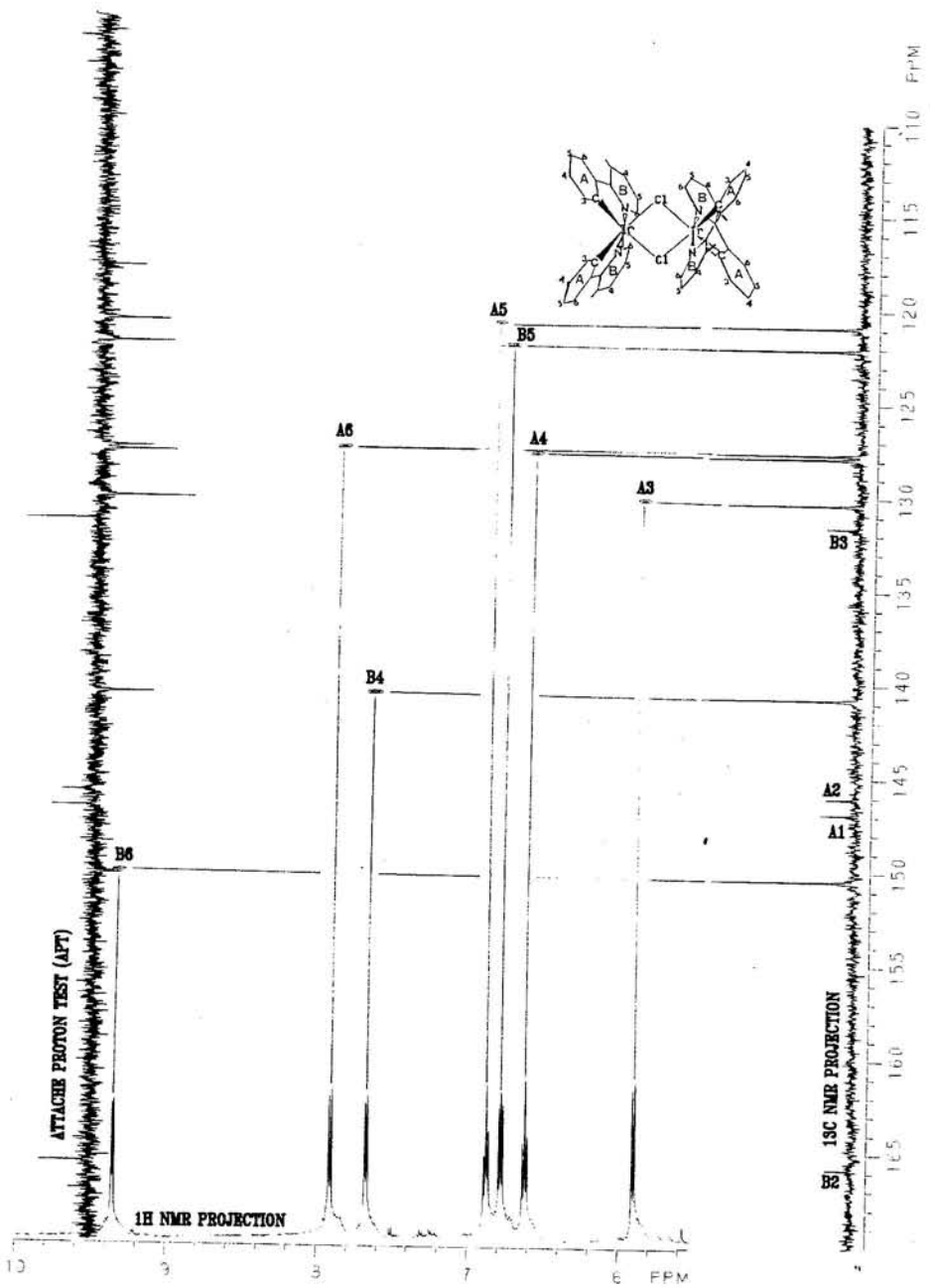

2. Cyclic Voltammetry

Cyclic voltammetric measurements for $[Ir(ptpy)_2Cl]_2$ and $[Ir(mppy)_2Cl]_2$ are illustrated by four curves a, b, c and d in Figures 2.2.1.a-d and 2.2.2.a-d respectively. Curves a represent the voltammograms for the solvent/electrolyte solution; curves b, for the $Fc^{+/0}$ reference; and curves c and d for the complex using two scanning techniques. Curve c measures the oxidative / reductive region by scanning between 0 and +/- 2.0V (vs. SCE) repetitively before the voltammograms. This curve is referred to as the "repetitive scan" curve. Curve d measures the oxidative / reductive region by recording the voltammogram without prior repetitive scanning. This is referred to as the "single scan" curve.

Cyclic voltammograms under single scan mode for both dimers show two reversible oxidative waves, $E_{1/2}$ ~ 0.85, 1.11 V, and a weak reductive wave, $E_{pc/2}$ ~ -0.95 V versus SCE, Figures 2.2.1.d and 2.2.2.d. The repetitive scan voltammogram curves show reversible oxidative waves in the CV's for $[Ir(mppy)_2Cl]_2$ but irreversible waves for $[Ir(ptpy)_2Cl]_2$. Redox potentials for these complexes are tabulated in Table 2.2 and Appendix B together with the $Fc^{+/0}$ reference potentials, $E_{1/2}$ ~ 0.45 V versus SCE.

Appendix B presents an extended discussed on the electrochemical techniques used here, and presents redox potentials of other iridium metal complexes for comparison.

TABLE 2.2

Redox Potentials for $[Ir(ptpy)_2Cl]_2$ and $[Ir(mppy)_2Cl]_2$ in TEAH/Alumina/dichloromethane. (V vs. SCE)

Complexes	E_{pa}	E_{pc}	$E_{pa/2}$	$E_{pc/2}$	ΔE_{p-p}	$E_{1/2}$
$[Ir(ppy)_2Cl]_2$						
Ox-scan 1st[a]	0.96	0.83	0.90	0.95	.13	0.93 (0.51)[b]
Ox-scan 2nd	1.20	1.08	1.15	1.15	.12	1.15 (0.73)
Re-scan	NO OBSERVABLE REDUCTION WAVES					
$Fc^{+/0}$	0.65	0.20	0.46	0.38	.45	0.42
$[Ir(ptpy)_2Cl]_2$						
Ox-scan 1st	0.90	0.80	0.84	0.85	.10	0.85 (0.39)
Ox-scan 2nd	1.18	1.08	1.10	1.13	.10	1.12 (0.66)
Re-scan 1st	-0.88	-1.00	-0.93	-0.90	.12	-0.92 (-1.38)
$Fc^{+/0}$	0.70	0.24	0.58	0.34	.46	0.46
$[Ir(mppy)_2CL]_2$						
Ox-scan 1st	0.90	0.83	0.85	0.85	.07	0.85 (0.41)
Ox-scan 2nd	1.15	1.08	1.10	1.10	.07	1.10 (0.66)
Re-scan 1st	-	-1.13	-	-1.00	-	-
$Fc^{+/0}$	0.60	0.28	0.45	0.43	.32	0.44

a) 1st (2nd) wave during oxidative / reductive scan
b) Values in parenthesis are $E_{1/2}$ vs. $Fc^{+/0}$

FIGURE 2.2.1:

Cyclic Voltammograms for $[Ir(ptpy)_2Cl]_2$ at room temperature, in TEAH/Alumina/Dichloromethane. (V vs. SCE)

Curves (a.) - TEAH/Alumina/dichloromethane CV scan
(b.) - Internal reference CV scan, $Fc^{+/0}$
(c.) - CV scan of complex under **repetitive** scan.
(d.) - CV scan of complex under **single** scan.

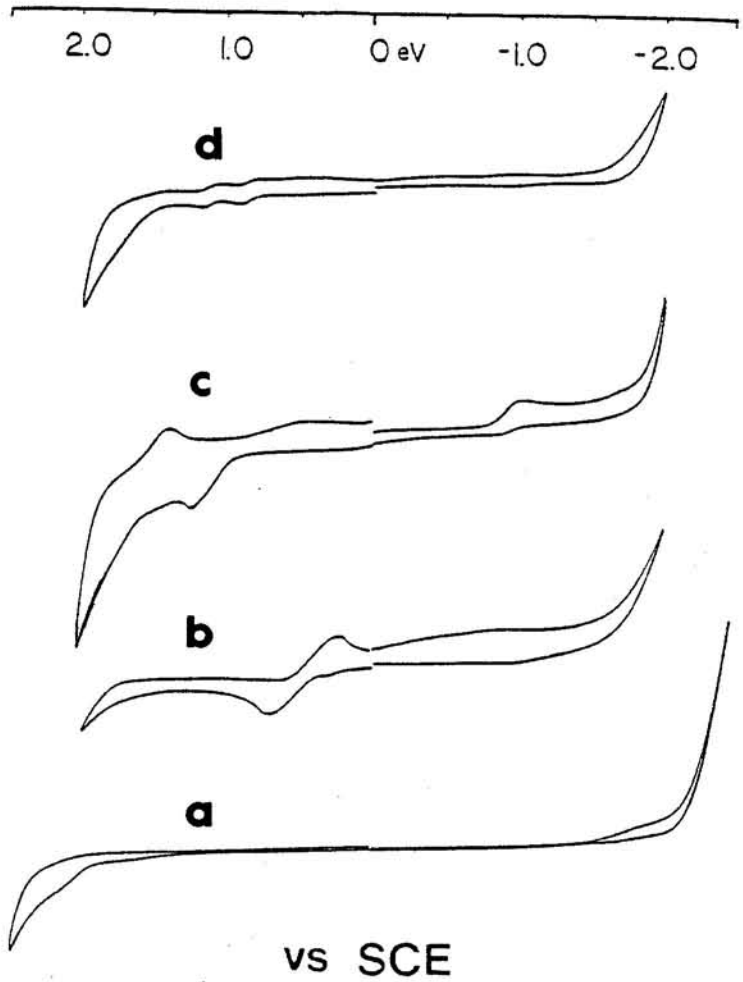

FIGURE 2.2.2:

Cyclic Voltammograms for $[Ir(mppy)_2Cl]_2$ at room temperature, in TEAH/Alumina/Dichloromethane. (V vs. SCE)

Curves (a.) - TEAH/Alumina/dichloromethane CV scan
(b.) - Internal reference CV scan, $Fc^{+/0}$
(c.) - CV scan of complex under **repetitive** scan.
(d.) - CV scan of complex under **single** scan.

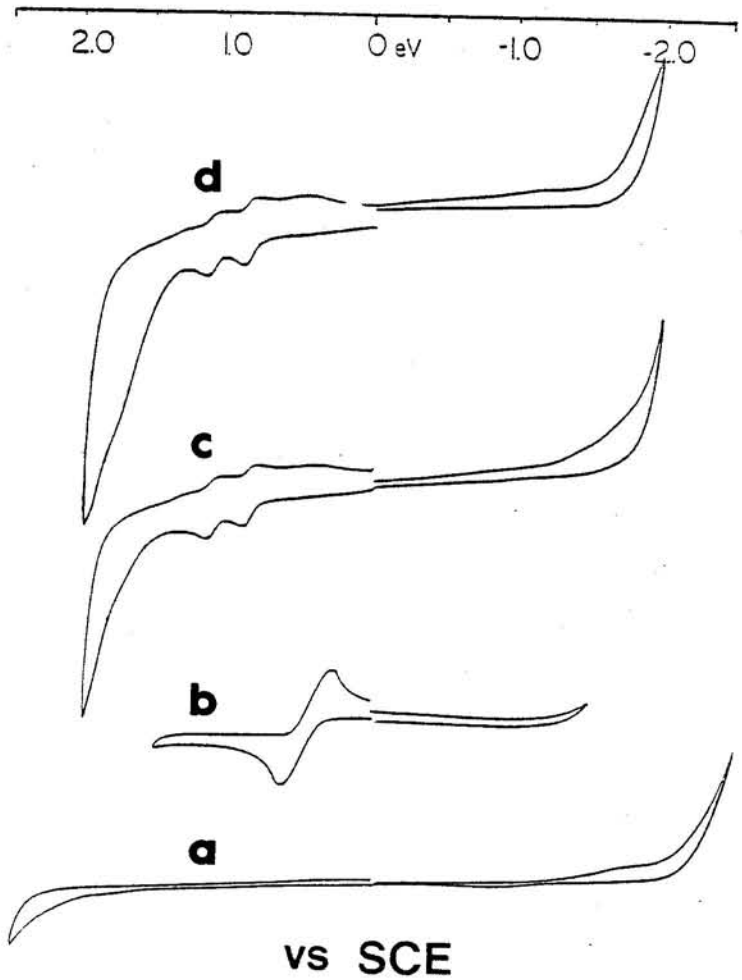

3. Absorption

Absorption spectra for $[Ir(ptpy)_2Cl]_2$ and $[Ir(mppy)_2Cl]_2$, Figure 2.3.1a and 2.3.1b respectively, show band maxima ranging from 480 to 260 nm. Extinction coefficients for these absorption maxima are compiled in Table 2.3. Beer's law behavior was followed in the concentration range from 10^{-4} to 10^{-6} M in dichloromethane.

The band maxima for $[Ir(ptpy)_2Cl]_2$, Figure 2.3.1a, are higher energy than those of $[Ir(mppy)_2Cl]_2$, Figure 2.3.1b. In the visible region, $[Ir(ptpy)_2Cl]_2$ shows absorption maxima at 482, 430 and 400 nm whereas the $[Ir(mppy)_2Cl]_2$ absorption maxima are red shifted to 484, 437 and 400 nm. For comparison, the band maxima for $[Ir(ppy)_2Cl]_2$ are also presented in Table 2.3.

TABLE 2.3

Absorption maxima and extinction coefficient in dichloromethane for $[Ir(ppy)_2Cl]_2$, $[Ir(ptpy)_2Cl]_2$, and $[Ir(mppy)_2Cl]_2$.

Complex	Absorption Features (nm)	ϵ ($M^{-1}cm^{-1}*10^{-3}$)
$[Ir(ppy)_2Cl]_2$	484 (sh)	1.1
	434	4.2
	400	6.3
	355 (sh)	11.0
	335	13.0
	260	68.0
$[Ir(ptpy)_2Cl]_2$	482	1.0
	430	4.5
	400	6.4
	355 (sh)	11.3
	310 (sh)	35.4
	280 (sh)	56.5
	263	73.3
$[Ir(mppy)_2Cl]_2$	484 (sh)	1.4
	437	5.0
	400	7.1
	355 (sh)	13.9
	337	16.4
	300	36.5
	270	68.6

FIGURE 2.3.1:

Absorption and emission spectra for
(a) $[Ir(ptpy)_2Cl]_2$ and (b) $[Ir(mppy)_2Cl]_2$ dimers.
——— Absorption and emission, Room temperature in DCM;
------- Emission, 77 K in EtOH-MeOH-DCM (4:1:1 v/v/v).

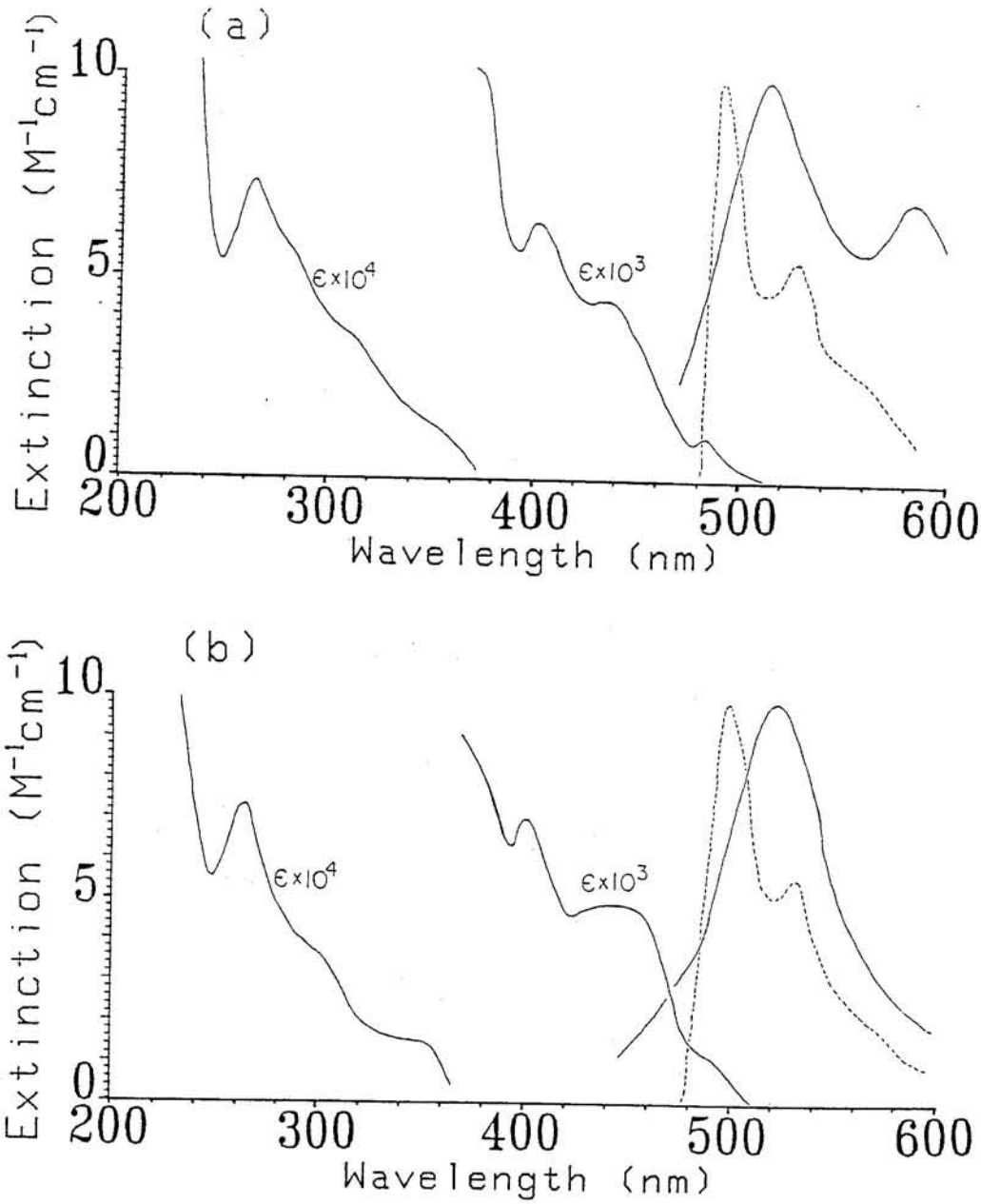

4. Luminescence

A. Emission

Emission band maxima for $[Ir(ptpy)_2Cl]_2$ and $[Ir(mppy)_2Cl]_2$, Figure 2.3.1a and 2.3.1b, are compiled in Table 2.4. Room temperature measurements taken in dichloromethane show band maxima at 510 and 580 nm for $[Ir(ptpy)_2Cl]_2$ and 520 nm for $[Ir(mppy)_2Cl]_2$. The low temperature (77 K) emission spectra taken in EtOH-MeOH-DCM (4:1:1 v/v/v) glasses, show structured emission profiles with band maxima at 490 and 526 nm for $[Ir(ptpy)_2Cl]_2$ and 497 and 530 nm for $[Ir(mppy)_2Cl]_2$.

A number of luminescence measurements were taken to probe the possible radiationless deactivation process of the excited state for these dimers. More specifically, the dependence of irradiation, temperature, solvent and excitation wavelength on dimer cleavage was investigated.

B. Variable Temperature Luminescence

The temperature dependence on the emission of $[Ir(ptpy)_2Cl]_2$ in dichloromethane at 380 nm excitation was determined at 180, 189, 196, 216, 227, 248, 268, 289 and 298 K, Figure 2.4.1. The spectra show a dominant band maximum at 500 nm that remains invariant throughout the temperature progression until 298 K when the band maximum finally red shifts to 510 nm and another emission band maximum grows in at 583 nm. This second band is first observed at 180 K, but decays and blue shifts to 574 nm with increasing

temperature, yet at 298 K the emission band emerges again.

To investigate the reversibility of the second band, the temperature was lowered for the same sample and the uncorrected emission spectra recorded, Figure 2.4.2. The emission profile shows the reversibility of this second band; at 300 K the emission starts as a maximum at 585 nm which decays into a shoulder toward lower (137 K) temperatures.

Similar variable temperature emission measurements for $[Ir(mppy)_2Cl]_2$ in dichloromethane at 150, 175, 200, 235, 250, 275 and 300 K are shown in Figure 2.4.3. The structured emission spectrum at 150 K with band maxima centered at 474, 505 and 530 nm, becomes broad and structureless at 300 K with band maxima centered at 480 and 497 nm. The most unusual feature during the temperature progression, however, is the development of the 440 nm band maximum. At 150 K, there is no indication of an emission band at 440, yet by 300 K, this band is surely an emission maximum albeit the intensity of 505 nm band maximum has decreased. The temperature was not lowered in this series as that for the variable temperature emission measurement of $[Ir(ptpy)_2Cl]_2$.

C. Emission-Excitation-Intensity Temperature studies

Emission-excitation-intensity (EEI) stacked plots for $[Ir(ptpy)_2Cl]_2$ in dichloromethane at 170, 200, 250 and 300 K are shown in Figure 2.4.4. Excitation wavelengths ranged between 345 to 390 nm incremented by 5 nm with the emission monitored between 450

to 650 nm. There was a twenty-four hour period in which the first stack plot at 170 K and the last stack plot at 300 K was recorded. During this time, the dimer may have thermally decomposed or photolytically cleaved, as indicated by the emission profiles at 300 K. Figure 2.4.5 shows the EEI spectra for a fresh sample of $[Ir(ptpy)_2Cl]_2$ at room temperature. As shown from this stack plot, there is structure at high energy excitation but no indication of a low energy band maximum at 580 nm.

EEI stack plots for $[Ir(mppy)_2Cl]_2$ in dichloromethane, taken at 150, 200, 250 and 300 K, are shown in Figures 2.4.6. Although these 3D stack plots were taken under identical conditions as the EEI plots of $[Ir(ptpy)_2Cl]_2$, no signs of sample deterioration or dimer cleavage were detected. At low temperatures, the spectra shows structured emission with band maxima at 480, 505 and 530 nm but at higher temperature, the spectra decrease in intensity and becomes less structured. No band maximum past 530 nm was detected.

D. Dependence on Solvent and Oxygen

The emission profile of $[Ir(ptpy)_2Cl]_2$ in acetonitrile shows a broad emission band at 511 nm and a shoulder at 529 nm. In toluene, the 511 nm band maximum decreases and new features at 576 nm and 620 nm are observed. Acetonitrile and toluene solvent were used for this study because the former solvent is thought to promote dimer cleavage while the latter is thought to be inert. Needless to say the results surprised us. Absorption measurements of

$[Ir(ptpy)_2Cl]_2$ in acetonitrile showed the decay of the visible bands over time with no observable isobestic points suggesting dimer decomposition.

Emission measurements were obtained for a solution of $[Ir(ptpy)_2Cl]_2$ in dichloromethane after purging with air and with helium and after addition of water. The uncorrected emission profiles for these conditions,Figure 2.4.7, indicate oxygen quenching of the emission maxima for air purge conditions and multi emission maxima for aqueous/dichloromethane conditions. The band maxima for the latter condition occurs at 475, 512 and 584 nm.

E. Irradiation

A freeze-pump-thawed sample of $[Ir(ptpy)_2Cl]_2$ was photolyzed in dichloromethane to promote dimer cleavage. The sample was monitored by absorption, emission and ^1H NMR spectroscopy. Room temperature luminescences were measured before photolysis (t = 0), during photolysis (t = 10 and 720 min), and after photolysis. The EEI plots in Figure 2.4.8 show structured emission before photolysis (t = 0), with band maxima at 478, 500 nm and a shoulder at 543 nm which becomes structureless after 10 minutes of photolysis. After 12 hours of photolysis, the EEI profile becomes broader and even less structured with band maximum at 490 nm. Even after refrigerating the sample for several days, the original emission structured profile can not be regenerated Figure 2.4.9. The ^{1} H NMR spectra of this sample before, during, and after photolysis, showed no

significant change as did the absorption spectra of the same sample.

F. Luminescence Lifetimes

Room temperature luminescence lifetimes in dichloromethane and toluene solvents were 140 ns for $[Ir(ptpy)_2Cl]_2$ and 40 ns for $[Ir(mppy)_2Cl]_2$; low temperature (77 K) lifetimes were 5.0 μs for both complexes in EtOH-MeOH (4:1 v/v) (Table 2.4). Quantum yields for both dimers were less than 1%.

FIGURE 2.4.1

Emission spectra for $[Ir(ptpy)_2Cl]_2$ in dichloromethane, with 380 nm excitation, at 180, 189, 196, 216, 227, 248, 268, 289 and 298K (Increasing Temperatures).

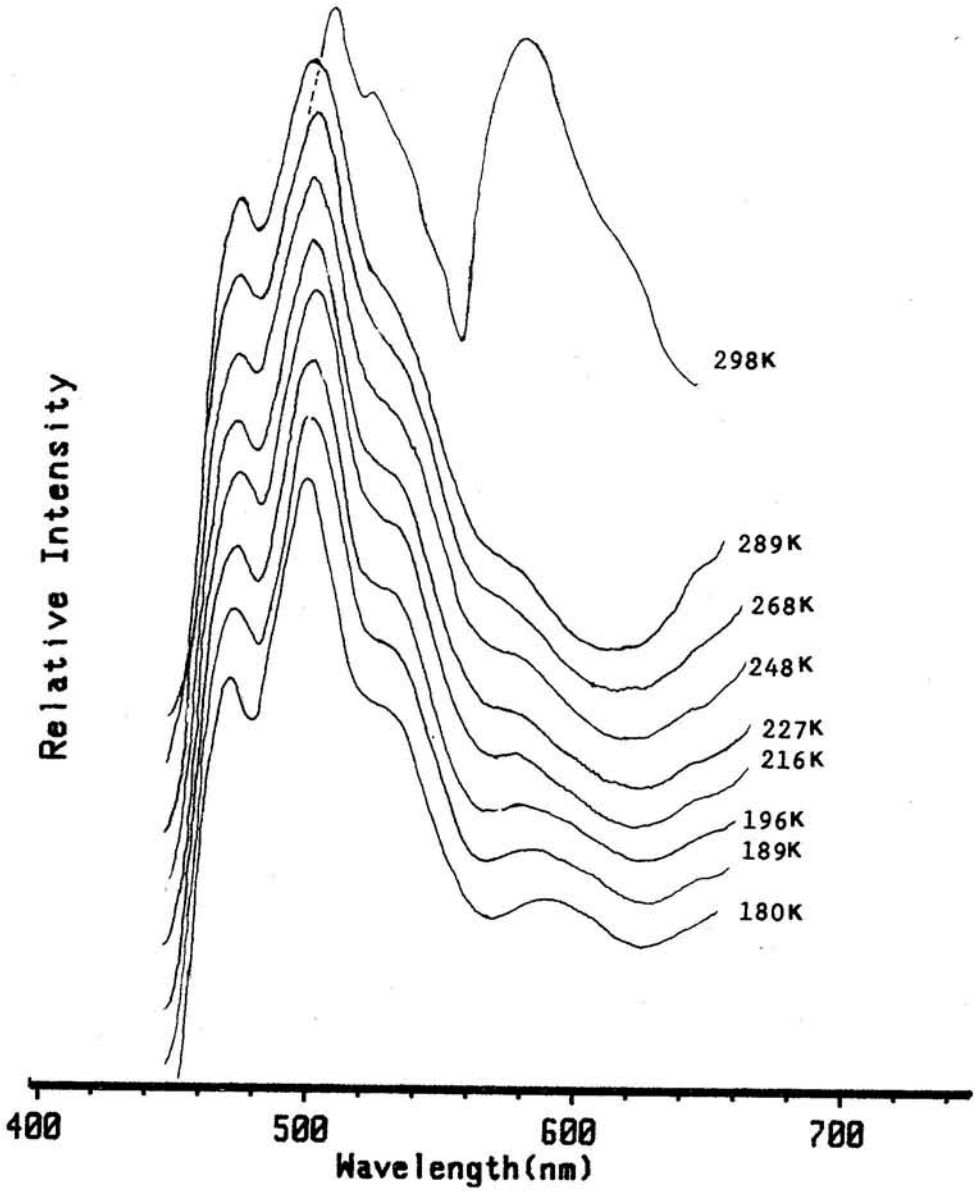

FIGURE 2.4.2

Emission spectra (uncorrected) for $[Ir(ptpy)_2Cl]_2$ in dichloromethane, with 380 nm excitation, at 300, 292, 284, 275, 250, 220, 202, 180, 170 and 137 K, (Decreasing temperatures).

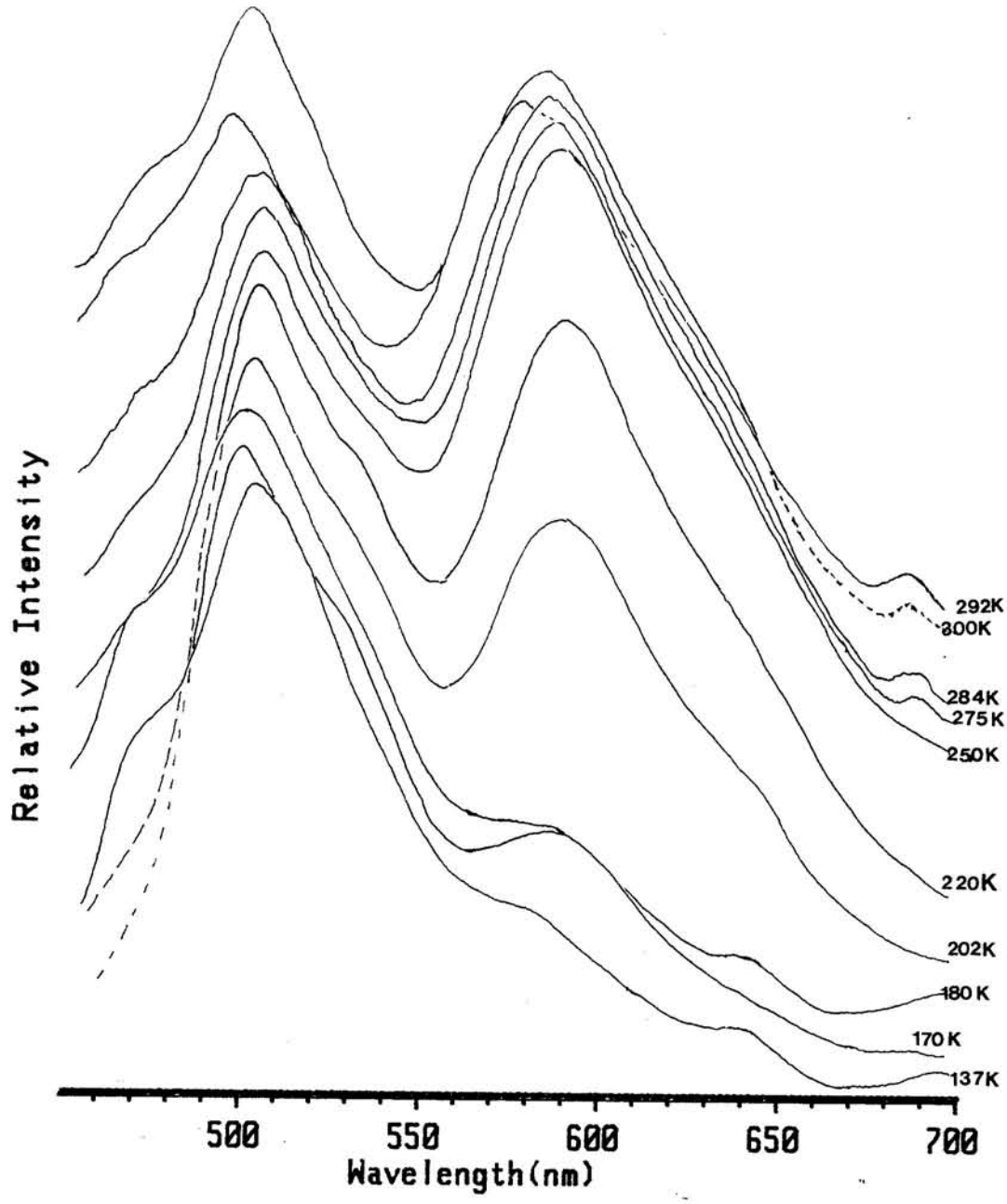

FIGURE 2.4.3

Emission spectra for $[Ir(mppy)_2Cl]_2$ in dichloromethane, with 380 nm excitation, at 150, 175, 200, 235, 250, 275, and 300 K.

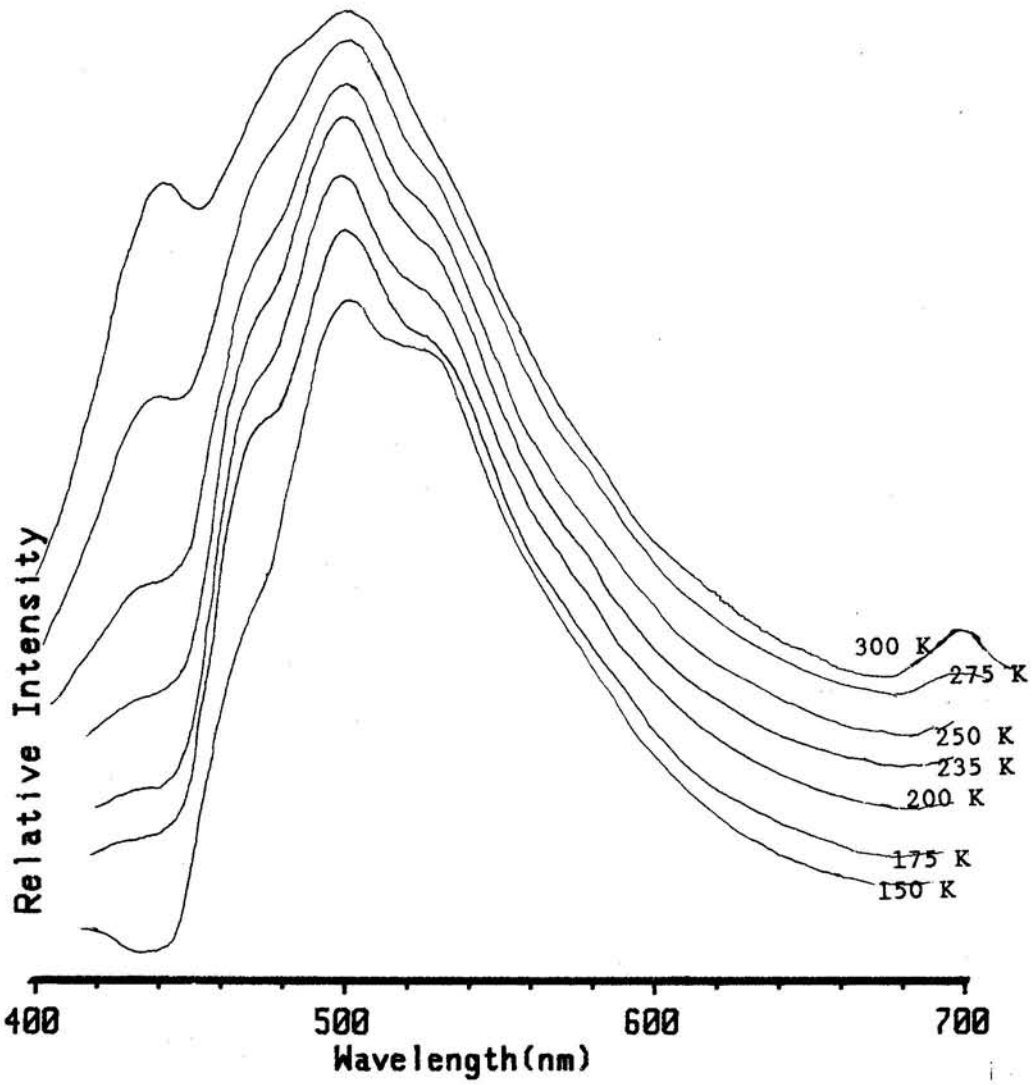

FIGURE 2.4.4

Emission-Excitation-Intensity stack plots for $[Ir(ptpy)_2Cl]_2$ in dichloromethane with excitation wavelength ranged from 345 to 390 nm at 5 nm increments. Stack plots were recorded at 170, 200, 250 and 300 K.

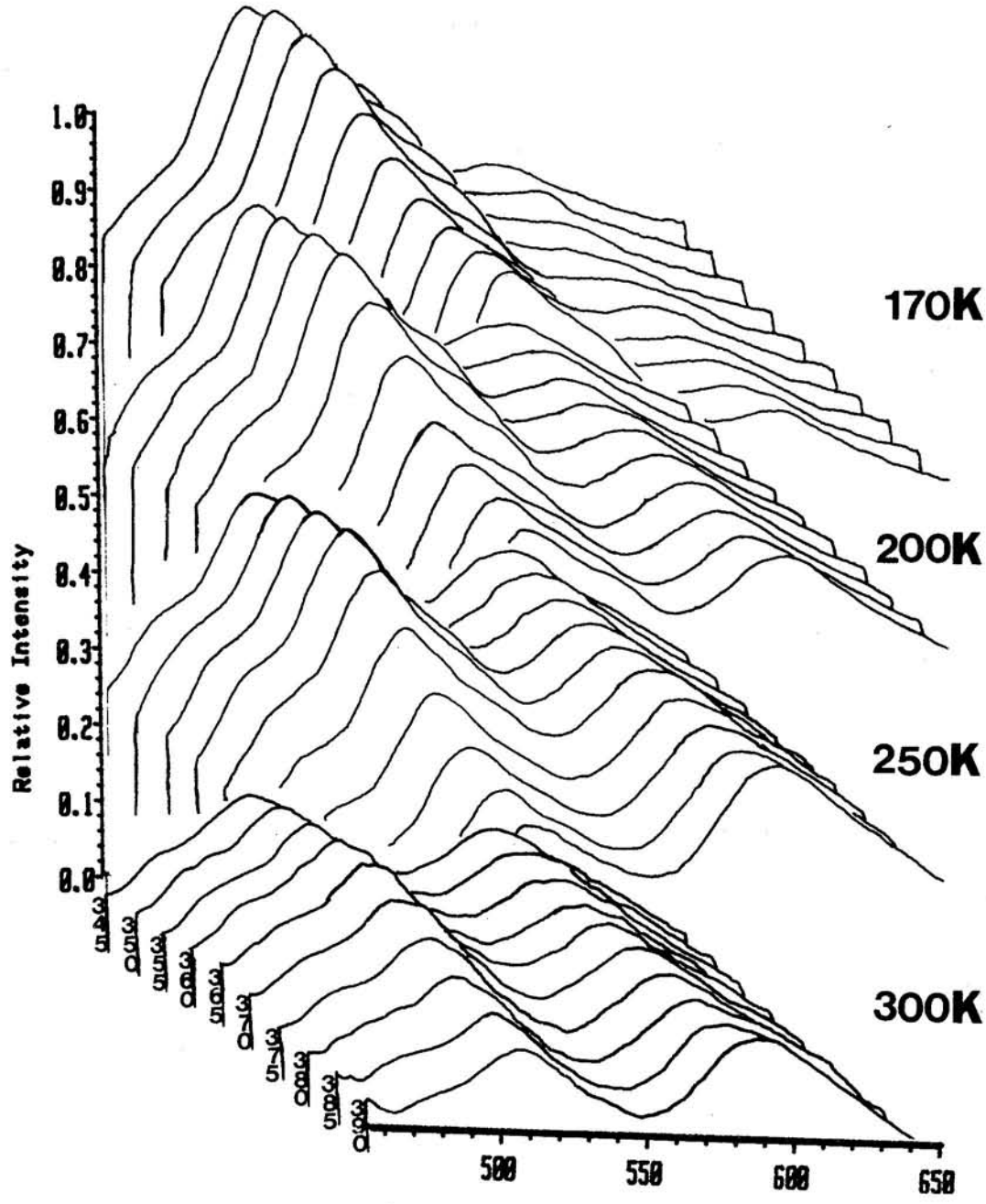

FIGURE 2.4.5

Emission-Excitation-Intensity stack plots for a fresh sample of $[Ir(ptpy)_2Cl]_2$ in dichloromethane with excitation wavelength ranged from 340 to 395 nm at 5 nm increments, at 300 K.

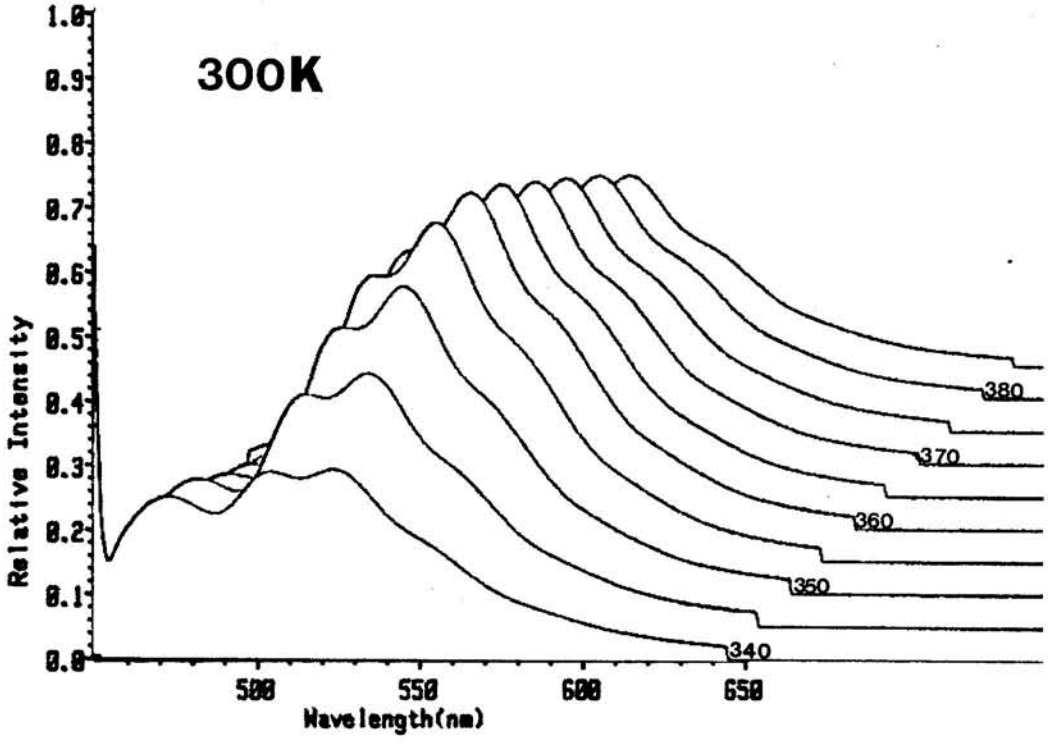

FIGURE 2.4.6

Emission-Excitation-Intensity stack plots for $[Ir(mppy)_2Cl]_2$ in dichloromethane with excitation wavelength ranged from 345 to 390 nm at 5 nm increments. Stack plots were recorded at 150, 200, 250 and 300 K.

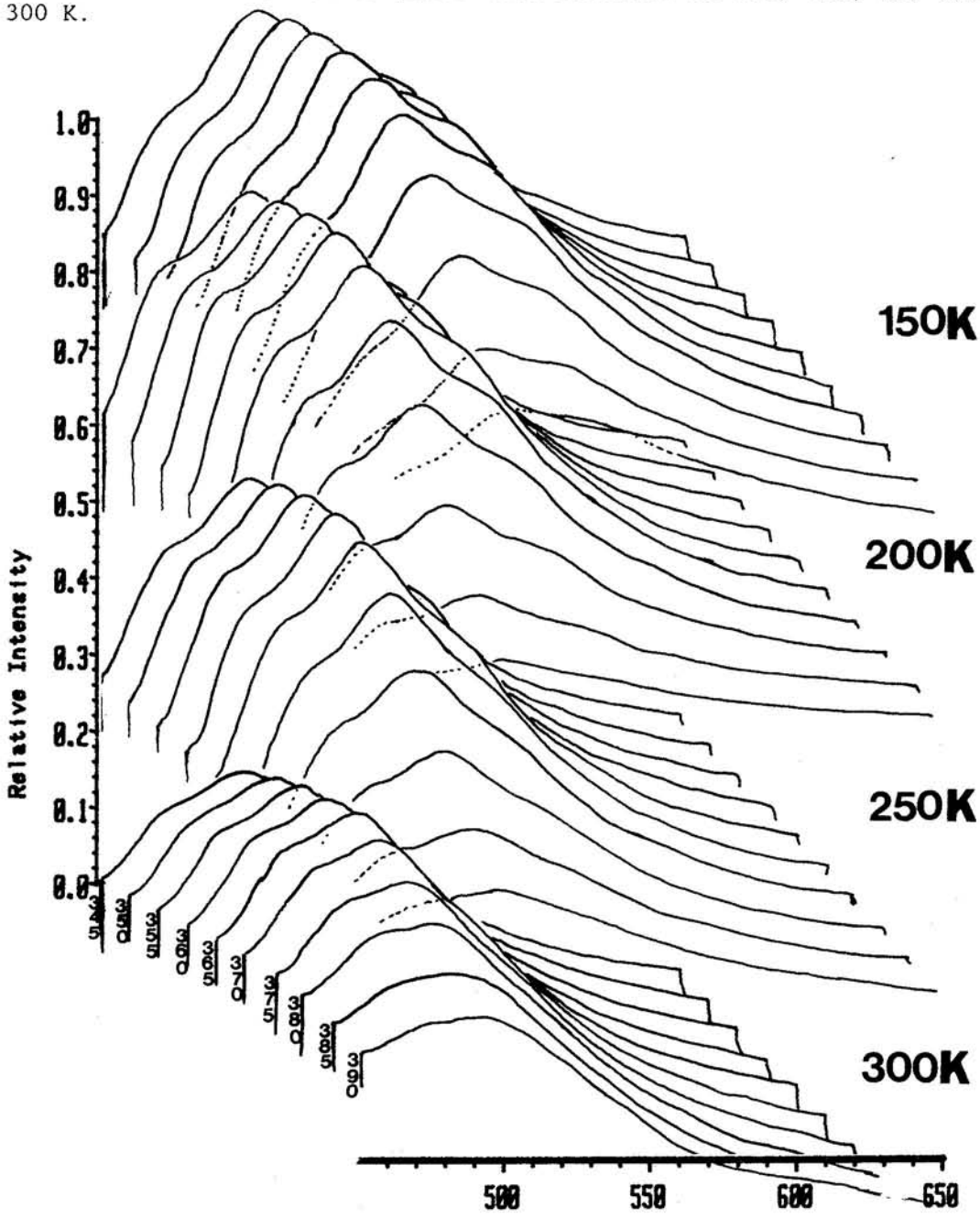

FIGURE 2.4.7

Room temperature emission spectra of $[Ir(ptpy)_2Cl]_2$ in dichloromethane for various conditions; (a.) O_2 (air) purge, (b.) He purge, (c.) normal or no purge and (d) addition of water.

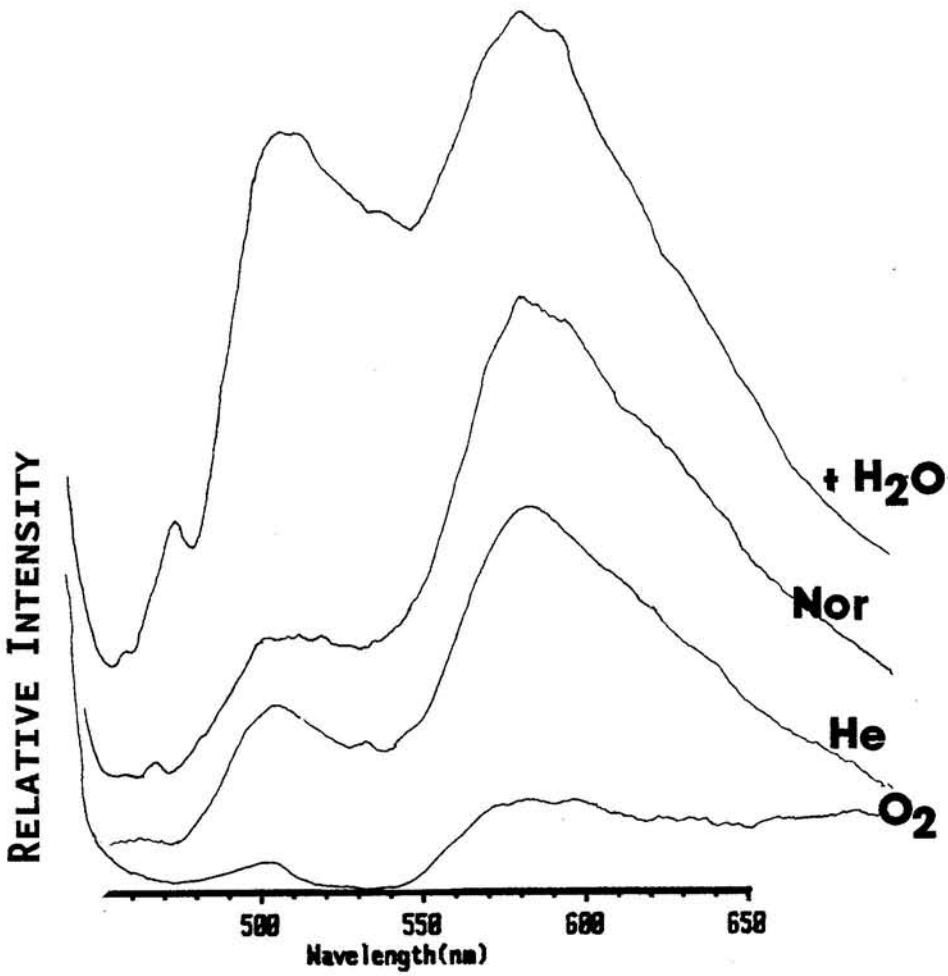

FIGURE 2.4.8

Room temperature emission spectra for a photolyzed $[Ir(ptpy)_2Cl]_2$ sample in dichloromethane. (a) before photolysis, t = 0 (b) after 10 min, t = 10 min. (c) after 12 hours, t = 12 hr.

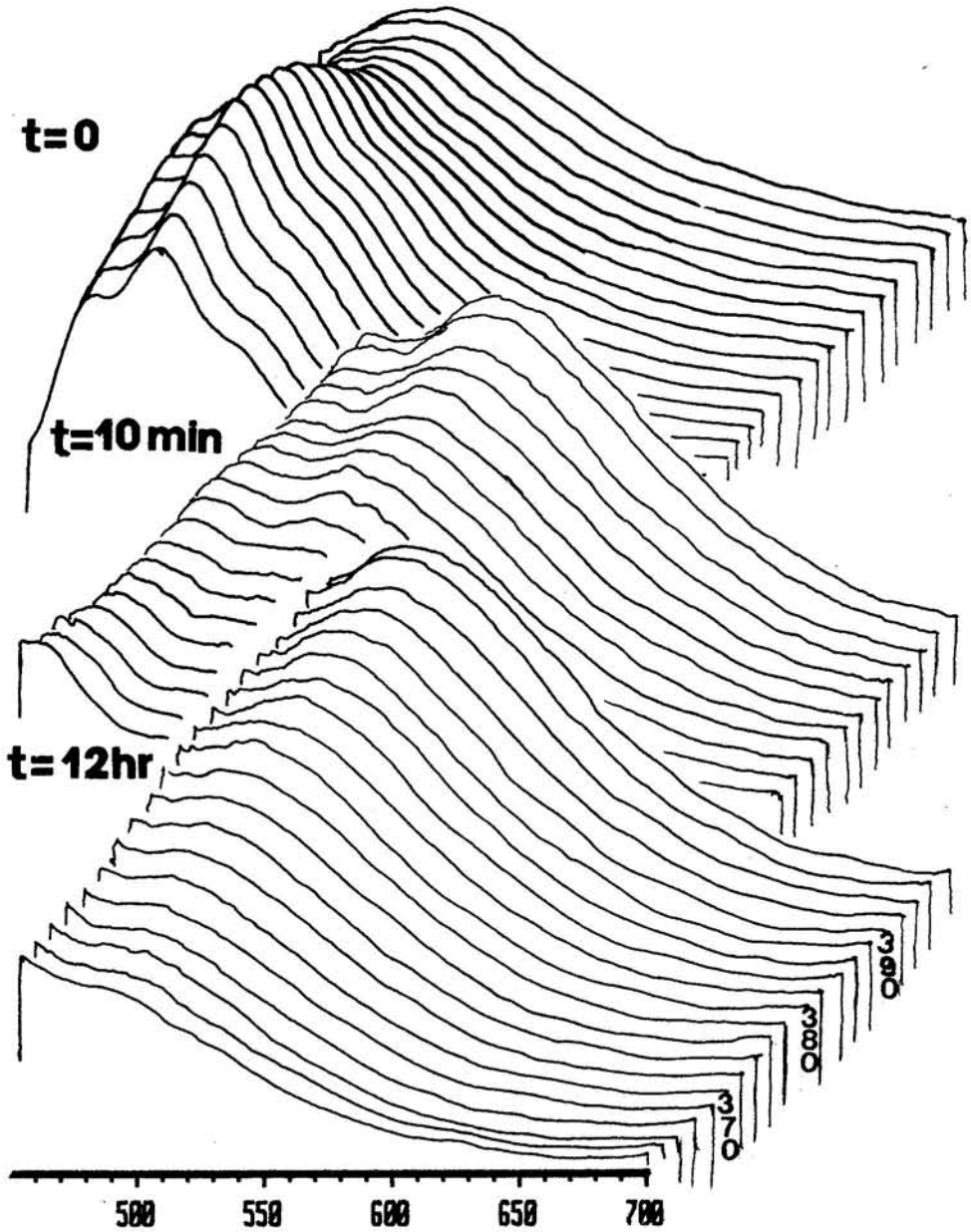

FIGURE 2.4.9

Room temperature emission spectra of the photolysis sample of $[Ir(ptpy)_2Cl]_2$ in dichloromethane after storage.

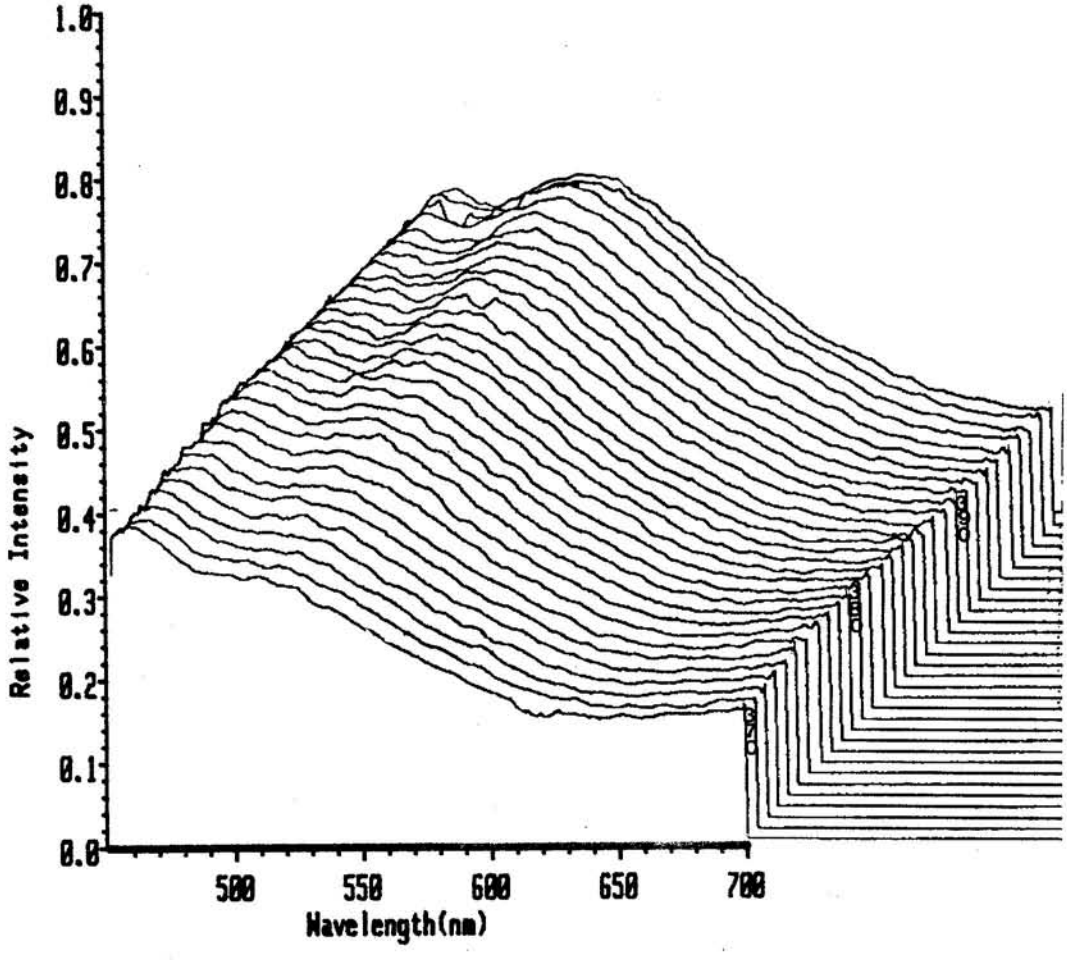

IV. DISCUSSION

1. Structural Consideration via NMR Analysis.

For comparison purposes, the proton and carbon resonance assignments for the free ligands, 2-(p-tolyl)pyridine and 3-methyl-2-phenylpyridine, are given in Appendix A, Table A.6.

The simplicity of the ^{1}H and ^{13}C NMR spectra, with eight distinct proton resonances and eleven distinct carbon resonances respectively, advocate one "type" of NC ligand in each of the dimers suggesting D_2 symmetry to both structures[25], as shown in Figure 2.1.2.

The ^{1}H NMR and COSY spectra for $[Ir(ptpy)_2Cl]_2$, Figures 2.1.3, 2.1.5, suggest a two ring system with coupled groups of two and four spins corresponding to the tolyl "A" and pyridyl "B" rings in 2-(p-tolyl)pyridine, Figure 2.1.1a. The uncoupled resonance at 5.7 ppm is assigned to the remote proton at the A_3 position. This assignment is consistent with the assignment of the A_3 protons in the nonsubstituted $[Ir(ppy)_2Cl]_2$ dimer, δ = 5.9.[16,22,23] The two remaining resonances from the "A" tolyl ring are assigned to the A_5 and A_6 protons; the downfield 7.4 ppm signal is assigned to the latter because protons in the 3-and 3'- positions (β position for free ligand) are strongly deshielded by protons in the other 3'- and 3- positions from the tether ring.[30-32] Assignment of the A_6 protons, as well as other β position protons, are consistent with similar proton assignments in the literature.[25,29,32-40]

The four remaining resonances at 9.2, 7.9, 7.8, and 6.8 ppm are assigned to the protons on the pyridyl "B" ring with the lowest field doublet assigned to the B_6 protons because of their juxtaposition over the bridging electronegative chlorides, a deshielded region of electron density (Figure 2.1.2).[25,33-35] This initial assignment of the B_6 resonance allows for J-correlation connective analysis[39] of the B_6 9.2 ppm doublet to the B_5 6.8 ppm triplet, the B_5 6.8 ppm triplet to the B_4 7.8 ppm triplet, and the B_4 7.8 ppm triplet to the B_3 7.9 ppm doublet, Figure 2.1.5. As noted above, the B_3 protons (β position) are assigned to the lower field resonance relative to the resonances of either B_4 or B_5. Residual toluene is observed as a multiplet at 7.24 ppm, in support of the elemental analysis.

The ^1H and COSY spectra for $[Ir(mppy)_2Cl]_2$, Figure 2.1.4 and 2.1.6, indicate two spin systems consisting of three resonances from the methylpyridyl "B" ring and four resonances from the phenyl "A" ring, Figure 2.1.2b. In accordance with the initial proton assignments for $[Ir(ptpy)_2Cl]_2$, the protons in the A_3 and B_6 positions for $[Ir(mppy)_2Cl]_2$ are assigned to the highest (5.8 ppm) and lowest (9.3 ppm) field signals respectively, thus allowing J-correlation connective analysis on the rest of the COSY spectrum. The results are consistent with assignment the ortho (β) A_6 resonance at 7.85 ppm downfield relative to the meta A_5 and para A_4 resonances at 6.80 and 6.54 ppm respectively. The sharp 2.87 ppm aliphatic singlet is assigned to the methyl protons and residual

toluene is assigned to the multiplet at 7.2 ppm.

The carbon resonances in the ^{13}C NMR and APT spectra for $[Ir(ptpy)_2Cl]_2$, Figures 2.1.7 and 2.1.9, show one methyl resonance at δ = 21.7; seven protonated carbon resonances at δ = 151.8, 136.8, 131.5 123.9, 122.7, 122.4, and 118.6; and four nonprotonated carbon resonances at δ = 168.4, 145.4, 141.8, and 139.6. The CSCM spectrum, Figure 2.1.11, shows the proton resonances from the "A" ring ^{J}C-H connected to the carbon resonances at 131.5, 123.9 and 122.7 ppm; and the proton resonances from the "B" ring, correlation to the carbon resonances at 151.8, 136.8, 122.4 and 118.6 ppm. The results suggest assignment of the B_6 and B_3 methine carbons to the lowest and highest field protonated carbon resonances at δ = 151.8 and 118.6 respectively; similarly the lowest and highest field "A" ring methine carbon resonances (δ = 139.6 and 122.7) are assigned to the A_4 and A_5 carbon respectively. The rest of the protonated carbon assignments are shown in Table 2.1 and Appendix A.

Using similar ^{J}C-H connectivity analysis on the CSCM spectrum for $[Ir(mppy)_2Cl]_2$, the methine carbons are assigned. The "A" ring methine carbons are assigned to resonances at 131.0 (A_3), 128.4 (A_4), 128.2 (A_6) and 121.4 ppm (A_5); and the "B" methine carbons are assigned to resonances at 151.0 (B_6), 141.3 (B_4), and 122.6 ppm (B_5). The methyl carbons are assigned to the resonance at 23.8 ppm.

Nonprotonated carbons do not give rise to modulations in the CSCM spectrum, Figure 2.1.11 and 2.1.12, because they lack attached

protons to ^{J}C-H couple. These carbons are easily assigned to their resonances based on the electronic environment due to differences between Ir-C and Ir-N bonding in these complexes.[40,41] For example the two downfield nonprotonated carbon resonances at 168.4 and 145.4 ppm for $[Ir(ptpy)_2Cl]_2$, and 166.4 and 147.4 ppm for $[Ir(mppy)_2Cl]_2$, assigned to the bridgehead carbons,[42] may be differentiated because bridgehead carbons adjacent to an electron withdrawing nitrogen are more deshielded than bridgehead carbons adjacent to a metalating anionic carbon. Thus the lower field resonances at 168.4 and 166.4 ppm (for $[Ir(ptpy)_2Cl]_2$ and $[Ir(mppy)_2Cl]_2$ respectively) can be assigned to the B_3 carbons and the higher field resonances at 145.4 and 147.4 ppm, can be assigned to the A_1 carbons.

The next set of quaternary carbon resonances are observed at 141.8 ppm for $[Ir(ptpy)_2Cl]_2$ and 146.6 for $[Ir(mppy)_2Cl]_2$. These resonances are assigned to the ortho-metalated carbons because their chemical shifts not only lie upfield from the 2 and 2′ bridgehead carbons, but also lie in a region in which ortho-metalated carbons bonded to iridium resonate.[35,36,41] Other carbon resonances of this type are give in Appendix A, Table A.6 and A.7. Ortho-metalating carbons generally resonate downfield in the aromatic region between 140 - 150 ppm because the π-back bonding from the iridium center counters the strong σ-donor character of the ortho-metalating carbon.

The remaining set of quaternary carbons upfield at 139.6 and at 132.1 ppm are assigned to the methylated A_4 and B_3 carbons for

$[Ir(ptpy)_2Cl]_2$ and $[Ir(mppy)_2Cl]_2$ respectively, because these carbons are susceptible to shielding from the methyl groups.

Protons at the 3, 3′ positions (B_3, and A_6) resonate lowest field for their respective ring system (excluding B_6). This is explained by the weak acidic nature of these protons cause by steric strain of the neighboring 3- proton.[30,31,43] There are no B_3 protons in $[Ir(mppy)_2Cl]_2$, as such, no comparison can be made. The corresponding carbon resonances at the 3, 3′ position are among the highest field signals.[43-46] Carbons at this position possess greater charge density as a results of their attached electropositive acidic protons. The B_3 carbons in $[Ir(mppy)_2Cl]_2$ can not be compared since these are methylated carbons.

The chemical shifts may be taken as a measure of the electronic density about a particular nucleus. The charge density or shielding parameter for a nucleus in theses complexes may be rationalized by two affects; (1) ring current anisotropy cause by the electron density from the π orbital from the aromatic phenyl or pyridyl rings of the ligands[30-40,47], and (2) inductive perturbation or the electronic influence of other atoms or functional groups near the nucleus of interest.[38,39,45,46] The former is most influential to proton nuclei, especially at the B_6 and A_3 positions, while the latter is observed for both proton and carbon nuclei, especially nuclei near an activating or deactivating moiety. An example of (1) and (2) is reflected in the chemical shift of the A_3 and B_6 protons.

In the former, the protons are spacially orientated towards the ring current of the adjacent ligand and are bonded adjacent to an anionic ortho-metalating carbon. These two effects reinforce each other and as such the chemical shift of the protons are among the highest upfield aromatic resonances for polypyridyl complexes. In the latter case, the B_6 protons are juxtaposed over the dichloro-bridge, a region void of electron density, and are bonded adjacent to the electronegative chelating nitrogen. These two effects also reinforce deshielding as reflected by the downfield chemical shift of these protons.

Comparing the protons at each position between the two dimers, it is worth noting that the tolyl A protons in $[Ir(ptpy)_2Cl]_2$ resonate higher field relative to those of the phenyl A protons in $[Ir(mppy)_2Cl]_2$. Similarly, the protons of the methylpyridyl B protons in $[Ir(mppy)_2Cl]_2$ resonate higher field relative than those of the pyridyl B protons in $[Ir(ptpy)_2Cl]_2$. If one views these ortho-metalating ligands as both strong σ-donors via the phenyl or tolyl A ring system and good π-acceptors through the pyridyl or methylpyridyl B rings, then the proton chemical shifts may be taken to indicate that the 2-(p-tolyl)pyridine ligand as both a better σ-donor and a stronger π-acceptor than that of the 3 methyl-2-phenylpyridine ligand. We note here, however, that carbon chemical shifts are less sensitive to the inductive effect of methylation which is demonstrated by the lack of correlation among the carbon resonances.

Finally several structural conclusions can be drawn from the chemical shift patterns of the dimer. As mentioned previously, the symmetry (point group) of these molecules can be deduced from the simplicity of the NMR spectra. The question arises, however, as to whether the ortho-metalating carbons or the chelating nitrogens occupy the axial positions? It has been argued that the dimeric structure possesses two mutually trans Ir-N bonds and two mutually cis Ir-C bonds trans to the bridging chlorides[33]; chemical shifts from the A_3 and B_6 protons support this contention.[25,35] The fact that in the dimer the A_3 protons are the highest field resonances and the B_6 are the lowest field resonances indicate that the ligands are aligned in a fashion which places the A_3 protons in a chemically shielded environment and the B_6 in a chemically deshielded environment. Such an environment can only be realized if the Ir-C bonds are mutually cis to each other and trans to the bridging chlorides as shown in Figures 2.1.2a. As will be discuss in Chapter 4, the X-ray crystal structures of both $[Rh(ppy)_2Cl]_2$,[48] $[Ir(ptpy)_2Cl]_2$ and $[Ir(mppy)_2Cl]_2$ support such a conformation.

2. Ground State Redox Potential from Cyclic Voltammograms.

Cyclic voltammograms for $[Ir(ptpy)_2Cl]_2$, Figure 2.2.1, under single scan conditions show two reversible oxidative waves at $E_{1/2}$ = 0.85 and 1.12 V and a weak reductive wave at $E_{1/2}$ = -0.92 V, Table 2.2. Under repetitive scan conditions, however, the oxidative voltammograms indicate a two-electron irreversible process and the reductive voltammograms show current ratios of Ic/Ia ~ 2. The deformation of these waves suggests dimer instability under these conditions.[27,49,50]

Cyclic voltammograms for $[Ir(mppy)_2Cl]_2$, however shows identical wave patterns for single and repetitive scan modes consisting of two reversible oxidative waves at $E_{1/2}$ = 0.85 and 1.10 V, and a very weak irreversible reductive wave at $E_{pc/2}$ = -1.00 V, Figure 2.2.2, Table 2.2. The consistent oxidative patterns shown for the two scan mode suggests stable oxidized Ir(III/IV) and Ir(IV/IV) dimeric species.

The weak reduction current seen in the CVs for both dimers suggests that the methyl-substituted dimers undergo some reduction and that the $[Ir(ptpy)_2Cl]_2$ dimer is easier to reduce (E_{pc}) by over 110 mV relative to the $[Ir(mppy)_2Cl]_2$ dimer. Previous studies of the parent complex[27,29] have indicated that reduction on the pyridyl ring occurs at more negative potentials than reduction on the phenyl ring since the electronegative nitrogen of the pyridyl ring serves to facilitate electro-reduction whereas the excess negative charge

in the metalated phenyl ring renders the metalated ring more difficult to reduce. Furthermore, ligand reduction in the methyl substituted dimers occurs more readily on the aromatic ring without the methyl group because of the methyl's electron donating influence.[51] The degree of reducibility for these dimers is consistent with initial reduction at the pyridyl ring of the NC ligand.[22-24,27-29,48]

Upon correcting the redox potentials for these dimers by the internal reference $Fc^{+/0}$, the oxidative potentials for the methyl substituted dimers (under reversible conditions) are lower than those of the nonsubstituted ppy dimers by 100 mV for the first oxidative wave and by 70 mV for the second oxidative wave. In the next chapter, it will be shown that a similar trend occurs for two other monomeric complexes suggesting that alteration of the ppy ligand by addition of methyl groups can enhance (cathodic shift) the oxidation potentials of methyl-substituted complexes such as in $[Ir(ptpy)_2Cl]_2$ and $[Ir(mppy)_2Cl]_2$ over their nonsubstituted counterpart, $[Ir(ppy)_2Cl]_2$, by as much as 100 mV.

3. Absorption assignments

The absorption features for $[Ir(ptpy)_2Cl]_2$ and $[Ir(mppy)_2Cl]_2$ in dichloromethane, Figures 2.3.1a,b are similar to the nonsubstituted $[Ir(ppy)_2Cl]_2$ dimer,[25,27-29] displaying band maxima near 483, 434, and 400 nm. From their hypsochromic shifts in polar solvents, these low energy bands are assigned MLCT transitions.[52,53] The methyl groups in these substituted complexes have only small effects on the energies of the charge transfer absorption bands as evident from the band maxima similarities in the absorption profiles.

Changes of the low energy band are difficult to monitor because of the low resolution of the absorption features caused by the overlap of several bands, Figure 2.3.1. The small differences in the low energy band maxima can be explained, however, by considering the opposing effects of methyl substituents on the σ-donor and π-acceptor abilities of phenylpyridine. The electron density at the metal is presumed to be enriched by methyl substitution through the σ-bonding framework, while the ligand's π-acceptor ability may be reduced in a corresponding manner. The net result is a very small effect on the spectroscopic metal-to-ligand charge-transfer energies as is observed in the absorption maxima of these complexes.

4. Photophysical Assignments from Emission

Emission spectra for $[Ir(ptpy)_2Cl]_2$ and $[Ir(mppy)_2Cl]_2$ in 77 K glasses, Figure 2.4.1, show structured emission profiles centered around 483-497 nm and 526-530 nm. A trend follows in which the nonsubstituted $[Ir(ppy)_2Cl]_2$ dimer[25,27-29] has the highest energy emissive features (483, 525 nm), followed by the $[Ir(ptpy)_2Cl]_2$ dimer (490, 526 nm), and finally, the $[Ir(mppy)_2Cl]_2$ dimer (497, 530 nm). The relative emission energies from these spectroscopic measurements suggest that the activating methyls on the NC ligands facilitate the lowest energy MLCT transitions. Lifetimes of 5 μs in 77 K glasses support MLCT assignments of these low energy emission bands.

The room temperature fluid solution emission spectra for $[Ir(ppy)_2Cl]_2$ and $[Ir(mppy)_2Cl]_2$ show a single broad emission feature near 515 nm, Figure 2.3.1a b, in addition however, the $[Ir(ptpy)_2Cl]_2$ dimer displays a second band at 580 nm.

Two findings suggest that this second band arises from a monomer solvento complex in thermal equilibrium with the $[Ir(ptpy)_2Cl]_2$ dimer. First, the 580 nm emission band maximum is very near that of the bpy-substituted monomers (λ_{max} for fluid emission for monomers are centered around 595 nm) and second, the emission profiles at high temperatures and ligating solvent indicate the formation of the second feature.[27]

Variable temperature emission spectra of $[Ir(ptpy)_2Cl]_2$, Figure 2.4.1 and 2.4.2, shows the growth of the 583 nm feature towards high

temperature but the collapse of this band as the temperature is lowered. The EEI stack plots, Figure 2.4.4 taken at 170, 200, 250 and 300 K reiterate the observation shown in the previous two figures. In these EEI spectra, the second band maxima begins to dominate the spectra by 200 K and at 380 nm excitation. The emission spectra for a fresh sample of $[Ir(ptpy)_2Cl]_2$, Figure 2.4.5, does not show the second 580 nm band and thus we reasoned that the elevated temperature and irradiation exposure during the acquisition of the stack plots of Figure 2.4.4 may have contributed to the formation of the second emission maximum at 580 nm. In general however, variable temperature emission spectra studies, Figure 2.4.1, 2.4.2 and 2.4.4, suggest a dimer-monomer equilibrium for the $[Ir(ptpy)_2Cl]_2$ complex in which monomer formation is favored thermally.

The variable temperature emission spectra for $[Ir(mppy)_2Cl]_2$ does not indicate a dimer-monomer equilibrium. At 150 K the emission spectrum shows a structured profile with band maxima at 474, 505 and 530 nm which becomes broad and structureless by 300 K. It is interesting to note the development of the 440 nm band towards higher temperature. The EEI stack plots are shown in Figure 2.4.6 and indicate a structured emission at low temperature and structureless profile at elevated temperature. The band maximum red shifts through the temperature progression and remains invariant during the excitation progression.

TABLE 2.4

Emission, Lifetimes, and Quantum Yield for

$[Ir(ppy)_2Cl]_2$[a], $[Ir(ptpy)_2Cl]_2$ and $[Ir(mppy)_2Cl]_2$

Complex	$\lambda_{em\ max}$[b] (nm)	Lifetimes (τ)	Quantum Yields (Φ)
Room Temperature:			
$[Ir(ppy)_2Cl]_2$	518[c]	140 ns[c]	
$[Ir(ptpy)_2Cl]_2$	510,580[c]	148.8 ns[c] 133.3 ns[d]	.7%
$[Ir(mppy)_2Cl]_2$	520[c]	60.3 ns[c] 32.2 ns[d]	<1%
Low Temperature (77 K):			
$[Ir(ppy)_2Cl]_2$	483,525[e]	4.0 μs[f]	
$[Ir(ptpy)_2Cl]_2$	490,526[e]	5.2 μs[f]	
$[Ir(mppy)_2Cl]_2$	497,530[e]	5.0 μs[f]	

(a) From references 27-29
(b) λexcit for R. T. and 77 K at 360 nm; $[Ir(ptpy)_2Cl]_2$ was also excited at 430 and 450 nm.
(c) Solvent; DCM
(d) Solvent; neat toluene
(e) in EtOH-MeOH (4:1) v/v) Glass
(f) in EtOH-MeOH-DCM (4:1:1 v/v/v) Glass

Room temperature emission measurements under various conditions were recorded in order to examine the effect of oxygen and water on the emission profile of $[Ir(ptpy)_2Cl]_2$ in dichloromethane. The results from Figure 2.4.7 shows quenching of the emission after oxygen, purge. Purging with helium nearly restores the emission intensity, while addition of water enhances the 500 nm band. These results suggest that the 500 and 580 bands are quenched by oxygen and that the high energy emission band at 500 nm is aqueous dependent.

Photolysis on $[Ir(ptpy)_2Cl]_2$, Figure 2.4.8 and 2.4.9, did not enhance the 580 nm band, and showed no evidence for a dimer-monomer equilibrium. The structureless and weak emission profile after only 10 minutes suggest rupture of the ligands from iridium due to the harsh photolysis conditions.

In summary the emission maxima for $[Ir(ptpy)_2Cl]_2$ are sensitive to experimental conditions. In some instances the 580 nm band maximum is observed, in other instances, it is suppressed. Helium purging, solvent, irradiation and temperature dependence of the emission profile for $[Ir(ptpy)_2Cl]_2$ suggest a dimer-monomer equilibrium. The 580 nm band probably arises from a monomer solvento complex in thermal equilibrium with the $[Ir(ptpy)_2Cl]_2$ dimer. The band attributed to the solvated monomer is enhanced at elevated temperatures and suppressed upon lowering the temperature.

CHAPTER 3

CHARACTERIZATION OF MIXED LIGAND ORTHO-METALATED IRIDIUM MONOMERS.

No amount of experimentation can prove me right;
a single experiment can prove me wrong

-Albert Einstein

Dimers described in Chapter 2 readily form monomers of the type $[Ir(NC)_2bpy]^+$ upon addition of 2,2'-bipyridine. This chapter describes the characterization of two such monomers, $[Ir(ptpy)_2bpy]^+$ and $[Ir(mppy)_2bpy]^+$. Mild synthetic conditions probably prevent bonding isomerization of the NC ligands to the iridium center giving rise to monomeric complexes with cisoid Ir-C conformation, Figure 3.2.1. This structural conformation is supported by ^1H and ^{13}C NMR results.

Ultraviolet-visible absorption spectra for these monomer complexes show charge transfer bands ranging from 468 to 325 nm. The emission spectra show broad emission profiles centered at 595 nm in fluid solutions but structured profiles with band maxima centered at 527 and 550 nm in rigid glass matrices. Emission lifetimes are around 200 ns under ambient conditions and 5 μs under 77 K

conditions, with luminescence quantum yield around 5%. The time-resolved emission spectra are indicative of dual emitting states, which are also supported by the variable temperature-excitation-emission studies. From the excited state absorption and electrochemical measurements, the lowest lying charge transfer state is MLCT to bpy; consistent with previous studies of $[Ir(ppy)_2bpy]^+$. Cathodic shifts of up to 90 mV for these monomers relative to the nonsubstituted $[Ir(ppy)_2bpy]^+$ are similar to the electrochemical results for the dimers and are consistent with kinetic estimates of the excited state oxidative potentials by Stern-Volmer quenching.

I. SYNTHESES

1. 2,2'-Bipyridyl bis(2-p-tolyl)pyridine Iridium (III) chloride. $[Ir(ptpy)_2bpy]^+$

Iridium 2-p-tolylpyridine dichloro-bridged dimer (55.0mg, 0.049mmol) in dichloromethane (4.0ml), was added to a mixture of 2,2'-bipyridyl (22.2mg, 0.14mmol) in dichloromethane (1.0ml). The preparation of this complex was carried out analogously to the $[Ir(ppy)_2bpy]Cl$[27-29] synthesis to give an amorphous yellow powder of the $[Ir(ptpy)_2bpy]Cl$ monomer (66.9mg, 92.5%).

2. 2,2'-Bipyridyl bis(3-methyl-2-phenyl)pyridine Iridium (III) chloride. $[Ir(mppy)_2bpy]^+$

The reaction and work up of this synthesis, using iridium methylphenylpyridine dichloro-bridged dimer (54.3mg, 0.048mmol) and bipyridine (22.2mg, 0.14mmol), was carried out analogously to the the $[Ir(ptpy)_2bpy]Cl$ synthesis to give $[Ir(mppy)_2bpy]Cl$ as an amorphous yellow powder (70.0mg, 90.3%).

II. MEASUREMENTS

1. NMR

The NMR analysis are described in Chapter 1 and in Appendix A. Monomer samples were dissolved in acetonitrile-d_3, dichloromethane-d_2 or chloroform-d for analysis.

2. Cyclic Voltammetry

The CV experimental procedures are described in Appendix B. Acetonitrile/TEAH was used for the supporting electrolyte solution.

3. Absorption

Samples were dissolved in either dichloromethane or acetonitrile for absorption measurements. See Appendix C.

4. Luminescence

Experimental procedures are in Appendix C. Luminescence measurements consisted of (1) emission, (2) emission-excitation-intensity (3) variable temperature, emission and excitation, (4) emission lifetimes, (5) quantum yields and (6) Stern-Volmer quenching. Samples for ambient temperature measurements were taken in dichloromethane, acetonitrile or EtOH-MeOH (4:1 v/v). Rigid glass matrix emission spectra were measured in EtOH-MeOH (4:1 v/v).

5. Excited State Absorption

The experimental procedure, described in Appendix D, was taken from a recent publication on the excited state absorption of $[Ir(ppy)_2bpy]^+$.[54] The experiments were performed in Professor Kobayashi's laboratory at the University of Tokyo.

III. RESULTS

1. ^{1}H and ^{13}C NMR

The structure of the monomers in Figure 3.1.1 and the labeled ligands in Figure 2.1:1 may be helpful in the following discussion.

The ^{1}H NMR spectra were more highly resolved in dichloromethane-d_2 than in any other solvent used, therefore, the NMR measurements were obtained using this solvent. The ^{1}H NMR spectra (10 - 0 ppm) for $[Ir(ptpy)_2bpy]^+$ and $[Ir(mppy)_2bpy]^+$, Figure 3.1.2a and 3.1.3a respectively, shows integration for eleven protons between 10 - 6 ppm. The resonances at 6.8 and 7.4 ppm for $[Ir(ptpy)_2bpy]^+$ (Figure 3.2.2b), and that at 6.7 ppm for $[Ir(mppy)_2bpy]^+$ (Figure 3.1.3b) are from superimposed signals.

The ^{1}H COSY spectra for $[Ir(ptpy)_2bpy]^+$ and $[Ir(mppy)_2bpy]^+$, Figure 3.1.4 and 3.1.5, separates the contours to three spin systems corresponding to rings "A", "B" and "C" in the monomer, Figure 3.1.1 and 2.1.1. Proton assignments were made using J-correlation connective analysis on the COSY spectra. The CSCM spectrum was used to elucidate the overlapping signals at 7.4 ppm for $[Ir(ptpy)_2bpy]^+$. Proton assignments are tabulated in Table 3.1 and Appendix A.

The $[Ir(mppy)_2bpy]^+$ ^{13}C NMR spectrum, Figure 3.1.7, shows sixteen aromatic resonances and one aliphatic resonance between 200 - 0 ppm but the corresponding ^{13}C NMR spectrum for $[Ir(ptpy)_2bpy]^+$, Figure, 3.1.6, shows only fifteen aromatic resonances and one

aliphatic resonance. The ^{13}C NMR and APT spectrum for $[Ir(ptpy)_2bpy]^+$, Figure 3.1.8, did not show all expected nonprotonated resonances (the CSCM spectrum cannot detect nonprotonated carbon resonances) but the the SFORD spectra, did show a complicated splitting pattern for the resonance at 119.8 ppm suggesting superimposed protonated and nonprotonated carbon resonances. However, the parent $[Ir(ptpy)_2Cl]_2$ dimer lacks nonprotonated carbon resonance higher field than 139 ppm and furthermore, the carbon chemical shifts in the monomers usually resonate at lower field because of the deshielding effect from the added bpy ligand. It is unlikely therefore that a nonprotonated carbon would resonate at 119 ppm. Upon closer inspection of the APT spectrum, see inset Figure 3.1.8, we discovered that the 141 ppm signal is actually the superposition of two nonprotonated resonances, A_2 and A_4, which is where these carbons should resonate based on their chemical shifts in the ^1H NMR spectrum for $[Ir(ptpy)_2Cl]_2$. All expected carbon resonances for $[Ir(ptpy)_2bpy]^+$ is thus full accounted for. Likewise, the aromatic ^{13}C NMR and APT for $[Ir(mppy)_2bpy]^+$, Figure 3.1.9 shows all five nonprotonated and eleven protonated carbon resonances.

The CSCM spectra for $[Ir(ptpy)_2bpy]^+$ and $[Ir(mppy)_2bpy]^+$, Figures 3.1.10 and 3.1.11 respectively, show the ^1H, ^{13}C and APT spectra as projections with the contours mapped and labeled to their designated proton/carbon resonances. Carbon assignments are compiled in Table 3.1 and Appendix Table A.6.

TABLE 3.1

^{1}H and ^{13}C NMR Assignments for $[Ir(ptpy)_2bpy]^+$ and $[Ir(mppy)_2bpy]^+$ in dichloromethane-d_2 (vs. TMS)

Position	$[Ir(ptpy)_2bpy]^+$ ^{1}H /^{13}C (δ)	$[Ir(mppy)_2bpy]^+$ ^{1}H /^{13}C (δ)
A_1	/150.8	/152.3
A_2	/141.4	/145.9
A_3	6.03/126.6	6.39/132.0
A_4	- /141.3	6.87/129.9
A_5	6.84/124.0	7.07/122.5
A_6	7.36/125.1	8.00/129.2
B_2	/156.4	/156.2
B_3	7.80/118.7	- /133.4
B_4	7.66/138.3	7.57/142.4
B_5	6.84/123.0	6.87/122.9
B_6	7.53/148.7	7.50/147.3
C_2	/168.2	/166.1
C_3	9.25/132.7	9.19/126.5
C_4	8.13/140.0	8.22/140.0
C_5	7.36/128.4	7.42/128.3
C_6	7.90/150.6	7.86/150.3
Me	2.06/21.8	2.84/23.9

FIGURE 3.1.1:

CHEM-X representative structures of (a.) $[Ir(ptpy)_2bpy]^+$ and (b.) $[Ir(mppy)_2bpy]^+$.

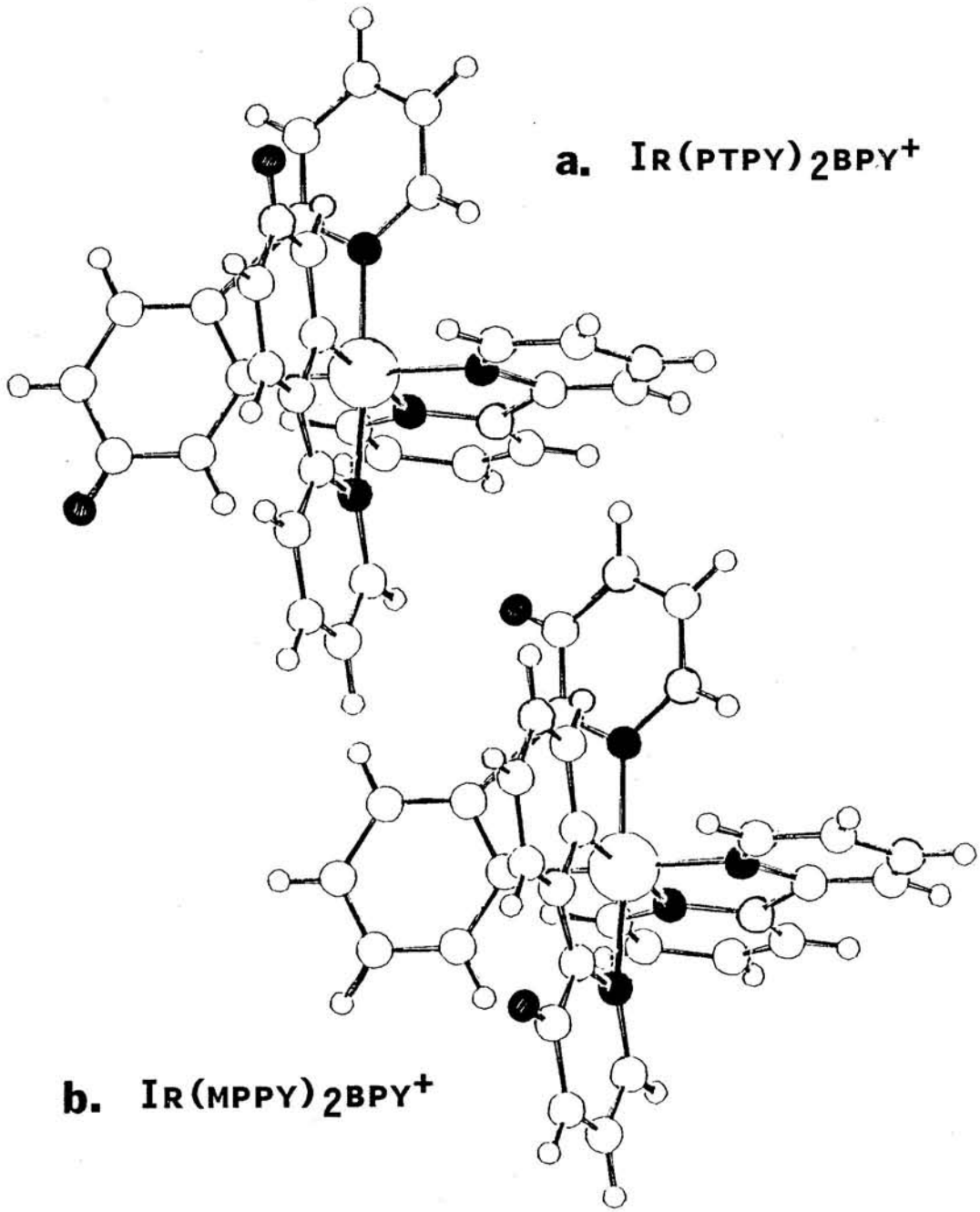

FIGURE 3.1.2:

^1H NMR spectra for $[Ir(ptpy)_2bpy]^+$ in dichloromethane-d_2 (a). 10 - 0 ppm and (b.) 10 - 5 ppm.

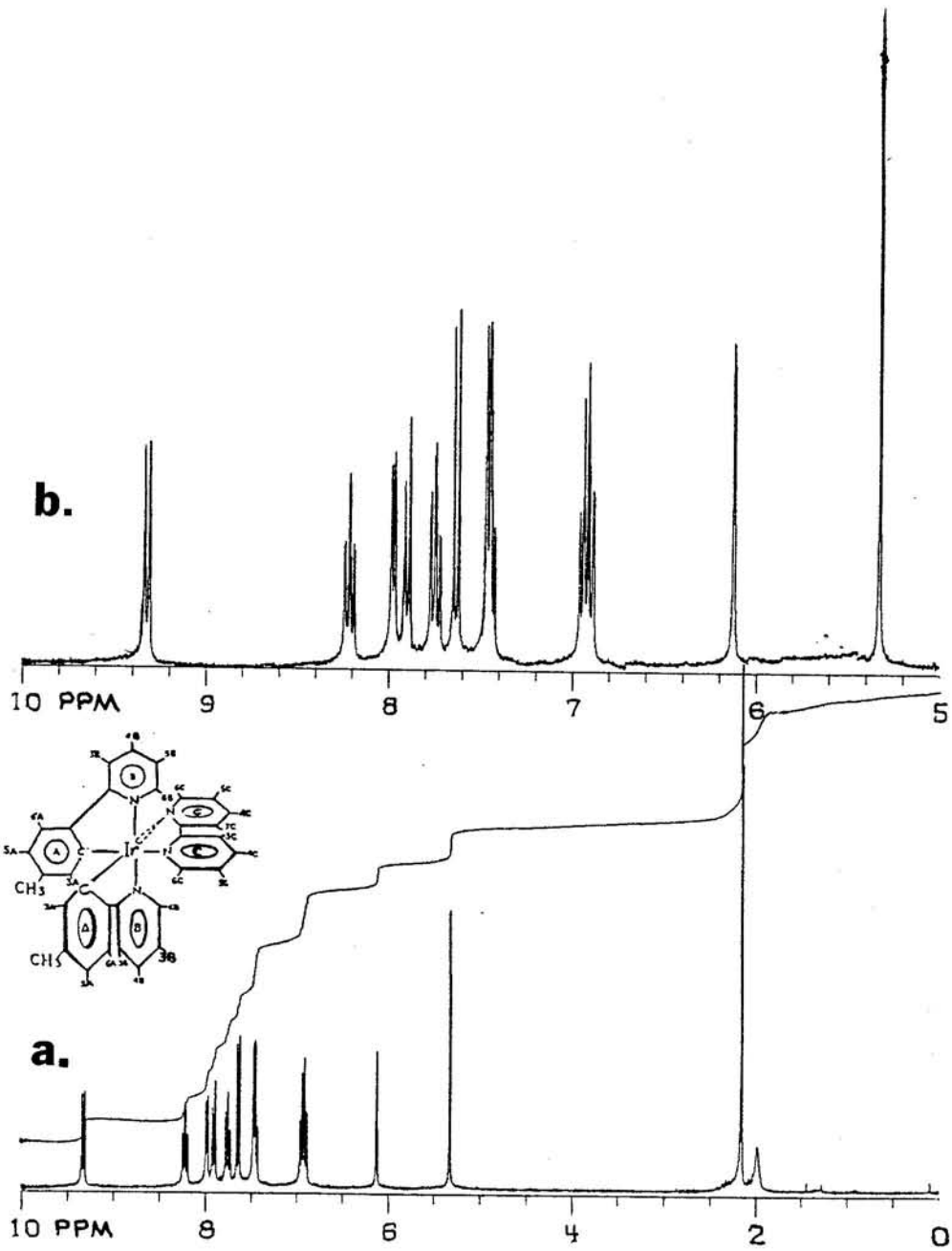

FIGURE 3.1.3:

^{1}H NMR spectra for $[Ir(mppy)_2bpy]^+$ dichloromethane-d_2 (a). 10 - 0 ppm and (b.) 10 - 5 ppm.

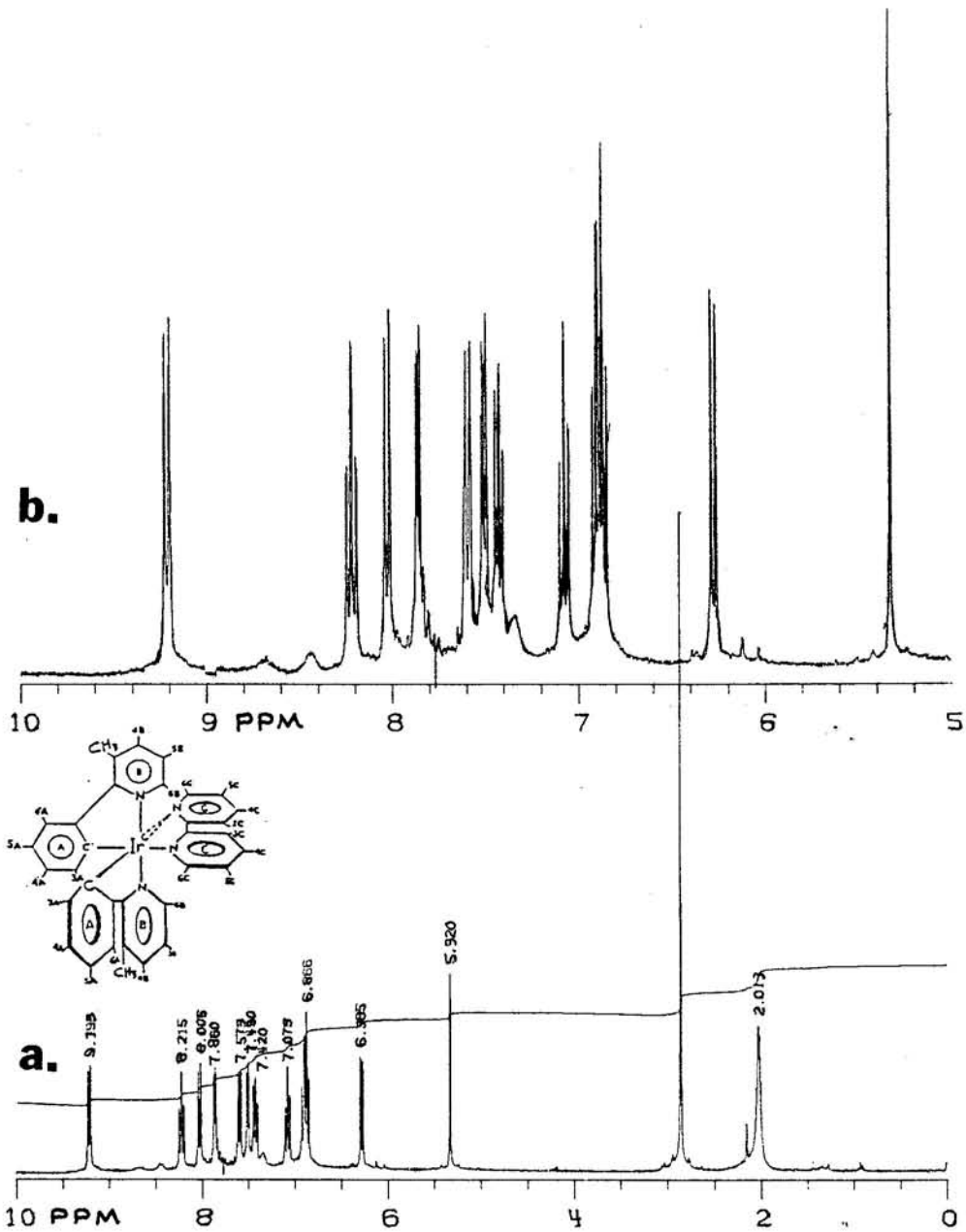

FIGURE 3.1.4:

^1H 2D-Correlation Spectroscopy (COSY) spectrum for $[Ir(ptpy)_2bpy]^+$ in dichloromethane-d_2.

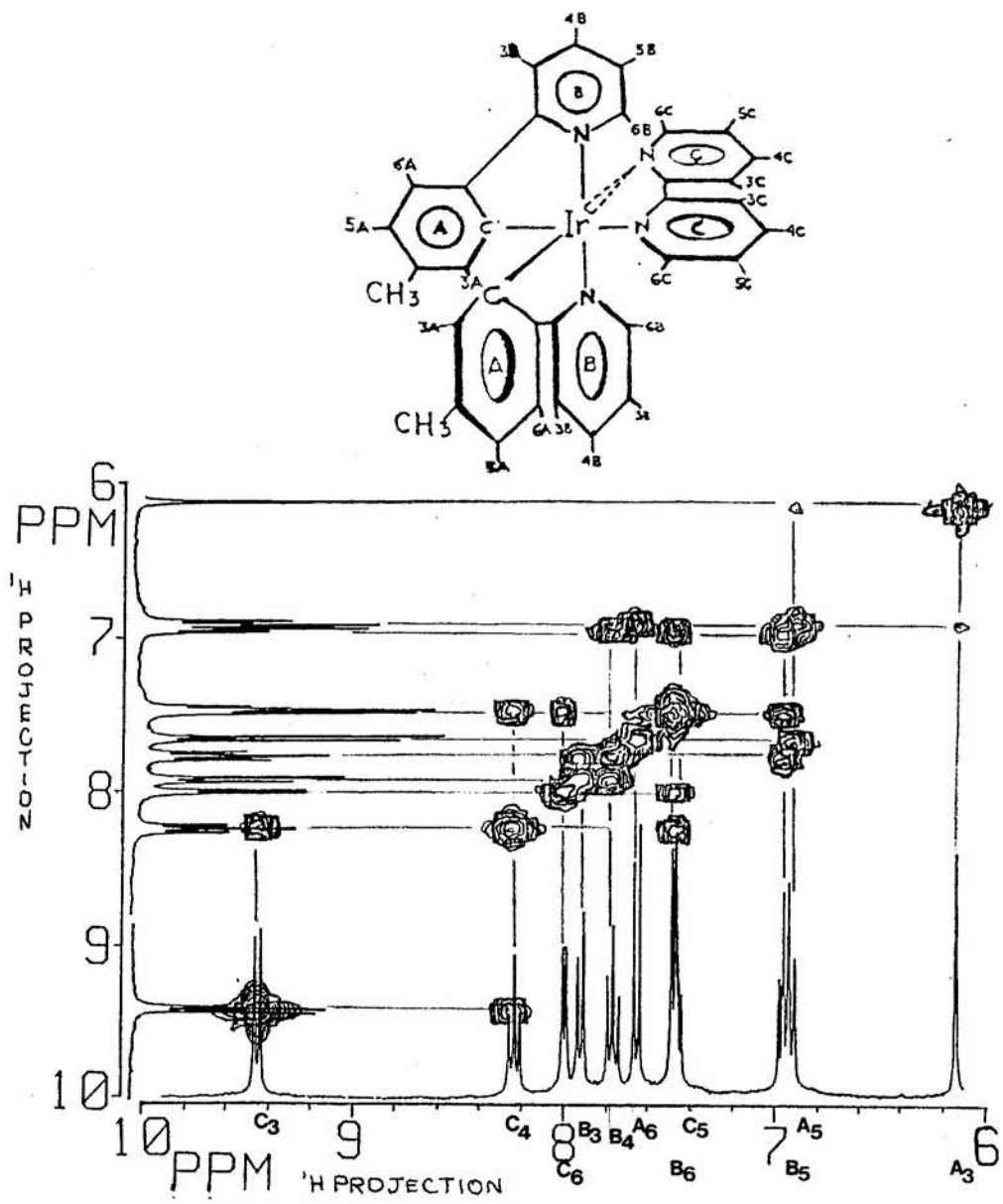

FIGURE 3.1.5:

^1H 2D-Correlation Spectroscopy (COSY) spectrum for $[Ir(mppy)_2bpy]^+$ in dichloromethane-d_2.

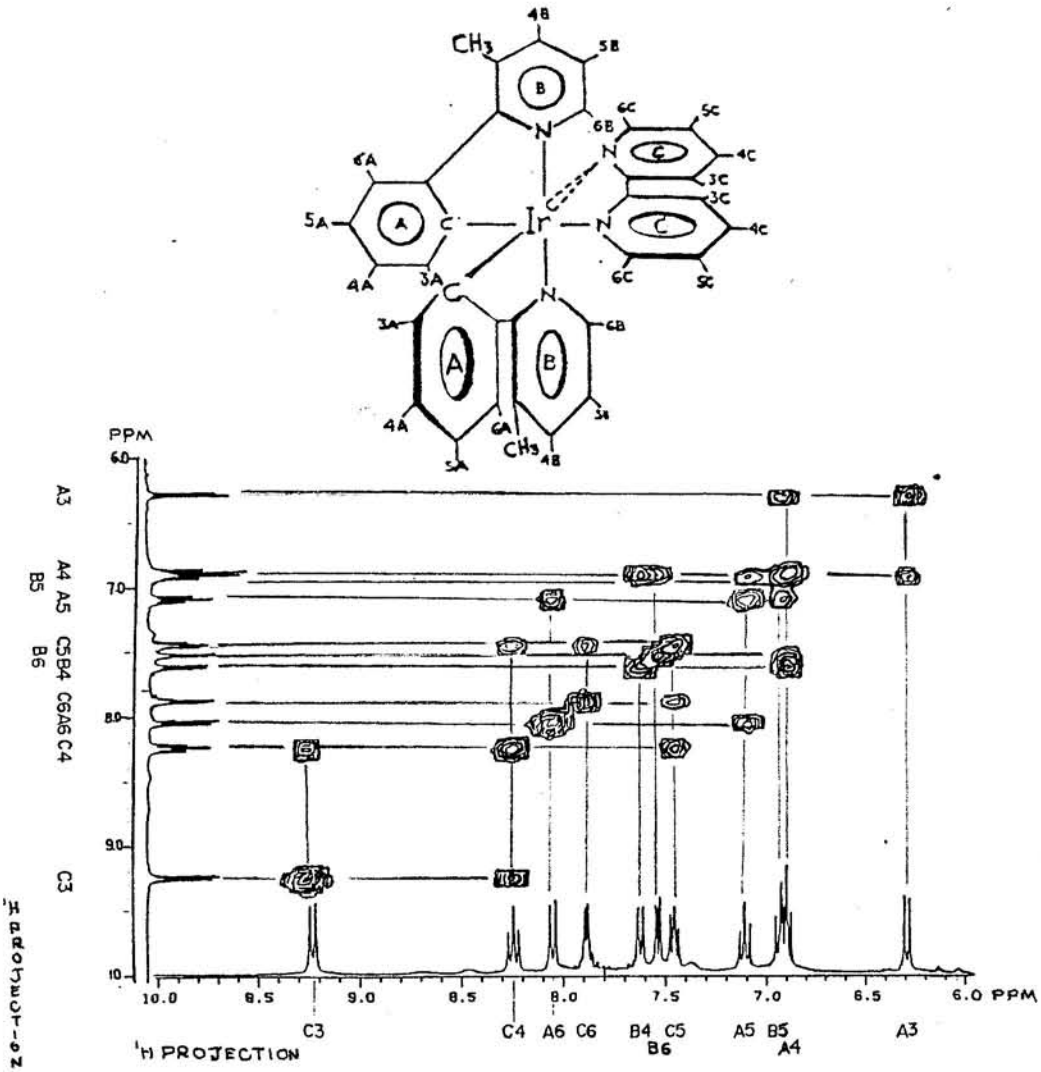

FIGURE 3.1.6:

^{13}C NMR spectrum for $[Ir(ptpy)_2bpy]^+$, (200 - 0 ppm) in DCM-d_2.

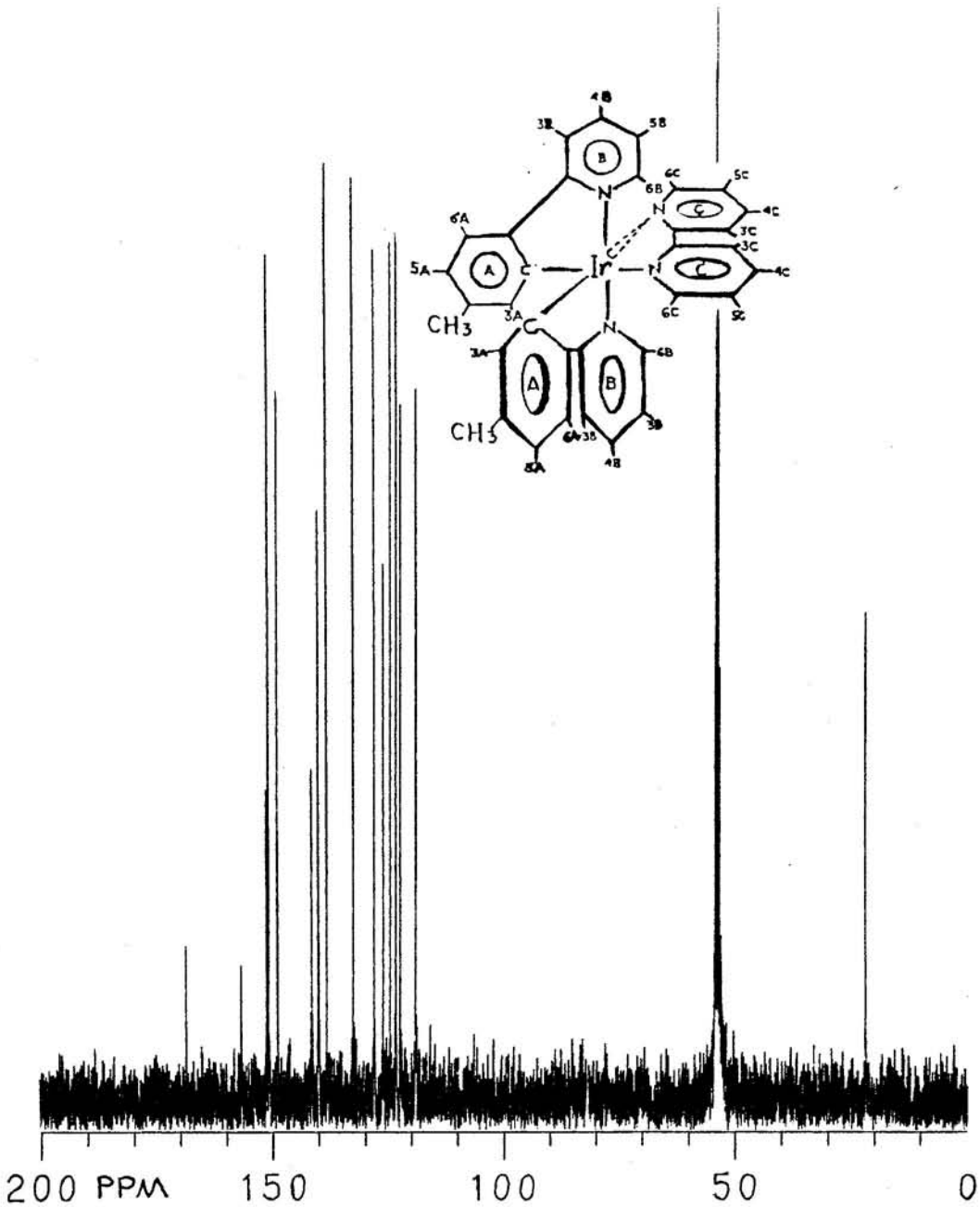

FIGURE 3.1.7:

^{13}C NMR spectrum for $[Ir(mppy)_2bpy]^+$, (200 - 0 ppm) in DCM-d_2.

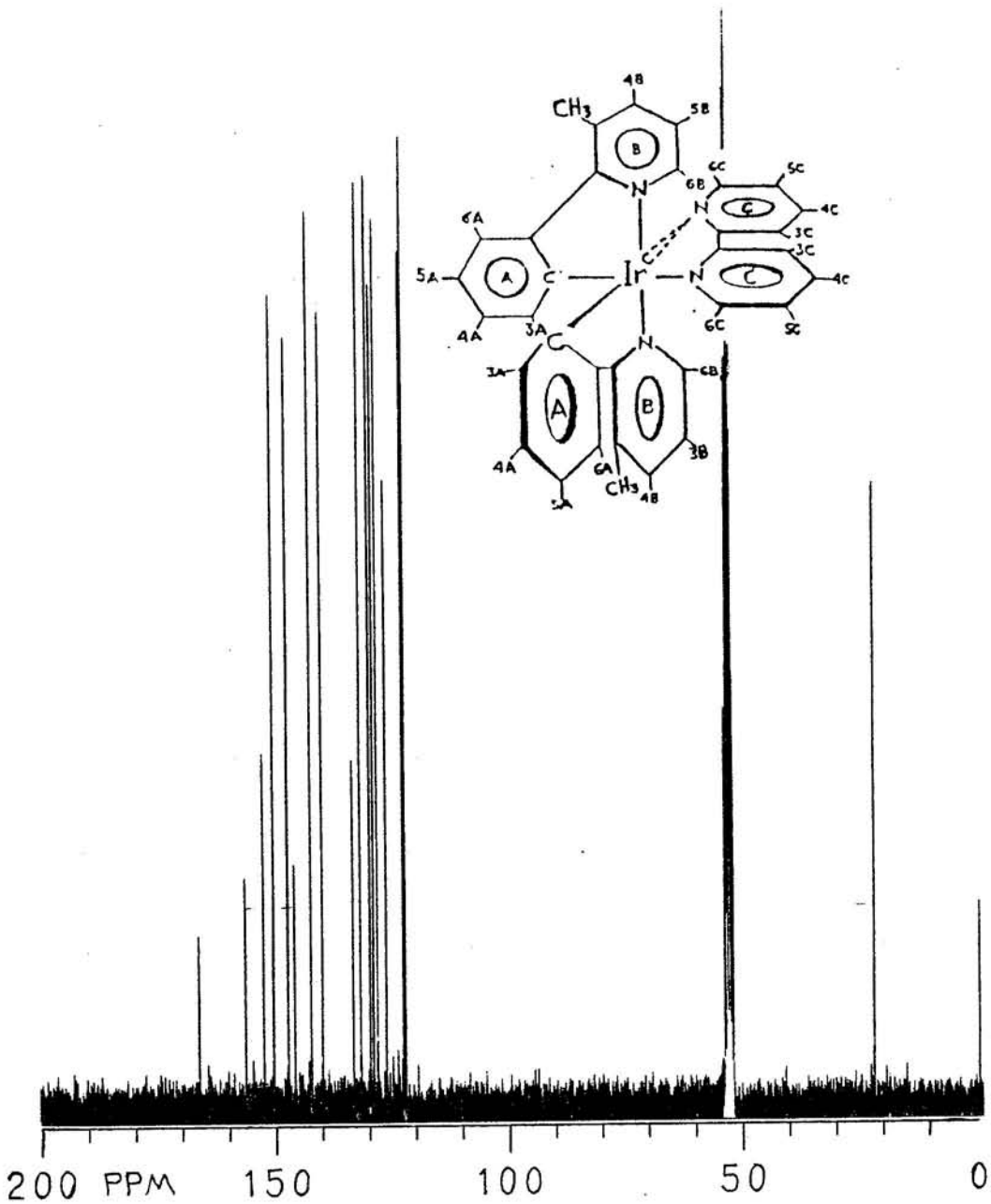

FIGURE 3.1.8:

^{13}C NMR spectra for $[Ir(ptpy)_2bpy]^+$, (170 - 110 ppm) in DCM-d_2. (a.) ^{13}C NMR spectrum and (b.) Attached Proton Test (APT) Spectrum.

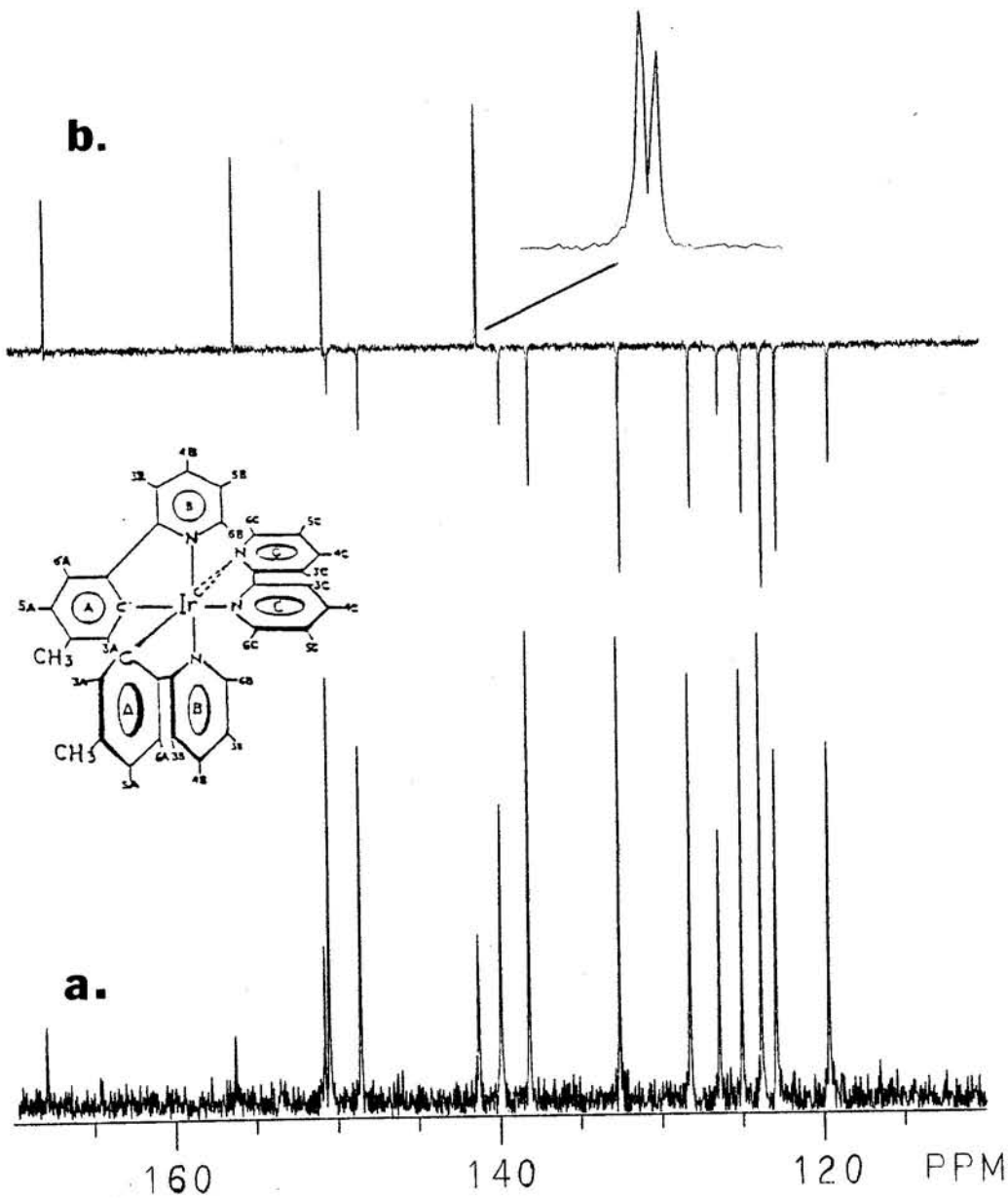

FIGURE 3.1.9:

^{13}C NMR spectra for $[Ir(mppy)_2bpy]^+$, (170 - 120 ppm) in DCM-d_2. (a.) ^{13}C NMR spectrum and (b.) Attached Proton Test (APT) Spectrum.

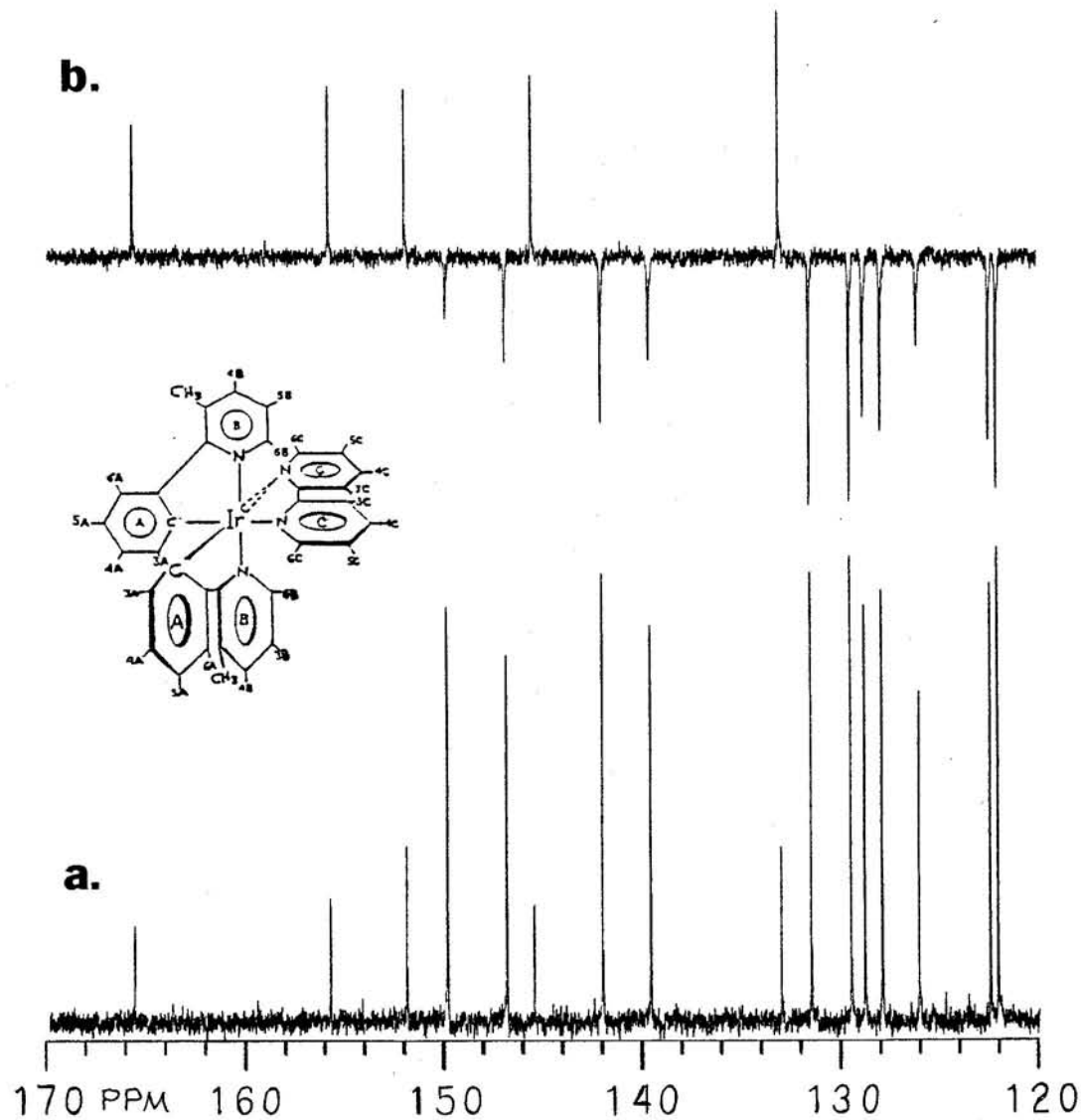

FIGURE 3.1.10:

^{1}H-^{13}C Heteronuclear Correlation Spectroscopy (CSCM) spectrum for $[Ir(ptpy)_2bpy]^+$ in dichloromethane-d_2.

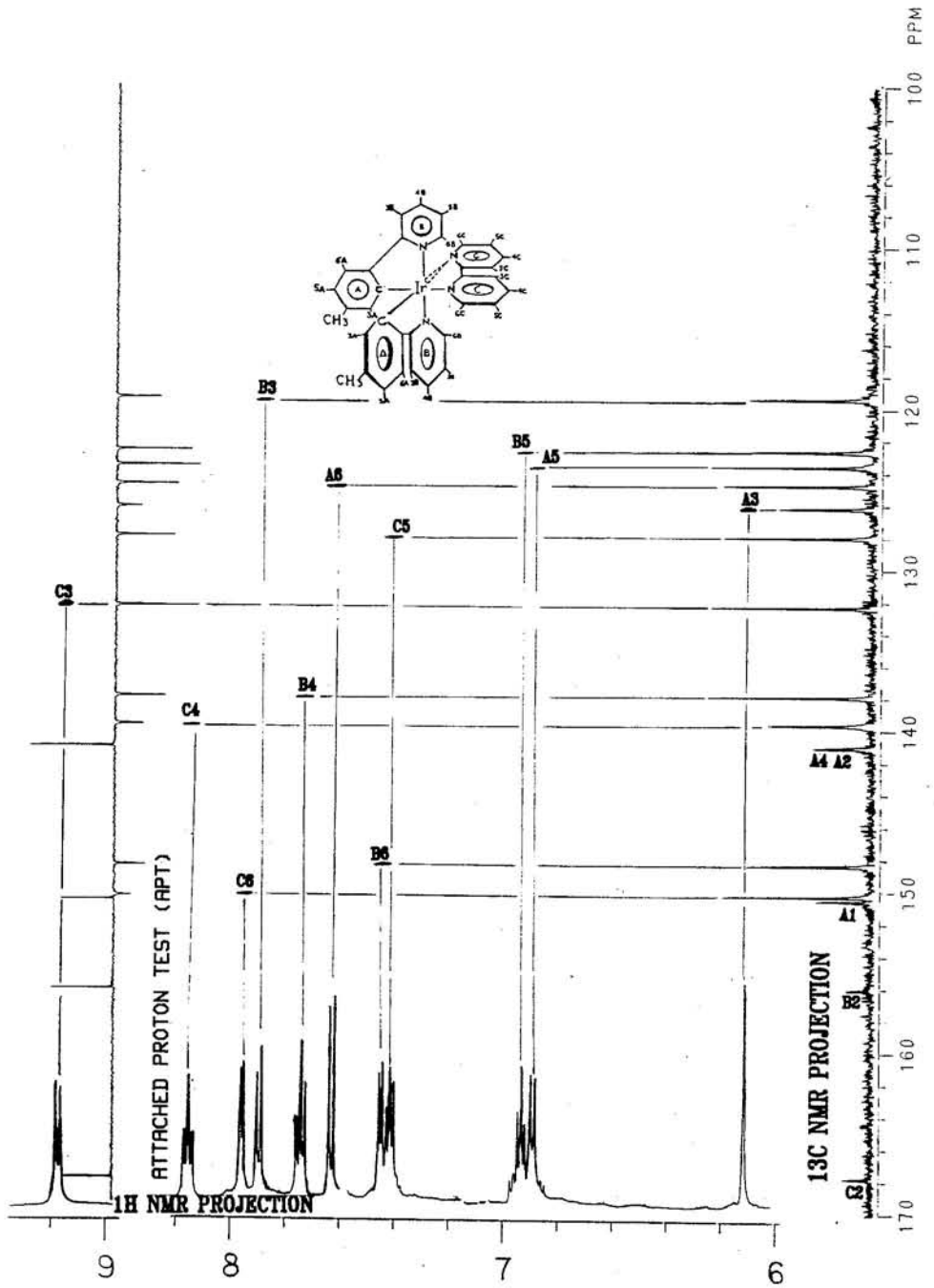

FIGURE 3.1.11:

^{1}H-^{13}C Heteronuclear Correlation Spectroscopy (CSCM) spectrum for $[Ir(mppy)_2bpy]^+$ in dichloromethane-d_2.

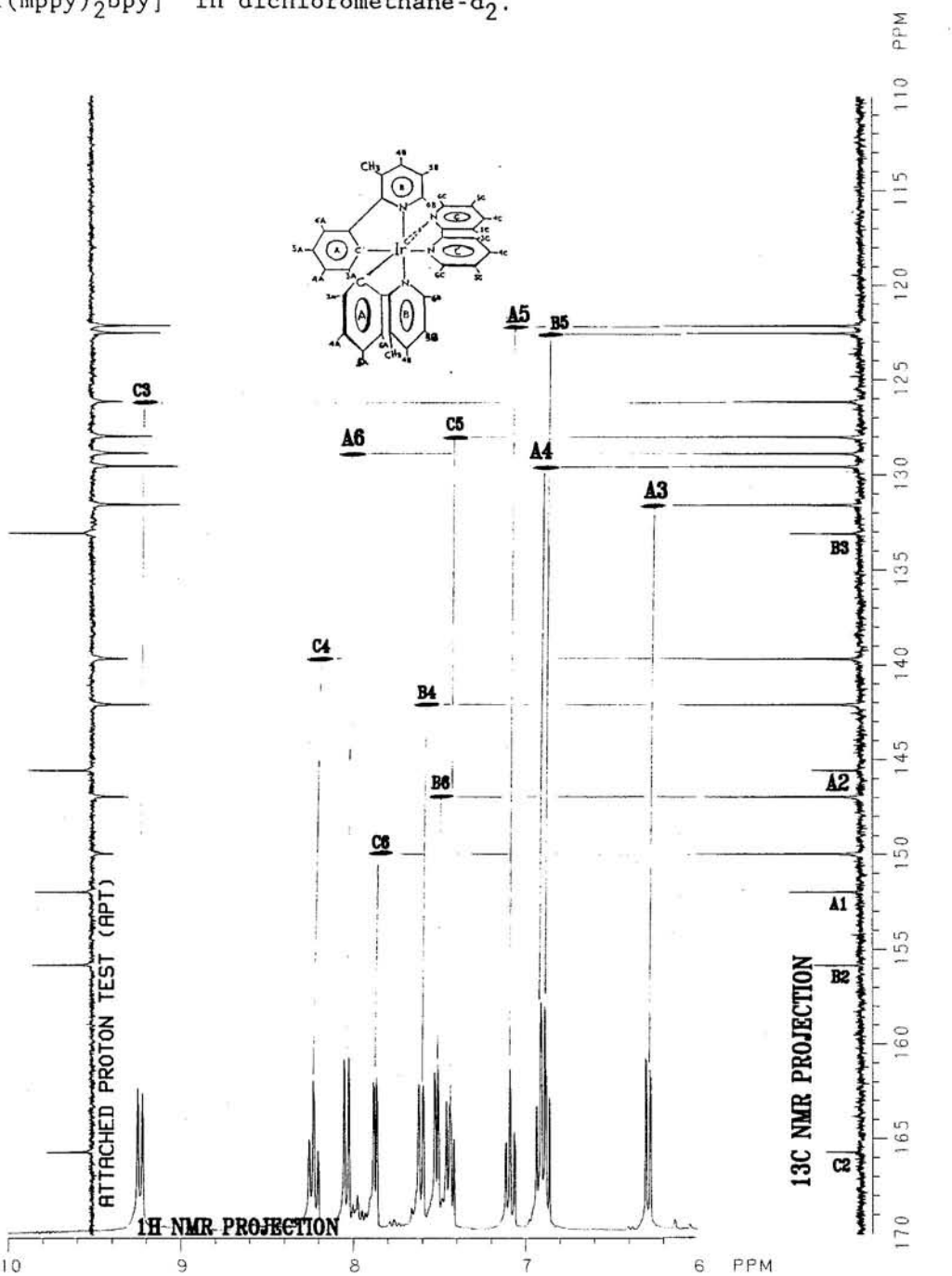

2. Cyclic Voltammetry

The room temperature cyclic voltammograms for $[Ir(ptpy)_2bpy]^+$ and $[Ir(mppy)_2bpy]^+$ in acetonitrile / TEAH supporting electrolyte, Figures 3.2.1**a-d** and 3.2.2**a-d** respectively, are illustrated by four curves **a**, **b**, **c** and **d** analogous to the dimer's cyclic voltammograms. CV's for both monomers have invariant redox patterns for repetitive and single scans, curves **c** and **d**; showing two oxidative waves and a single reduction wave. Only the second oxidative wave at $E_{1/2}$ = 1.20 V and the reductive wave at $E_{1/2}$ = -1.41 V versus SCE, shows reversible behavior. Potentials for the $Fc^{+/0}$ couple, $E_{1/2}$ = 0.40 V versus SCE, are shown in curves **b**, Figure 3.2.1 and 3.2.2. Redox potentials for the monomers are summarized in Table 3.2. and Appendix B, Table B.1.

TABLE 3.2

Redox Potentials for $Ir(ptpy)_2bpy^+$ and $Ir(mppy)_2bpy^+$

in TEAH/Alumina/dichloromethane. (V vs. SCE)

Complex	E_{pa}	E_{pc}	$E_{pa/2}$	$E_{pc/2}$	ΔE_{p-p}	$E_{1/2}$
$[Ir(ppy)_2bpy]^+$ [a]						
Ox-scan 1st[b]	1.32	1.24	1.12	1.20	.08	1.28 (0.88)[c]
Re-scan 1st	-1.34	-1.42	-1.37	-1.35	.08	-1.38 (-1.78)
$[Ir(ptpy)_2bpy]^+$						
Ox-scan 1st	0.95	-	-	-	-	-
Ox-scan 2nd	1.20	1.18	1.15	1.20	.02	1.18 (0.79)
Re-scan 1st	-1.40	-1.45	-1.43	-1.41	.05	-1.42 (-1.81)
$Fc^{+/0}$	0.51	0.28	0.40	0.38	.23	0.39
$[Ir(mppy)_2bpy]^+$						
Ox-scan 1st[d]	1.05	-	1.01	-	-	-
Ox-scan 2nd	1.25	1.18	1.19	1.23	.07	1.21 (0.81)
Re-scan 1st	-1.36	-1.45	-1.41	-1.40	.09	-1.41 (-1.81)
$Fc^{+/0}$	0.50	0.29	0.40	0.40	.21	0.40

a) Taken from references 27 and 29.
b) 1st (2nd) wave of oxidative or reductive scan.
c) Values in parenthesis are $E_{1/2}$ vs. $Fc^{+/0}$.
d) irreversible oxidation wave at Epa = 1.1 V assigned to chloride oxidation.

FIGURE 3.2.1:

Cyclic Voltammograms for $[Ir(ptpy)_2bpy]^+$ at room temperature, in TEAH/Alumina/acetonitrile. (V vs. SCE)

Curves (a.) - TEAH/Alumina/acetonitrile CV scan
(b.) - Internal reference CV scan, $Fc^{+/0}$
(c.) - CV scan of complex under **repetitive** scan.
(d.) - CV scan of complex under **single** scan.

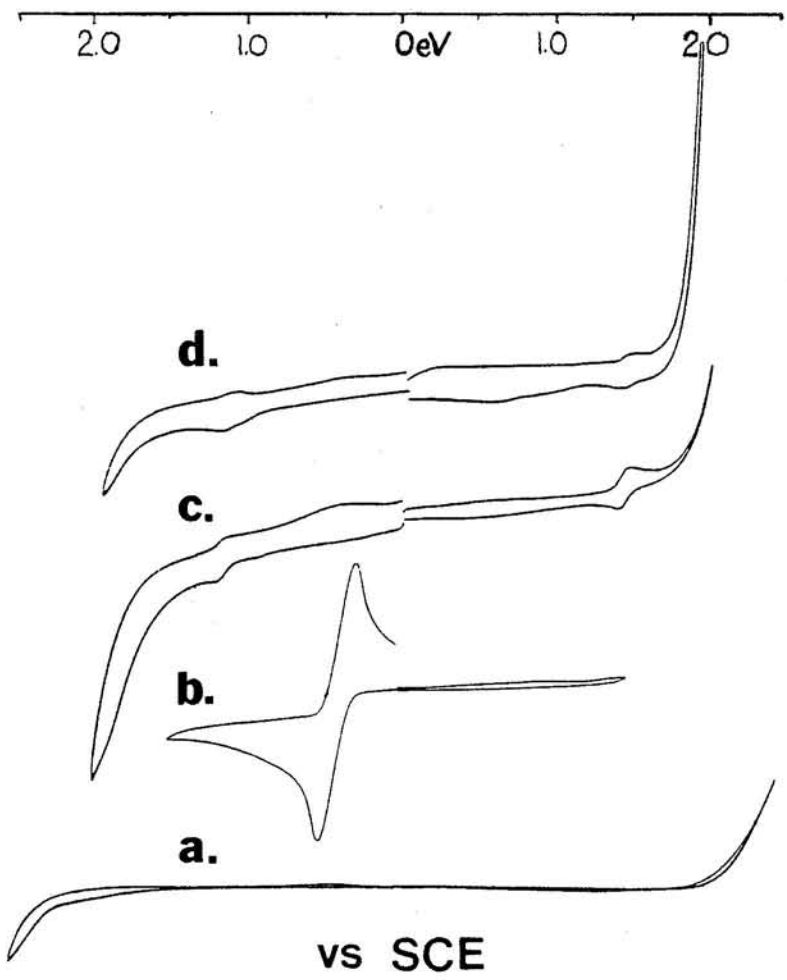

FIGURE 3.2.2:

Cyclic Voltammograms for $[Ir(mppy)_2bpy]^+$ at room temperature, in TEAH/Alumina/acetonitrile. (V vs. SCE)

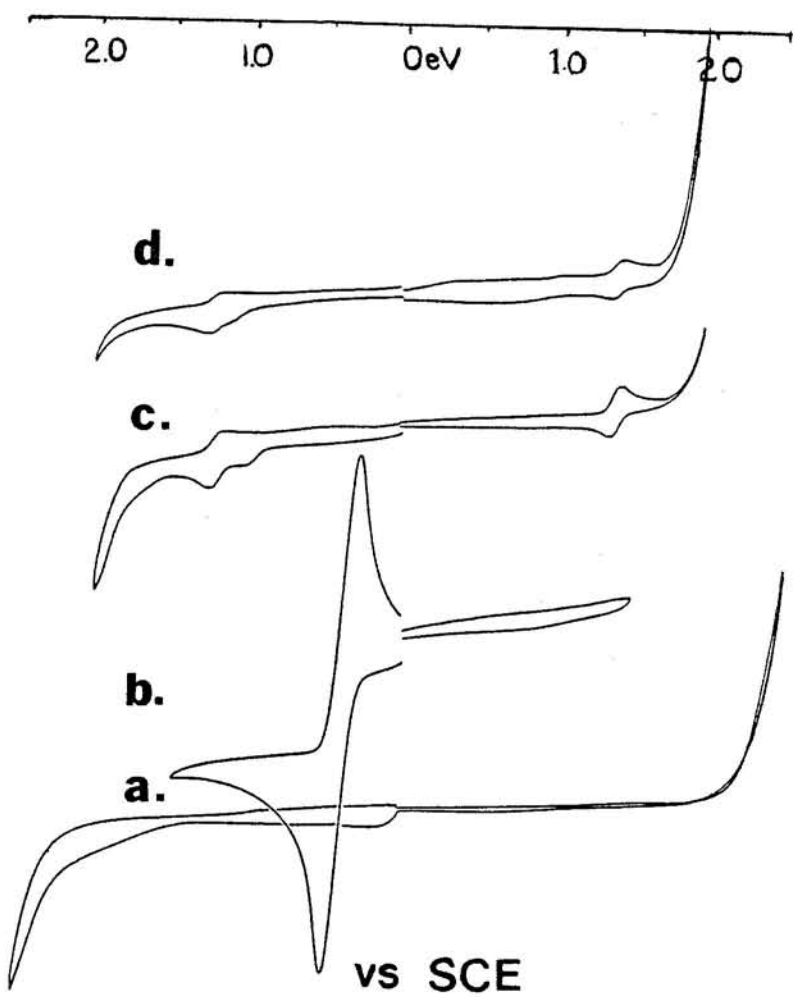

3. Absorption

Absorption maxima for $[Ir(ptpy)_2bpy]^+$ and $[Ir(mppy)_2bpy]^+$ in dichloromethane, Figure 3.3.1a and b respectively, are compiled in Table 3.3. The absorption profiles follow Beer's law between 10^{-4} and 10^{-6} M.

In the visible region, $[Ir(ptpy)_2bpy]^+$ and $[Ir(mppy)_2bpy]^+$ show absorption maxima at 468 and 411 nm and at 467 and 416 nm respectively. For comparison, the band maxima for $[Ir(ppy)_2bpy]^+$ are also presented in Table 3.3.

TABLE 3.3

Absorption maxima and extinction coefficient in dichloromethane for $[Ir(ppy)_2bpy]^+$, $[Ir(ptpy)_2bpy]^+$, and $[Ir(mppy)_2bpy]^+$.

Complex	Absorption Features (nm)	ϵ ($M^{-1}cm^{-1}x10^{-3}$)
$[Ir(ppy)_2bpy]^+$	465	0.58
	410	2.8
	375	4.7
	335 (sh)	-
	310	16.1
	265	36.1
$[Ir(ptpy)_2bpy]^+$	468	0.71
	411 (sh)	4.03
	380	6.6
	325 (sh)	12.8
	314 (sh)	20.9
	273	45.9
	258	42.6
$[Ir(mppy)_2bpy]^+$	467	0.87
	416 (sh)	4.41
	382	6.82
	363 (sh)	7.2
	340	10.3
	311 (sh)	29.8
	266	47.9
	255	52.4

FIGURE 3.3.1:

Absorption and emission measurements for Ir(III) monomer complexes.

a) $[Ir(ptpy)_2bpy]^+$ b) $[Ir(mppy)_2bpy]^+$

——— Absorption and emission; Room temperature in DCM
------ Emission; 77K in EtOH:MeOH (4:1 v/v)

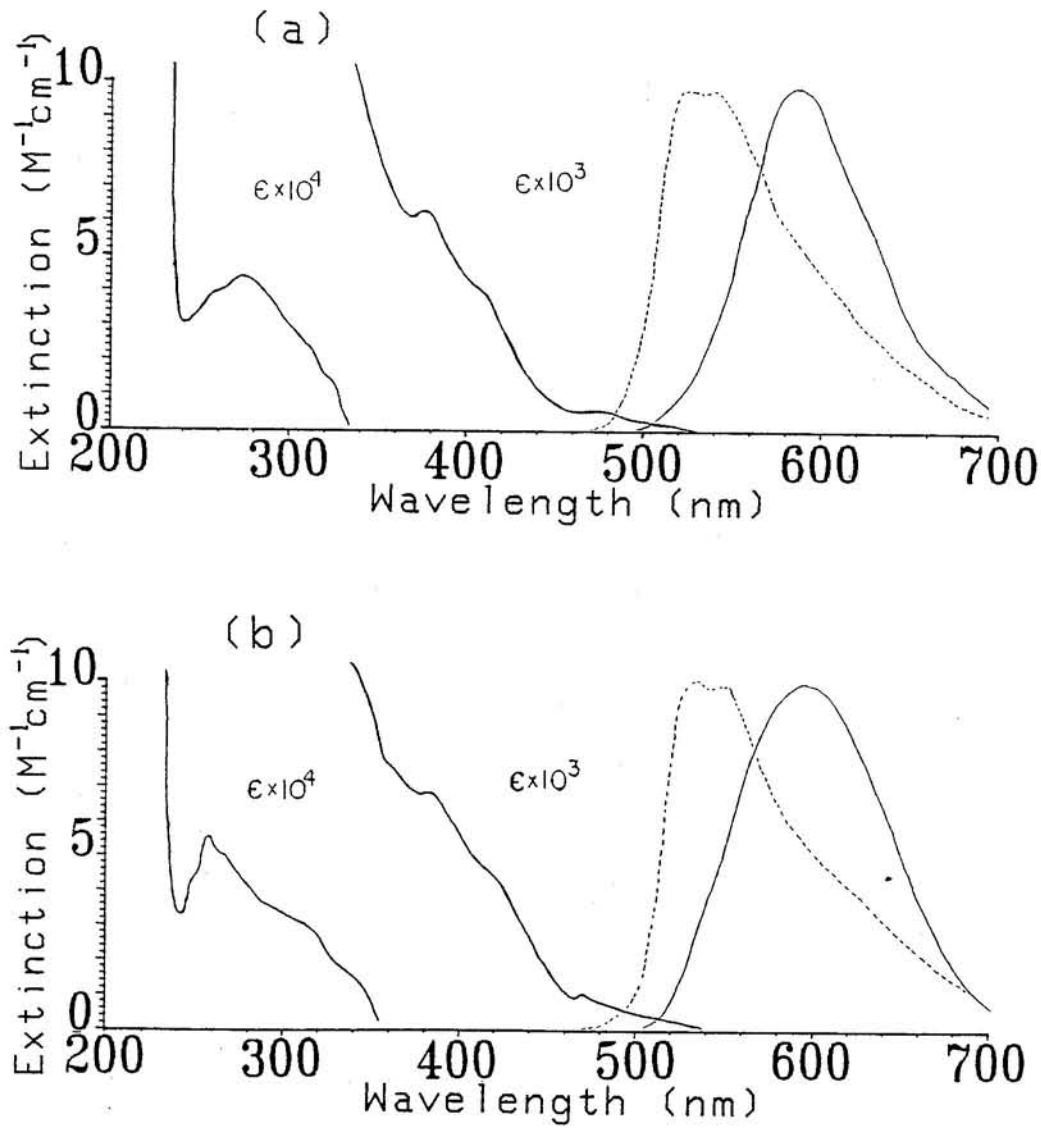

4. **Luminescence**

A. Emission

Ambient and low temperature (77K, glasses) emission maxima for $[Ir(ptpy)_2bpy]^+$ and $[Ir(mppy)_2bpy]^+$, Figure 3.3.1ab, are tabulated in Table 3.4. Dichloromethane was used for ambient temperature measurements and EtOH-MeOH (4:1 v/v) was used to form 77 K glasses. The emission spectra for both methyl substituted monomers are similar to the nonsubstituted ppy monomer, $[Ir(ppy)_2bpy]^+$, showing a broad profile centered at 595 nm under ambient conditions and structured profiles with maxima near 527 and 550 nm in 77 K conditions.

B. Emission-Excitation-Intensity (R.T.)

The room temperature EEI stack plots, Figure 3.4.1, for freeze-pump-thawed samples of $[Ir(ptpy)_2bpy]^+$ in dichloromethane show broad profiles centered at 596 nm. Samples were excited between 350 and 395 nm at 5 nm increments and monitored between 500 to 700 nm. Although there is an increase of the emission intensity towards higher excitation wavelength, the emission maximum remains at 596 nm. Figure 3.4.2 shows the corresponding EEI stack plots for $[Ir(mppy)_2bpy]^+$ with the band maximum invariant at 601 nm through the excitation progression.

C. Emission-Excitation-Intensity (77 K)

The 77 K EEI spectra taken in EtOH-MeOH (4:1 v/v) of $[Ir(ptpy)_2bpy]^+$ are shown in Figures 3.4.3 and 3.4.4 with the excitation wavelengths incremented every 2 nm between 200 to 238 nm

in the former and 360 to 428 nm in the latter spectrum. The excitation stack plots in Figure 3.4.3 show poorly resolved emission band maxima at 525, 542 and 553 nm but shows signs of structure towards lower energy excitation. At excitation past 360, Figure 3.4.5, the emission spectra show a structured profiles with band maxima at 521 and 546 nm, with the intensity beginning to decay past 420 nm excitation. The shift of the emission energies are difficult to estimate because the poor resolution of these stack plots.

The corresponding EEI stack plots for $[Ir(mppy)_2bpy]^+$, Figure 3.4.5 and 3.4.6, do not show emission maxima changes over the excitation progression. In both EEI stack plots, the emission band maxima remain centered at 526 and 550 $\pm$ 2 nm. We note however that the maximum excitation wavelength for these spectra is limited to 438 nm; as will be shown next, changes in the emission energies do not begin to take place until 460 nm excitation.

Variable excitation luminescence spectra were measured for $[Ir(ptpy)_2bpy]^+$ in EtOH-MeOH (4:1 v/v) in order to assess changes in the emission energies over a broader excitation wavelength range. Figure 3.4.7 shows the emission profiles for excitation between 200 to 515 nm. At high energy excitation, 200 - 320 nm the emission maxima are centered at 526 and 548 nm. Towards moderate energy excitation, 400 - 480 nm, these emission bands begin to blue shift toward 522 and 540 nm. Finally at low energy excitation, these bands red shift toward 540 and 575 nm.

The variable excitation luminescence spectra for $[Ir(mppy)_2bpy]^+$, Figure 3.4.8, show similar behavior. Excitation between 200 to 460 nm shows emission maxima centered at 526 and 550 nm; between 460 and 480 nm, only the first band at 526 nm shifts (to 523 nm), finally at excitation above 480 nm, the emission band maxima red shift from 523 and 554 nm to 541 and 576 nm. The cartoon in Figure 3.4.12 is use to illustrate these results.

D. Time Resolved Emission

Time resolved emission spectra for $[Ir(ptpy)_2bpy]^+$ in ETOH-MeOH (4:1 v/v) are shown in Figure 3.4.10. Looking for 10 ns , the delay after pulse excitation of the sample were set to 20, 15, 10, 5, 2.5, 1.0 and 0.1 μs respectively. Although the emission profile is poorly resolved at 20 μs delay, the emission spectra does show a more structured profile than those of the corresponding emission spectra at 0.1 μs delay.

The corresponding time resolved emission spectra for $[Ir(mppy)_2bpy]^+$, Figure 3.4.11, is similar, showing structured profiles towards longer delay time.

E. Luminescence Lifetimes

Room temperature luminescence lifetimes for freeze-pumped-thawed samples of $[Ir(ptpy)_2bpy]^+$ and $[Ir(mppy)_2bpy]^+$ in acetonitrile are 248 ns and 200 ns respectively. Single exponential fit on the luminescence decay curves taken in EtOH-MeOH (4:1 v/v) 77 K glasses give lifetimes of 4.93 and 4.38 μs respectively. Double

exponential fits give 3.5 / 6.0 μs and 3.1 / 6.2 μs lifetimes respectively. See Table 3.4.

F. Quantum Yields

Quantum yields determined by optically dilute methods[62] for $[Ir(ptpy)_2bpy]^+$ and $[Ir(mppy)_2bpy]^+$, are 7.8% and 4.9% respectively, Table 3.4. Appendix C gives a brief description of the calculations.

G. Stern Volmer Quenching

Characterization of the excited state oxidative and reductive potential were determined by Stern-Volmer luminescence lifetime quenching studies; Table 3.5, lists the oxidative and reductive quenchers used in this study and Appendix C gives a brief description of the calculation. The log of the bimolecular rate constant, log k_q for each monomer (calculated from equation 1.4 in Chapter 1) and the correlation coefficient R (for equation 1.4) are also tabulated in Table 3.5. Kinetic estimates of the excited state potential for $[Ir(ptpy)_2bpy]^+$ and $[Ir(mppy)_2bpy]^+$, taken from the breaking region between the diffusion controlled limit and the linear region, Figure 3.4.11, predicts an excited state oxidative potential of .80 eV and .55 eV (vs. NHE) respectively. The excited state reduction potentials are difficult to estimate from the distorted curves in Figure 3.4.11 suggesting a distorted geometry upon ligand reduction of the excited state.

TABLE 3.4

Emission, Lifetimes, and Quantum Yield for

$[Ir(ppy)_2bpy]^+$ [a], $[Ir(ptpy)_2bpy]^+$ and $[Ir(mppy)_2bpy]^+$

Complex	λ_{emis}^{max} (nm) [b]	Lifetimes (τ)	Quantum Yields (Φ)
Room Temperature:			
$[Ir(ppy)_2bpy]^+$	606[c]	337.5 ns[d]	.040[d]
$[Ir(ptpy)_2bpy]^+$	596[e]	248.5 ns[d]	.074[e]
$[Ir(mppy)_2bpy]^+$	594[e]	199.7 ns[d]	.049[e]
Low Temperature (77 K):			
$[Ir(ppy)_2bpy]^+$	532[f]	5.24 μs[f]	
$[Ir(ptpy)_2bpy]^+$	526,548[f]	4.93 μs[f]	
$[Ir(mppy)_2bpy]^+$	528,551[f]	4.38 μs[f]	

(a) From references 27-29.
(b) λexcit for R. T. and 77 K were 380 and 360 nm respectively.
(c) Solvent; neat methanol
(d) Solvent; neat acetonitrile
(e) Solvent ; dichloromethane
(f) in EtOH-MeOH/(4:1 v/v) GLASS

TABLE 3.5

Bimolecular rate constants for oxidative and reductive quenching of $[Ir(ptpy)_2bpy]^+$ and $[Ir(mppy)_2bpy]^+$ (V vs. NHE)

Oxidative and Reductive Quenchers	E°	$[Ir(ptpy)_2bpy]^+$ (log K_q)[a]	$[Ir(mppy)_2bpy]^+$ (log K_q)
pDNB p-dinitrobenzene	-0.69	-9.89(.99)	-9.97(.70)
mDNB m-dinitrobenze	-0.90	-9.80(.99)	-9.72(.99)
NBA m-nitrobenzaldehyde	-1.02	-9.76(.94)	-9.63(.99)
CNB p-chloronitrobenzene	-1.06	-9.59(.99)	-9.40(.99)
NB nitrobenzene	-1.15	-8.95(.98)	-9.36(.93)
MNB p-methylnitrobenzene	-1.20	-8.76(.76)	-8.26(.80)
ANB p-aminonitrobenzene	-1.34	-8.70(.99)	-7.93(.99)
Pt phenothiazine	0.53	9.96(.83)	9.51(.86)
DMA N,N-dimethylaniline	0.81	9.38(.99)	9.30(.99)
DPA diphenylamine	0.83	9.36(.99)	8.63(.97)
AN aniline	0.98	8.89(1.0)	8.93(.99)
TMB 1,2,4-trimethoxybenzene	1.12	8.33(.96)	8.76(.97)
DMB 1,4-Dimethoxybenzene	1.34	8.13(.96)	8.92(.99)
mTMB 1,3,5-trimethoxybenzene	1.49	7.50(.96)	8.37(.99)

a) correlation for linear fit for equation 1.4

FIGURE 3.4.1:

Room temperature Emission-Excitation-Intensity (EEI) stack plots for $[Ir(ptpy)_2bpy]^+$ in dichloromethane, with excitation from 350 to 395 nm at 5 nm increments and emission range of 500 to 700 nm.

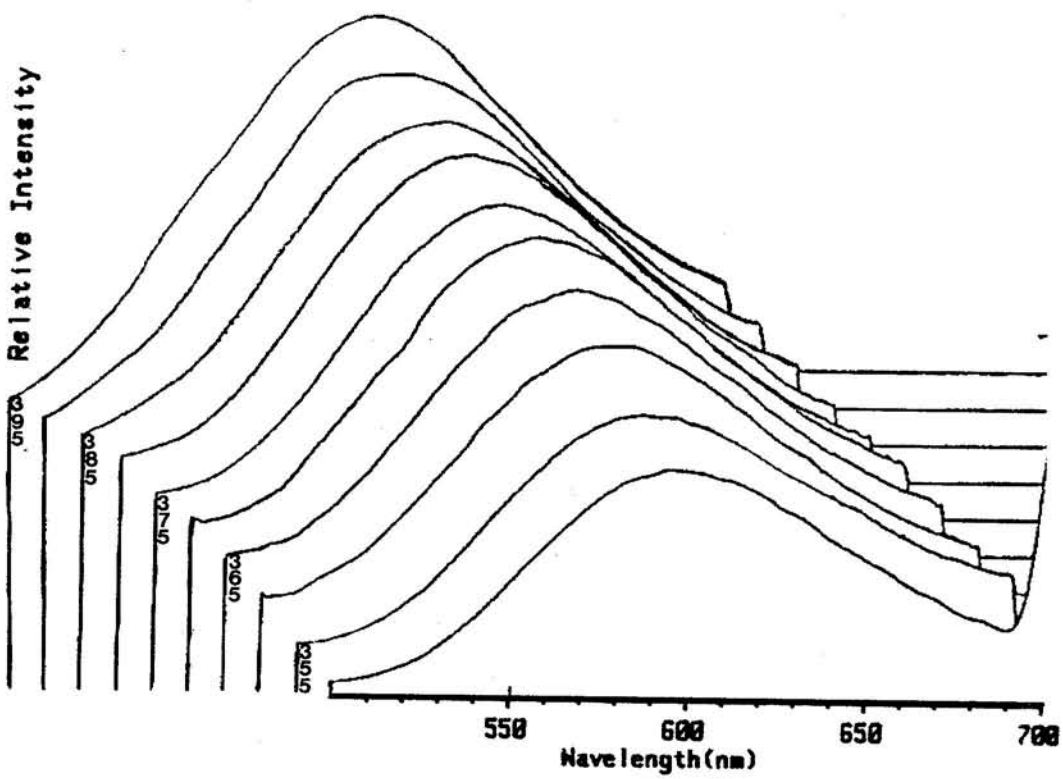

FIGURE 3.4.2:

Room temperature Emission-Excitation-Intensity (EEI) stack plots for $[Ir(mppy)_2bpy]^+$ in dichloromethane, with excitation from 350 to 395 nm at 5 nm increments and emission range of 500 to 700 nm.

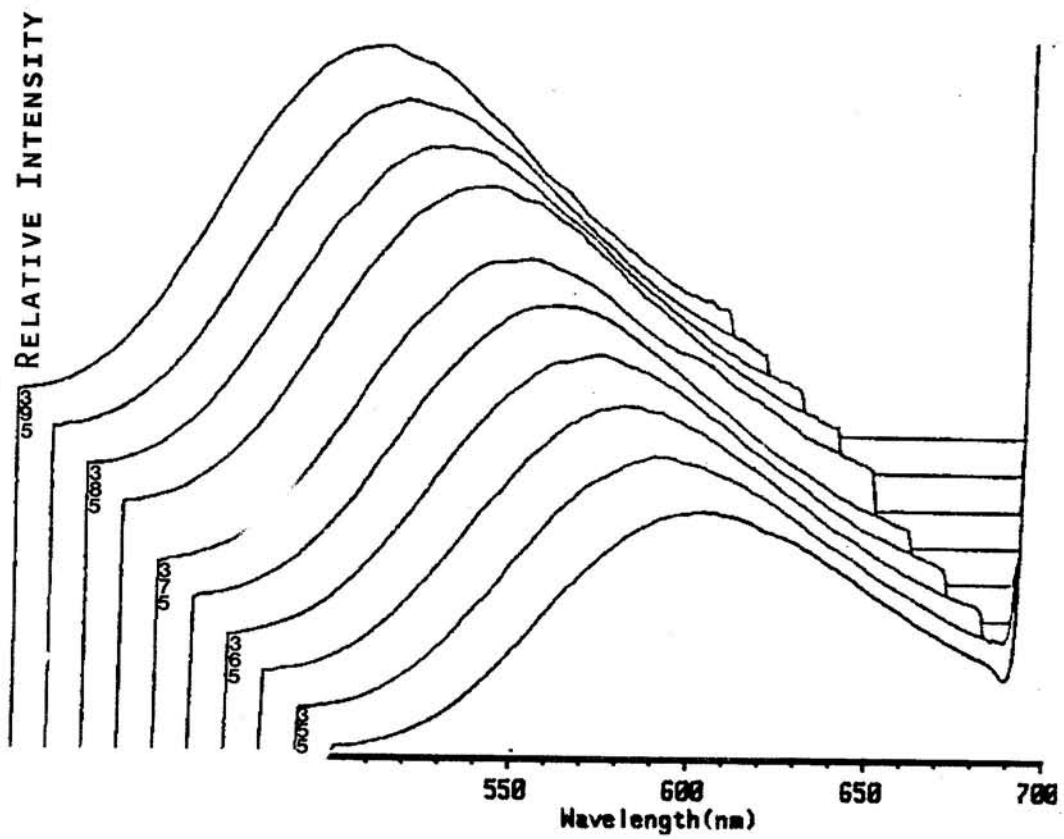

FIGURE 3.4.3:

Low temperature (77 K), Emission-Excitation-Intensity (EEI) stack plots for $[Ir(ptpy)_2bpy]^+$ in EtOH-MeOH (4:1 v/v) with excitation from 200 to 238 nm at 2 nm increments and emission range from 500 to 650 nm.

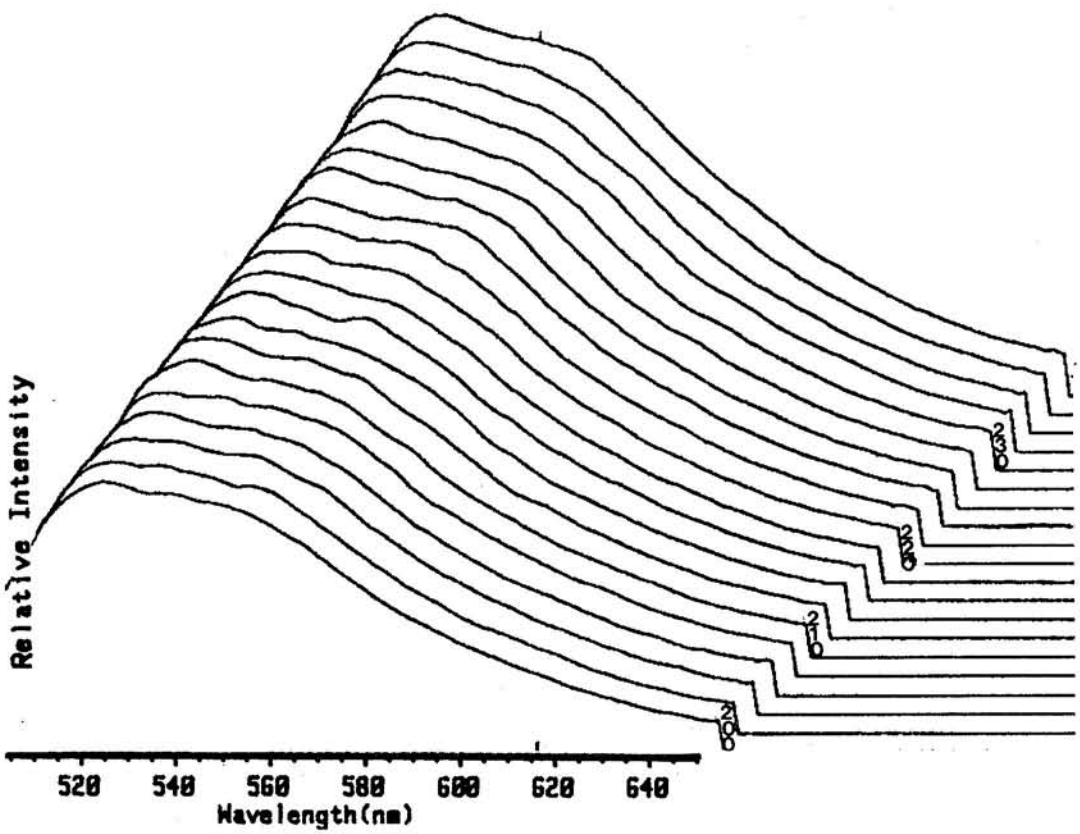

FIGURE 3.4.4:

Low temperature (77 K), Emission-Excitation-Intensity (EEI) stack plots for $[Ir(ptpy)_2bpy]^+$ in EtOH-MeOH (4:1 v/v) with excitation from 360 to 428 nm at 2 nm increments and emission range from 450 to 650 nm.

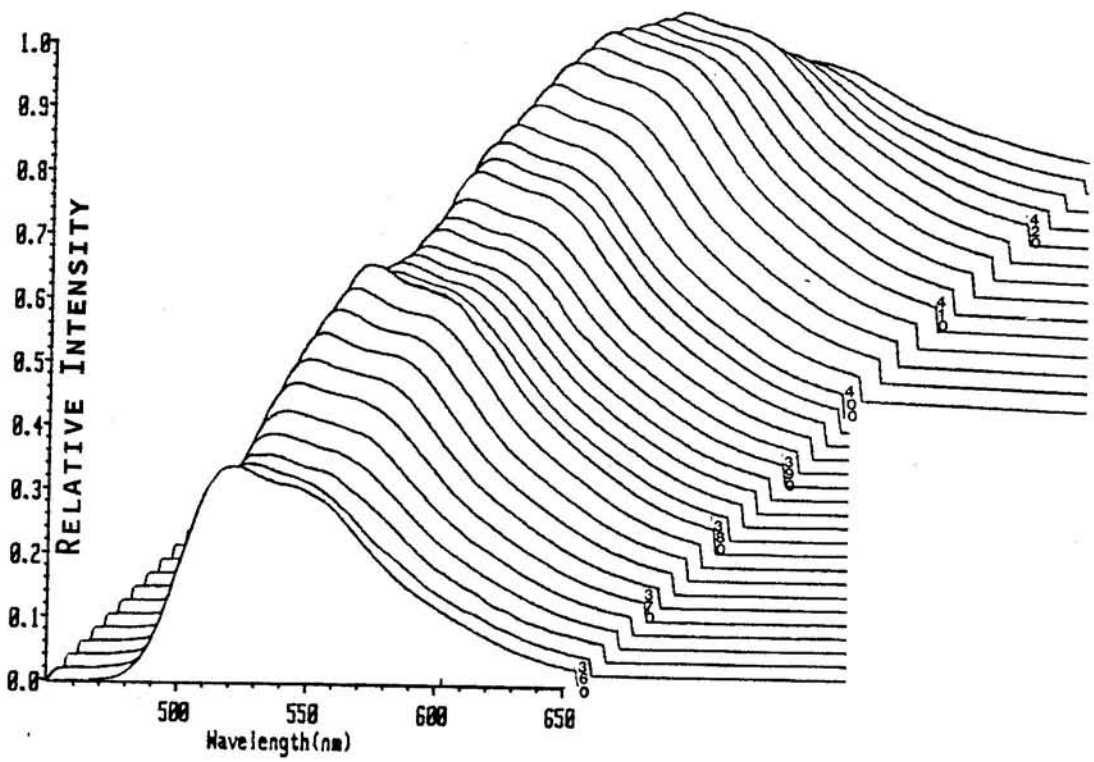

FIGURE 3.4.5:

Low temperature (77 K), Emission-Excitation-Intensity (EEI) stack plots for $[Ir(mppy)_2bpy]^+$ in EtOH-MeOH (4:1 v/v) with excitation from 200 to 238 nm at 2 nm increments and emission range from 450 to 650 nm.

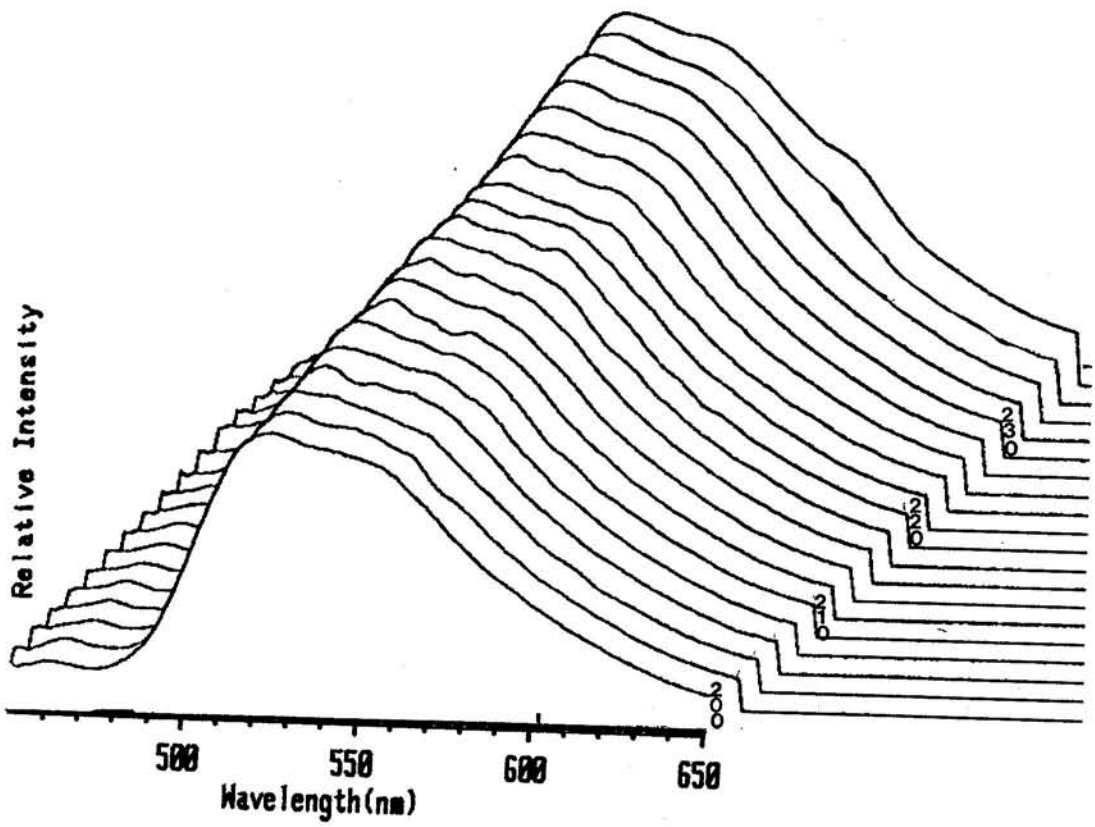

FIGURE 3.4.6:
Low temperature (77 K), Emission-Excitation-Intensity (EEI) stack plots for $[Ir(mppy)_2bpy]^+$ in EtOH-MeOH (4:1 v/v) with excitation from 360 to 438 nm at 2 nm increments and emission range from 450 to 650 nm.

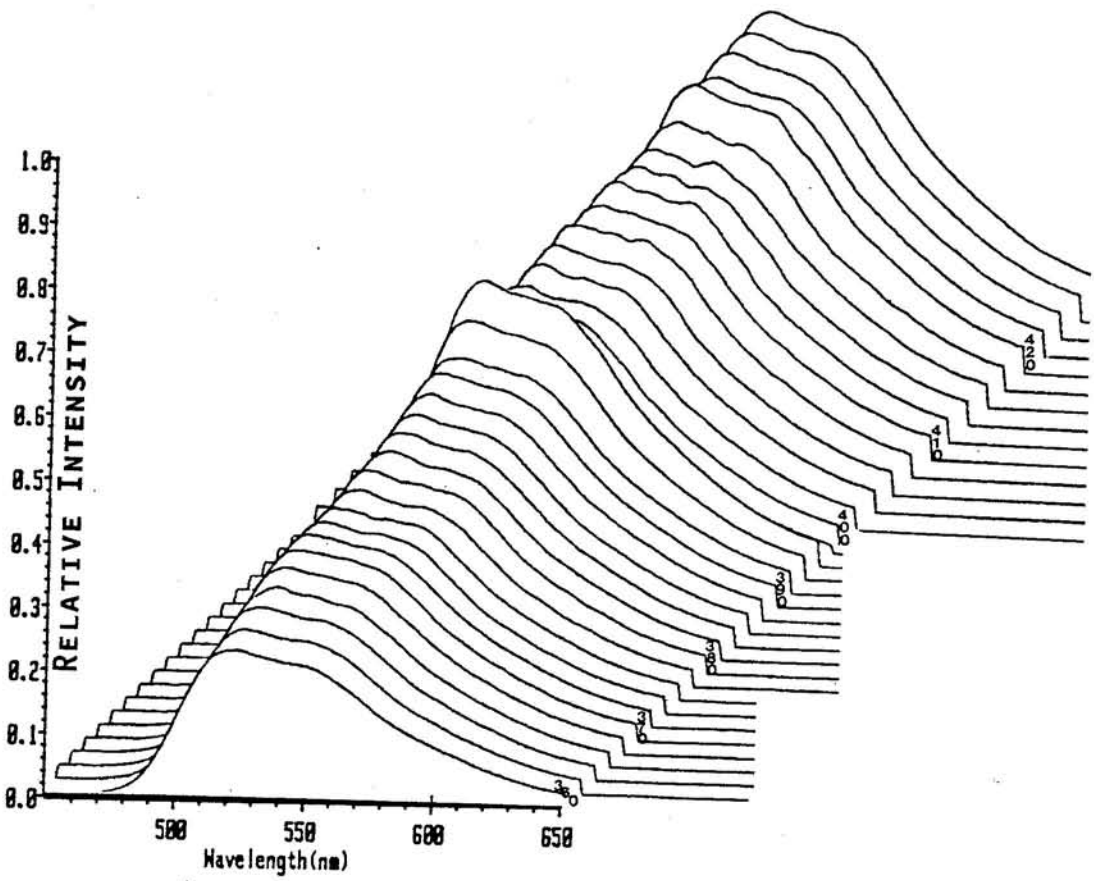

FIGURE 3.4.7:

Low temperature (77 K), emission spectra for $[Ir(ptpy)_2bpy]^+$ in EtOH-MeOH (4:1 v/v) taken with excitation at 200, 210, 220, 230, 240, 280, 320, 400, 440, 480, 485, 490, 495, 500, 505, 510, and 515 nm, with emission range from 450 to 700 nm.

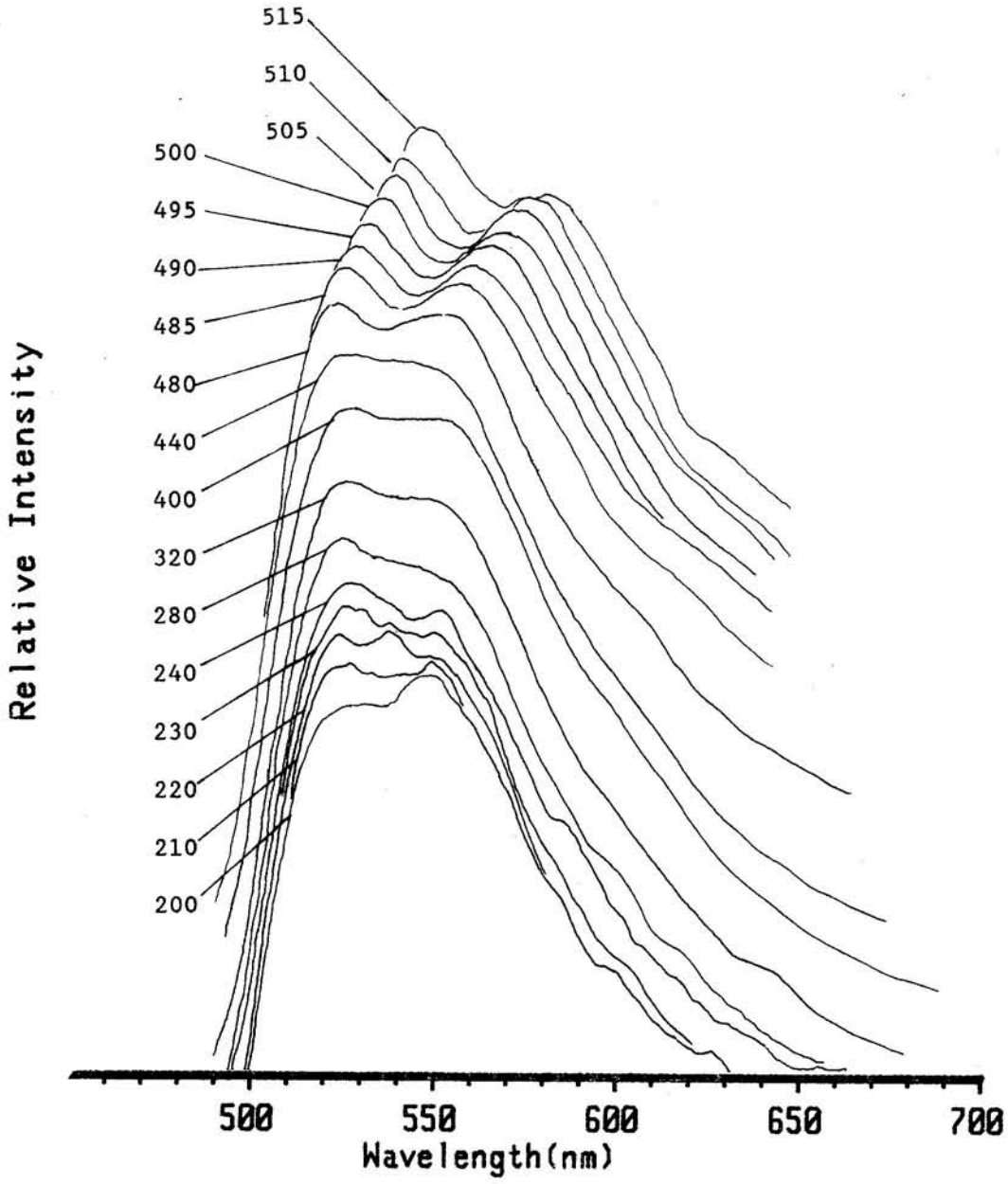

FIGURE 3.3.8:

Low temperature (77 K), emission spectra for $[Ir(mppy)_2bpy]^+$ in EtOH-MeOH (4:1 v/v) taken with excitation at 200, 240, 280, 320, 340, 360, 380, 400, 420, 440, 460, 480, 485, 490, 495, 500, 505, and 510, with emission range from 450 to 700 nm.

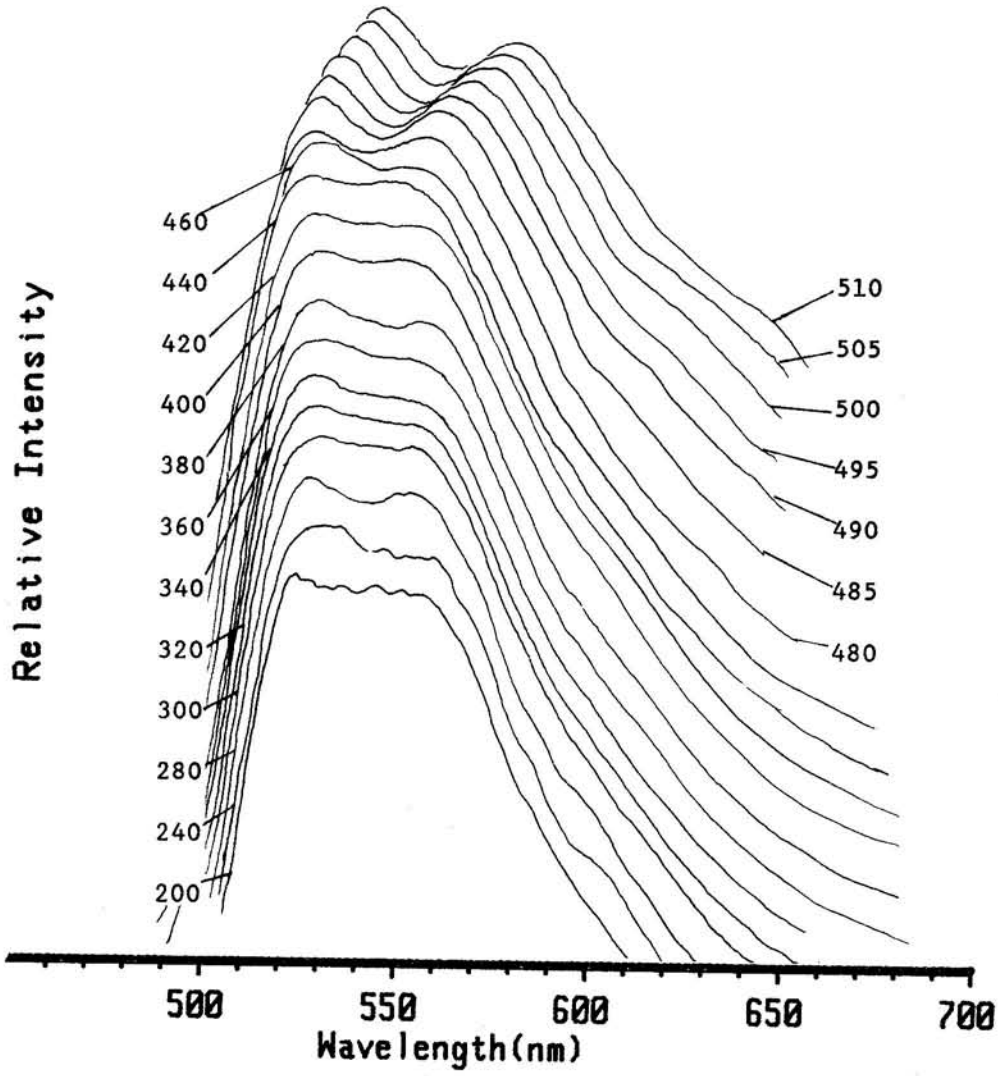

FIGURE 3.4.9:

Time resolved emission spectra for $[Ir(ptpy)_2bpy]^+$ in EtOH-MeOH (4:1 v/v) with time delays of 0.1, 1.0, 2.5, 5.0, 10.0, 20.0 us. 10 ns look, and 10 nm / min scan.

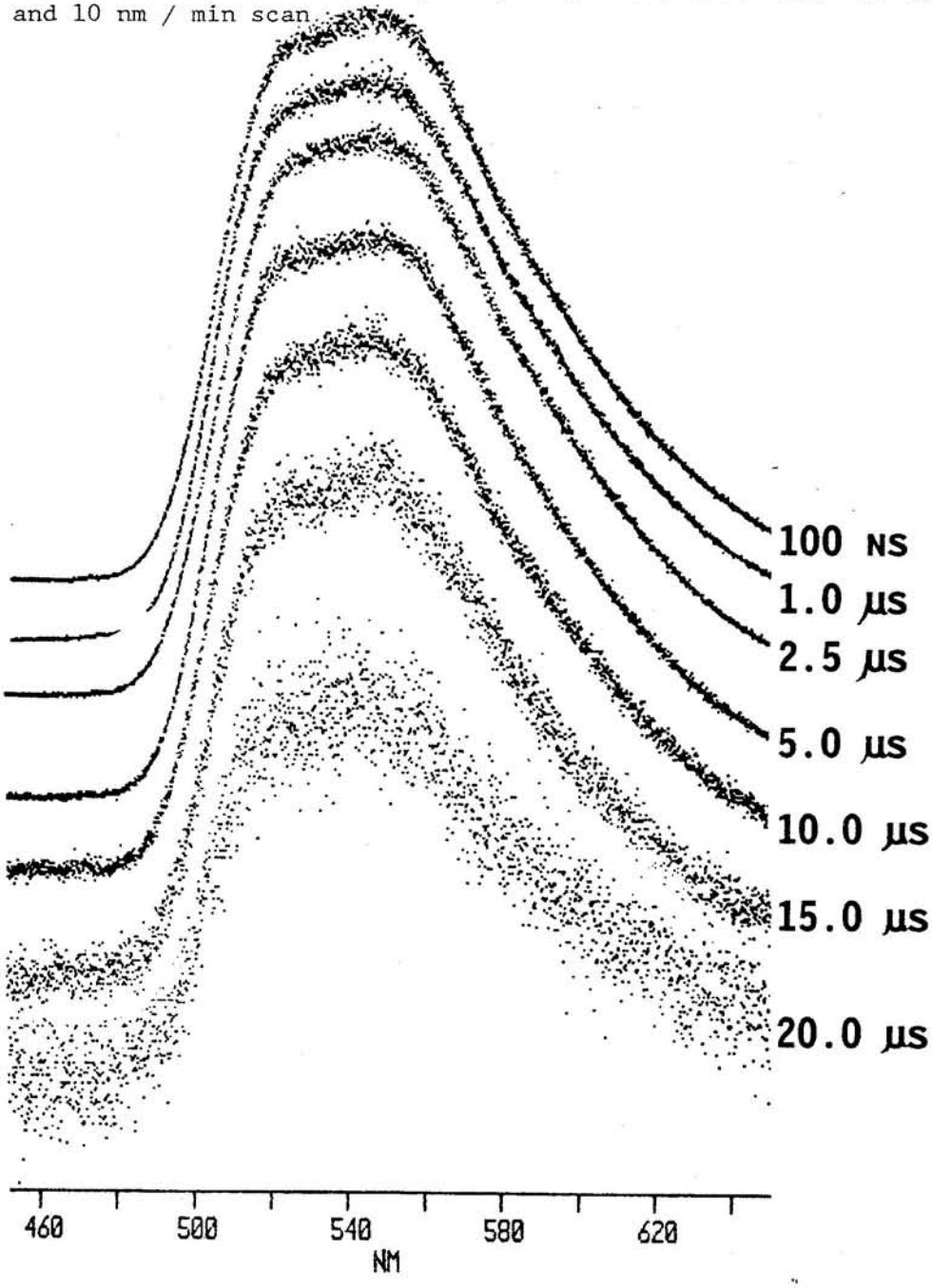

FIGURE 3.4.10:

Time resolved emission spectra for $[Ir(mppy)_2bpy]^+$ in EtOH-MeOH (4:1 v/v) with time delays of 0.1, 1.0, 2.5, 5.0, 10.0, 20.0 us. 10 ns look, and 10 nm / min scan.

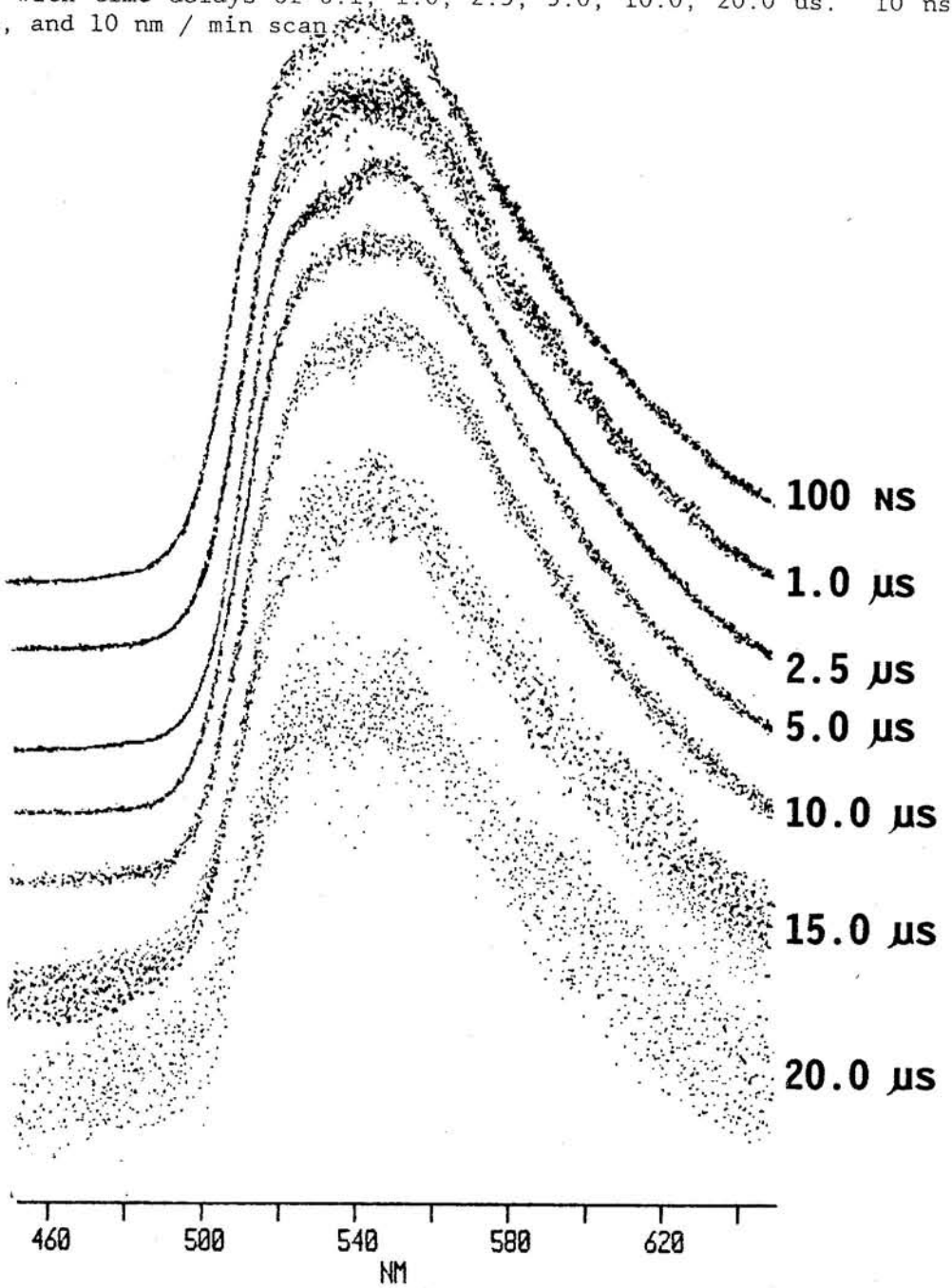

FIGURE 3.4.11:

Outer-sphere electron transfer, Stern-Volmer quenching, Log Kq vs. E^{o} (NHE) for $[Ir(ptpy)_2bpy]^+$ and $[Ir(mppy)_2bpy]^+$ in acetonitrile for a series of oxidative (Ox Q) and reductive (Rd Q) quenchers. [Ox Q: p-dinitrobenzene(pDNB), m-dinitrobenze(mDNB), m-nitrobenzaldehyde (NBA), p-chloro-nitrobenzene(CNB), nitrobenzene(NB), p-methylnitro-benzene (MNB), p-aminonitrobenzene(ANB); Rd Q: pheno-thiazine(Pt), DMA N,N-dimethylaniline, diphenylamine(DPA), aniline(AN), 1,2,4 tri-methoxybenzene(TMB) 1,4 Dimethoxybenzene(DMB),1,3,5trimethoxybenzene (mTMB).]

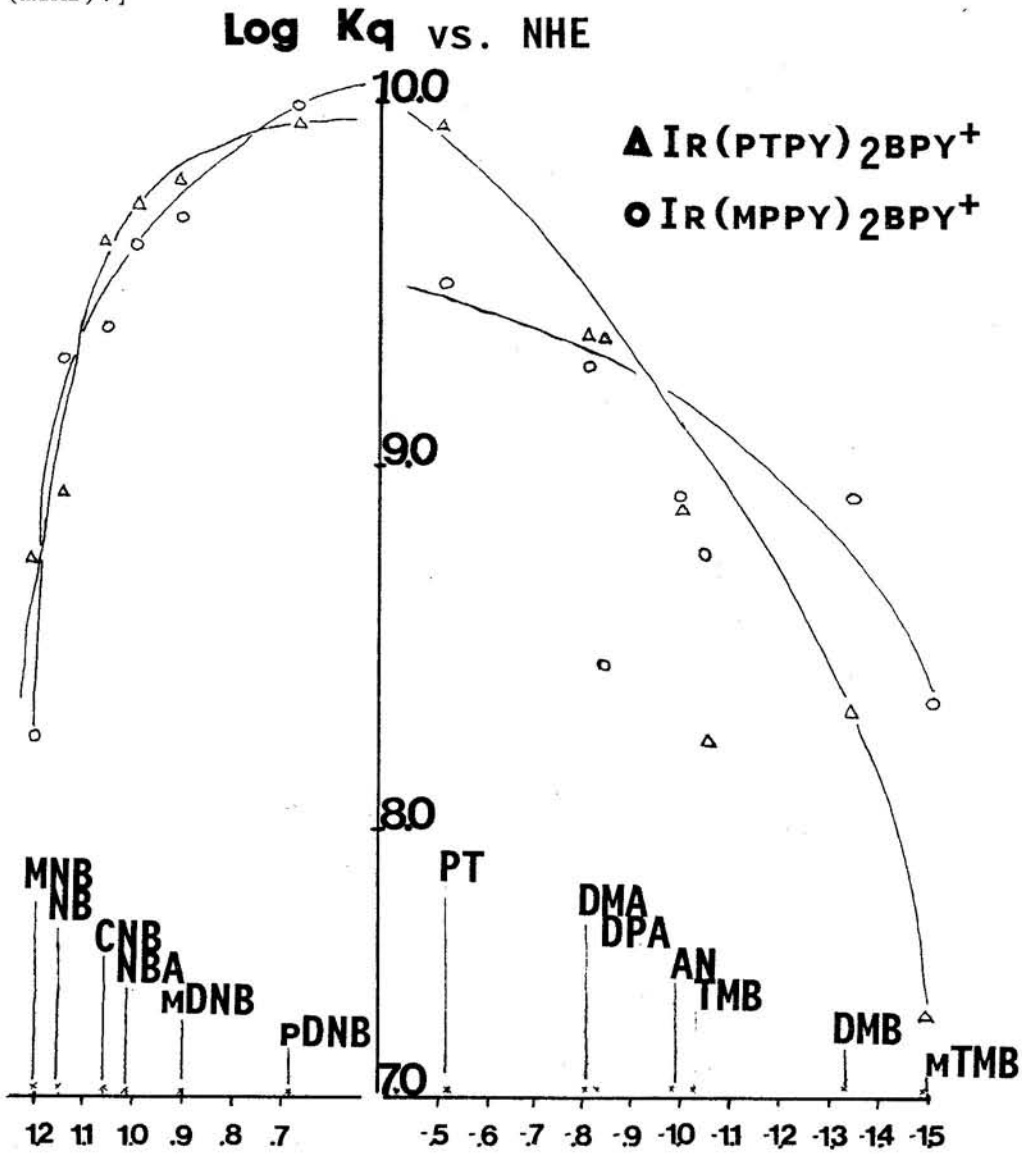

FIGURE 3.4.12:

Representative dual emission potential well from NC and NN charge transfer transition for $[Ir(ptpy)_2bpy]^+$ and $[Ir(mppy)_2bpy]^+$ systems.

From the time-resolved emission data, we've interpreted the excitation data as follow:

1 At higher energy the NC and BY ligands are both populated The resulting emission are the average of both the NC and BY excited states.

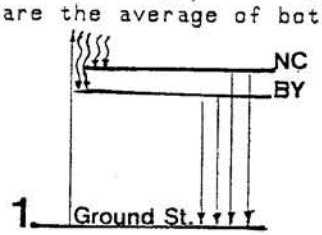

2 At intermediate excitation the population are localized to the NC ligands and thus the band maxima blue shifts.

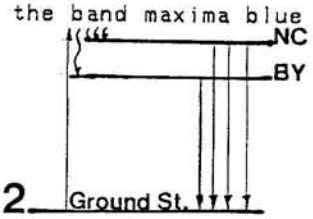

3 At Low energy excitation the BY ligands are populated and the emission band red shifts.

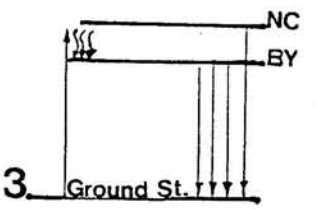

This is summarized by the potential wells shown below.

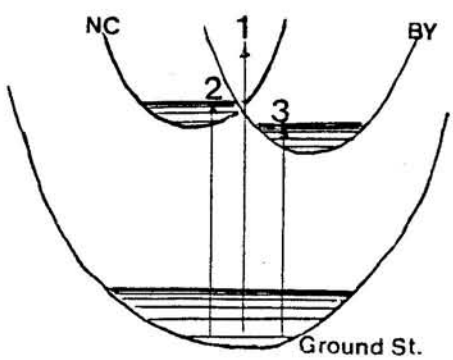

5. Excited State Absorption

Figure 3.5.1a and b, show the excited state absorption spectra for $[Ir(ptpy)_2bpy]^+$, between 340 - 720 and 700 - 1000 nm respectively, in acetonitrile at room temperature. Figure 3.5.2a and b show the corresponding excited state spectra for $[Ir(mppy)_2bpy]^+$. There are three absorption features; the first is in the near UV between, 360 - 400 nm ($\epsilon^* \approx$ 10000-15000), the second is in the visible, 460 - 540 nm ($\epsilon^* \approx$ 2000 - 4000), and the third stretches into the infrared, 660 - 1000+ nm ($\epsilon \approx$ 2000). The extinction coefficients for $[Ir(mppy)_2bpy]^+$ are generally stronger than those of $[Ir(ptpy)_2bpy]^+$, but for both methyl substituted dimers, the absorption features in the infrared region are poorly resolved and extend past the limit of the measurements (1000 nm).

FIGURE 3.5.1:

Excited-state absorption spectra for $[Ir(ptpy)_2bpy]^+$ in acetonitrile at room temperature (a) 340 - 720 nm (b) 700 - 1000nm

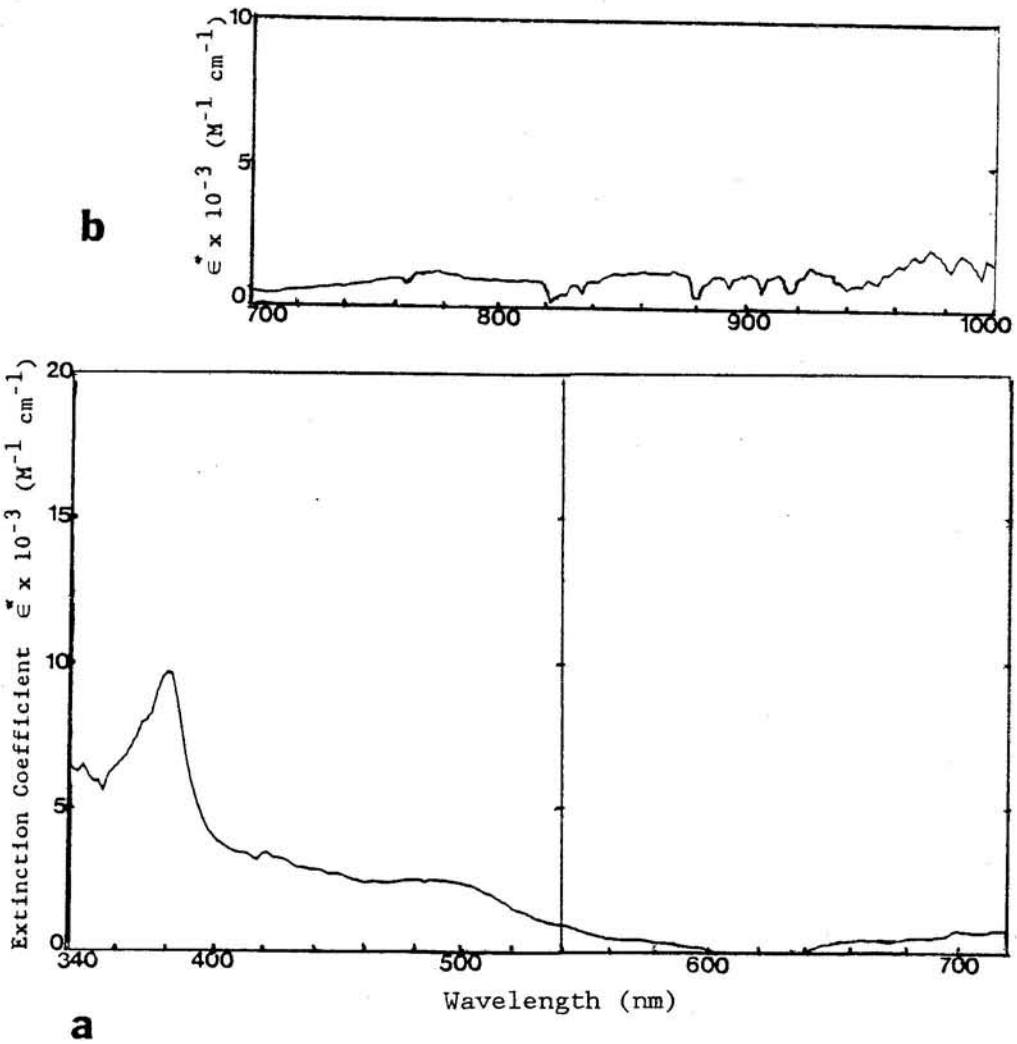

FIGURE 3.5.2:

Excited-state absorption spectra for $[Ir(mppy)_2bpy]^+$ in acetonitrile at room temperature (a) 340 - 720 nm (b) 700 - 1000nm

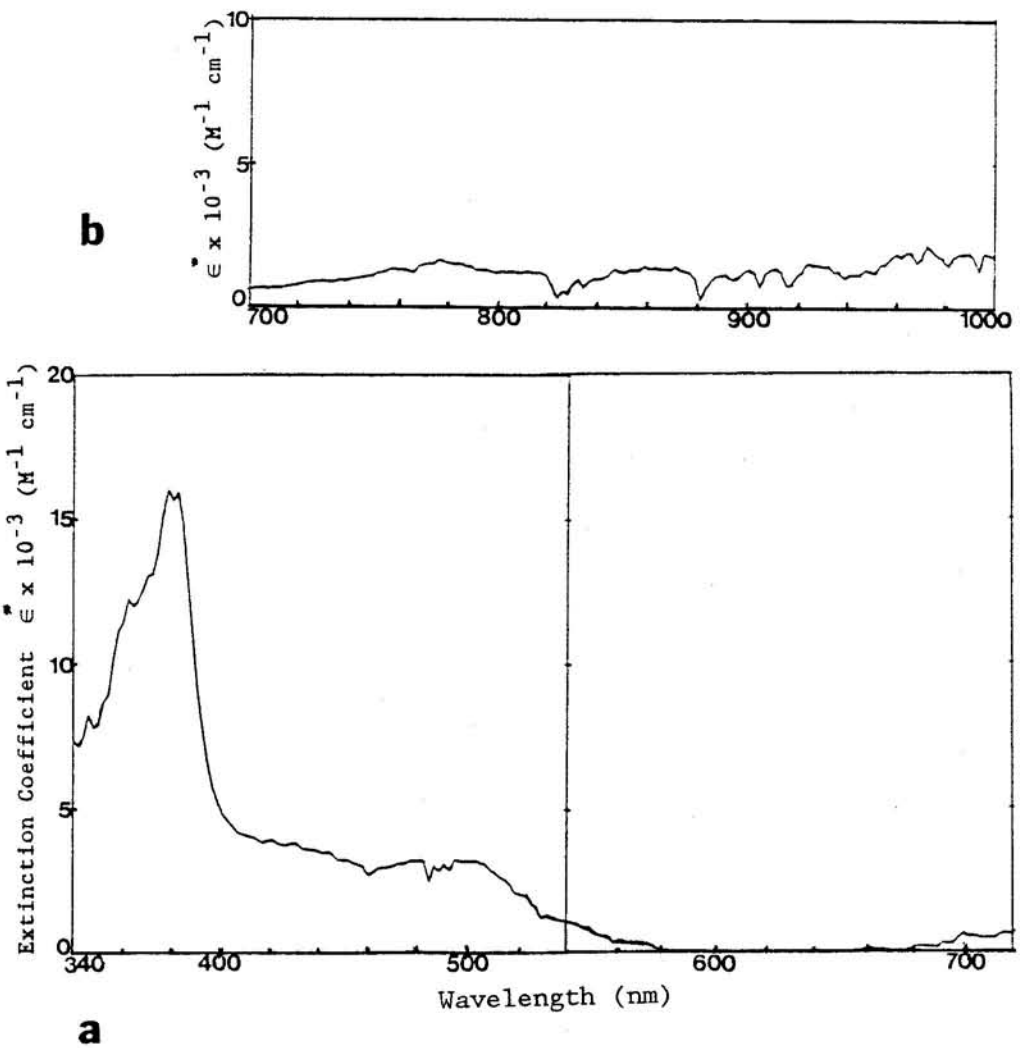

VI. DISCUSSION

1. Structural Considerations via NMR Analysis

The dimers react readily with the chelating 2,2'-bipyridine under mild conditions to form the $[Ir(NC)_2NN]Cl$ monomer with yields in excess of 90%. The mild synthetic conditions probably prevent bonding isomerization of the NC ligands to the iridium center, giving rise to monomeric complexes with the Ir-C bonds cis to each other, Figure 3.2.1.[27-29] In such a structure, the two ortho-metalating ligands in each complex, i.e., ptpy or mppy, are equivalent to each other as are the pyridyl halves in bipyridine[27,30,39,55] as evidenced by the eleven aromatic proton resonances in the ^1H NMR and twenty aromatic carbon resonances in the ^{13}C NMR spectra, Figures 3.1.2 and 3.1.3.

The COSY spectra for $[Ir(ptpy)_2bpy]^+$, Figure 3.1.4, shows three coupled groups consisting of "four", "three" and "four" resonances, indicative of a C_2 point group symmetric monomer containing three unique rings. These rings, labeled "A", "B" and "C", Figure 2.1.1, can be correlated to their appropriate coupled spin system by using the methyl groups on the NC ligands as labels. The $[Ir(ptpy)_2bpy]^+$ COSY spectrum for example, shows a three coupled spin system from the protons on the "A" tolyl NC rings, a four coupled spin system from the protons on the "B" pyridyl NC rings, and a four coupled spin system from the protons on the "C" pyridyl NN rings. In comparison, the methyl groups on the B pyridyl NC rings of $[Ir(mppy)_2bpy]^+$ lead to a three coupled spin system from the protons

on the "B" methylpyridyl NC rings, a four coupled spin system from the protons on the "A" phenyl NC rings and a four coupled spin system from the protons on the "C" pyridyl NN rings. These ring assignments support monomeric structures in which the halves of the two pyridyl rings in bpy form equivalent four-spin sets. Furthermore, if the lowest field resonances, δ = 9.25 for $[Ir(ptpy)_2bpy]^+$ and δ = 9.19 for $[Ir(mppy)_2bpy]^+$, are assigned to one of the "C" pyridyl protons, then the four coupled resonances from the "C" pyridyl NN rings may be distinguished from the other system of four coupled resonances. It follows that the remaining system of four coupled spins are assigned to the pyridyl "B" rings of the ptpy ligands in the $[Ir(ptpy)_2bpy]^+$ ^1H NMR spectrum and to the the phenyl "A" rings of the mppy ligands in the $[Ir(mppy)_2bpy]^+$ ^1H NMR spectrum.

Protons adjacent to the C-Ir and N-Ir bonds (C_6, B_6 and A_3 protons) are susceptible to shielding because of ring current anisotropy[30-40,47] from an adjacent ligand, thereby suggesting high field assignments to these protons. Whereas the A_3 protons are shielded not only by the ring currents but also by the electron rich Ir-C moiety,[32,35,39,40] the B_6 and C_6 protons are deshielded by an adjacent electronegative nitrogen atom which offsets the shielding effect from the ring current. This facilitates assignment of the B_6 and C_6 protons resonances to the middle of the aromatic region at δ = 7.4 and 7.9 respectively, and the A_3 protons resonance upfield at δ = 6.0. The lowest field resonance at 9.25 ppm is assigned to the

C_3 protons (β-position). Similarly, the β-position A_6 and B_3 protons have low field assignments at 7.5 and 7.8 ppm, respectively. Using these initial assignments, it follows from J-correlation analysis that the superposition of signals at 7.4 and 6.8, arising from protons in magnetically equivalent environments, belong to the B_6, C_5 and A_5, B_5 protons respectively.[30-32,35] Finally, the methyl protons are unambiguously assigned to the 3.1 ppm sharp singlet. Proton assignments for the monomers are compiled in Table 3.1 and Appendix A.

The ^1H NMR assignments for $[Ir(mppy)_2bpy]^+$ are also compiled in Table 3.1 and Appendix Table A.6. The $[Ir(mppy)_2bpy]^+$ proton contours from the COSY spectrum, Figure 3.1.5, are assigned using the same strategy used for those in the $[Ir(ptpy)_2bpy]^+$ COSY spectrum, with the A_3, B_6 and C_6 protons again assigned to high field resonances because of ring current anisotropy with the A_3 proton assigned the highest field signal because of the added shielding from the adjacent electron rich Ir-C moiety. The ortho bridgehead C_3 and A_6 protons are assigned to lowest field resonances, with respect to their ring systems, for the reasons stated above. The signal from the B_3 protons is absent in this spectrum.

The ^{13}C NMR and APT spectra for the $[Ir(ptpy)_2bpy]^+$ monomers barely resolved all sixteen aromatic carbon resonances, Figure 3.1.6 and 3.1.8. The complexity of the ^{13}C NMR spectrum arises from the

near degenerate environments of these ligands causing their resonances to overlap as described by Marker[46]. The ^{13}C NMR and APT spectra for $[Ir(mppy)_2bpy]^+$, Figure 3.1.7 and 3.1.9, resolved all eleven protonated and five nonprotonated carbon resonances. The aliphatic resonance at δ = 23.9 is assigned the methyl carbon resonance.

The CSCM spectrum for $[Ir(ptpy)_2bpy]^+$, Figure 3.1.10, shows the ^1H A-spin resonances mapped to carbon resonances at 126.6 (A_3), 125.1 (A_6) and 124.0 ppm (A_5); the ^1H B-spin resonances mapped to carbon resonances at 148.7 (B_6), 138.3 (B_4), 123.0 (B_5) and 118.7 ppm (B_3); and the ^1H C-spin resonances mapped to 150.6 (C_6), 140.0 (C_4), 132.7 (C_3) and 128.4 ppm (C_5). Connectivity for $[Ir(mppy)_2bpy]^+$, Figure 3.1.11, was accomplished in a similar way. The CSCM spectrum for $[Ir(ptpy)_2bpy]^+$ was especially useful in the assignment of the overlapping proton resonances at 7.53 ppm because ^1H-^1H J-connectivity of this resonance in the COSY was vague.

As mentioned in the NMR discussion for the dimer the CSCM spectrum does not show contours for the quaternary carbons because these carbons do not ^JC-H couple to any proton. The quaternary carbons are easily distinguish from their phases in the APT spectrum however. For $[Ir(ptpy)_2bpy]^+$ the quaternary carbons resonate at 168.2, 156.4, 150.8, 141.4, and 141.3 ppm and for $[Ir(mppy)_2bpy]^+$, the quaternary carbons resonate at 166.1, 156.2, 152.3, 145.9 and 133.4 ppm. The lowest field resonances for both complexes are assigned to bridgehead carbons (C_2, B_2 and A_1), with

the C_2 carbon resonances assigned downfield from the B_2 carbon resonances and the B_2 resonances assigned downfield from the A_1 carbon resonances. The shielding effect from the anionic ortho-metalating carbon in the phenyl rings of the ptpy, and mppy ligands causes the bridgehead, A_1, carbons to resonate higher field relative the bridgehead, B_2, carbons; furthermore since the B_2 carbons are part of the metalating NC ligand, their chemical shifts are higher field than that of C_2. These assignments are consistent with those published for similar 2-, 2′- bridgehead carbon resonances.[30-32,35,36,41]

The ortho-metalated carbons for $[Ir(ptpy)_2bpy]^+$ and $[Ir(mppy)_2bpy]^+$ are assigned to 141.4, and 145.9 ppm resonances respectively. Ortho-metalating carbons resonate up field, relative to the bridgehead carbons because of π-back bonding to the iridium due to the strong σ-donor character of the ortho-metalating carbon.[25,35,36,38,39]

The methylated carbon resonates highest field of all quaternary carbons because of the shielding nature of the methyl group. As noted earlier however, the resonance of the methylated carbon, A_4, for $[Ir(ptpy)_2bpy]^+$ is superimposed upon the ortho-metalated carbon resonance, at 141.3 ppm. This is due to a downfield shift of the A_4 resonances (which appears at 139 ppm in the dimer), due to deshielding effects of the bpy ligands in the monomers.

As mentioned in the NMR discussion for the dimers in Chapter 1,

the B_6 carbons resonate lowest field in analogy to their attached protons; this trend is also observed for the monomers. For the carbon resonances at the B_6 and C_6 position, the resonances are located downfield around 150 and 148 ppm. No such correlation could be made for the A_3 carbon resonance however.

Protons at the β position e.g., C_3, B_3, A_6 resonate lowest field for their respective spin (excluding protons in the δ-positions e.g., C_6 and B_6). We note however that the corresponding *carbon* resonances, C_3 and B_3, are among the highest resonating carbons with regard to their respective spin. The only exception being the C_5 carbon resonance of $[Ir(ptpy)_2bpy]^+$. Weak acidity of the protons at this position may explain this trend; the protons are shielded by steric effects and the carbons are shielded by their partial anionic charge.[30-32,43] Because B_3 carbons of $[Ir(mppy)_2bpy]^+$ are methylated, they can not be compared.

In summary the anionic character of these ortho-metalating ligands have a shielding influence on the chemical shifts of these complexes as demonstrated by the chemical shift trends discussed above. The carbon resonances are less sensitive to methylation than are the proton resonances. It was argued before that the methylated spin system resonates higher field than the spin system without the methyl group, but this is true only for the proton chemical shifts and not for the carbon's. The carbon resonances are less sensitive to the inductive effects from methylation.

2. Ground State Redox Potentials from Cyclic Voltammetry.

The electrochemical data for $[Ir(ptpy)_2bpy]^+$ and $[Ir(mppy)_2bpy]^+$ show similar CV patterns, Figure 3.2.1 and 3.2.2, Table 3.2. In general the methyl substituted monomer complexes are better behaved than their dimer counterparts, giving single reversible oxidative and reductive waves. Two conclusions can be drawn from the redox potentials of the monomer complexes. First the lower oxidative potential for $[Ir(ptpy)_2bpy]^+$ ($E_{1/2}$ = 1.18 V) over $[Ir(mppy)_2bpy]^+$ ($E_{1/2}$ = 1.21 V) by 30 mV suggests that the iridium of the ptpy monomer possesses higher charge density, in good agreement with other spectroscopic data. Second, the identical reduction potentials ($E_{1/2}$ = -1.41 V) for these monomers suggests that reduction occurs on the bipyridyl ligand, and is independent of the charge density on the iridium center. These observations suggest localized reduction of the bpy ligands in these monomers.[27-29,56] No additional reductive features were observed up to potentials of -2.5 V (vs. SCE), the limit of the solvent window at dry-ice acetone temperatures.

When the redox potentials are corrected by the internal reference $Fc^{+/0}$, the oxidative potentials indicate that the methyl substituted monomers are easier to oxidize and harder to reduce than the nonsubstituted ppy monomer $[Ir(ppy)_2bpy]^+$ by 90 mV and 30 mV respectively. In the literature, chelated polypyridyl complexes containing functional groups such as carboxylic acids, diethyl

esters, and methyls on bipyridine exhibit only a 30 mV anodic enhancement relative to their nonsubstituted counterparts.[57-61] The greater enhancement of the anodic potentials for the methyl substituted complexes of ortho-metalated complexes studied here, suggest that the methyls influence the electron density on the metal in these ppy complexes to a greater extent than do methyls on chelating ligands such as bipyridine.

3. Absorption assignments.

The absorption profiles for the $[Ir(ptpy)_2bpy]^+$ and $[Ir(mppy)_2bpy]^+$, Figure 3.3.1, emulate that of $[Ir(ppy)_2bpy]^{2+}$.[27-29] Absorption maxima for the monomers are at 467, 414, 381 and 335 nm with π-π^* transitions at 270 and 256 nm. The low energy bands between 480 and 300 nm are assigned MLCT transitions analogous to the dimers. The methyl groups in these substituted complexes have only small effects on the energies of the charge transfer absorption bands as is evident from the band maxima similarities in the absorption profiles. Changes of the low energy band are difficult to monitor because of the low resolution of the absorption features caused by the overlap of several bands, Figure 3.3.1. The small differences in the low energy band maxima can be explained, however, by considering the opposing effects of methyl substituents on the σ-donor and π-acceptor abilities of phenylpyridine. The electron density at the metal is presumed to be enriched by methyl substitution through the σ-bonding framework, while the ligand's π-acceptor ability may be reduced in a corresponding manner. The net result is a very small effect on the spectroscopic metal-to-ligand charge-transfer energies as is observed in the absorption maxima of these complexes (similar to those found for the dimers).

4. Luminescence Properties

A. Emission

The room temperature emission spectra for $[Ir(ptpy)_2bpy]^+$ and $[Ir(mppy)_2bpy]^+$ in DCM, Figure 3.3.1ab, show broad structureless band maxima centered at 596 nm and 594 nm respectively, but modest emission profiles with band maxima at 526/548 and 528/551 nm respectively, in 77 K, MeOH-EtOH-DCM (4:1:1 v/v/v) glasses. The structure in the emission profiles in 77 K glass matrices may be interpreted as the result of a potential barrier between the ppy and bpy MLCT states. At 77 K the luminescence observed is the average of both states as a result of the localized states introduced by Franck-Condon distortion of the excited state[5,27,63] This observation is consistent with the Stern-Volmer quenching results. Outer sphere electron transfer rates (log kq vs. E°) to be discussed later, suggest large distortion of the excited state upon ligand reduction. The distortion causes a potential barrier between the ppy and bpy resulting in localization of the two states, as seen from the structured double emission maxima at 77 K.[5-12,64] At room temperature, the two states are equilibrated and population of the higher ppy states results in intersystem crossing to the lower bpy states as a result of thermally accessible manifolds. The resulting emission originates from the lower bpy state observed as a broad emission profile in the emission spectrum.

From the 77 K emission maxima, the E_{o-o} is estimated to be 2.37 eV (526 nm) for $[Ir(ptpy)_2bpy]^+$ and 2.35 eV (528 nm) for $[Ir(mppy)_2bpy]^+$.

B. Emission-Excitation-Intensity; evidence for dual emission

The EEI stack plots at room temperature for the monomers, Figure 3.4.1 and 3.4.2, shows no additional emission features at different excitation wavelengths. However the corresponding EEI plots at 77 K, Figures 3.4.3,4 and 3.4.5,6 for $[Ir(ptpy)_2bpy]^+$ and $[Ir(mppy)_2bpy]^+$ respectively, show changes in the emission maxima through the excitation progression. These changes are accentuated in the stack plots in Figure 3.4.7 and 3.4.8 and suggest dual emission for these monomers as illustrated in the cartoon in Figure 3.4.12.[27-29,63] At high energy excitation ({1}, 200 - 360 nm), both the NC and NN ligands are populated and the emission is an average of the two MLCT states. Towards intermediate energy excitation ({2} 400 - 480 nm), the population is localized on the NC ligand causing a blue shift of the emission maxima. Finally at low energy excitation ({3} 480 -520 nm), the low lying bpy excited state becomes selectively populated causing the band maximum to red shift.

C. Dual emission; evidence from time-resolved-emission

Time-resolved emission of the monomers, Figure 3.4.9 and 3.4.10, at 77 K are also supportive of dual emission behavior.[63] Time-resolved emission and excitation studies by A.P.Wilde[65] on $[Ir(ppy)_2bpy]^+$ suggest that the short lived and high energy emitting

state originates from localized charge transfer associated with ppy, while the long lived, low energy emitting state originates from the bpy localized charge transfer (determined from time-resolved emission data). The results here are supportive of Wilde's finding, indicating that at short delays, 100 ns, the emission profile is characteristic of overlapping emissions from the ppy and bpy charge transfer states with the band maximum centered at 540 nm. After 5 μs delay, the profile begins to develop structure, with band maxima centered around 520 and 530 nm. Finally at delays longer than 15 μs, the emission profiles show structure characteristic of the bpy charge transfer state, albeit the poor resolution of the spectrum makes these band maxima difficult to monitor.

The emission lifetimes of 4 μs for the monomer support MLCT assignments of these bands. A double exponential fit on the decay curve at 77 K showed lifetimes of 3 and 6 μs for both monomers. The luminescence quantum yield of about 5% for these monomers is consistent with the nonsubstituted $[Ir(ppy)_2bpy]^+$ monomer.[27-29]

D. Stern-Volmer quenching and kinetic estimates of the excited state redox potential

The kinetics of excited state oxidation and reduction reactions of these monomers were characterized by Stern-Volmer quenching studies.[28,29,66,67] The results, Table 3.5, and Figure 3.4.11, show the quenching of the emission of $[Ir(ptpy)_2bpy]^+$ (Δ) and $[Ir(mppy)_2bpy]^+$ (O) by a series of oxidative and reductive

quenchers.[29,68,69] Kinetic estimates of the excited state oxidation potentials taken from the breaking region between the diffusion controlled limit and the linear region, indicate an E°(*+/0) value of 0.80 and 0.55 eV vs. NHE, for $[Ir(ptpy)_2bpy]^+$ and $[Ir(mppy)_2bpy]^+$ respectively. This is in good agreement with the cyclic voltammetric and the E_{o-o} measurements which predicted an E°(*+/0) of 0.76 and 0.54 eV vs. NHE, respectively. The narrow breaking region, at least for $[Ir(ptpy)_2bpy]^+$, suggests little or small reorganizational barriers toward oxidative electron transfer. On the other hand it is difficult to estimate the excited state reduction potentials for these monomers from the distorted curves in Figure 3.4.11. This distortion represents a large distortion of the excited state resulting from reorganizational barriers.[5-11]

As mentioned above, we suggest that the reduction of a ligand causes a distortion of the geometry of the NC and NN ligands thus introducing a potential barrier and localizing the states. The results here support this contention suggesting localized NN and NC MLCT states. Furthermore, these results support some recent solvent studies on $[Ir(ppy)_2bpy]^+$ indicating a highly distorted excited state arising from large dipole changes during the charge transfer transition.[65]

5. Excited state absorption properties

Excited state absorption measurements may be used to assign low lying charge transfer transitions. The positions of the excited state absorption maxima in the near ultraviolet for $Ir(bpy)_3^{3+}$ and $[Ir(bpy\text{-}C^3,N')(bpy\text{-}N,N')_2]^{2+}$ have been associated with the presence of an Ir^{IV} center in the excited state[70,71]. More recently, the excited state absorption spectra of $Ir(ppy)_2bpy^+$ and $Ir(bzq)_2bpy^+$ have been reported.[54] The observation of four excited state absorption band maxima has led to formulation of the excited states as $Ir^{IV}(ppy)_2(bpy^-)$ and $Ir^{IV}(bzq)_2(bpy^-)$ species. The results from the excited state absorption spectra for $Ir(ptpy)_2bpy^+$ and $Ir(mppy)_2bpy^+$ are consistent with these results. The first three absorption features centered at 380, 500, and 780 nm are consistent with the presence of a bpy radical anion, bpy^-. The poorly resolved near IR band stretching from 820 to 1000+ nm is a feature that was first reported for $Ir^{IV}(ppy)_2(bpy^-)$ and $Ir^{IV}(bzq)_2(bpy^-)$ and is also observed for these monomers. This feature has been assigned to a π^*-π^* transition on bpy or interligand π^* bpy to π^* ppy transition.

For the methyl substituted monomers it has been shown by cyclic voltammetry that oxidation of Ir^{III} to Ir^{IV} and the reduction of bpy to bpy^- occurs at less positive potential (more cathodic) than for the unsubstituted monomers. It is expected that the excited state absorption maxima for these monomers would occur at lower energy. The resolution in these spectra makes it difficult to estimate changes in the absorption maxima. The results, however, are

consistent with the lowest lying charge transfer to bpy ligand rather than to ppy.54,70-72

In summary, the appearance of four absorption features in the excited state absorption spectra for $[Ir(ptpy)_2bpy]^+$ and $[Ir(mppy)_2bpy]^+$ and the 380 nm absorption maximum give evidence consistent with the previous study of $Ir^{IV}(ppy)_2(bpy^-)$ and $Ir^{IV}(bzq)_2(bpy^-)$ suggestive of $Ir^{IV}(NC)_2(NN^-)$ excited state species. Furthermore, the highest absorption feature band centered at 380 nm for these monomers compared to 385 nm for $Ir^{IV}(ppy)_2(bpy^-)$ and $Ir^{IV}(bzq)_2(bpy^-)$ suggest that Ir^{III} to Ir^{IV} oxidation for $Ir(ptpy)_2bpy^+$ and $Ir(mppy)_2bpy^+$ is more difficult than that of the nonsubstituted $[Ir(ppy)_2bpy]^+$ monomer. This is inconsistent with the CV results which show that the ground state oxidation fro these methyl substituted iridium monomers occurs at more cathodic potential. This inconsistency may be attributed to the small differences in the low energy band maxima, from the opposing effects of methyl substituents on the σ-donor and π-acceptor abilities of pyridyl moiety in the ligands as was mentioned for the ground state absorption spectra.

CHAPTER 4

CRYSTALLOGRAPHIC STUDIES OF METHYL-SUBSTITUTED PHENYLPYRIDINE ORTHO-METALATED IRIDIUM (III) COMPLEXES *

In science, like love matters,
one must dare in time and go all the way.

-Giacomo Ciamician (1857 - 1922)

In the crystal structure of $[Rh(ppy)_2Cl]_2$,[48] it was shown that the Rh-N bonds are in the axial position trans to each other, and the Rh-C bonds are in the equatorial position cis to each other and trans from the bridging chlorides. It was noted in the analysis that since the scattering factor for the nitrogen atom is similar to the carbon atom there is some ambiguity in assigning the Rh-C and Rh-N bonds in the rhodium dimer, but that the best refinement was achieved for the structural configuration described above.

If the phenylpyridine ligands contain a functional group to identify the pyridyl ring from the phenyl ring then the M-C and M-N bonds can be unambiguously assigned. Ligands such as 2-(p-tolyl)pyridine and 3-methyl-2-phenylpyridine have such functional groups which serves to unambiguously identify the phenyl ring from the pyridyl ring in the dimeric and monomeric ortho-metalated complexes described in Chapters 2 and 3.

In Chapter 2, the structures of $[Ir(ptpy)_2Cl]_2$ and $[Ir(mppy)_2Cl]_2$ were discussed in terms of NMR results; the structural configurations were based primarily on chemical shifts of the A_3 and B_6 protons. The conclusion from those results reiterates the structural configuration set forth by the $[Rh(ppy)_2Cl]_2$ crystal structure.

This chapter will describe the preparation and crystallographic analysis of $[Ir(ptpy)_2Cl]_2$, $[Ir(mppy)_2Cl]_2$ and $[Ir(mppy)_2bpy]^+$. The structure of $[Ir(ptpy)_2Cl]_2$ was refined to an R-factor of 6%. The refinement for $[Ir(mppy)_2Cl]_2$ was not so successful with an R-factor of 12%. The symmetric arrangement of the Ir and Cl atoms is broken in this case by the position of the ligands, making refinement difficult. Finally, the solution of $[Ir(mppy)_2bpy]^+$ was unsuccessful mainly because movement of the crystal in the capillary as the diffractometer rotated through chi resulted in a poor data set.

*I'd like to dedicate this Chpater to Nancy Keder. Thanks Nancy.

I. EXPERIMENTAL

A. Preparation of Complexes

Reaction of ortho-metalating ligands (NC) (e.g., ppy) with the chloride salts of Ir(III) and Rh(III) affords an ortho-metalated dichloro-bridged dimeric complex, $[M(NC)_2Cl]_2$, where M = Ir or Rh, and NC = ppy, ptpy or mppy, Figure 2.1.1. The preparation of these dimers are described in Chapter 2 and are discussed in details in references [16,25-29]. Addition of 2,2'-bipyridine to these dimers results in the mixed ligand monomeric complex, $[M(NC)_2bpy]^+$. [27-29]

X-ray quality crystals of the $[Ir(ptpy)_2Cl]_2$, $[Ir(mppy)_2Cl]_2$ and $[Ir(mppy)_2bpy]^+$ were obtained by dissolving 50 mg of the dimer or monomer in 50 ml dichloromethane in a 100 ml beaker. To this solution, 10 ml of toluene was pipetted down the inside wall of the beaker taking care that no mixing occurred between the toluene and dichloromethane solution. To this, 5 ml hexanes was added in the same manner. The beaker containing the three separate layers of dichloromethane, toluene and hexanes was covered by a 250 ml beaker and stored in the dark for several weeks at which time X-ray quality crystals were obtained. The solution containing $[Ir(ptpy)_2Cl]_2$ was evaporated to dryness because the crystals were stable and didn't loose solvent. The final product was in two forms; a bright yellow amorphous powder and dark tan golden pyramidal crystals. The $[Ir(mppy)_2Cl]_2$ and $[Ir(mppy)_2bpy]^+$ crystals were sensitive to solvent loss; after a few minutes outside the mother liquor, the

golden triangular plate-like $[Ir(mppy)_2Cl]_2$ crystals, and tannish square plate-like $[Ir(mppy)_2bpy]^+$ crystals became amorphous. For this reason the $[Ir(mppy)_2Cl]_2$ and $[Ir(mppy)_2bpy]^+$ crystals were stored in solvent in capillaries throughout the data collection.

This crystal growth technique (solvent diffusion/evaporation) may be modified by using 5 mm or 10 mm NMR tubes instead of beakers, especially if a small amount of material is to be recrystallized.

B. X-ray Data Collection

A crystal of $[Ir(ptpy)_2Cl]_2$ was epoxied on to a glass fiber which had previously been glued on to a brass pin. Single crystals of $[Ir(mppy)_2Cl]_2$ and $[Ir(mppy)_2bpy]^+$ contained in their mother liquor were mounted inside 0.5 mm O.D. glass capillaries, sealed with epoxy and fastened to a pin. A Blake Industries four-circle Huber diffractometer[73] interfaced to a DEC micro-VAX computer with stepping motor controllers from Crystal Logic was used to obtain the diffraction data. Three standard reflections were measured after every 97 reflections to monitor crystal decay. Cell constants and other crystallographic data are summarized in Table 4.1.

1. Solution and refinement of the structure of $[Ir(ptpy)_2Cl]_2$.

Systematic absences h00, h=2n+1; 0k0, k=2n+1; 00ℓ, ℓ=2n+1; hk0, k=2n+1; h0ℓ, k=2n+1, ℓ=2n+1; 0kℓ, k=2n+1, ℓ=2n+1; hkℓ, h+k+ℓ=2n+1 are supportive of the space group $I4_1cd$. The unit cell volume of 9281 $Å^3$ contains eight molecules which lie on 2-fold axes, Figure 4.1.1.

The Ir and Cl atoms of $[Ir(ptpy)_2Cl]_2$ were located by direct methods (**MULTAN80**)[74]. The z coordinate of the Ir atom was fixed to define the origin of the unit cell and the two half Cl's atoms are located on the 2-fold axis at x = 1/2, y = 0. Carbon and nitrogen atoms were located by successive cycles of least-squares refinement and difference Fourier synthesis. Hydrogen atom positions were calculated (C-H = 0.95 Å), and included as fixed contributors with thermal parameters of 3.0 $Å^2$.

A difference map revealed a toluene solvate disordered about the 2-fold axis at x = y = 1/2. It was refined as a rigid-group with idealized geometry (C-C = 1.395 Å) and individual isotropic thermal parameters.

In the final refinement, the x and y coordinates of the Ir; the z coordinates of the Cl's; and the x, y, z coordinates for all carbon and nitrogen atoms of the ligands were refined. Isotropic thermal parameters were refined for all non-H atoms; the thermal parameters of the methyl carbons were refined anisotropically. The final cycle afforded the convergence of R to 5.9% and R_w to 7.0% with the error of fit at 1.88.

Bond distances, bond angles and atomic positions, for $[Ir(ptpy)_2Cl]_2$ are summarized in Table 4.2-4.4. Anisotropic and isotropic parameters for non-hydrogen atoms are summarized in Table 4.5. Figure 4.1.2 shows the labeling scheme for the ΛΛ enantiomer, and selected views for both the ΛΛ and ΔΔ isomers of $[Ir(ptpy)_2Cl]_2$

are shown in Figures 4.1.3-4.1.6. A space filling diagram for the ΔΔ isomer is shown in Figure 4.1.7.

2. Solution and refinement of the structure of $[Ir(mppy)_2Cl]_2$

The space group Aba2 for the $[Ir(mppy)_2Cl]_2$ structure was based on systematic absences of h00, h=2n+1; 0k0, k=2n+1; 00$\underline{l}$, $\underline{l}$=2n+1; hk0, k=2n+1; h0$\underline{l}$, k=2n+1, $\underline{l}$=2n+1; 0k$\underline{l}$, k=2n+1, $\underline{l}$=2n+1; and hk$\underline{l}$, k+$\underline{l}$=2n+1. There are four molecules which lie on the 2-fold symmetry axes with a unit cell volume of 5489.1 $Å^3$, Figure 4.2.1.

The Ir and Cl atoms of $[Ir(ptpy)_2Cl]_2$ were located by direct methods (MULTAN80)[74]. The z coordinate of the Ir atom was fixed to define the origin of the unit cell and the two half Cl's atoms are located on the 2-fold axis at x = 0, y = 0. Carbon and nitrogen atoms were located by successive cycles of least-squares refinement and difference Fourier synthesis.

Attempts to refine the positions of the ligand's atoms resulted in physically unreasonable bond distances and angles. Therefore the mppy ligands were input as rigid groups (phenyl and pyridyl rings as idealized hexagons, C-C = C-N = 1.395; 12° angle between the two rings). The overall orientation of the ligands was refined. Mppy was treated as a TLS[75] group; the six translational and three diagonal librational elements were refined.

The ORTEP diagram of $[Ir(mppy)_2Cl]_2$, Figure 4.2.3, indicates that the C(109), C(110), C(111), C(209), C(210) and C(211) possess excessively large thermal parameters. These are the same atoms that

gave anomalous bond distances and angles when refined individually. Furthermore, the difference map showed a large amount of residual electron density near these atoms. The Ir and Cl atoms dominate the scattering and their positions conform to the space group Aba2. But overall, the anomalously high thermal parameters for several atoms in this structure suggest that the real space group is probably lower symmetry than that of Aba2.[76] The difficulty refining the phenyl portion of the mppy ligand implies that it is these few atoms which break the Aba2 symmetry. Refinement in lower symmetry space groups such as Pba2 or Pcn2 should be attempted in order to ascertain the true symmetry.

In the final refinement, only the Ir atom was refined anisotropically; the chloride atoms were refined isotropically. The final R-factor of 11.8% and R_w of 18.8%, with an error of fit at 6.105, gave the most chemically reasonable atomic positions. The poor R-factor did not warrant calculation of the hydrogen atom positions.

Atomic positions, bond distances, and bond angles for $[Ir(mppy)_2Cl]_2$ are summarized in Table 4.6-4.8. Anisotropic and isotropic parameters are summarized in Table 4.9. Figure 4.2.2 shows the labeling scheme for the ΔΔ enantiomer, and Figures 4.2.3-4.2.6 shows selected views of the ΔΔ and ΛΛ isomers of $[Ir(mppy)_2Cl]_2$.

3. Solution and refinement of the structure of $[Ir(mppy)_2bpy]^{\pm}$.

Based on the space group and the unit cell size, there are probably two unique molecules per unit cell. Two Ir atoms, located by a combination of Patterson and Direct Methods, reduced the R-factor to 30%. However, the remaining atoms in the structure could not be located.

Three stereoisomers are possible for $[Ir(NC)_2bpy]^+$; a pair of enantiomers, A and B, having C_2 symmetry point group, and C, which has no symmetry elements.[29,32,35,40,41] Isomer C can be disregarded since it contains six unique rings conflicting the NMR results. NMR analysis, however, can not distinguish between isomers A and B since each has C_2 symmetry and each contains three unique rings. It was argued, however, that the mild synthetic conditions,[27-29] in the preparation of the monomers from the dimers, probably prevent bond isomerization favoring structural configuration A over B (based on the structure of the dimers).

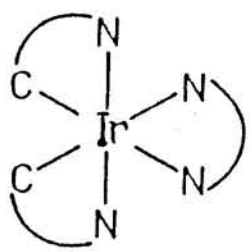

A

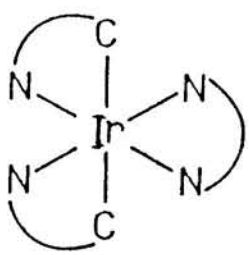

B

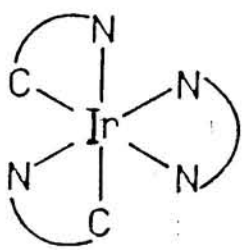

C

TABLE 4.2

Selected bond lengths (Å) for $[Ir(ptpy)_2Cl]_2$.

From	To	Distance
IR(1)	C(1)	1.97
IR(1)	C(21)	2.05
IR(1)	N(2)	2.06
IR(1)	N(1)	2.07
IR(1)	CL(2)	2.51
IR(1)	CL(1)	2.53
N(1)	C(7)	1.33(4)
N(1)	C(11)	1.36(4)
C(1)	C(6)	1.41(4)
C(1)	C(2)	1.45(5)
C(2)	C(3)	1.54(5)
C(3)	C(4)	1.33(4)
C(3)	C(103)	1.52(5)
C(4)	C(5)	1.40(5)
C(5)	C(6)	1.33(4)
C(6)	C(7)	1.39(4)
C(7)	C(8)	1.45(4)
C(8)	C(9)	1.38(5)
C(9)	C(10)	1.37(4)
C(10)	C(11)	1.37(4)
N(2)	C(31)	1.37(4)
N(2)	C(27)	1.37(4)
N(2)	C(28)	2.43(4)
C(21)	C(22)	1.40(4)
C(21)	C(26)	1.45(4)
C(22)	C(23)	1.43(4)
C(23)	C(203)	1.49(5)
C(23)	C(24)	1.54(5)
C(24)	C(25)	1.29(5)
C(25)	C(26)	1.38(4)
C(26)	C(27)	1.44(4)
C(27)	C(28)	1.45(4)
C(28)	C(29)	1.30(4)
C(29)	C(30)	1.33(5)
C(30)	C(31)	1.45(4)

TABLE 4.3
Selected bond angles (°) for $[Ir(ptpy)_2Cl]_2$.

From	Thru	To	Angle
C(1)	IR(1)	C(21)	95.
C(1)	IR(1)	N(2)	97.
C(1)	IR(1)	N(1)	80.
C(1)	IR(1)	CL(2)	92.
C(1)	IR(1)	CL(1)	171.
C(21)	IR(1)	N(2)	80.
C(21)	IR(1)	N(1)	92.
C(21)	IR(1)	CL(2)	172.
C(21)	IR(1)	CL(1)	90.
N(2)	IR(1)	N(1)	171.
N(2)	IR(1)	CL(2)	96.
N(2)	IR(1)	CL(1)	91.
N(1)	IR(1)	CL(2)	93.
N(1)	IR(1)	CL(1)	92.
CL(2)	IR(1)	CL(1)	84.
IR(1)	CL(1)	IR(1)	96.
IR(1)	CL(2)	IR(1)	97.
C(7)	N(1)	IR(1)	112.
C(7)	N(1)	C(11)	121.(2)
C(6)	C(1)	C(2)	122.(3)
C(6)	C(1)	IR(1)	116.
C(1)	C(2)	C(3)	113.(4)
C(4)	C(3)	C(103)	129.(4)
C(4)	C(3)	C(2)	120.(4)
C(103)	C(3)	C(2)	111.(3)
C(3)	C(4)	C(5)	123.(4)
C(6)	C(5)	C(4)	121.(3)
C(5)	C(6)	C(7)	127.(3)
C(5)	C(6)	C(1)	120.(3)
N(1)	C(7)	C(6)	119.(3)
N(1)	C(7)	C(8)	121.(3)
C(6)	C(7)	C(8)	119.(3)
C(9)	C(8)	N(1)	87.(2)
C(11)	C(10)	C(9)	118.(3)
N(1)	C(11)	C(10)	121.(3)
C(31)	N(2)	C(27)	125.(2)
C(31)	N(2)	IR(1)	120.
C(31)	N(2)	C(26)	157.(2)
C(27)	N(2)	IR(1)	115.
IR(1)	N(2)	C(30)	157.
C(22)	C(21)	C(26)	117.(3)
C(22)	C(21)	IR(1)	127.
C(26)	C(21)	C(23)	88.(2)
C(21)	C(22)	C(23)	122.(3)
C(22)	C(23)	C(24)	113.(3)
C(203)	C(23)	C(24)	123.(3)
C(25)	C(24)	C(23)	126.(4)
C(24)	C(25)	C(26)	117.(4)
C(25)	C(26)	C(27)	124.(3)
C(25)	C(26)	C(21)	124.(3)
C(27)	C(26)	C(21)	112.(3)
N(2)	C(27)	C(26)	118.(3)
N(2)	C(27)	C(28)	119.(3)
C(26)	C(27)	C(28)	123.(3)
C(29)	C(28)	N(2)	91.(3)
C(28)	C(29)	C(30)	117.(4)
C(29)	C(30)	C(31)	130.(4)
N(2)	C(31)	C(30)	109.(3)
C(22)	C(203)	C(24)	57.(1)

TABLE 4.4

Positional parameters for (A.) atoms of $[Ir(ptpy)_2Cl]_2$. and (B.) group parameters for the solvated toluene.

A.	Atom	X	Y	Z
	IR(1)	0.5078( )	0.1113(1)	0.2030
	N(1)	0.6315(10)	0.1110(13)	0.2036(10)
	C(1)	0.5300(20)	0.1896(20)	0.1600(11)
	C(2)	0.4664(20)	0.2312(20)	0.1391(11)
	C(3)	0.4966(20)	0.2813(21)	0.1030(10)
	C(4)	0.5731(27)	0.2794(22)	0.0929(12)
	C(5)	0.6309(20)	0.2403(20)	0.1162(11)
	C(6)	0.6110(16)	0.1977(17)	0.1487(9)
	C(7)	0.6616(17)	0.1524(17)	0.1729(8)
	C(8)	0.7471(23)	0.1583(23)	0.1670(12)
	C(9)	0.7922(18)	0.1170(22)	0.1949(11)
	C(10)	0.7610(22)	0.0740(22)	0.2264(11)
	C(11)	0.6799(19)	0.0735(20)	0.2307(10)
	C(103)	0.4274(31)	0.3231(40)	0.0820(13)
	N(2)	0.3865(11)	0.1296(15)	0.2066(10)
	C(21)	0.5030(15)	0.1935(18)	0.2491(9)
	C(22)	0.5674(17)	0.2276(18)	0.2699(9)
	C(23)	0.5561(20)	0.2805(19)	0.3033(10)
	C(24)	0.4680(27)	0.3010(24)	0.3109(12)
	C(25)	0.4076(19)	0.2710(21)	0.2922(11)
	C(26)	0.4236(20)	0.2198(20)	0.2603(10)
	C(27)	0.3625(18)	0.1822(19)	0.2361(10)
	C(28)	0.2787(23)	0.2027(21)	0.2389(11)
	C(29)	0.2269(22)	0.1666(23)	0.2163(12)
	C(30)	0.2550(19)	0.1136(22)	0.1898(9)
	C(31)	0.3365(19)	0.0905(21)	0.1806(10)
	C(203)	0.6233(23)	0.3214(24)	0.3241(12)
	CL(1)	0.5000	0.0000	0.2544(6)
	CL(2)	0.5000	0.0000	0.1525(6)
	H(2)	0.4064	0.2284	0.1470
	H(4)	0.5914	0.3197	0.0723
	H(5)	0.6851	0.2494	0.1064
	H(8)	0.7769	0.1771	0.1431
	H(9)	0.8521	0.1146	0.1926
	H(10)	0.8041	0.0428	0.2434
	H(11)	0.6579	0.0452	0.2566
	H(22)	0.6210	0.2067	0.2632
	H(24)	0.4591	0.3455	0.3329
	H(25)	0.3555	0.2847	0.2996
	H(28)	0.2661	0.2359	0.2603
	H(29)	0.1674	0.1798	0.2185
	H(30)	0.2098	0.0827	0.1720
	H(31)	0.3523	0.0525	0.1595
	H(13A)	0.4417	0.3504	0.0575
	H(13B)	0.3992	0.3625	0.1016
	H(13C)	0.3794	0.2828	0.0745
	H(23A)	0.6775	0.2907	0.3269
	H(23B)	0.6053	0.3420	0.3511
	H(23C)	0.6367	0.3740	0.3072
B.				
	C(T1)	0.5000	0.5000	0.2397
	C(T2)	0.5228	0.4317	0.2186
	C(T3)	0.5228	0.4317	0.1764
	C(T4)	0.5000	0.5000	0.1552

TABLE 4.5

Temperature factors for the non-hydrogen atoms of $[Ir(ptpy)_2Cl]_2$.
A. Anisotropic Temperature Factors.
B. Isotropic Temperature Factors.

A.

Atom	$U_{11}10^3$	$U_{22}10^3$	$U_{33}10^3$	$U_{12}10^3$	$U_{13}10^3$	$U_{23}10^3$
C(103)	153(42)	345(82)	80(38)	88(51)	-6(32)	110(47)
C(203)	102(28)	111(29)	104(28)	-7(23)	18(23)	12(23)

The complete temperature factor is:

$$\text{Exp}[-\pi^2(a^2U_{11}h^2 + b^2U_{22}k^2 + c^2U_{33}l^2 + 2abU_{12}hk + 2acU_{13}hl + 2bcU_{23}kl)].$$

B.

Atom	$U*10^3$	Atom	$U*10^3$	Atom	$U*10^3$
IR(1)	60( )	C(21)	64(8)	H(10)	63
CL(1)	71(2)	C(22)	74(8)	H(11)	63
N(1)	66(5)	C(23)	78(9)	H(22)	63
C(1)	70(8)	C(24)	95(12)	H(24)	63
C(2)	86(10)	C(25)	89(10)	H(25)	63
C(3)	79(9)	C(26)	89(10)	H(28)	63
C(4)	110(12)	C(27)	83(9)	H(29)	63
C(5)	93(10)	C(28)	105(11)	H(30)	63
C(6)	67(7)	C(29)	112(12)	H(31)	63
C(7)	66(8)	C(30)	91(11)	H(13A)	63
C(8)	107(13)	C(31)	84(10)	H(13B)	63
C(9)	99(11)	CL(2)	71	H(13C)	63
C(10)	94(10)	H(2)	63	H(23A)	63
C(11)	85(10)	H(4)	63	H(23B)	63
N(2)	85(7)	H(5)	63	H(23C)	63
		H(8)	63		
		H(9)	63		

The complete temperature factor is:

$$\text{Exp}\left[\frac{-U8\pi^2\sin^2\theta}{\lambda^2}\right] \quad \text{or}$$

$$\text{Exp}\left[\frac{-B\sin^2\theta}{\lambda^2}\right], \quad \text{where } B = U8\pi^2.$$

TABLE 4.6

Positional parameters for (A.) atoms of $[Ir(mppy)_2Cl]_2$. and (B.) group parameters for mppy ligand rigid group.

A.

Atom	X	Y	Z
Ir(01)	-0.0851(1)	0.0823(1)	0.0000
CL(01)	0.0000	0.0000	0.0763(1)
CL(02)	0.0000	0.0000	-0.0771(1)

B.

C(106)	-0.0183	0.2395	0.0494
N(10)	-0.0084	0.1796	0.0036
C(102)	0.0577	0.1854	-0.0381
C(103)	0.1139	0.2511	-0.0340
C(104)	0.1041	0.3111	0.0118
C(105)	0.0380	0.3053	0.0535
C(113)	0.0281	0.3652	0.0993
C(107)	-0.0885	0.2188	0.0843
C(108)	-0.1128	0.2688	0.1336
C(109)	-0.1831	0.2481	0.1685
C(110)	-0.2278	0.1805	0.1553
C(111)	-0.1922	0.1253	0.0949
C(112)	-0.1220	0.1460	0.0600
C(206)	-0.2418	0.0124	-0.0479
N(20)	-0.1797	0.0031	-0.0032
C(202)	-0.1829	-0.0632	0.0380
C(203)	-0.2483	-0.1200	0.0346
C(204)	-0.3104	-0.1107	-0.0101
C(205)	-0.3072	-0.0445	-0.0513
C(213)	-0.3693	-0.0352	-0.0960
C(207)	-0.2233	0.0830	-0.0825
C(208)	-0.2759	0.1068	-0.1307
C(209)	-0.2574	0.1773	-0.1653
C(210)	-0.1897	0.2227	-0.1529
C(211)	-0.1313	0.1877	-0.0938
C(212)	-0.1498	0.1172	-0.0592

TABLE 4.7

Selected bond lengths (Å) for $[Ir(mppy)_2Cl]_2$.

From	To	Distance
Ir(01)	Cl(01)	2.520
Ir(01)	Cl(02)	2.532

TABLE 4.8

Selected bond angles (°) for $[Ir(mppy)_2Cl]_2$.

From	Thru	To	Angle
Cl(01)	Ir(01)	Cl(02)	82.21
Ir(01)	Cl(01)	Ir(01)	98.08
Ir(01)	Cl(02)	Ir(01)	97.49

TABLE 4.9

Temperature factors for Ir and Cl atoms of $[Ir(mppy)_2Cl]_2$.
A. Anisotropic Temperature Factors.
B. Isotropic Temperature Factors.

A.

Atom	$U_{11}10^4$	$U_{22}10^4$	$U_{33}10^4$	$U_{12}10^4$	$U_{13}10^4$
Ir(01)	433(7)	390(7)	493(7)	-9(5)	-12(16)

The complete temperature factor is:

$$\text{Exp}[-\pi^2(a^2U_{11}h^2 + b^2U_{22}k^2 + c^2U_{33}l^2 + 2abU_{12}hk + 2acU_{13}hl + 2bcU_{23}kl)].$$

B.

Atom	$U*10^4$
Cl(01)	565(57)
Cl(02)	442(47)

The complete temperature factor is:

$$\text{Exp}\left[\frac{-U8\pi^2\sin^2\theta}{\lambda^2}\right] \quad \text{or}$$

$$\text{Exp}\left[\frac{-B\sin^2\theta}{\lambda^2}\right], \quad \text{where } B = U8\pi^2.$$

FIGURE 4.1.1:

Packing diagram for the unit cell of $[Ir(ptpy)_2Cl]_2$ down the (a) C-axis, (b) A-axis, and (c) B-axis.

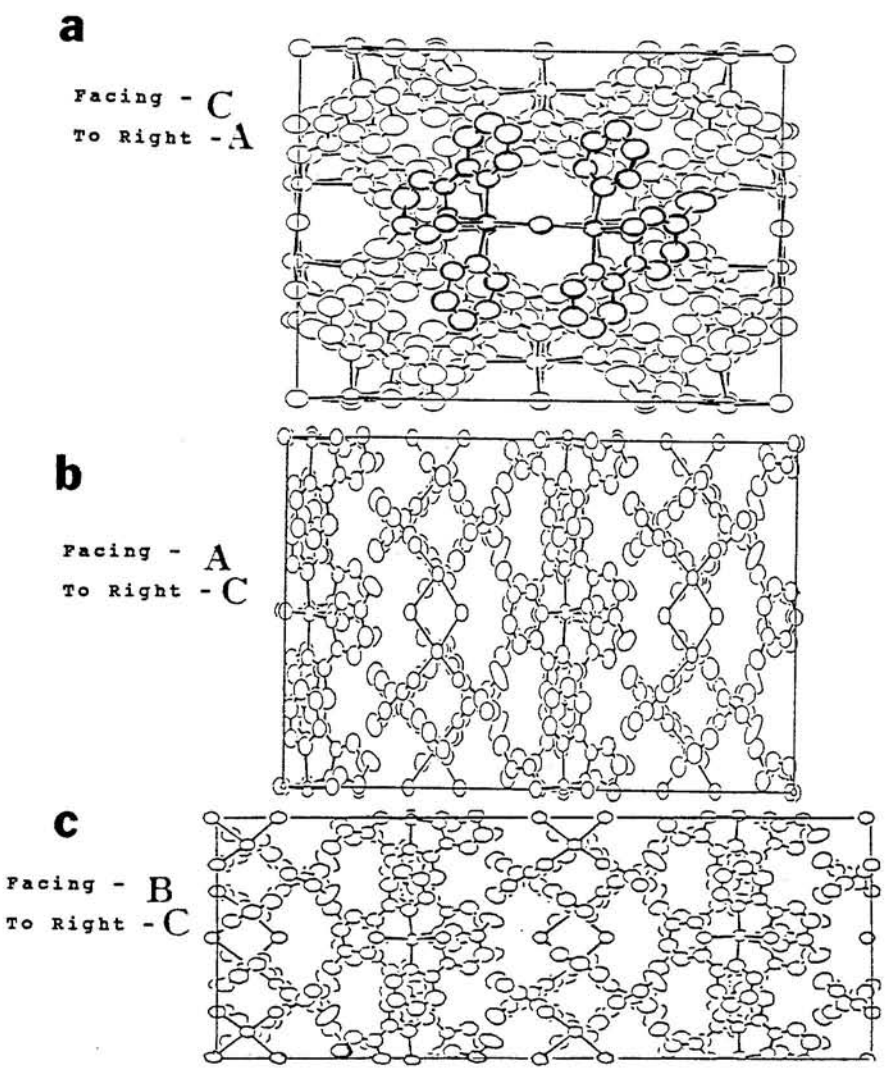

FIGURE 4.1.2:
Labeling Scheme for ΛΛ enantiomers of $[Ir(ptpy)_2Cl]_2$ at rotation, (X, Y, Z = 45, 0 , 0).

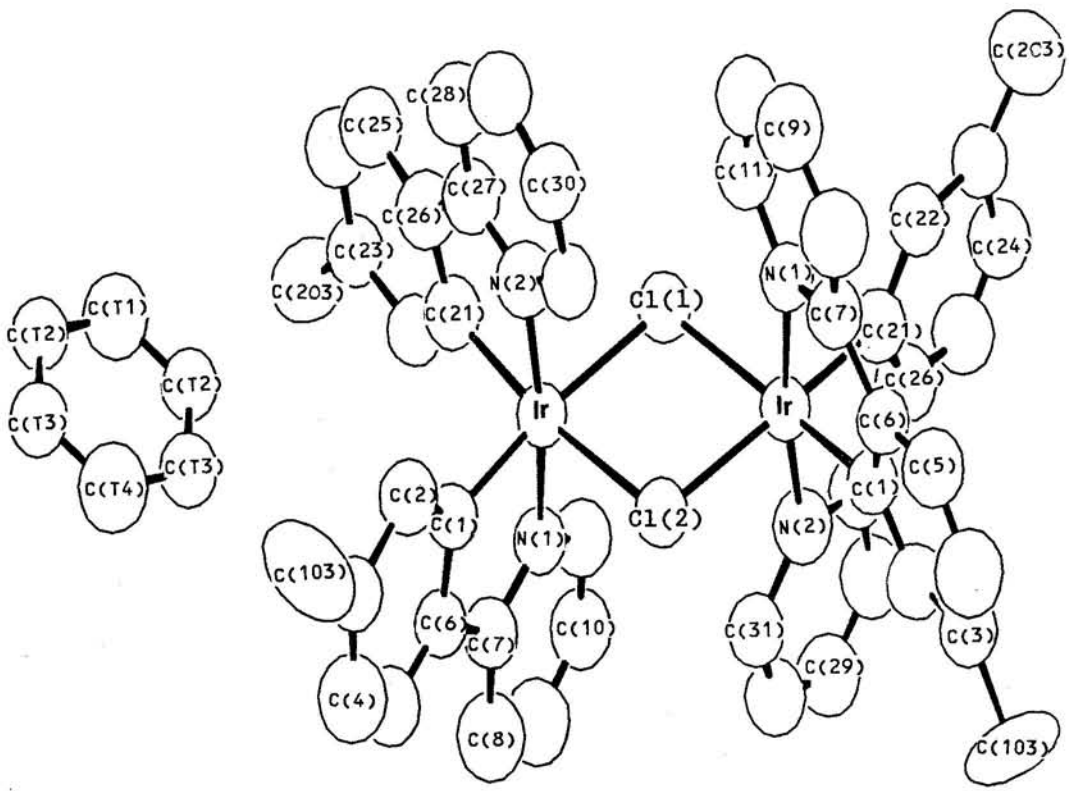

FIGURE 4.1.3:

ORTEP diagram for ΛΛ enantiomers of $[Ir(ptpy)_2Cl]_2$ at rotation, (X, Y, Z = 45, 0 , 0).

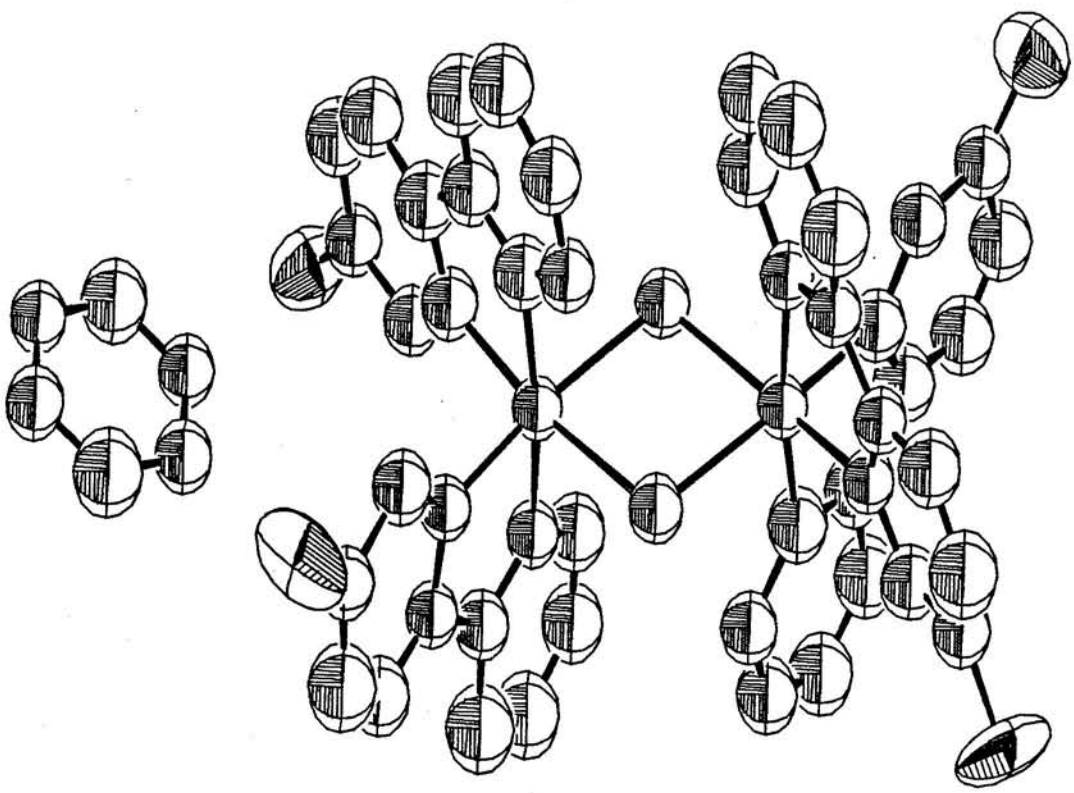

FIGURE 4.1.4:

ORTEP diagram for ΔΔ enantiomer of $[Ir(ptpy)_2Cl]_2$ at rotation, (X, Y, Z = 45, 0, 0).

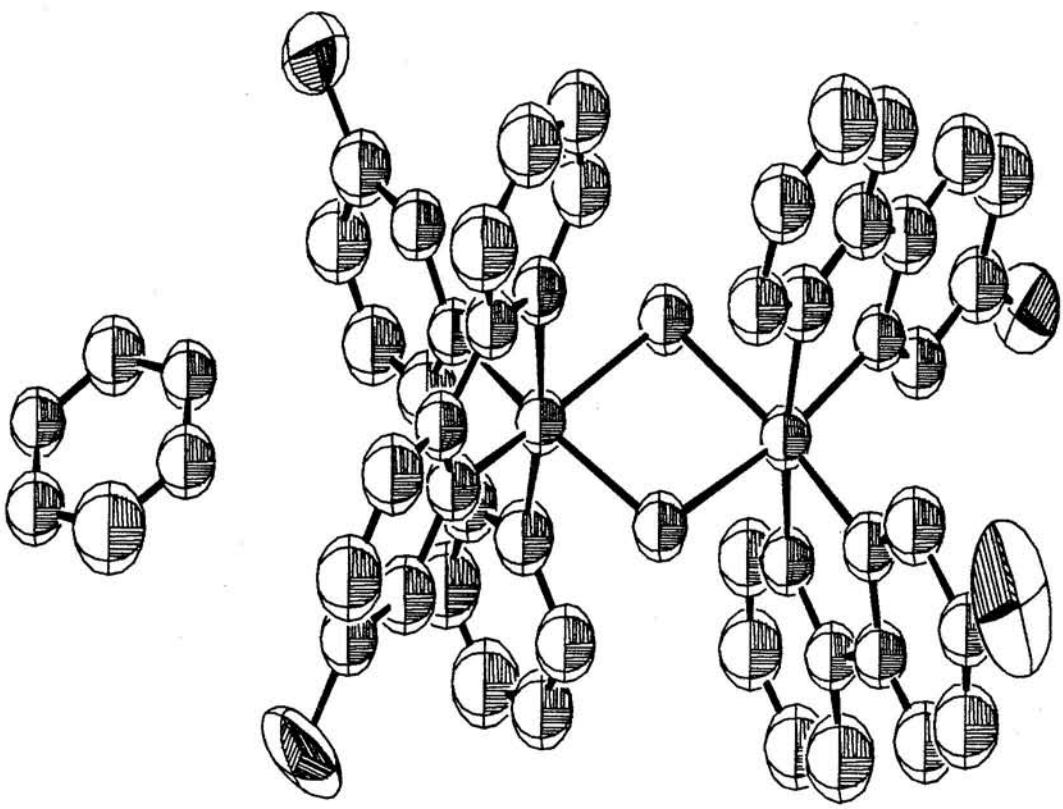

FIGURE 4.1.5:

ORTEP diagram for ΛΛ enantiomer of $[Ir(ptpy)_2Cl]_2$ at rotation, (X, Y, Z = 45, 90, 45).

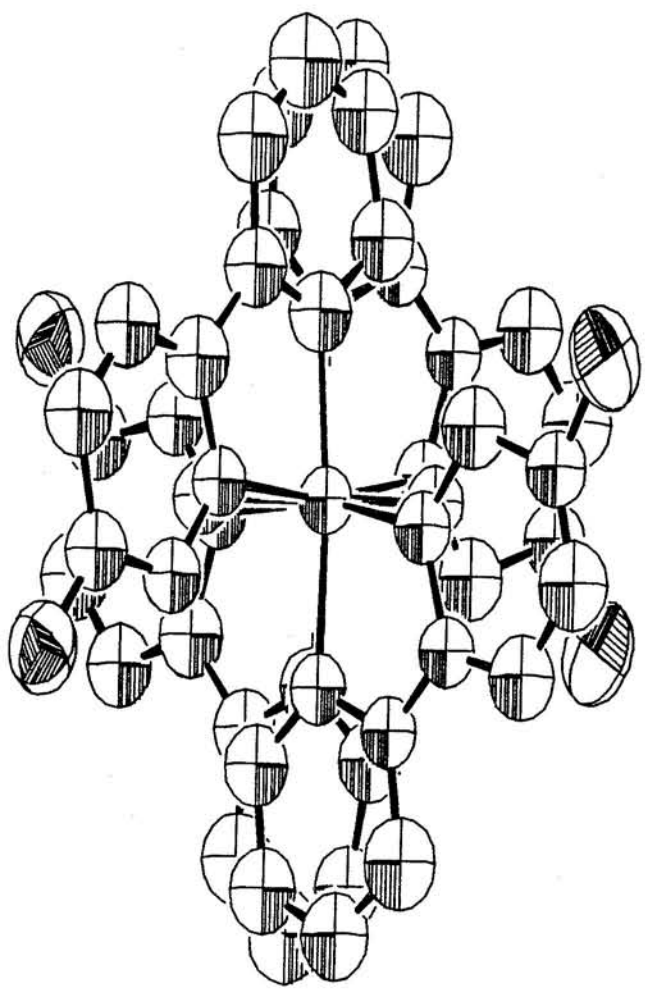

FIGURE 4.1.6:

ORTEP diagram for ΔΔ enantiomer of $[Ir(ptpy)_2Cl]_2$ at rotation, (X, Y, Z = 45, 90, 45).

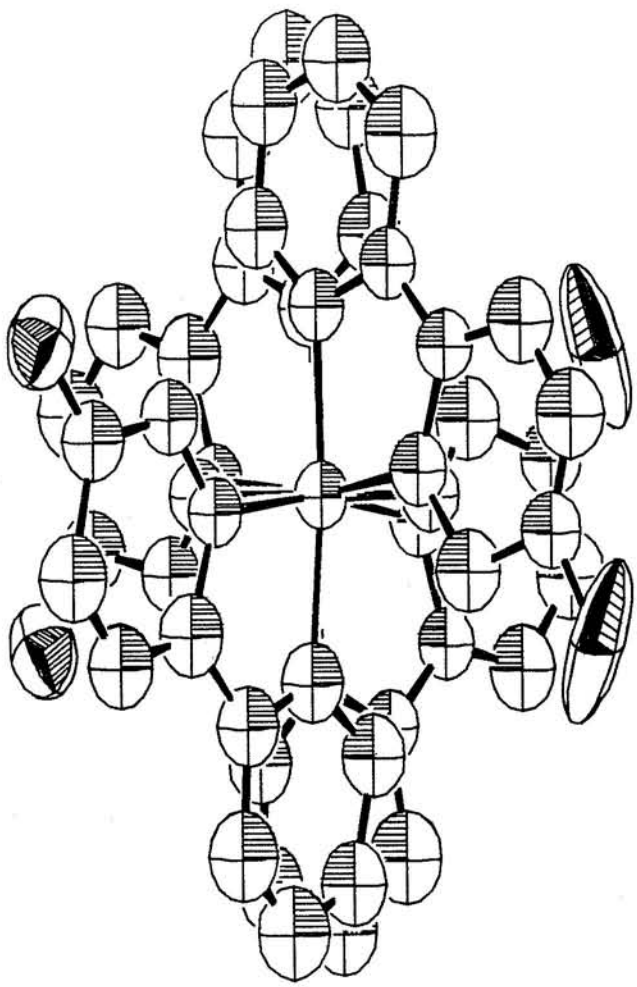

FIGURE 4.1.7:

Space-filling diagram for ΔΔ enantiomer of $[Ir(ptpy)_2Cl]_2$ at rotation, (X, Y, Z = 45, 0, 0).

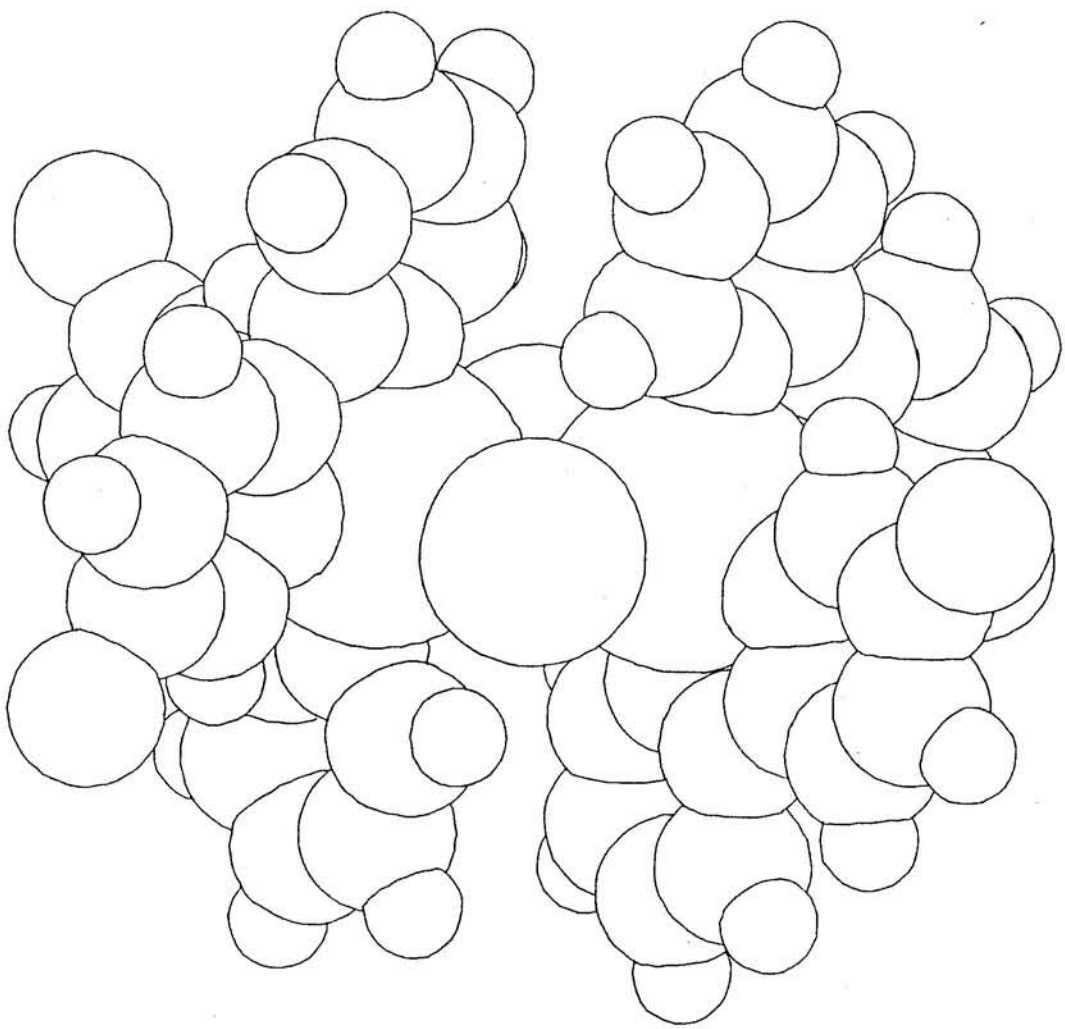

FIGURE 4.2.1:

Packing diagram for the unit cell of $[Ir(mppy)_2Cl]_2$ down the (a) A-axis, (b) B-axis, and (c) C-axis.

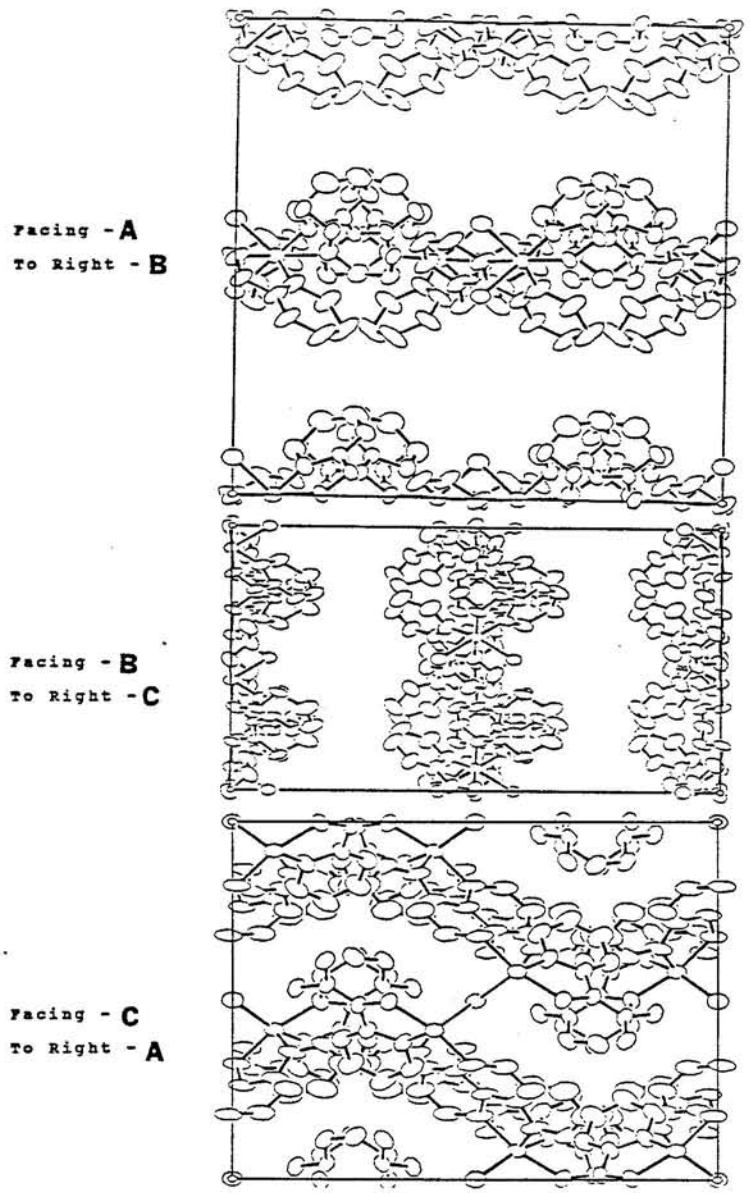

FIGURE 4.2.2:

Labeling Scheme for ΔΔ enantiomers of $[Ir(mppy)_2Cl]_2$ at (X, Y, Z = 45, 0 , 0).

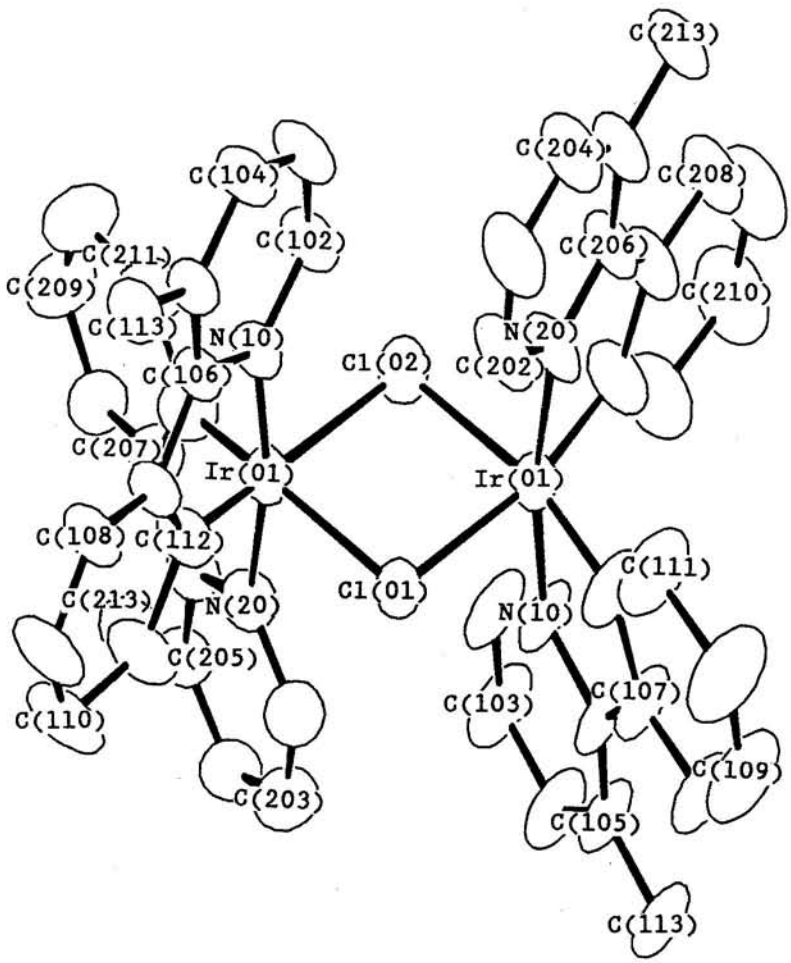

FIGURE 4.2.3:

ORTEP diagram for ΔΔ enantiomer of $[Ir(mppy)_2Cl]_2$ at (X, Y, Z = 45, 0, 0).

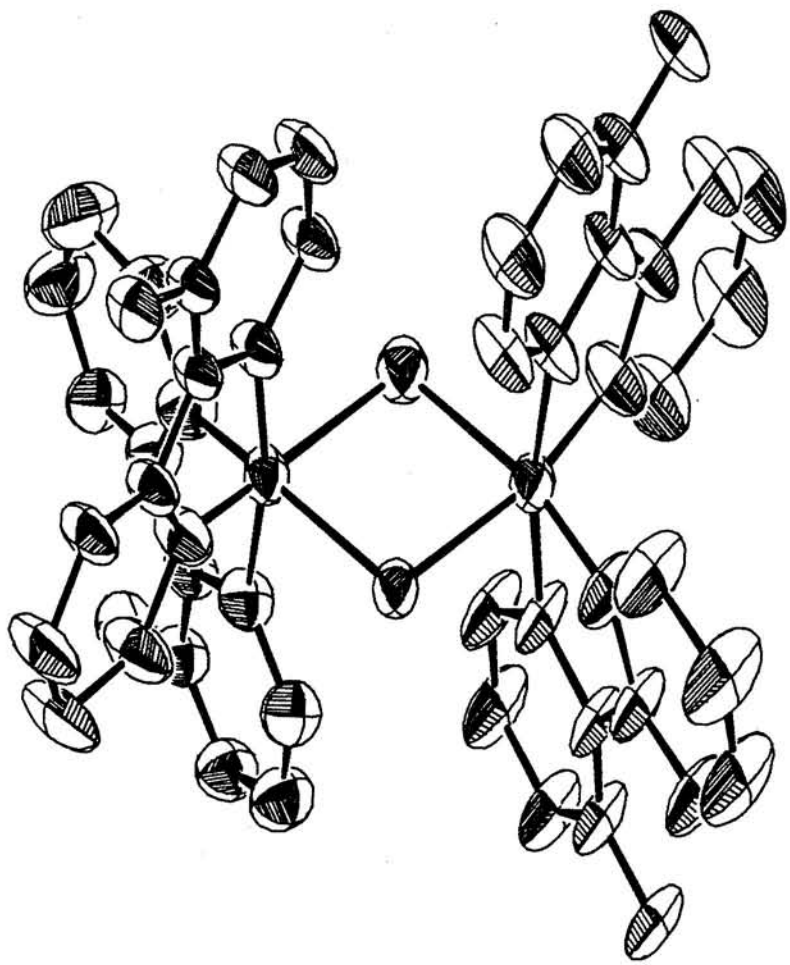

FIGURE 4.2.4:

ORTEP diagram for ΛΛ enantiomer of $[Ir(mppy)_2Cl]_2$ at (X, Y, Z = 45, 0, 0).

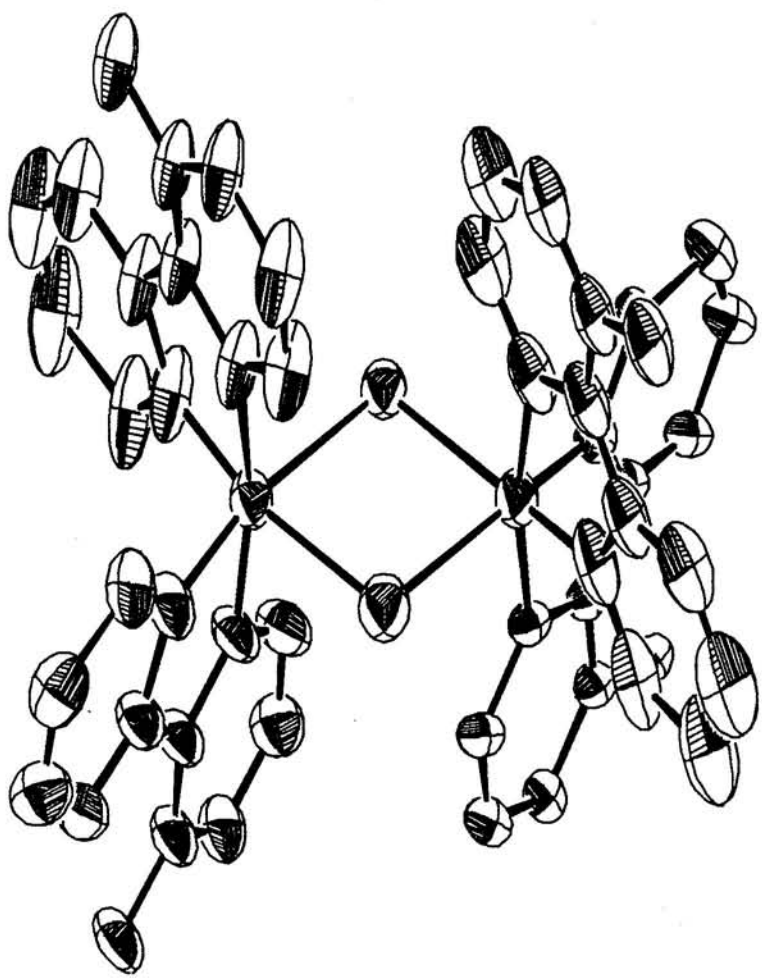

FIGURE 4.2.5:

ORTEP diagram for ΔΔ enantiomer of $[Ir(mppy)_2Cl]_2$ at (X, Y, Z = 45, 90, 45).

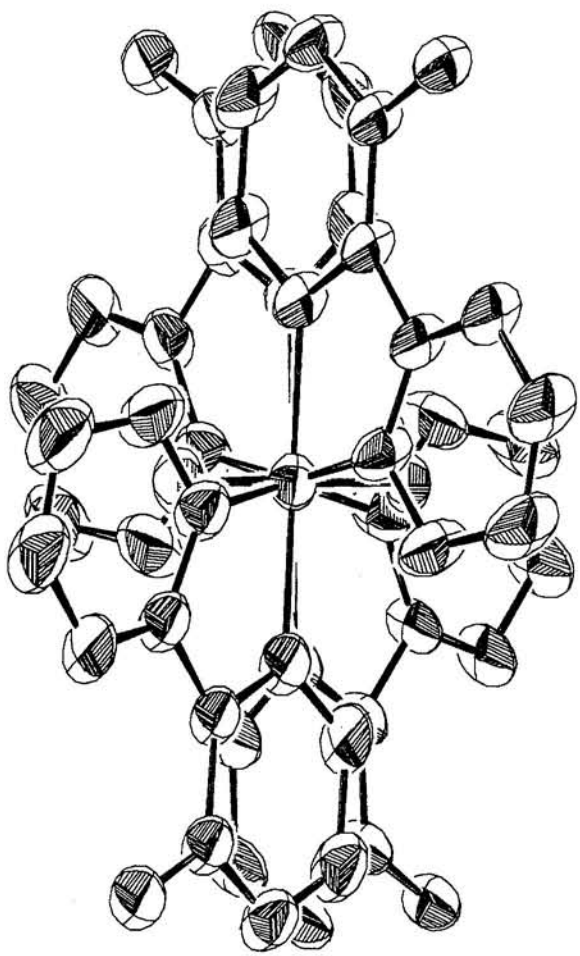

FIGURE 4.2.6:

ORTEP diagram for ΛΛ enantiomer of $[Ir(mppy)_2Cl]_2$ at (X, Y, Z = 45, 90, 45).

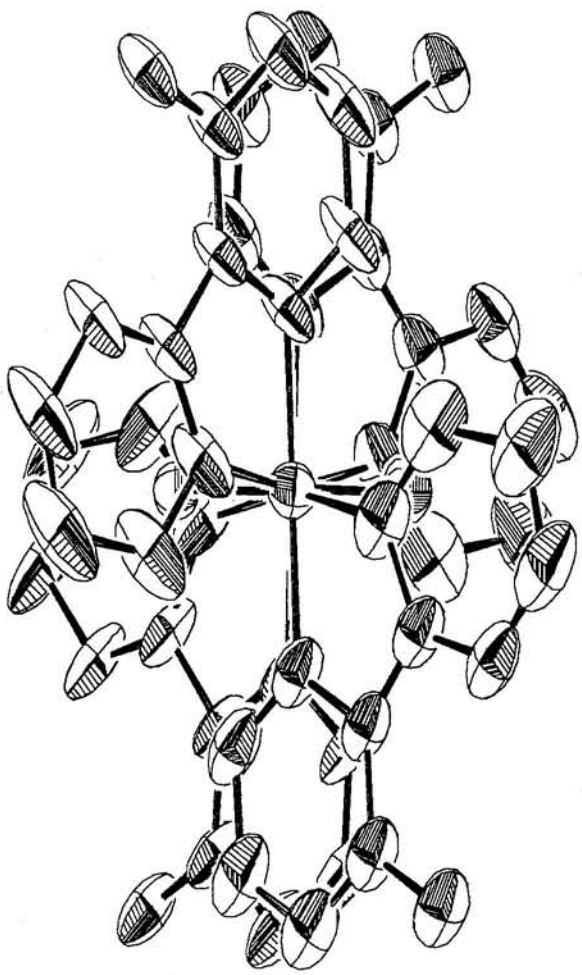

II. RESULTS AND DISCUSSION

These results show unambiguously that the nitrogens on the 2-(p-tolyl)pyridine and 3-methyl-2-phenylpyridine are across from each other and in the axial position and that the Ir-C bonds are adjacent to each other and trans from the bridging chlorides. The methyl groups not only enhance the photoreducing power of $[Ir(ppy)_2Cl]_2$ and $[Ir(mppy)_2Cl]_2$, but just as important, serve as a key label to identify the Ir-C from the Ir-N bonds in these complexes.

The $[Ir(ptpy)_2Cl]_2$ structure, shows an Ir(01)-CL(01) bond distance of 2.53 Å and an Ir(01)-Cl(02) bond distance of 2.51 Å; the Cl(01)-Ir(01)-Cl(02) bond angle is found to be 83.9°. On the other hand, the $[Ir(mppy)_2Cl]_2$ structure shows an Ir(01)-Cl(01) bond distance of 2.52 Å and an Ir(01)-Cl(02) bond distance of 2.53 Å and a Cl(01)-Ir(01)-Cl(02) bond angle of 82.21°. The methyl groups at different sites in the ptpy and mppy ligands probably account for these small differences in bond length and angle. Assorted bond length and bond angles are summarized in Table 4.2 and 4.3.

Whereas the Rh dimer possesses perfect D_2 symmetry, the Ir dimers are distorted as evidenced by the differences in the Ir-Cl(1) and Ir-Cl(2) bond distances. In the Rh dimer, only a quarter of the molecule is unique; in the Ir dimer, half the molecule is unique. The Rh-Rh distance is 3.742 Å, compared to 3.816 Å and 3.802 Å for the Ir-Ir distances of $[Ir(ptpy)_2Cl]_2$ and $[Ir(mppy)_2Cl]_2$ respectively. Overall these three structures are consistent with each other and support the NMR structural conclusions.

PART I: SUMMARY

Ir (III) complexes with methyl substituted ppy ligands possess higher electron density about the metal center than do their non-substituted parent complex. This increase in electron density is demonstrated by the shielding enhancement in the ^{1}H NMR chemical shifts of the nuclei of the ring system containing the methyl group, and by the cathodic shifts of the oxidative and reductive potentials shown in the CV measurements. In good agreement with the CV results, absorption/emission data indicates competing σ-donor and π-acceptor effects from the methyl groups during charge-transfer processes. That is, although MLCT transitions are facilitated by the added electron density on the metal, the poorer π-accepting ability of the methyl-substituted ligands renders charge-transfer more difficult. As a result, transitions occur at energies similar to the nonsubstituted ppy complexes.

From the electrochemical and spectroscopic data, Table I is constructed. This table indicates that methyl groups on the ppy ligand of ortho-metalated monomer complexes enhance the photo-redox potential, E(2+/*+), of the low energy state by as much as 100 mV over their nonsubstituted counterpart. The results from this study indicate that the electron density about the iridium metal, and consequently the reducing power of Ir (III) phenylpyridine ortho-metalated complexes, are enhanced via structural modification of the ligand, thereby creating a stronger photoreducing agent.

TABLE I

Redox Potentials for Ir(III) Dimer and Monomer Complexes (vs. NHE)

Complex:	Emis E^a	$Eox_{1/2}$ E(2+/+)	$Erd_{1/2}$ E(+/0)	Photoredox E(2+/*+)	E(*+/0)
$[Ir(ppy)_2Cl]_2$	2.57 (483)	0.51	-	-1.89	-
$[Ir(ptpy)_2Cl]_2$	2.53 (490)	0.39	-1.38	-2.01	-
$[Ir(mppy)_2Cl]_2$	2.49 (497)	0.41	-	-1.99	-
$[Ir(ppy)_2bpy]^+$	2.33 (532)	0.88	-1.78	-1.46	0.56
$[Ir(ptpy)_2bpy]^+$	2.37 (526)	0.79	-1.81	-1.55	0.76 (0.80)[b]
$[Ir(mppy)_2bpy]^+$	2.35 (528)	0.81	-1.78	-1.54	0.54 (0.55)

a) Values in parenthesis are emission maxima (E_{o-o}) at 77 K, see Table 2.4 and 3.4
b) Stern-Volmer Kinetic estimates, Figure 3.4.11.

Note, SCE = NHE + 0.40 V.
and for our measurements, NHE = $Fc^{+/0}$

LITERATURE CITED:

1. Kirch,M.; Lehn,J.-M.; Sauvage,J.-P. Helv.Chem.Acta. **1979** 62 1345

2. Lehn,J.-M. in "Photochemical Conversion and Storage of Solar Energy"; Connolly,J.S. ed., Academic Press: New York, N.Y., 1981; Chapter 6

3. Kalyanasundaram,K. Coord.Chem.Rev. **1982** 46 159

4. Kutal,C. J.Chem.Ed. **1983** 60:10 882

5. Scandola,F.; Balzani,V.; Ibid.

6. Sutin,N.; Creutz,C. Accts.Chem.Res. **1968** 1 225

7. Meyer,T.J. Accts.Chem.Res. **1978** 11 94

8. Sutin,N.; Creutz,C. J.Chem.Ed. **1983** 60 809

9. Balzani,V.; Scandola,F. Reference 2 Chp. 4

10. Adamson,A.W.; J.Chem.Ed. **1983** 60 797

11. Balzani,V.; Bolletta,F.; Gandolfi,M.T.; Maestri,M. Topics Current Chemistry **1978** 75 1

12. Sutin,N.; Creutz,C. Advances in Chemistry **1977** 168 1

13. Watts,R.J. J.Chem.Ed. **1983** 60 834

14. Launikonis,A.; Lay,P.A.; Mau,A.W.-H.; Sargeson,A.M.; Sasse,W.H.F. Aust.J.Chem. **1986** 39 1053

15. Sabbatini,N.; Dellonte,S.; Bonazzi,A.; Ciano,M.; Balzani,V. Inorg.Chem. **1986** 25 1738

16. Nonoyama,M.; Yamasaki,K. Inorg.Nucl.Chem.Lett. **1971** 7 943

17. Nonoyama,M. Bull.Chem.Soc.Jpn. **1974** 47 767

18. Dehand,J.; Pfeffer,M. Coord.Chem.Rev. **1976** 18 327

19. Omae,I. Chem.Rev. **1979** 79 287

20. Selbin,J.; Gutierrez,M.A. J.Organomet.Chem. **1981** 214 253

TABLE 4.1

Cell and data collection parameters for $[Ir(ptpy)_2Cl]_2$ and $[Ir(mppy)_2Cl]_2$.

Compound	$[Ir(ptpy)_2Cl]_2$	$[Ir(mppy)_2Cl]_2$
Formula Wt.	1128.2	1128.2
Xtal dim. (mm)	pyramidal 0.26 x 0.36 x 0.45	triangular plate 0.27 x 0.27 x 0.10
Crystal system	Tetragonal	Orthorombic
Space group	$I4_1cd$	Aba2
z	8	4
a,(Å)	16.7661(0)	15.8979
b,(Å)	16.7661(0)	16.0509
c,(Å)	33.0167(0)	21.5112
$\alpha=\beta=\gamma$ (°)	90	90
Volume ($Å^3$)	9281.1	5489.1
ρ calc, (g/cc)	1.71	1.34
Rad. and λ	Mo Kα (.7107 Å)	Mo Kα (.7107 Å)
Monochrom.	graphite	graphite
Temp. (K)	298	298
Scan range,		
below Kα1	1.2	1.2
above Kα2	1.6	1.4
Scan rate, (°/min)	4.5	4.5
Scan mode	$\theta - 2\theta$	$\theta - 2\theta$.
2θ max	50	55
Octants collect	+h,+k,+l	+h,+k,+l
Tot. # refl.	9801	7070
# unique refl.	3963	3311
# of ref obs; $I>3\sigma(I)$	1339	2530
Abs coef,(cm^{-1})	58.7	48.6
Abs. correction	analytic	analytic
Transmission factor	0.2174 (max) 0.1075 (min)	0.2334(max) 0.1436(min)
Extinction Parameter	-	-
R	.059	.118
Rw	.070	.188
EOF	1.88	6.105
# param refined	127	43
Data/param.	10.6	58.8

21. Newkome,G.R.; Puckett,W.E.; Gupta,V.K.; Kiefer,G.E. Chem.Rev. **1986** 86 451

22. Maestri,M.; Sandrini,D.; Balzani,V.; Chassot,L.; Von Zelewsky,A. J. Am. Chem. Soc. **1987** 109 7720, and ref. therein.

23. Maestri,M.; Sandrini,D.; Balzani,V.; Chassot,L.; Von Zelewsky,A.; Jolliet,P. Helve. Chim. Acta. **1988** 71 134.

24. Maestri,M.; Sandrini,D.; Balzani,V.; Chassot,L.; Von Zelewsky, A.; Deuschel-Cornioley,C.; Jolliet,P. Helv. Chim. Acta. **1988** 71 1053, and ref. therein.

25. Sprouse,S.D.; King,K.A.; Spellane,P.J.; Watts,R.J. J.Am. Chem. Soc. **1984** 106 6647

26. King,K.A.; Spellane,P.J.; Watts,R.J. J. Am. Chem. Soc. **1985** 107 1431

27. Ohsawa,Y.; Sprouse,S.D.; King,K.A.; DeArmond,M.K.; Hanck,K.W.; Watts,R.J. J.Phys.Chem. **1987** 91 1047

28. King,K.A.; Finlayson,M.F.; Spellane,P.J.; Watts,R.J. Sci. Pap. Inst. Phys. Chem. Res. **1984** 64 273

29. King,K.A. "Ph.D.Thesis"; University of California, Santa Barbara, 1986

30. Castellano,S.; Gunther,H.; Ebersole,S. J. Phys. Chem. **1965** 69:12 4166

31. Tanzer,C.; Price,R.; Breitmaier,E.; Jung,G.; Voelter,W. Angew. Chem., Int. Ed. Engl. **1970** 9 963

32. Orellana,G.; Ibarra,C.A.; Santoro, J. Inorg. Chem. **1988** 27 1025

33. Nanoyama,M. Bull.Chem.Soc.Jpn. **1979** 52:12 3749

34. Kahl,J.L.; Hanck,K.; DeArmond,K. J.Inorg.Nucl.Chem. **1979** 41 495

35. Spellane,P.J. "Ph.D.Thesis" University of California, Santa Barbara, 1985

36. Spellane,P.J.; Watts,R.J.; Curtis,C.J. Inorg.Chem. **1983** 22 4060

37. Farver,O.; Monsted,O.; Nord,G. J.Am.Chem.Soc. **1979** 101:20 6118

38. Gutierrez,M.A.; Newkome,G.R.; Selbin,J. J.Organomet.Chem **1980** 202 341

39. Reveco,P.; Medley,J.; Garber,A.R.; Bhacca,N.S.; Selbin,J. Inorg.Chem. **1985** 24 1096

40. Mader,U.; Jenny,T.; Zelewsky,A.-V. Helv.Chim.Acta **1986** 69 1085

41. Steel,P.J.; LaHousse,F.; Lerner,D.; Marzin,C. Inorg.Chem. **1983** 22 1488

42. Retcofsky,H.L.; Friedel,R.A. J. Phys. Chem. **1968** 72:7 2619

43. Constable,E.C.; Seddon,K.R. J. Chem. Soc., Chem. Comm. **1982** 34

44. Garber,A.R.; Garrou,P.E.; Hartwell,G.E.; Smas,M.J.; Wilkinson, J.R.; Todd,L.J. J.Organomet.Chem. **1975** 86 219

45. Lavallee,D.K.; Baughman,M.D.; Phillips,M.P. J.Am.Chem.Soc. **1977** 99:3 718

46. Marker,A.; Canty,A.J.; Brownlee,R.T.C. Aust.J.Chem. **1978** 31 1255

47. DeSimone,R.E.; Drago,R.S. Inorg.Chem. **1969** 8:11 2517

48. Sprouse,S.D. "Ph.D.Thesis"; University of California, Santa Barbara, 1984

49. Brown,E.R.; Large,R.F. "Physical Methods of Chemistry. Part IIA: Electrochemical Methods"; Wiley-Interscience: New York, N.Y., 1971

50. Kahl,J.L.; Hanck,K.; DeArmond,K. J. Phys. Chem. **1978** 82:5 540

51. Dose,E.V.; Wilson,L.J. Inorg.Chem **1978** 17 2660

52. Turro,N.J. "Modern Molecular Photochemistry"; Benjamin/ Cummings: Menlo Park, CA 1978

53. Drago,R.S. "Physical Methods in Chemistry"; W.B.Saunders Co: Philadelphia, PA 1977

54. Ichimura,K.; Kobayashi,T.; King,K.A.; Watts,R.J. J. Phys. Chem. **1987** 91 6104

55. Cook,M.J.; Lewis,A.P.; McAuliffe,G.S.G.; Thomson,A.J. Inorg. Chim. Acta. **1982** 64 25

56. Reveco,P.; Cherry,W.R.; Medley,J.; Garber,A.R.; Gale,R.J.; Selbin,J. Inorg.Chem. **1986** 25 1842

57. Saji,T.; Aoyagui,S. Electroanlt.Chem.Interf.Electrochem. **1975** 60 1

58. Gaines Jr.,G.L.; Behnken,P.E.; Valenty,S.J. J.Am.Chem.Soc. **1978** 100 6547

59 Ferguson,J.; Mau,A.W.-H.; Sasse,W.H.F. Chem.Phys.Lett. **1979** 68:1 21

60 Constable,E.C.; Holmes,J.M. J.Organomet.Chem. **1981** 214 253

61 Donohoe,R.J.; Tait,C.D.; DeArmond,M.K. J.Phys.Chem. **1986** 90 3923

62. Demas,J.N.; Crosby,G.A.; J. Phys. Chem. **1971** 75 991

63. King,K.A.; Watts,R.J. J. Am. Chem. Soc **1987** 109 1589

64. Lees,A.J. Chem. Rev. **1987** 87 711, and ref therein.

65. Wilde, A.P. "M.S. Thesis"; University of California, Santa Barbara, 1988

66. Stern, O.; Volmer, M. Physik. Z. **1919** 20 183.

67. "Creation and Detection of the Excited States"; Wagner,P.J. ed., Vol. I Part A, Marcel Dekker: New York, N.Y., 1971.

68. Brock, C.R.; Meyer, T.J.; Whittern, D.G. J. Am. Chem. Soc. **1974** 97 2909.

69. Marshall, J.L.; Stobart, S.R.; Gray, H.B. J. Am. Chem. Soc. **1984** 106 3027.

70. Ohashi,Y.; Kobayashi,T. Bull. Chem. Soc. Jpn. **1979** 52 2214

71. Finlayson,M.F.; Ford,P.C.; Watts,R.J. J. Phys. Chem. **1986** 90 3916

72. Rillema,D.P.; Mack K.B. Inogr. Chem. **1982** 21 3849

73. The Blake Industries four-circle diffractometer consists of a Huber 440 2θ goniometer, a Huber 430 θ goniometer, and a Huber 512 Eulerian Cradle. The diffractometer is interfaced to a DEC micro-VaxII computer with stepping motor controllers from Crystal Logic, Inc. Software for data collection was supplied by Crystal Logic.

74. Chin-Choy,T.; Keder,N.L.; Stucky,G.D.; Ford,P.C.; J. Organomet. Chem. **1988** 346 225 and reference therein.

a. The UCLA computing package was used for structural solution and refinement. The package includes modified versions of the following: CARESS (Broach; includes the program PROFILE, (Coppens, Becker and Blessing)), peak profile analysis apply Lorentz and polarization corrections; MULTAN (Main), package of programs including dirt methods, structure factor normalization. Fourier transform and peak search; ORFLS (Bushing, Martin and Levy), structure factor calculation and full-matrix. least-squares refinement; ORFFE (Bushing, Martin and Levy), distance, angle and error calculation; ABSORB (Coppens; includes the program CRYST (Edwards and Hamilton)), absorption correction calculation; ORTEP (Johnson), figure plotting; HYDROGEN (Trueblood), calculated hydrogen atom positions.

b. All least-squares refinements computed the agreement factors R and Rw according to:

$$R = [(E\|F_o|-\phi F_c\|)/(E|F_o|-\phi)]$$

$$R = \mathrm{sqrt}[(E\omega\|F_o|-\phi F_c\|^2)/(E\omega|F_o|-\phi^2)]$$

where: F_o is the observed structure factor, F_c is the calculated structure factor, and $\omega = 1/F_o^2$.

c. Scattering factors and correction for anomalous dispersion were taken from "International Tables for X-ray Crystallography"; Kynoch Press: Birmingham, England, 1974; Vol. IV.

75. Personal Communication with Dr. Nancy Keder UCSB crystallographic specialist.

PART 2

NOVEL 2,2′-BIPYRIDYL ORTHO-METALATED AND CHELATED IRIDIUM COMPLEXES.

In recent years many research groups have been interested in ortho-metalating complexes because of their similarities to classical chelating polyamine complexes.[1-10] Since the identification and characterization of an ortho-metalated bipyridine (bpy) complex, $[Ir(bpy\text{-}C^3,N)(bpy\text{-}N,N')_2]^{2+}$,[11-15] our laboratory has identified and characterized numerous iridium complexes containing ortho-metalated 2-phenylpyridine (ppy) and benzo[h]quinoline ligands.[1,4-7] Ortho-metalating Ir-C σ-bonds impart favorable photophysical properties such as visible absorption, low energy excited states, cathodic oxidation potentials and long emission lifetimes to traditional chelating complexes. In fact, $[Ir(bpy\text{-}C^3,N')(bpy\text{-}N,N')_2]^{2+}$ (an ortho-metalated linkage tautomer of $Ir(bpy)_3^{3+}$), possesses such favorable excited state properties, that it is used as a sensitizer to photo-isomerize norbornadiene to quadricyclene,[16,17] and to photo-oxidize bromide

to bromine.[18] In the ten years since $[Ir(bpy\text{-}C^3,N')(bpy\text{-}N,N')_2]^{2+}$ was discovered, however, no other ortho-metalated bpy complex has been reported–until now.

Preparation and characterization of four iridium bipyridyl complexes are discussed in Part 2 of this dissertation. The first product isolated upon combination of iridium (III) and (IV) with 2,2′-bipyridine under controlled conditions is proposed as a novel ortho-metalated dichloro-bridged bpy dimer, $[Ir(bpy\text{-}C^3,N')(bpy\text{-}N,N')Cl]_2Cl_2$ (herein referred as I), first thought to be a <u>trans</u>-$IrCl_2(bpy)_2^+$ species,[19] Recrystallization of I from DMSO/(aq)EtOH solution results in two other crystalline substance which we formulate as $[Ir(bpy\text{-}C^3,N')(bpy\text{-}N,N')Cl_2]^+$ $[IrCl_4(bpy)]^-$ (referred to as II), and $[Ir^{IV}(bpy)_2Cl_2]Cl_2$ (referred to as III). Both products are suitable for X-ray analysis but only II has been characterized by crystallographic techniques. If iridium (IV) is used in the synthesis instead of a mixture of iridium (III)/(IV), then the yield for I increases, but more importantly, a new material is isolated which is identified as the trans-$Ir(bpy)_2Cl_2^+$, IV.[19]

While dichloro-bridged dimers of Ir(III) with traditional ortho-metalating ligands such as 2-phenylpyridine are common in the literature,[1-10,20-25] product I represents the first example of a dichloro-bridged dimer of a bpy complex of Ir(III) and only the second instance of ortho-metalation of Ir(III) to 2,2′-bipyridine.[11-15] The reaction conditions suggest that the presence of Ir(IV) enhances ortho-metalation of bpy, as would be expected in

73. The Blake Industries four-circle diffractometer consists of a Huber 440 2θ goniometer, a Huber 430 θ goniometer, and a Huber 512 Eulerian Cradle. The diffractometer is interfaced to a DEC micro-VaxII computer with stepping motor controllers from Crystal Logic, Inc. Software for data collection was supplied by Crystal Logic.

74. Chin-Choy,T.; Keder,N.L.; Stucky,G.D.; Ford,P.C.; J. Organomet. Chem. **1988** 346 225 and reference therein.

a. The UCLA computing package was used for structural solution and refinement. The package includes modified versions of the following: CARESS (Broach; includes the program PROFILE, (Coppens, Becker and Blessing)), peak profile analysis apply Lorentz and polarization corrections; MULTAN (Main), package of programs including dirt methods, structure factor normalization. Fourier transform and peak search; ORFLS (Bushing, Martin and Levy), structure factor calculation and full-matrix. least-squares refinement; ORFFE (Bushing, Martin and Levy), distance, angle and error calculation; ABSORB (Coppens; includes the program CRYST (Edwards and Hamilton)), absorption correction calculation; ORTEP (Johnson), figure plotting; HYDROGEN (Trueblood), calculated hydrogen atom positions.

b. All least-squares refinements computed the agreement factors R and Rw according to:

$$R = [(E\|F_o|-\phi F_c\|)/(E|F_o|-\phi)]$$

$$R = \mathrm{sqrt}[(E\omega\|F_o|-\phi F_c\|^2)/(E\omega|F_o|-\phi^2)]$$

where: F_o is the observed structure factor, F_c is the calculated structure factor, and $\omega = 1/F_o^2$.

c. Scattering factors and correction for anomalous dispersion were taken from "International Tables for X-ray Crystallography"; Kynoch Press: Birmingham, England, 1974; Vol. IV.

75. Personal Communication with Dr. Nancy Keder UCSB crystallographic specialist.

CHAPTER 5

CHARACTERIZATION OF A NEW ORTHO-METALATED 2,2'-BIPYRIDYL DICHLORO-BRIDGED IRIDIUM (III) COMPLEX.

The important thing is not to stop questioning.

-Albert Einstein.

The synthetic, structural, electrochemical and photophysical characterization of a dichloro-bridged ortho-metalated 2,2'bipyridyl iridium(III) complex is reported in this chapter. A mixture of Ir(III) and Ir(IV) with 2,2'-bipyridine (bpy) in aqueous ethanol yields an orange-yellow amorphous material with the composition $[Ir(bpy\text{-}C^3,N')(bpy\text{-}N,N')Cl]_2Cl_2$ (I). The elemental, molecular weight, mass spec, and NMR analysis are all consistent with the $[Ir(NC)_2Cl]_2$ dimeric species described in Part 1. More specifically, the ^1H and ^{13}C NMR, electrochemical, and acid-base luminescence properties of I indicate that the C^3 carbon of one of pyridyl rings in bpy is coordinated to the iridium metal in an ortho-metalated fashion. These properties are reminiscent of another ortho-metalated bpy complex, $[Ir(bpy\text{-}C^3,N')(bpy\text{-}N,N')_2]^{2+}$, a linkage isomer of $Ir(bpy)_3^{3+}$.

I. SYNTHESES

Bis(2,2'-bipyridyl-C^3,N')bis(2,2'-bipyridyl-N,N')-μ-Dichlorodiiridium. $[Ir(bpy\text{-}C^3,N')(bpy\text{-}N,N')Cl]_2Cl_2$

Potassium hexachloroiridium(IV) (74.6 mg, .154 mmol) and potassium hexachloroiridium(III) (80.4 g, .154 mmol) are combined with 2,2-bipyridine (290.1 mg, 1.86 mmol) in 60 ml 50% aqueous ethanol and refluxed for an hour. This solution turns orange-red in 15 minutes with orange material precipitating from solution. The reaction mixture is reduced to 20 ml volume by flash evaporation and stored overnight. During this period, more red-orange material precipitates from solution; this is collected over a glass frit with the filtrate containing **II** and **III** (Chapter 6) stored for later work-up. The precipitate is then washed with ethyl ether (60 ml) and hexanes (60 ml) until no evidence of bipyridine is detected by TLC. For several days the precipitate is vacuum dried to afford a red-orange material (105 mg). ^1H NMR analysis indicates that this material contains **I** and a mixture of several other bipyridyl iridium complexes, thus the red-orange material (91.2 mg) is dissolved in .5 ml DMSO and 25 ml hot (aq)EtOH and stirred for several hours. After reducing the volume of the solution (10 ml), the product is filtered and vacuum dried to yield an amorphous orange material, $[Ir(bpy\text{-}C^3,N')(bpy\text{-}N,N')Cl]_2Cl_2$, (19.4 mg, 12.5%). Calculated for $Ir_2C_{40}H_{30}N_8Cl_4 \cdot 3(H_2O)$ -Analysis: C,39.94%; H,3.02%; N,9.31%; MW. 1203g/mol. -Found: C,39.99%; H,3.15%; N,9.09%; MW. 1228g/mol.

II. MEASUREMENT

Mass spectra were obtained with ionization voltage of 2.2 eV, under desorption chemical ionization conditions using methane as the carrier gas at 240°C in an NBA matrix. A lower ionization voltage, I = 14 mV, was utilized to detect ion fragments above 1000 m/e.

An IBM EC-225 voltammetric analyzer was used to measure cyclic voltammograms (CV). The CV's were recorded under room temperature conditions with an electrolyte solution consisting of a saturated solution of tetraethylammonium hexafluorophosphate (TEAH) and alumina in 50 ml dimethylformamide (Burdrick and Jackson, used without further purification), degassed by dry dinitrogen. Voltammograms for the ferrocenium/ferrocene couple ($Fc^{+/0}$) were measured under the same conditions as the complex. The half-wave potential $E_{1/2}$, of $Fc^{+/0}$ in dimethylformamide (DMF) was 0.57 V vs. standard calomel electrode (SCE). All cyclic voltammograms were monitored at scan rates of 1.0 V/s. See Appendix B.

The ^{1}H, ^{13}C, attached proton test (APT), nuclear Overhauser effect (nOe) difference, 2D Homonuclear (COSY) and 2D Heteronuclear (CSCM) correlation spectroscopy spectra were obtained from a General Electric GN-500 FT NMR spectrometer. Samples were dissolved in 99.9 atom % DMSO-d_6 for analysis. T_1 relaxation was measured at 1.86 seconds by inversion recovery techniques. See appendix A.

Absorption spectra were obtained from a Hewlett Packard 8452A Diode array spectrophotometer interfaced to a HP 9000/300 work

station with spectra provided by HP 7475A plotter. Extinction coefficients were measured in (aq) EtOH (50%), EtOH-MeOH (1:1 v/v) and neat DMF solvents with concentration ranging from 10^{-4} to 10^{-6}M. Absorption measurements under neutral, acidic and basic conditions were recorded in EtOH-MeOH, EtOH-MeOH (0.1 M HCl), EtOH-MeOH (0.1 M NaOH). Excitation and emission (corrected/uncorrected) spectra were recorded in similar solvent conditions as in the absorption spectra measurements. For room temperature measurements, samples were generally degassed with dinitrogen or by freeze-pump-thawed cycles. Under 77 K conditions, capillary samples or freeze-pump-thawed samples were submersed in a finger quartz optical dewar filled with liquid nitrogen. Room temperature and low temperature (77 K) measurements were obtained from a Spex Fluorolog 2 series spectrophotometer equipped with single monochromators. Lifetimes and time-resolved emission spectra were measured with an AVCO-Everett C-950 nitrogen laser with 337 nm pulses. See Appendix C.

III. RESULTS AND DISCUSSION

1. Mass Spectroscopy; evidence for a dimeric species.

The first mass spectrum for I was obtained under desorption chemical ionization conditions with an ionization voltage of 2.2 eV in an NBA matrix. This spectrum, Figure 5.1.1, shows signals at 574 m/e (12.2%), 539 m/e (34.9%), 503 m/e (4.6%), 185 m/e (16.9%) and 157 m/e (100.0%). The peak at 574 m/e corresponds to the ion fragment $Ir(bpy\text{-}C^3,N')(bpy\text{-}N,N')Cl_2^+$, a heptolyptic cleavage of the dimer. The 539 m/e and 503 m/e peaks correspond to successive chloride loss from the 574 m/e fragment. The base peak at 157 m/e and 185 m/e correspond to the protonated free bipyridyl ligand (bpy + H^+) and bipyridine + $C_2H_5^+$ (156 + 29) respectively. The $C_2H_5^+$ fragment forms in high concentrations in the mass spectrometer if methane is used as the carrier gas under chemical ionization conditions, it usually couples to an ion in the plasma in the mass spectrometer. Fragments and m/e peaks are summarized in Table 5.1.

At lower ionization voltage, I=14 mV, signals at 1078 m/e and 1113 m/e are observed, Figure 5.1.1 (inset). The 1113 m/e and 1078 m/e peaks correspond to the $[Ir(bpy\text{-}C^3,N')(bpy\text{-}N,N')Cl]_2Cl^+$ and $[Ir(bpy\text{-}C^3,N')(bpy\text{-}N,N')Cl]_2^+$ fragments, respectively. Isotopic cluster abundance simulation for $Ir_2C_{40}H_{30}N_8Cl_3$ and $Ir_2C_{40}H_{30}N_8Cl_2$ agree nicely with the signal distributions at 1113 and 1078 m/e.

Recrystallization of $[Ir(bpy\text{-}C^3,N')(bpy\text{-}N,N')Cl]_2Cl_2$ in H_2SO_4 gives a mass spectrum, Figure 5.1.2, showing signal distributions

at 613m/e (10%), 593m/e (7%), 575m/e (60%), 538m/e (60%), 503m/e (20%), 460 m/e (60%), 440 m/e (20%), 424 m/e (20%) and other peaks below 307m/e. The abundance of signals in this spectrum, Figure 5.1.2, relative to that in Figure 5.1.1, arises from the sulfate ions present because of the recrystallization conditions. The pattern of the m/e distribution in Figure 5.1.2, however, suggests a protonated dimer probably with the composition $[Ir(Hbpy\text{-}C^3,N')(bpy\text{-}N,N')Cl]_2Cl_2^+$. This is evident from the 575 m/e signal, which is characteristic of a heptolyptic cleavage of the protonated dimer. The 460 m/e fragment, not seen in the mass spectrum in Figure 5.1.1, corresponds to $Ir(bpy\text{-}N,N')(C_5NH_4)Cl^+$, a fragment in which one of the bipyridyl ligand is dissected in half to a pyridyl ring.

Interpreting the mass spectral data as a combination of simple bond-cleavage processes,[27] there is strong evidence that I exist as a dimeric species. The presence of the 1113 m/e and 1078 m/e fragment, Figure 5.1.1, is consistent with the proposed dichloro-bridge bipyridyl iridium dimer. These signals, together with the 574 m/e, 539 m/e and 503 m/e signals, support the contention that one of the bipyridyl ligands in this complex is bonded to the iridium metal via the C^3 carbon in an ortho-metalated fashion. A complex in which all the bipyridyl ligands were chelated through the nitrogen atoms would give dominant ion fragments corresponding at 575 m/e 540 m/e and 503 m/e. Elemental analysis and molecular weight analysis are consistent with the results obtained here.

TABLE 5.1

Mass Spectrum Ion Fragment Distribution for

$[Ir(bpy\text{-}C^3,N')(bpy\text{-}N,N')Cl]_2Cl_2$.

Mass/Charge (m/e)	Intensity (%)	Ion Fragments
157	100.0	$bpy + H^+$
185	6.9	$(bpy + C_2H_5\bullet)^+$
503	4.6	$Ir(bpy\text{-}C^3,N')(bpy\text{-}N,N')^+$
539	34.9	$Ir(bpy\text{-}C^3,N')(bpy\text{-}N,N')Cl^+$
574	12.2	$Ir(bpy\text{-}C^3,N')(bpy\text{-}N,N')Cl_2^+$
1078	< 1	$[Ir(bpy\text{-}C^3,N')(bpy\text{-}N,N')Cl]_2^+$
1113	< 1	$[Ir(bpy\text{-}C^3,N')(bpy\text{-}N,N')Cl]_2Cl^+$

FIGURE 5.1.1:

Mass spectrum of $[Ir(bpy\text{-}C^3,N')(bpy\text{-}N,N')Cl]_2Cl_2$.

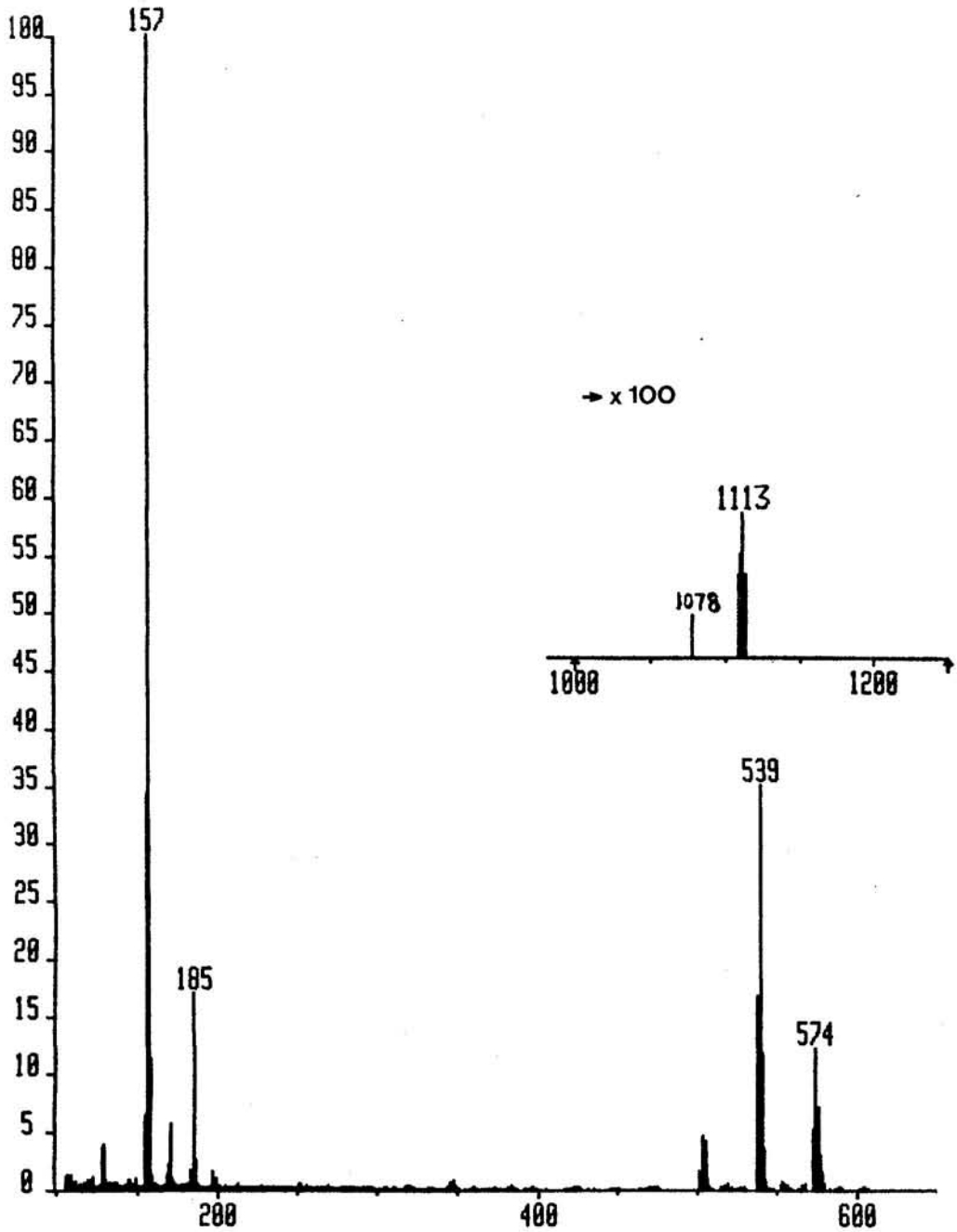

FIGURE 5.1.2:

Mass spectrum of $[Ir(bpy\text{-}C^3,N')(bpy\text{-}N,N')Cl]_2Cl_2$ after recrystallization in H_2SO_4.

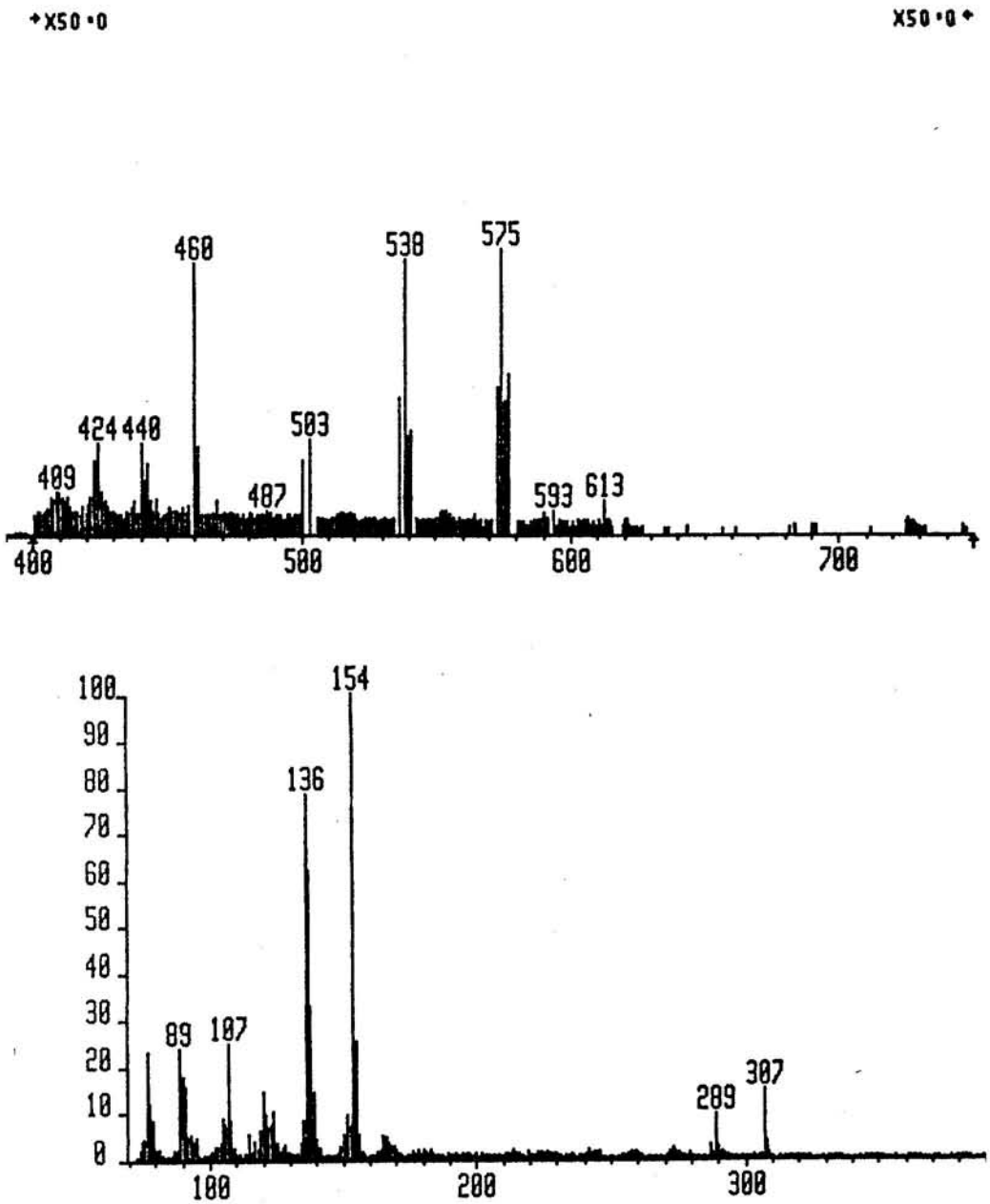

2. Electrochemistry; a dinuclear species.

The redox potentials for $[Ir(bpy\text{-}C^3,N')(bpy\text{-}N,N')Cl]_2Cl_2$ in DMF with TEAH supporting electrolyte at room temperature are summarized in Table 5.2. Cyclic voltammograms are illustrated by eight curves **a**, **b**, **c1**, **c2**, **c3**, **d1**, **d2**, and **d3** as shown in Figure 5.2.1. Curve **a** represents the voltammogram for the solvent/electrolyte solution, curve **b** represents the voltammogram for the $Fc^{+/0}$ reference, and curves **c** and **d** represent the voltammograms for the complex using two scanning modes. Curves **c1**, **c2** and **c3** are CVs in which the switching potentials were set to 2.0, 1.75 and 1.5 V (vs. SCE) respectively. These CV curves, referred to as *single* scan curves, were recorded by measuring the CV of **I** between 0.0 V and the switching potential. Curves **d1**, **d2** and **d3**, referred to as the *repetitive* scan curves, were generated by scanning the oxidative (or reductive) region in a repetitive fashion before recording the CV's.

Although there are signs of solvent/electrolyte deterioration (E = 1.10 and -1.38 V vs. SCE), curve **a**, these waves are minimal and do not overlap any of the redox waves of the complex. Curve **b**, the ferrocenium/ferrocene ($Fc^{+/0}$) redox couple, shows a reversible half-wave oxidative potential at $E_{1/2}$ = 0.57 V (vs. SCE). The insensitivity of this potential to solvent and temperature allows comparison of the redox potentials of this complex to other redox potentials of similar complexes monitored in different solvents and temperatures.[4] For this reason the $Fc^{+/0}$ couple was used as an internal reference.

The oxidative CV scan in curves **c1**, **c2** and **c3** shows two redox waves at $E_{1/2}$ = 1.17 and 1.52 V (vs. SCE). The first oxidative wave is reversible only at switching potential of 1.5 V, **c3**; at switching potentials past 1.75 V, curves **c2** and **c1**, the current ratio, Ic/Ia, decreases from unity. Under repetitive conditions, **d1**, **d2** and **d3**, the first oxidative wave becomes irreversible as shown by its decay, the second oxidative wave however, remains reversible. In fact, the second wave at $E_{1/2}$ = 1.52 V is reversible under all our experimental conditions.

Ohmic losses and recorder lag are likely to be responsible for the deviation of the peak separation (ΔE_{p-p} = 120 mV) from the theoretical value (43 mV) for these oxidative waves.[29]

The reductive portion of the cyclic voltammograms shows a more complicated wave pattern than the oxidative portion, showing five reductive waves under single scan mode. The first reductive wave occurs at E_{pc} = -0.25 V and although the ΔE_{p-p} suggests reversible behavior, the deformation of this wave and the deviation of Ia/Ic from unity, indicate irreversible behavior. The third and fourth reductive waves, E_{pc} = -1.00 and -1.32 V, are irreversible for all our experimental conditions, the latter is observed as a slight swell on the fifth wave. Reductive waves at $E_{1/2}$ = -0.68 and -1.25 V are reversible during single scan conditions, curves **d1-d3**. However, the wave at $E_{1/2}$ = -0.68 V does becomes irreversible after prolonged repetitive scans. The reduction occurring at E_{pa} = -1.38

V, curves d, is solvent deterioration. No further reduction waves were observed up to switching potential of -2.5 V.

For traditional ortho-metalated dimers $[Ir(NC)_2Cl]_2$ (Part I), the two reversible oxidative waves have been interpreted as the removal of metal-localized electrons;[30] the CV results obtained for I, is consistent with this mechanism. The reversible oxidation waves at switching potential of 1.5 V and single scan mode, support a stable oxidized Ir(III/IV) and Ir(IV/IV) species. Yet at switching potentials greater than 1.5 V or repetitive conditions, the irreversible behavior of the first oxidative wave corresponding to the Ir(III/IV) species, leads to decomposition of the original material most likely due to cleavage of the dimer resulting in a monomeric solvento species.

Electrochemical reaction mechanism of $[Ir(bpy)_2Cl_2]^+$ were determined in acetonitrile[31] and N,N'-dimethylformamide[32]. In acetonitrile the mechanism for reduction was interpreted as successive one electron transfer interrupted at several steps by elimination of chlorides. In DMF, the mechanism takes into account four reductive waves; the first, second and fourth waves involve reversible one electron reduction with the third attributed to ligand liberation. In our case, the complicated reversible reduction pattern for I indicates that ligand liberation occurs before the reversible one step reduction of the bpy ligands. The only bonafide reversible reductive wave at $E_{1/2}$ = -1.25 V, is the aftermath of two irreversible reductions. It is this fifth wave

which is assigned to the reduction of the bpy ligand.

CV results for ortho-metalated Ir(III) dimers and mixed-ligand Ir(III) monomers,[4,30] indicate that species containing ortho-metalated ligands are easier to oxidize but harder to reduce than similar complexes containing only bpy ligands. If the ortho-metalating bpy-C^3,N′ ligand in $[Ir(bpy\text{-}C^3,N')(bpy\text{-}N,N')Cl]_2Cl_2$ is approximated for a ppy-C^2,N′ ligand as in $[Ir(ppy)_2Cl]_2$, then the oxidation potential for $[Ir(bpy\text{-}C^3,N')(bpy\text{-}N,N')Cl]_2Cl_2$ should lie beyond the oxidation potentials of $[Ir(ppy)_2Cl]_2$ but short of the oxidative potential for $IrCl_2(bpy)_2^+$. The results in Table 5.2 support this assertion. The oxidation potentials for I are 20 - 30 mV greater than those of $[Ir(ppy)_2Cl]_2$ [4,31] but nearly 100 mV less than that of $IrCl_2(bpy)_2^+$.[31,32] Similarly, the reduction for I occurs at 10 mV more cathodic than for $IrCl_2(bpy)_2^+$, and less cathodic by 100 mV than that of $[Ir(ppy)_2Cl]_2$. We conclude that the presence from the anionic character of the Ir-C moiety in I lowers the oxidation potential and raises the reduction potential for this iridium bpy complex compared to those of traditional bipyridyl chelating complexes. It is interesting to note as well that the reduction potential for I and $IrCl_2(bpy)_2^+$ are nearly identical, which is expected for ligand localized reduction of the chelating bpy-N,N′ ligand. Appendix C, Table B.1 summarizes redox potential for I and other ortho-metalated complexes found in Part I.

TABLE 5.2

Cyclic Voltammetric Potentials for

$[Ir(bpy\text{-}C^3,N')(bpy\text{-}N,N')Cl]_2Cl_2Cl_2$ (V vs. SCE)[a]

COMPLEX	Epa	Epc	Epa/2	Epc/2	ΔEp-p	$E_{1/2}$
Oxidative Scan (0.0V to +2.0 V)[b]						
1st wave[c]	1.25	1.13	1.17	1.18	.12	1.17 (0.60)[d]
2nd wave	1.58	1.46	1.50	1.54	.12	1.52 (0.95)
Reductive Scan (0.0V to -2.0 V)						
1st wave[e]	-0.17	-0.25	-	-0.15	.08	-
2nd wave[e]	-0.54	-0.72	-0.70	-0.65	.18	-0.68 (-1.25)
3rd wave	-	-1.00	-	-.99	-	-
4th wave	-	-1.33	-	-	-	-
5th wave	-1.30	-1.21	-1.28	-1.22	.05	-1.25 (-1.82)
Ferrocenium/ferrocene couple (0.0 to +2.0 V)						
$Fc^{+/0}$	0.78	0.50	0.53	0.60	.25	0.57

a) Solvent; dimethylformamide
b) A minor reversible wave in curve c3 at $E_{1/2}$ = 0.60 V is assigned to chloride oxidation.
c) reversible only at switching potential of 1.5 V.
d) Values in parenthesis are $E_{1/2}$ vs. $Fc^{+/0}$.
e) Impurities or solvent deterioration.

FIGURE 5.2.1:

Cyclic voltammograms for $[Ir(bpy\text{-}C^3,N')(bpy\text{-}N,N')Cl]_2Cl_2$ in DMF/TEAH, room temperature (vs. SCE).

Curve a - DMF/TEAH CV scan. Curve b - $Fc^{+/0}$, Ref. CV scan.
Curve c1, c2, c3 - CV scan of complex under single scans at 2.00, 1.75 and 1.50 V switching potential.
Curve d1, d2, d3 - CV scan of complex under repetitive scan, 1st, 2nd and 3rd cycle.

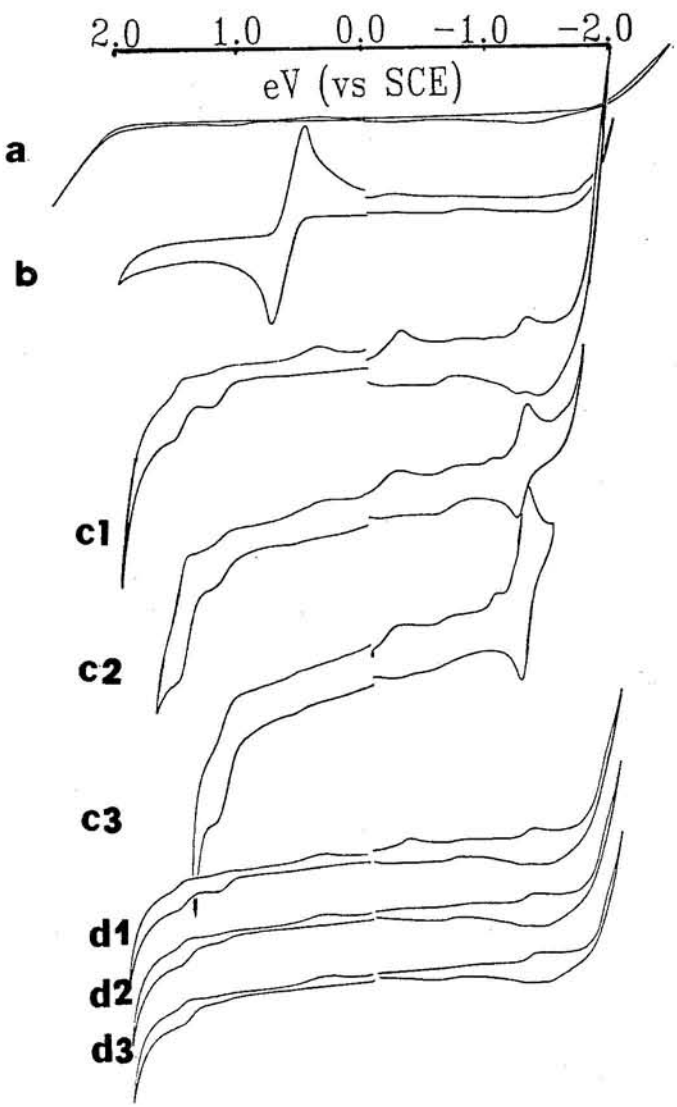

3. ^{1}H and ^{13}C NMR Analysis; A cis Ir-C, Ir-Cl configuration for I.

The ^{1}H and ^{13}C NMR spectra for I suggest either a cis dichlorobis(2,2'-bipyridyl) iridium (III) or a tetrakis (2,2'-bipyridyl)-μ-dichloro iridium (III) complex; each containing two types of bipyridyl ligands with nondegenerate halves of each bipyridyl ligand. As discussed earlier, elemental analysis, molecular weight determination and mass spectroscopy support a dimeric species. The proposed structure of I is shown again in Figure 5.3.1 with the bpys ligands labeled for this NMR discussion.

The ^{1}H NMR spectrum (10.0 - 7.0 ppm) for I, Figure 5.3.2b, shows fourteen resonances between 7.2 and 9.7 ppm which integrate for *fifteen* protons; the resonance at 7.8 ppm integrates for two protons. The full ^{1}H NMR window (10.0 - 0.0 ppm), Figure 5.3.2a, shows a large peak at 3.3 ppm for the H_2O resonance and a high field signal at 2.49 ppm for the dMSO-d_6 solvent resonance.

Twenty carbon resonances are shown in the proton decoupled ^{13}C NMR spectrum between 120 and 166 ppm (two resonances at δ = 124.9), Figure 5.3.3b; of these, five have weak intensities, δ = 145, 156, 159, 163 and 166, suggestive of five nonprotonated carbon resonances. The APT spectrum, Figure 5.3.3c, supports the ^{13}C NMR interpretation showing five negative signals for the nonprotonated carbons and fifteen positive signals for the protonated carbons. The signal at 40 ppm is the DMSO-d_6 resonance as shown in the ^{13}C NMR spectrum (200 - 20 ppm), Figure 5.3.3a.

The ^{1}H 2D homonuclear COSY spectra, Figure 5.3.4, decipher the

^{1}H resonances of I to four spin systems containing "three", "four", "four" and "four" resonances. These spin systems are labeled "A", "B", "C" and "D" corresponding to the labeled ring system A,B,C and D for the bpy ligands in I, see Figure 5.3.1. Only modulations arising from ^{1}J coupled protons are observed in this COSY spectrum, Figure 5.3.4a, because the contour level was set to 5. As such, the resonances from spin system A and D are clearly partitioned, unfortunately, resonances from spin systems B and C are difficult to separate in Figure 5.3.4a because of mutually overlapping signals at 7.8 ppm. Figure 5.3.4b shows a more detailed COSY spectrum with the contour level set to 13. In this spectrum, ^{2}J and ^{3}J coupling are observed which permits separation of the B and C spin resonances. For clarity, the contours are mapped to their assigned proton. J-connective analysis is presented in Appendix A, Section iii.

J-correlation connectivity of the contour in the COSY spectrum from Figure 5.3.4a, suggests that resonances at δ = 8.5, 8.4, and 7.3 compose one spin system, and resonances at δ = 9.67, 8.8, 8.4, 8.06 constitute another spin system. The former, because of its three proton integration, is assigned to the ortho-metalated "A" spin system, while the latter, because it contains the lowest field resonance δ = 9.7, is assigned to the "D" spin system.[7,24,31-33] Since no resonance attributed to the A_3 proton is observed, the ortho-metalated carbon is assigned to the A_3 position of the "A" spin system, as shown by the labeled structure in Figure 5.3.1.

Increasing the contour level of the COSY spectrum, Figure 5.3.4b, disentangles the δ = 7.8 resonance of spin system "B" and of spin system "C". The long range coupling, depicted by the smaller contours in the spectra discriminate the "B" spin resonances at δ = 8.2, 7.78, 7.5, and 7.12 from the "C" spin resonances at δ = 8.7, 7.9, 7.76, and 7.32. Cross coupling from the signals at 8.8 ppm (D_3) and 8.7 ppm (C_3) are also observed in this COSY spectrum at even deeper contour levels (not shown) which suggest that the D and C spin systems are contained in the same bipyridyl ligand. J-connectivity of the COSY spectrum provides complete assignment of the ^{1}H NMR spectrum.

Proton nuclear Overhauser effect (nOe) analysis, Figure 5.3.5, supports the COSY interpretation in which the "C" and "D" spin systems comprise a bipyridyl ligand, Figure 5.3.1. The nOe difference spectra are shown in Figure 5.3.5 **a-e**. For comparison, the regular ^{1}H NMR spectrum is shown in spectrum **f**. Spectrum **a**, shows saturation of the A_4 resonance which produces nOe to only the A_5 resonance. Similarly, saturation at A_6 and B_3, spectra **b** and **c** respectively, produce Overhauser effect to only the A_5 and B_4 resonances, respectively. Saturation of the C_3 resonance, spectrum **d**, produce nOe to the D_3 and C_4 resonances and vice versa (not shown). Finally saturation at the D_6 resonance produce nOe to only D_5, spectrum **e**. Saturation of other resonances in the A or B rings indicates no nO relationship between protons in the "B" spin systems and protons in the "A" spin systems (not shown).

The proton-carbon heteronuclear correlation spectrum (CSCM) shows fifteen protonated carbon resonances J_{C-H} coupled to fifteen proton resonances, Figure 5.3.6, consistent with the ^{13}C and APT spectra. For clarity, the APT and ^{13}C spectra are superimposed along the axes of the CSCM spectrum. The five nonprotonated carbon resonances do not give rise to any perturbation in the CSCM spectrum as expected since these carbons lack protons to J_{C-H} couple. The ^{1}H, 7.78 ppm overlapping resonances show coupling to two carbon resonances which confirms the two proton integration for this signal. Connectivity of the ^{1}H resonances via the contours in the CSCM spectrum leads to direct assignment of the ^{13}C resonances. See Table 5.3.

The $^{13}C\{^{1}H\}$ and APT spectra shows a nonprotonated carbon resonance at δ = 144.7 ppm suggestive of an ortho-metalated carbon.[7,18,31,32] The chemical shift of this resonance is placed not only up field from the two 2- and 2′ bridgehead carbons (δ = 152.9, 155.6, 163.0, 166.0), but also placed in a region in which ortho-metalated carbons resonate, Appendix A, Table A.6. Ortho-metalating carbons resonate up field because of the π-back bonding (shielding effect) of the iridium due to the strong σ-donor character of the ortho-metalating carbon.[4,7,31-36]

The other nonprotonated carbon resonances are assigned as follow; the two higher field carbon resonances at 155.70 and 163.05 ppm are assigned to the A_2 and B_2 carbons of the metalating bpy

ligand, respectively and the resonance at 158.45 and 166.00 ppm are assigned to the D_2 and C_2 bridgehead carbons of the chelating bpy ligand, respectively. The lower field assignment for each pair, i.e., A_2/B_2 and D_2/C_2, are assigned to the ring system trans to the chloride bridges, i.e., B_2 and C_2.

Two lines of evidence in the NMR spectra suggest that ortho-metalation occurs in I. The first is the fifteen proton integration. The removal of the degeneracy of the bipyridyl rings because of metalation of one of the bpy ligands through C^3 accounts for the fifteen proton integration in the ^1H NMR spectrum.[15,33-38] The COSY spectra, Figure 5.3.4, show that these ^1H resonances belong to a "four", "four", "four" and "three" spin system with the three proton spin system assigned to the ortho-metalated ring. The second evidence for ortho-metalation is the quaternary carbon resonance at 144.7 ppm in the ^{13}C and APT NMR spectra, Figure 5.3.3, which is characteristic of a carbon resonance bound to iridium; it is this resonance which is assigned to the A_3 carbon.[15]

Aside from establishing ortho-metalation, the NMR analysis favors the proposed structural configuration of I shown in Figure 5.1, in which the Ir-C bonds are in an axial position across the Ir-N bonds and cis to the bridging chlorides rather than in the equatorial position trans to the bridging chlorides as in traditional ortho-metalated NC dimers such as in $[Ir(ptpy)_2Cl]_2$.[7,30] We justify this by the the ^1H NMR spectrum, Figure 5.3.2, which shows a downfield resonance at 9.67 ppm that integrates for only one

proton. For dimeric species like $[Ir(ppy)_2Cl]_2$, the lowest field proton signals around 9 ppm arise from the protons adjacent to a deshielding nitrogens and orientated spacially over the bridging chlorides.[7,24,25,30,33] The "one" proton integration in the ^1H NMR spectrum for I, suggests a configuration in which the ortho-metalated ring is adjacent to the bridging chlorides, Figure 5.3.1. A ^1H NMR spectrum for such a structural arrangement would show the D_6 proton resonating downfield around 9.5 ppm and the A_4 proton resonating up field around 8 ppm. For traditional ortho-metalated ppy dichloro-bridged iridium dimers, protons of the latter type (protons adjacent to the ortho-metalating carbons) are the highest field aromatic protons, resonating at δ = 5.7 - 5.9 ppm.[7,30,33] Thus for $[Ir(bpy\text{-}C^3,N')(bpy\text{-}N,N')Cl]_2Cl_2$, the NMR result suggests assignment of the A_4 proton to the resonance at 8.4 ppm; the lowest field "A" spin resonance. The reason this assignment is nearly 2 ppm lower field than the corresponding A-proton resonance in $[Ir(ppy)_2Cl]_2$ arises from the opposing shielding effects experienced by the A_4 protons in I.[15,30-37] It is deshielded because of its orientated over the electronegative chloride bridges and shielded because of its position adjacent to the anionic ortho-metalating A_3 carbon.[7,24,30-37] The opposing shielding effects cancel each other and the A_4 proton resonate in the middle to the aromatic frequencies, δ = 8.37. This is consistent with a structural configuration in which the Ir-C bonds of the ortho-metalating bpys

are placed cis to the dichloro-bridges. Furthermore, there is evidence for this type of structural arrangement from the crystal structure of II (a precursor or I), to be discussed in Chapter 6.

In summary, NMR evidence leads to a structural configuration in which ortho-metalation exists and in which Ir-C ortho-metalated bonds are cis to the chloro bridges. This is the first example of an ortho-metalated complex with this unique configuration.

TABLE 5.3

^{1}H and ^{13}C NMR assignments for $[Ir(bpy\text{-}C^{3},N')(bpy\text{-}N,N')Cl]_2Cl_2$ in DMSO-d_6 (vs. TMS)

Position	^{1}H (δ) PPM	^{13}C (δ) PPM
A_2	-	155.62
A_3	-	144.70
A_4	8.50	142.32
A_5	7.26	124.50
A_6	8.37	143.65
B_2	-	162.97
B_3	8.18	120.77
B_4	7.76	138.68
B_5	7.12	124.86
B_6	7.54	150.15
C_2	-	165.97
C_3	8.66	124.35
C_4	7.95	138.35
C_5	7.34	127.44
C_6	7.78	153.06
D_2	-	152.90
D_3	8.83	123.92
D_4	8.41	139.50
D_5	8.10	127.89
D_6	9.67	148.51

FIGURE 5.3.1:

Structural representation of $[Ir(bpy\text{-}C^3,N')(bpy\text{-}N,N')Cl]_2Cl_2$ with the four spin system of the bpy ligands labeled.

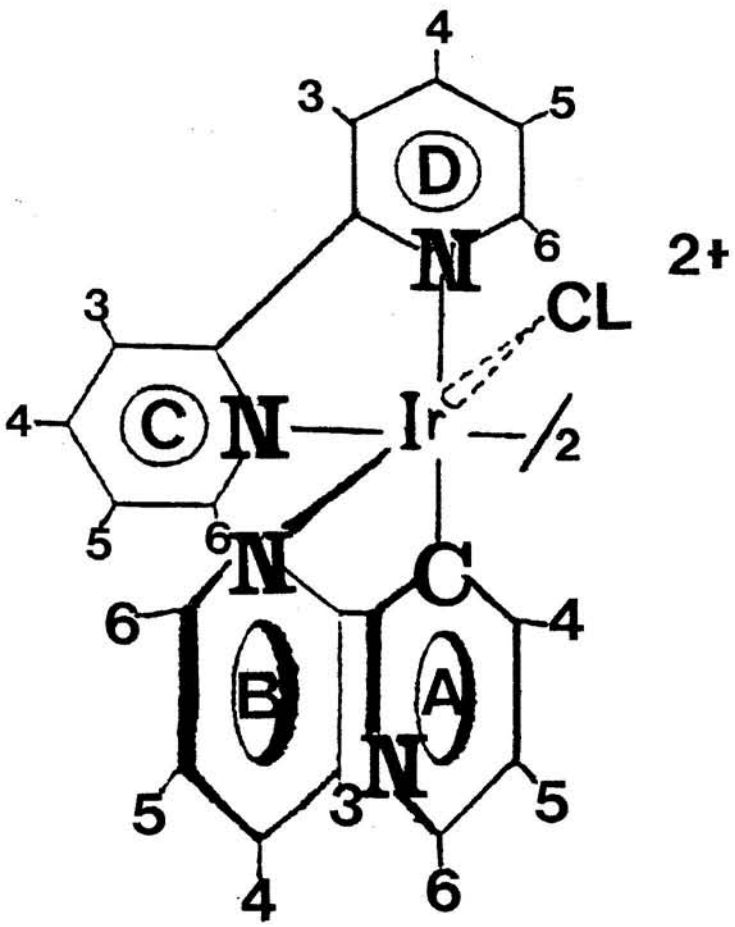

FIGURE 5.3.2:

^1H NMR spectra for $[Ir(bpy\text{-}C^3,N')(bpy\text{-}N,N')Cl]_2Cl_2$ in DMSO-d_6.

a) ^1H NMR spectrum (10.0 - 0.0 PPM)
b) ^1H NMR spectrum (10.0 - 7.0 PPM)

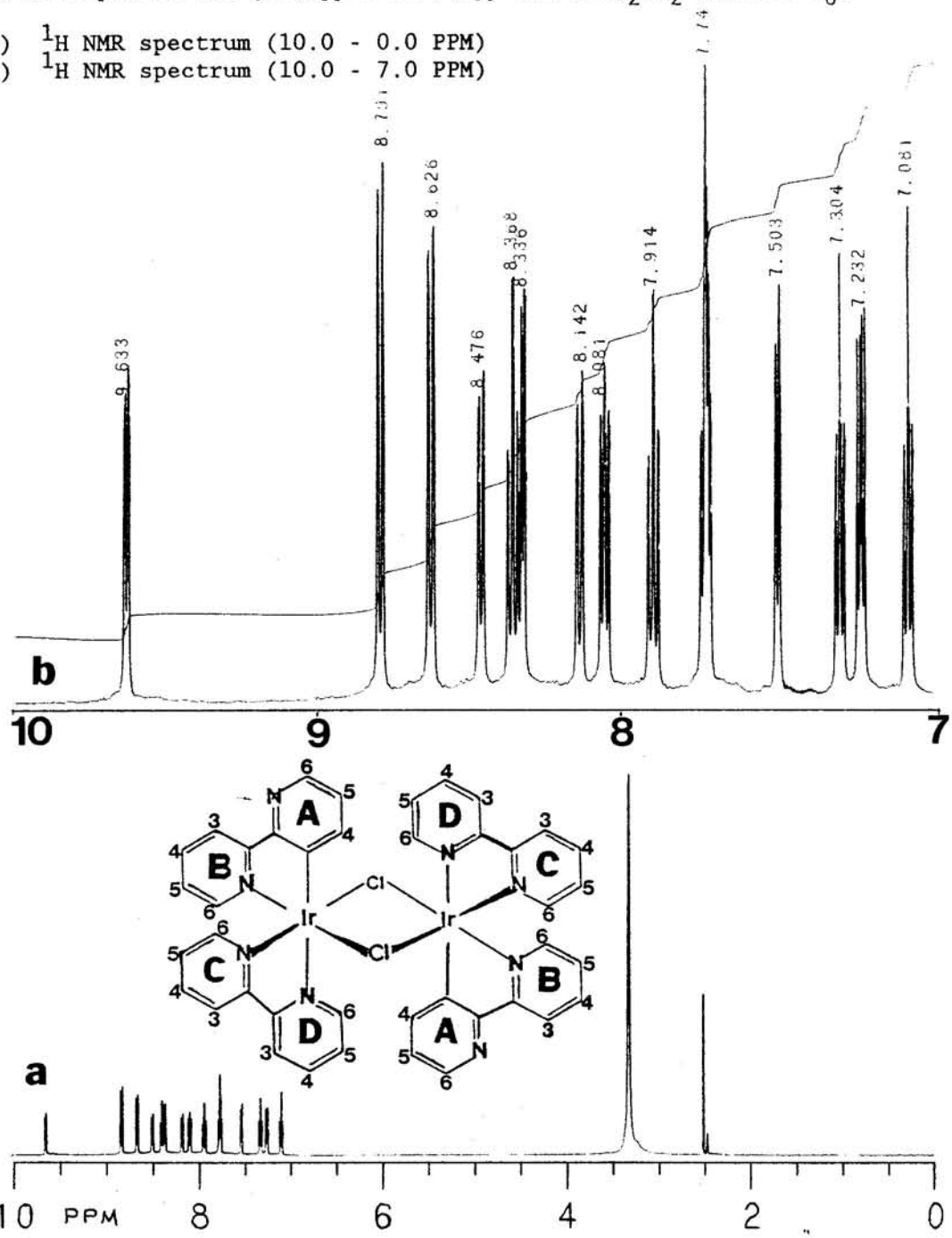

FIGURE 5.3.3:

^{13}C NMR and APT spectra for $[Ir(bpy\text{-}C^3,N')(bpy\text{-}N,N')Cl]_2Cl_2$ in DMSO-d_6.

a) ^{13}C NMR spectrum (200 - 20 PPM)
b) ^{13}C NMR spectrum (170 - 120 PPM)
c) APT spectrum (170 - 120 PPM)

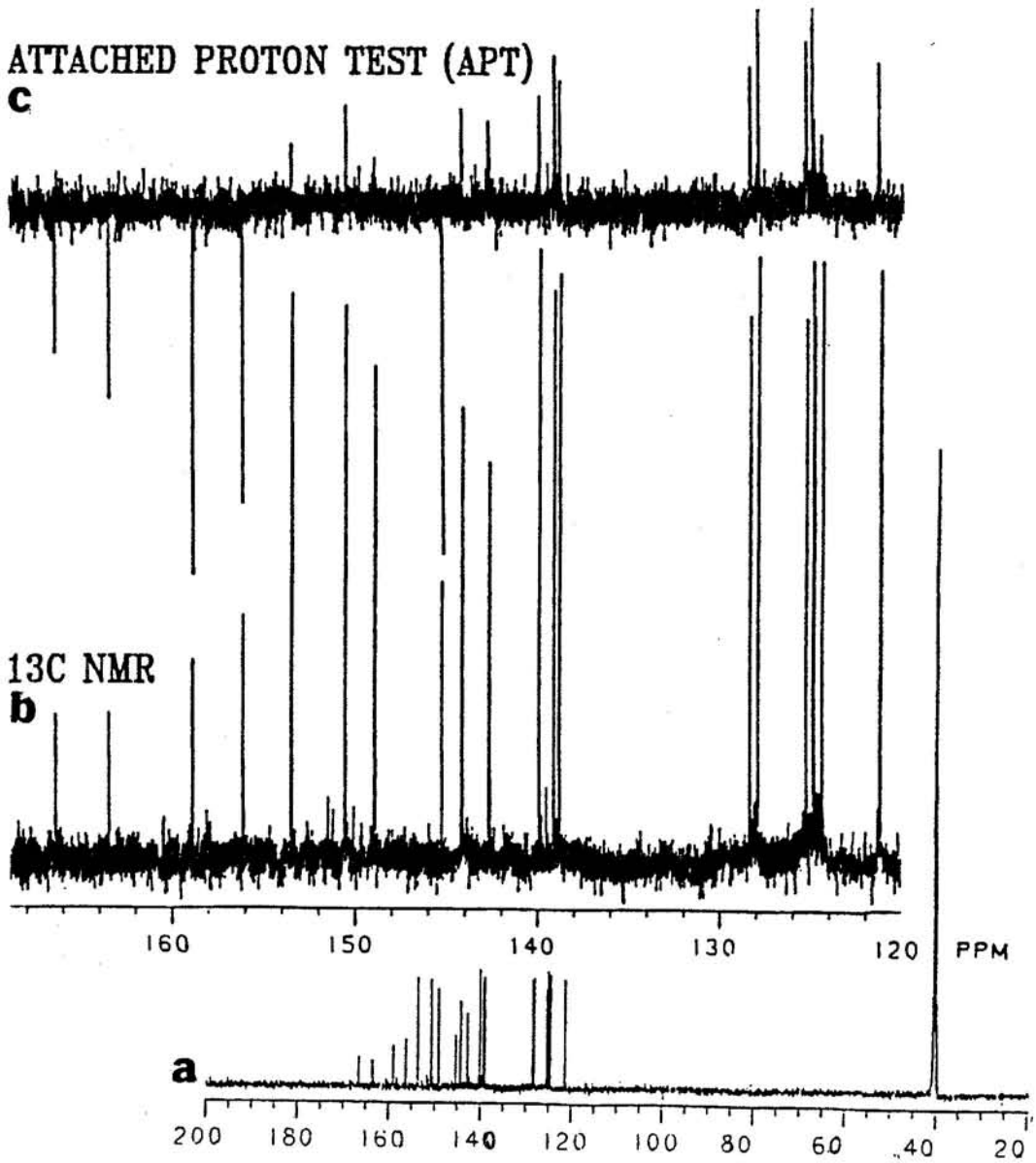

FIGURE 5.3.4

^{1}H COSY contour plots for I in DMSO-d_6.

a) COSY spectrum with contour level set to 5.
b) COSY spectrum with contour level set to 13.

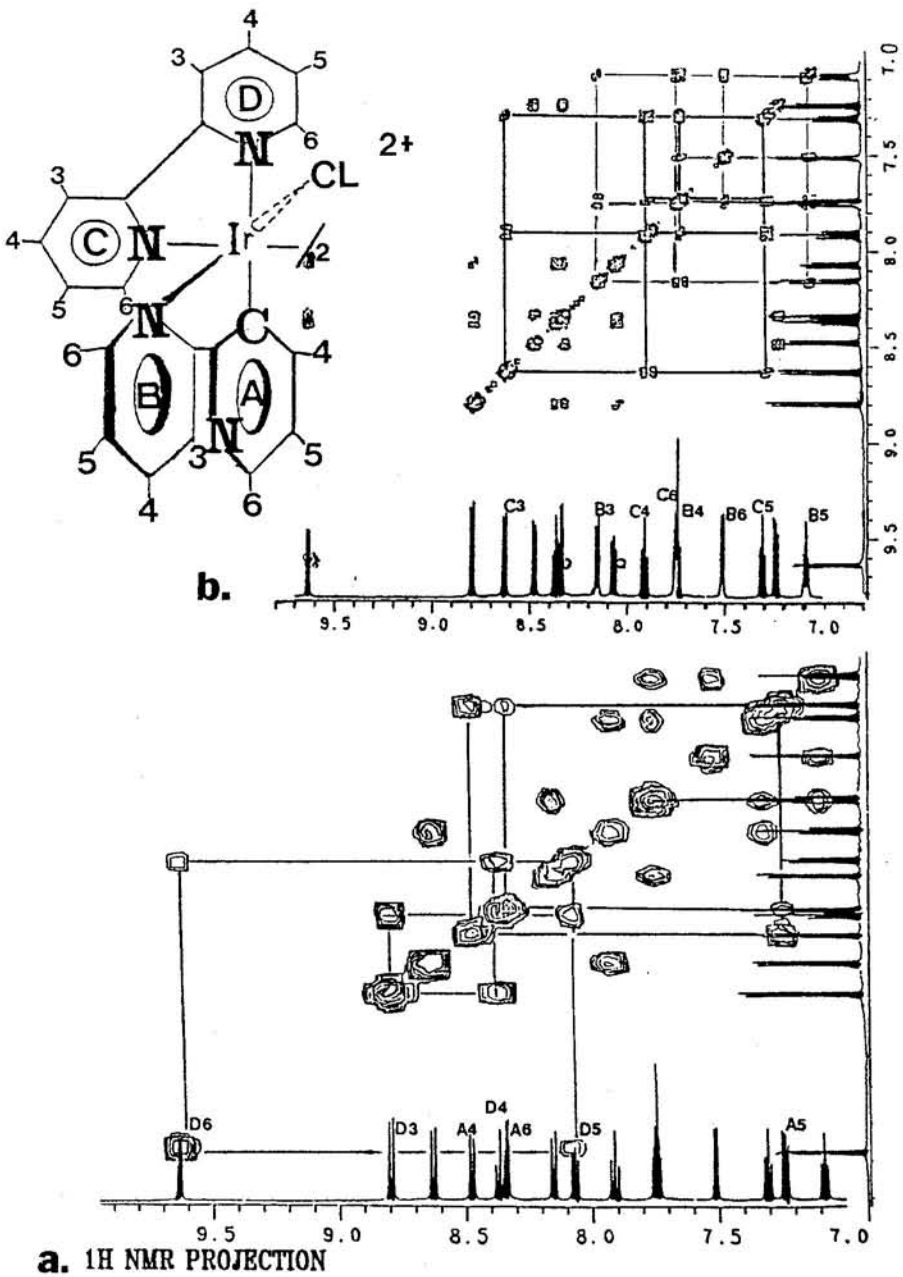

FIGURE 5.3.5:

^{1}H NOE difference spectra for [Ir(bpy-C^3,N')(bpy-N,N')Cl]$_2Cl_2$ in DMSO-d_6.

Saturated resonances are indicated by curly brackets {}.

a) nOe, Saturate {A_4}.
b) nOe, Saturate {A_6}.
c) nOe, Saturate {B_3}.
d) nOe, Saturate {C_3}.
e) nOe, Saturate {D_6}.

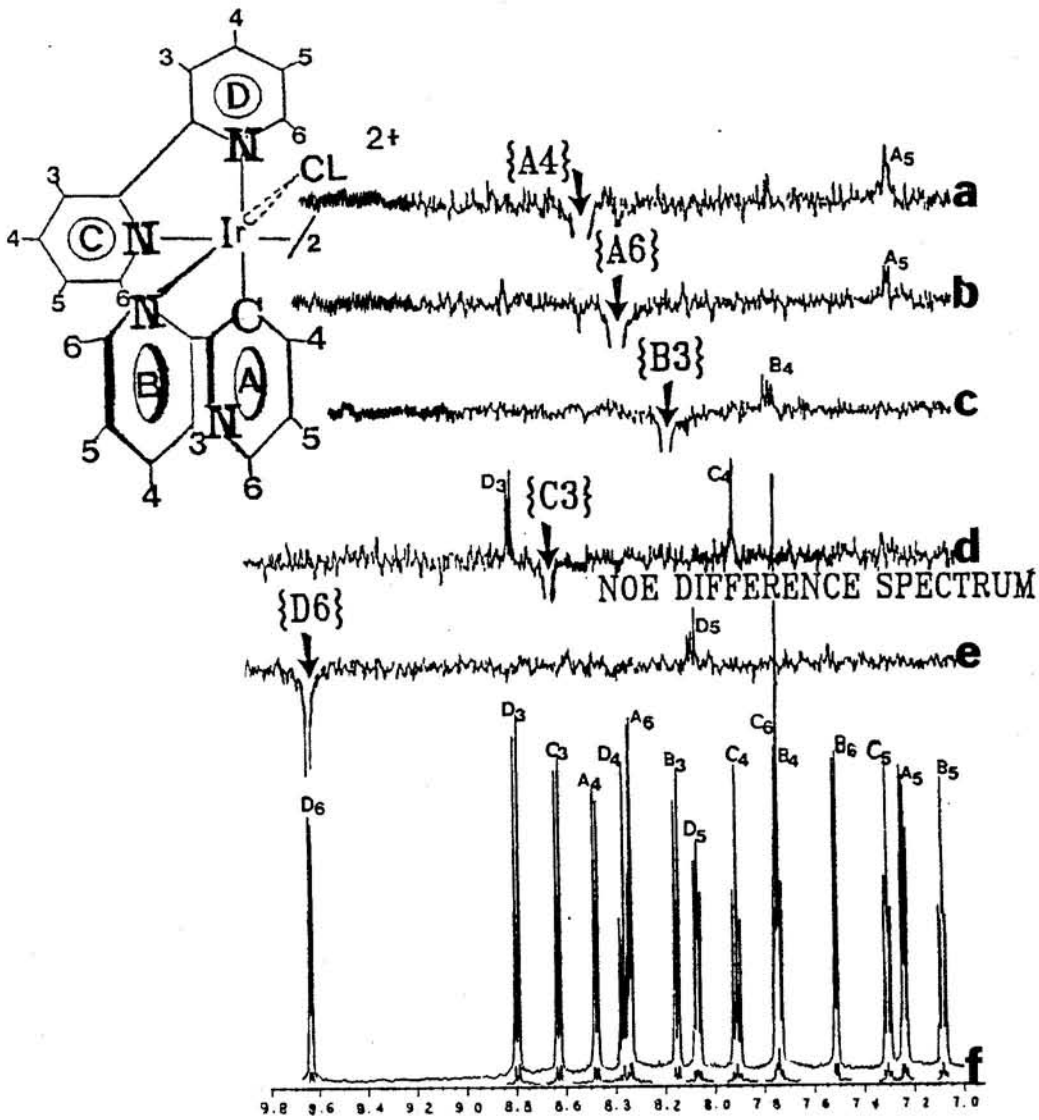

FIGURE 5.3.6:

^{1}H-^{13}C Heteronuclear correlation spectroscopy (CSCM) for $[Ir(bpy\text{-}C^{3},N')(bpy\text{-}N,N')Cl]_2Cl_2$ in DMSO-d_6.

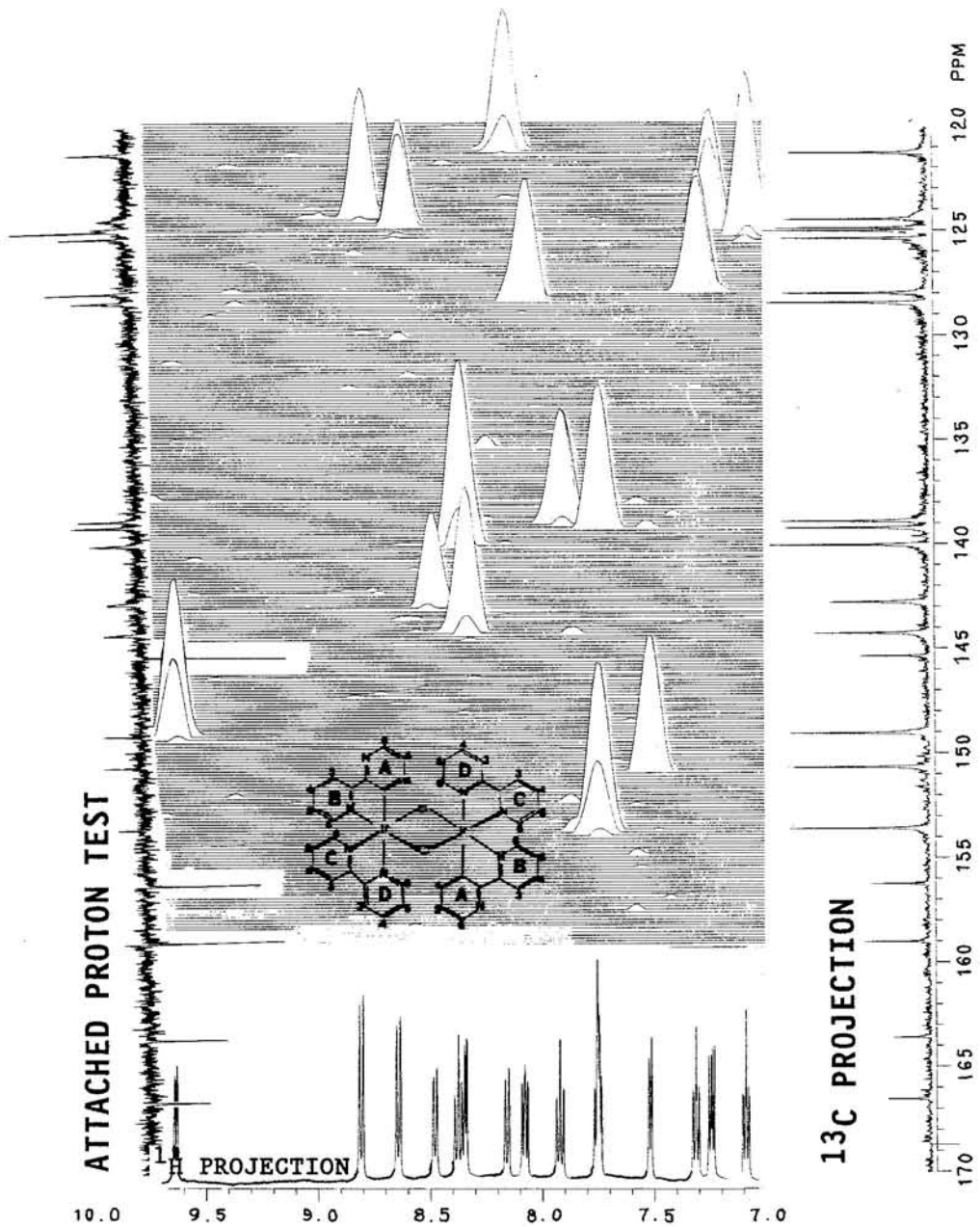

4. Absorption and Emission; acid / base dependence.

Absorption spectra were obtained in EtOH-MeOH (1:1 v/v), EtOH-MeOH-HCl (0.1 M HCl), EtOH-MeOH-NaOH (0.1 M NaOH), (aq)EtOH and neat DMF solvents. Extinction coefficients were determined in EtOH-MeOH, DMF and (aq)EtOH, see Table 5.4 and Figure 5.4.1a-c. It is uncertain if Beer's law was obeyed over the concentration range (10^{-4} - 10^{-6} M) because of the limited solubility of I in some solvents.

The absorption band maxima and extinction coefficients show large solvent dependence as illustrated by the overlay of absorption spectra in Figure 5.4.1. In the UV region, the spectrum taken in EtOH-MeOH, spectrum **a** shows band maxima at 222 and 280 nm, in (aq)EtOH, spectrum **c**, the band maxima occur at 208 and 270 nm, and in neat DMF, spectrum **b**, only the band maximum 284 nm is observed. In DMF, the solvent window prevents observation of any bands above 260 nm. The absorption spectra between 300 and 340 nm show a shoulder at 298 nm in only EtOH-MeOH and (aq)EtOH. In the visible region, spectrum **a** shows band maxima at 340, 364, 416, 456 and 484 nm; spectrum **b** shows these bands slightly red-shifted to 346, 370, 392, 422 and 484 nm; and finally spectrum **c** shows a structured profile with band maxima blue-shifted to 342, 356 and 452 nm.

Acid/base absorption studies for I provide good evidence for an ortho-metalated species. Figure 5.4.2**a-c** shows the acid/base normalized absorption spectra measured in EtOH-MeOH-HCl (0.1 M), EtOH-MeOH-NaOH (0.1 M) and EtOH-MeOH, respectively. There are four regions of interest in these spectra: (**i**) 210 - 240 nm, (**ii**) 280 -

320 nm, (**iii**) 340 - 380 nm and (**iv**) 420 - 480 nm. The absorption profiles in region **i** are similar under neutral and acidic conditions showing a band maximum at 212 nm. In region **ii**, the spectra Figure 5.4.2**b** and **c** both have a band maximum at 280 nm and spectrum 5.4.2a shows a band maximum at 290 nm. In regions **ii** and **iii**, the absorption profiles under neutral and basic conditions shadow each other with band maxima at 340, 364, and 416, and 460 nm. The corresponding spectrum taken in acidic conditions shows less structured absorption profile with band maxima at 356 and 414 nm.

In a detailed acid/base study of **I**, absorption measurements were recorded between pH 1 and pH 10 using 0.1 M HCl and 0.1 M NaOH in EtOH-MeOH, see Figure 5.4.3, spectra **a-g**. Spectrum **a** was obtained in EtOH-MeOH at pH 6; spectra **b** and **c** were measured after acidification of this solution by HCl to pH 2 and 1 respectively; Spectra **d** and **e** were measured after raising the pH with NaOH to 6 and 10, respectively; and spectra **f** and **g** were obtained by acidification of this sample to pH 6 and 1 respectively. Changes in the absorption profile are most apparent in regions **i** and **ii**; most band maxima changes occurring between 230 and 300 nm. The absorption feature at 348 nm for example, is invariant through the pH progression. Band maxima changes that appear at high energy, $\lambda <$ 208 nm, are ignored because they lie near the 220 nm band edge of EtOH-MeOH solvent. Spectral changes in Figure 5.4.3 are similar to changes in Figure 5.4.2 in which neutral and basic conditions show

comparable band maxima at 280 nm while in acidic conditions, the band maxima are red-shifted to 290 nm.

The changes in the absorption band maxima as a result of acid/base conditions suggest an equilibrium between protonated and nonprotonated species.[11,12] Under neutral conditions, the equilibrium favors the nonprotonated species. At pH 2 the protonated species starts to dominate the equilibrium as suggested by the spectral changes in the absorption spectrum. The red shift of the MLCT bands under acidic conditions is consistent with protonation of the external nitrogen of the ortho-metalating bpy ligand. A cationic Hbpy-C^3,N' would favor the MLCT transition (a protonated pyridyl ring would easily accommodate reduction) as shown by the red shift of these transitions. Under neutral or basic conditions again, the equilibrium is forced back to the non-protonated species. The blue shift of the absorption maxima is characteristic of the nonprotonated species. In short, the bathochromic and hypsochromic shifts of the absorption maxima under acid/base conditions may be used as a probe to characterize the equilibrium between the protonated and nonprotonated species of $[Ir(bpy\text{-}C^3,N')(bpy\text{-}N,N')Cl]_2Cl_2$.

Room temperature and 77 K glass matrices emission and excitation spectra were measured in EtOH-MeOH neutral, acidic and basic conditions. The MLCT assignments for the low energy emission bands, $\lambda > 340$ nm is supported by the structureless emission profile at room temperature but structured profile at 77 K. Furthermore,

100 ns ambient temperature lifetimes and 10 μs rigid glass (77 K) lifetimes are also supportive of charge transfer transitions (lifetime results will be discussed in more detail later).

The luminescence spectra were measured in the following solvents: EtOH-MeOH, Figures 5.4.4; EtOH-MeOH-HCl , Figure 5.4.5; EtOH-MeOH- NaOH, Figure 5.4.6; (aq)EtOH, Figure 5.4.7; and DMF, Figure 5.4.8. There are three types of spectra representative of the luminescence data: (a) the three dimensional excitation/ emission/intensity spectra measured at room temperature, (b) the excitation and emission spectra measured at room temperature and (c) the excitation and emission spectra measured at 77 K. The excitation range for the EEI spectra generally covered 360 - 404 nm; for the R.T. and 77 K measurements, the excitation ranged from 300 - 520 nm; and finally, the emission for the EEI, R.T., and 77 K emission spectra were usually monitored between 430 - 700 nm. The band maxima for each spectrum are summarized in Table 5.5.

The similarities between the emission spectra taken at room temperature in EtOH-MeOH neutral and basic conditions, Figure 5.4.4b and 5.4.6b respectively are in good agreement with the absorption data which suggest that under neutral conditions the equilibrium favors the nonprotonated form; in acidic conditions, Figure 5.4.5b, the band maximum occurs at 601 nm. At 77 K however, the emission band maxima at 534 and 563 nm for the EtOH-MeOH neutral conditions, Figure 5.4.4c, resembles the emission band maxima at 534 and 558 nm

for the acidic EtOH-MeOH (HCl) emission spectrum, Figure 5.4.5c. This suggests that at 77 K glass matrices, the equilibrium favors the protonated species. The emission band maximum in basic conditions, Figure 5.4.6c, remains at 589 nm as observed at room temperature, although another band does develop at 670 nm.

The room temperature emission spectrum in (aq)EtOH, Figure 5.4.7, resembles the emission spectrum obtained in EtOH-MeOH(HCl), both spectra showing band maxima near 601 nm. In neat DMF, Figure 5.4.8, the room temperature emission spectrum resembles that of the basic emission spectrum, showing band maxima near 590 nm. However at 77 K, these trends reverse; the emission spectrum in DMF is similar to that taken in EtOH-MeOH(HCl) with band maxima near 530 and 560 nm while the emission spectra taken in (aq) EtOH, resembles that of the EtOH-MeOH(NaOH) emission spectrum showing band maxima at 580 and 670 nm and 560 nm. The trend from these results suggests that aqueous conditions favor the protonated species at room temperature but the nonprotonated species at 77 K. In contrast, organic solvents favor the nonprotonated species at room temperature conditions but resemble the protonated species at 77 K.

The lifetimes for I in the solvents described above are also tabulated in Table 5.5. Ambient temperature lifetimes ranged from 74 ns, taken in EtOH-MeOH-HCl, to 220 ns, taken in neat DMF. At 77 K, single exponential fits give lifetimes ranging from 2.4 μs ((aq) EtOH), to 8.6 μs (neat DMF). Double exponential fits give lifetimes from .8/6.0 μs to 5.5/15 μs, Table 5.4.5. The time-resolved-

emission spectra taken in EtOH-MeOH at 77 K, Figure 5.4.9, taken with delay times at 100 ns and 25 μs respectively were inconclusive because of the poor resolution at 25 μs delay.

Quantum yields in (aq)EtOH neutral, acidic (.1M HCl), and basic (0.1M NaOH) conditions were measured as 0.104, 0.0399 and 0.0107 respectively, Table 5.5.

In summary, acid/base luminescence properties shown for this iridium bpy complex, I, are consistent with species possessing a basic nitrogen site (as in $[Ir(bpy\text{-}C^3,N)(bpy\text{-}N,N')_2]^{2+}$). The proposed structure is consistent with this property.

TABLE 5.4

Extinction Coefficient data for $[Ir(bpy\text{-}C^3,N')(bpy\text{-}N,N')Cl]_2Cl_2$

Solvent	Absorption Features (nm)	ϵ ($M^{-1}cm^{-1}*10^{-4}$)
EtOH-MeOH	210(sh)	6.54
	222	9.15
	280	9.52
	298(sh)	7.15
	340	2.81
	364	2.52
	416	0.86
	456	0.56
	484	0.37
EtOH (aq)	208	4.97
	220(sh)	4.49
	270	4.53
	298(sh)	3.17
	316(sh)	1.97
	342	1.24
	356	1.16
	452	0.17
DMF	266(sh)	5.54
	284	7.66
	316(sh)	3.05
	346	2.03
	370	1.74
	392	1.17
	422	0.57
	484	0.33

TABLE 5.5

Emission, Lifetimes and Quantum Yields for $[Ir(bpy\text{-}C^3,N')(bpy\text{-}N,N')Cl]_2Cl_2$

EtOH-MeOH	EtOH-MeOH-HCl	EtOH-MeOH-NaOH	(aq)EtOH	DMF
{Room Temperature}				
Emission (nm):				
592(380)[a]	601(380)	589(380)	602(380)	592(380)
Excitation (nm):				
412(580)[b]	406(590)	367(580)	368(580)	395(590)
467	424	378	398	421
	466	398	415	469
		457	463	
Lifetimes, τ (ns):				
118(575)[b]	74.0(600)	110.4(600)	128.0(600)	220.2(600)
{Low Temperature}				
Emission (nm):				
534(380)[a]	534(380)	589(380)	578(380)	525(380)
563	558	730	678	557(sh)
Excitation (nm):				
363(530)[b]	375(540)	390(540)	400(570)	376(520)
389	391	462	426	405
418	423		464	453
465	459			468
Lifetimes, τ (μs):				
6.5(540)[b]	5.8(540)	5.4(540)	2.4(570)	8.6(540)
12.0/4.1[c]	7.8/4.2	10.9/4.0	6.0/.78	14.7/5.5
Quantum Yield, Φ:				
0.104	0.0399	0.017		

a) Excitation set to this wavelength
b) Emission monitored at this wavelength
c) Double exponential fit

FIGURE 5.4.1:

Absorption spectra for $[Ir(bpy\text{-}C^3,N')(bpy\text{-}N,N')Cl]_2Cl_2$
(a) EtOH:MeOH (1:1 v/v) (b) neat DMF (c) (Aq) EtOH

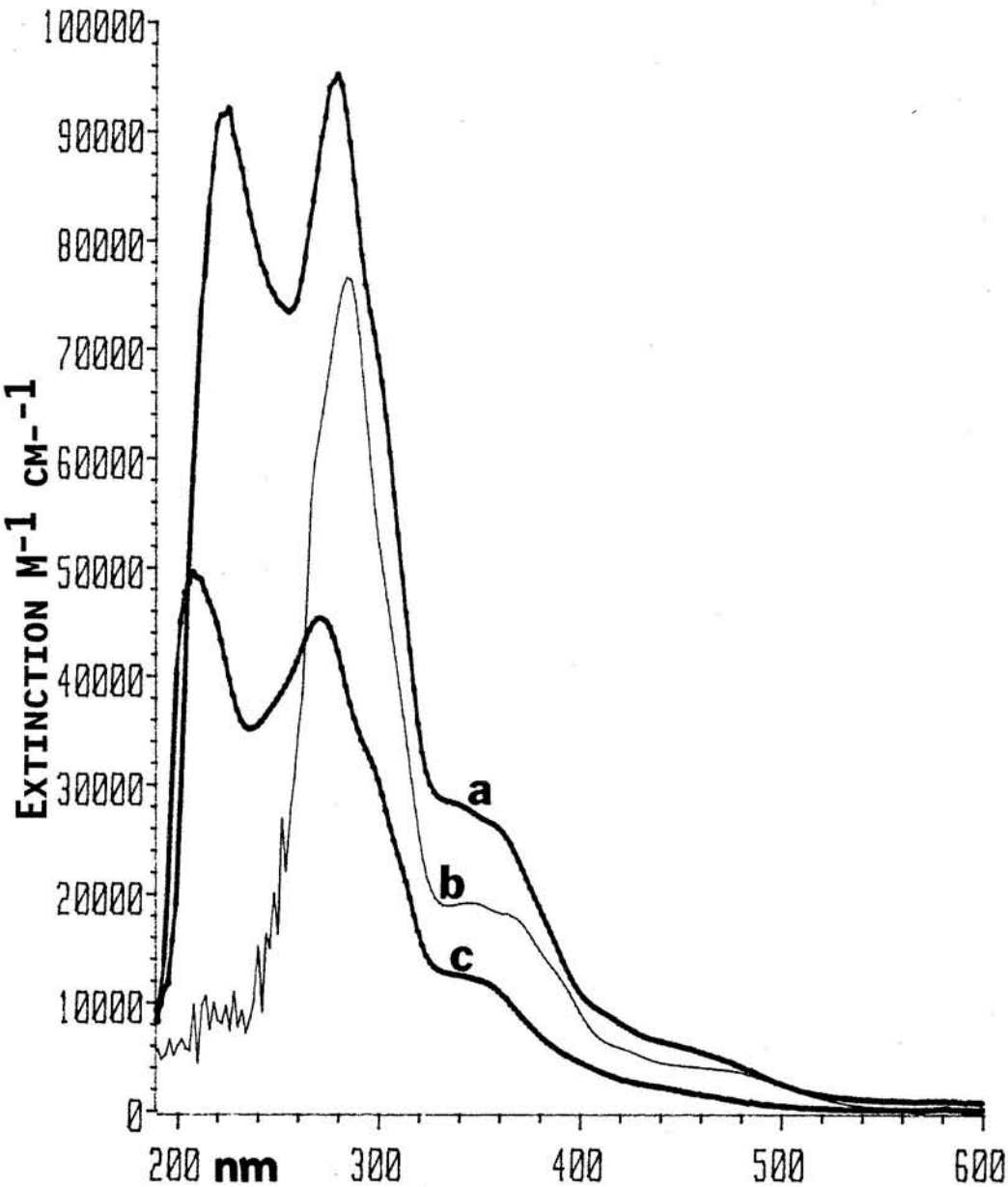

FIGURE 5.4.2:

Absorption spectra for $[Ir(bpy\text{-}C^3,N')(bpy\text{-}N,N')Cl]_2Cl_2$
(a)EtOH:MeOH .1 M HCl (b) EtOH:MeOH .1 M NaOH (c) EtOH:MeOH

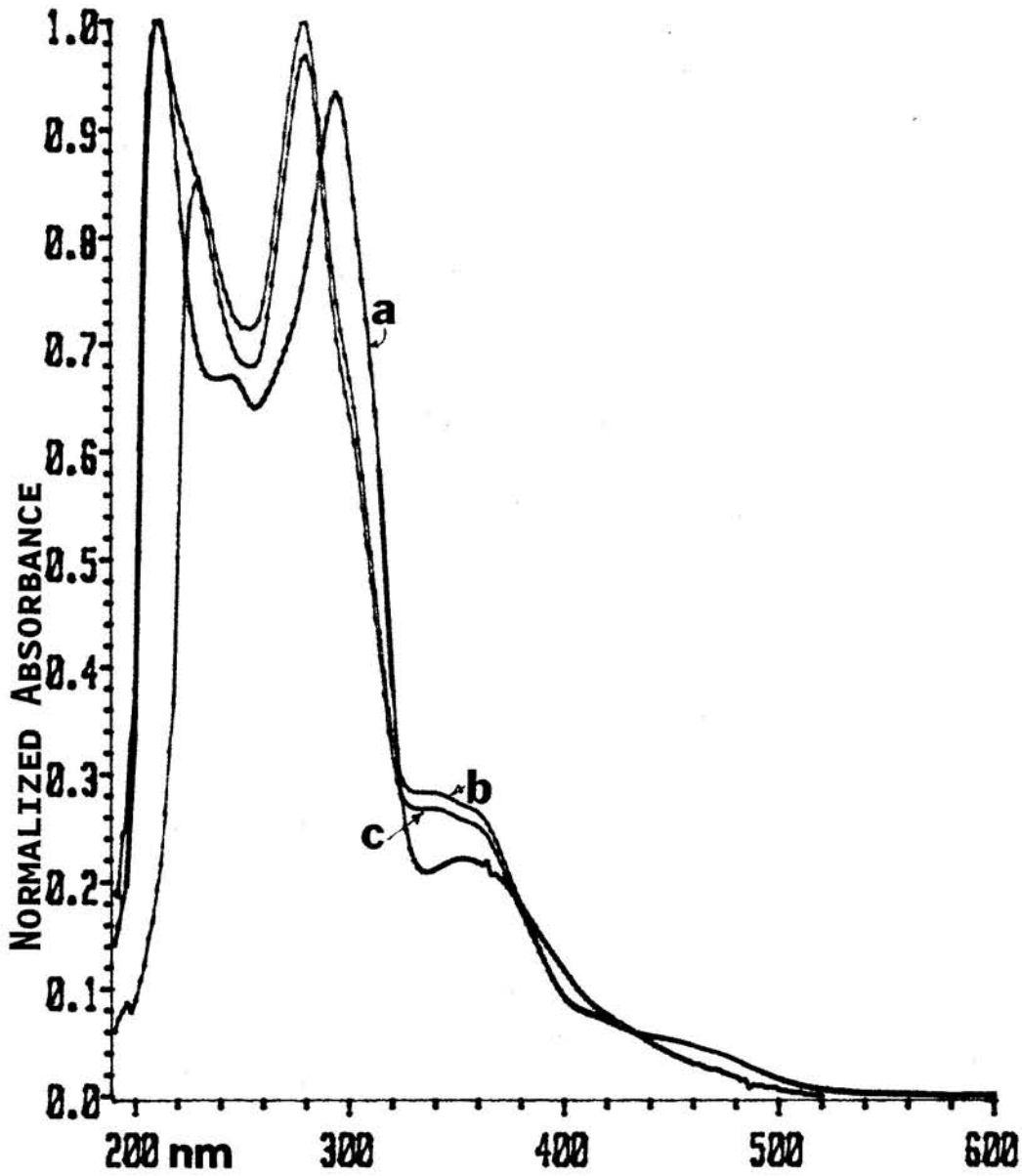

FIGURE 5.4.3:

Absorption spectra for $[Ir(bpy\text{-}C^3,N')(bpy\text{-}N,N')Cl]_2Cl_2$ as a function of pH. (a) pH 6; (b) pH 2; (c) pH 1; (d) pH 6; (e) pH 10; (f) pH 6; (g)pH 1.

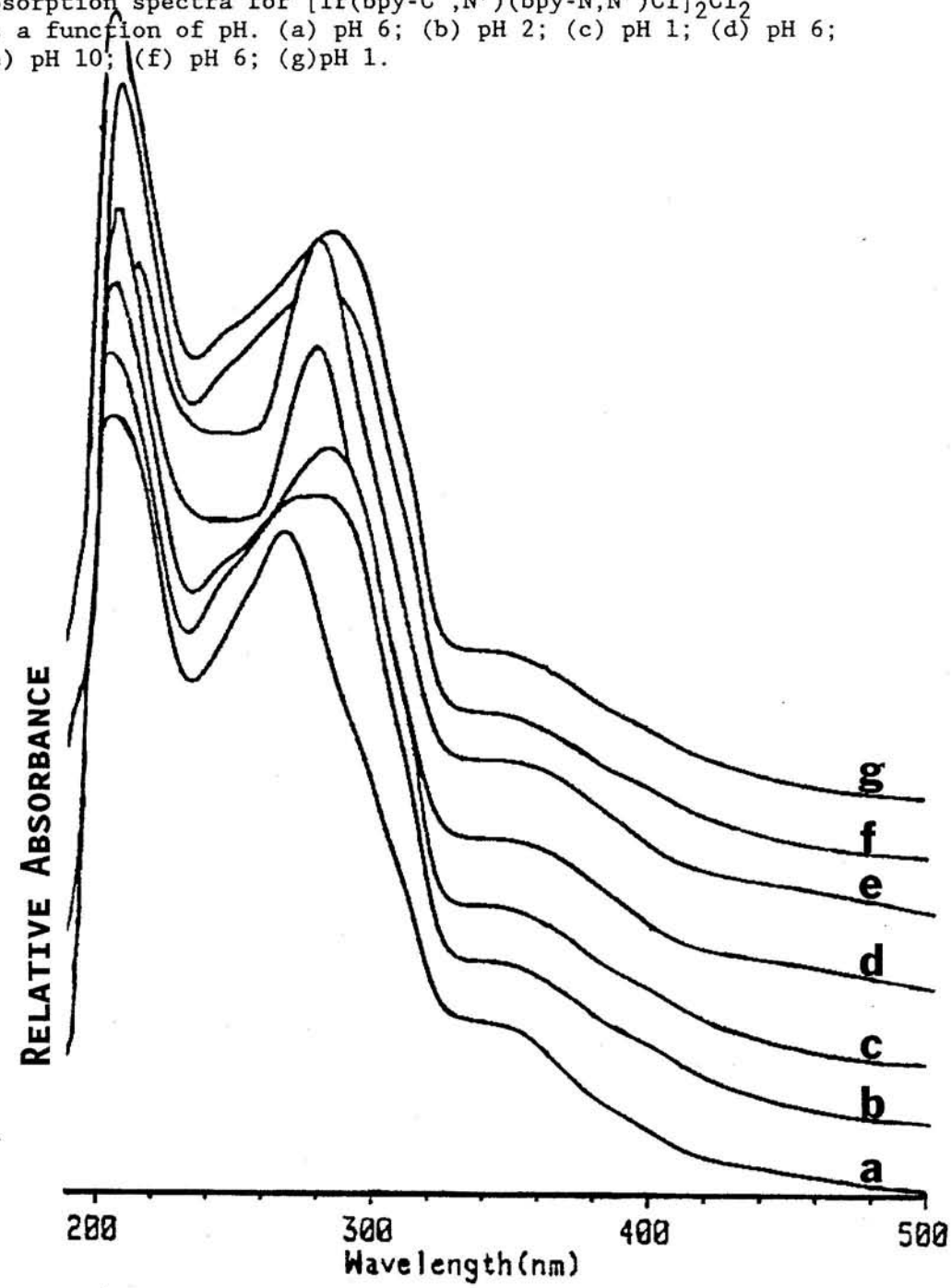

FIGURE 5.4.4:

Emission spectra for $[Ir(bpy\text{-}C^3,N')(bpy\text{-}N,N')Cl]_2Cl_2$ in EtOH:MeOH

(a) EEI stack plots, λexcit = 364-404 nm, λemis = 430-700 nm
(b) R.T. ; ————emission, --------excitation,
(c) 77 K ; ————emission, --------excitation.

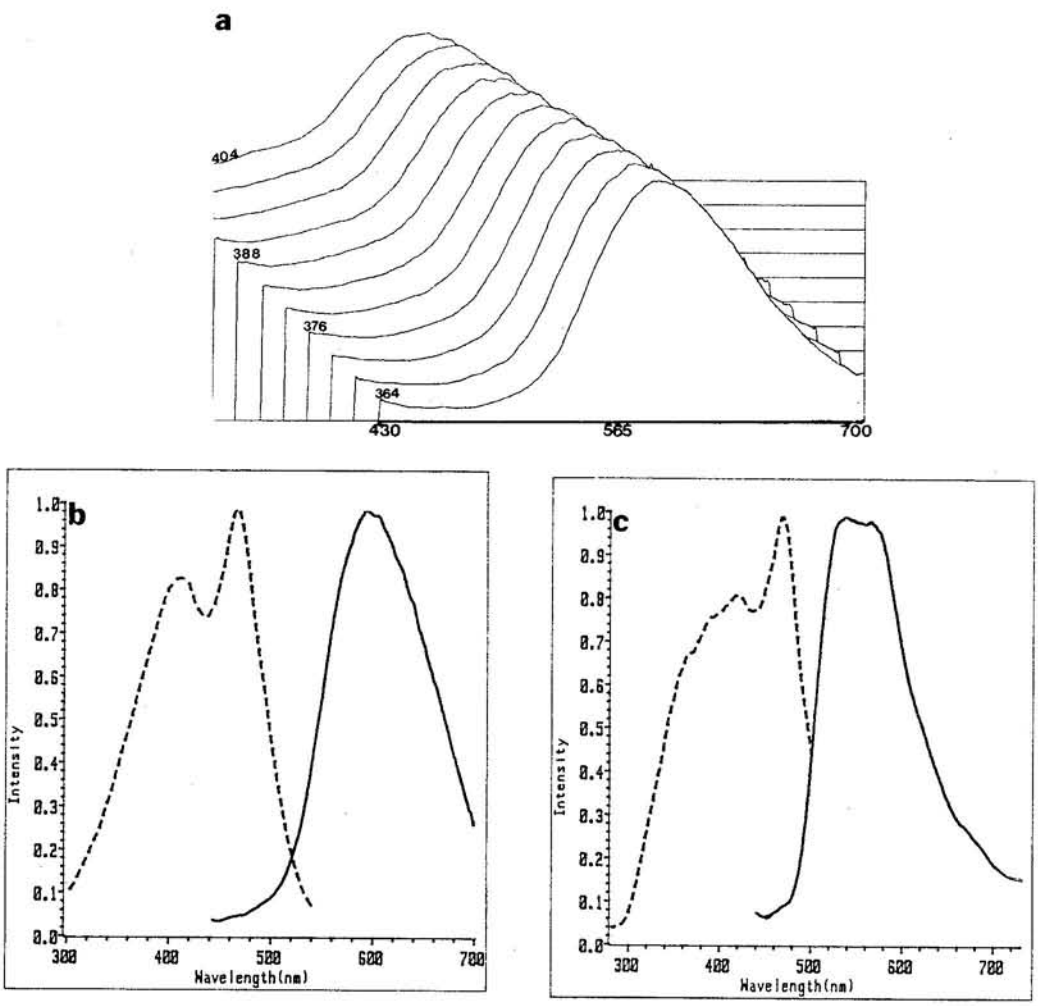

FIGURE 5.4.5:

Emission spectra for $[Ir(bpy\text{-}C^3,N')(bpy\text{-}N,N')Cl]_2Cl_2$ in EtOH:MeOH (0.1M HCl)

(a) EEI stack plots, λexcit = 364-404 nm, λemis = 430-700 nm
(b) R.T. ; ————emission, --------excitation,
(c) 77 K ; ————emission, --------excitation.

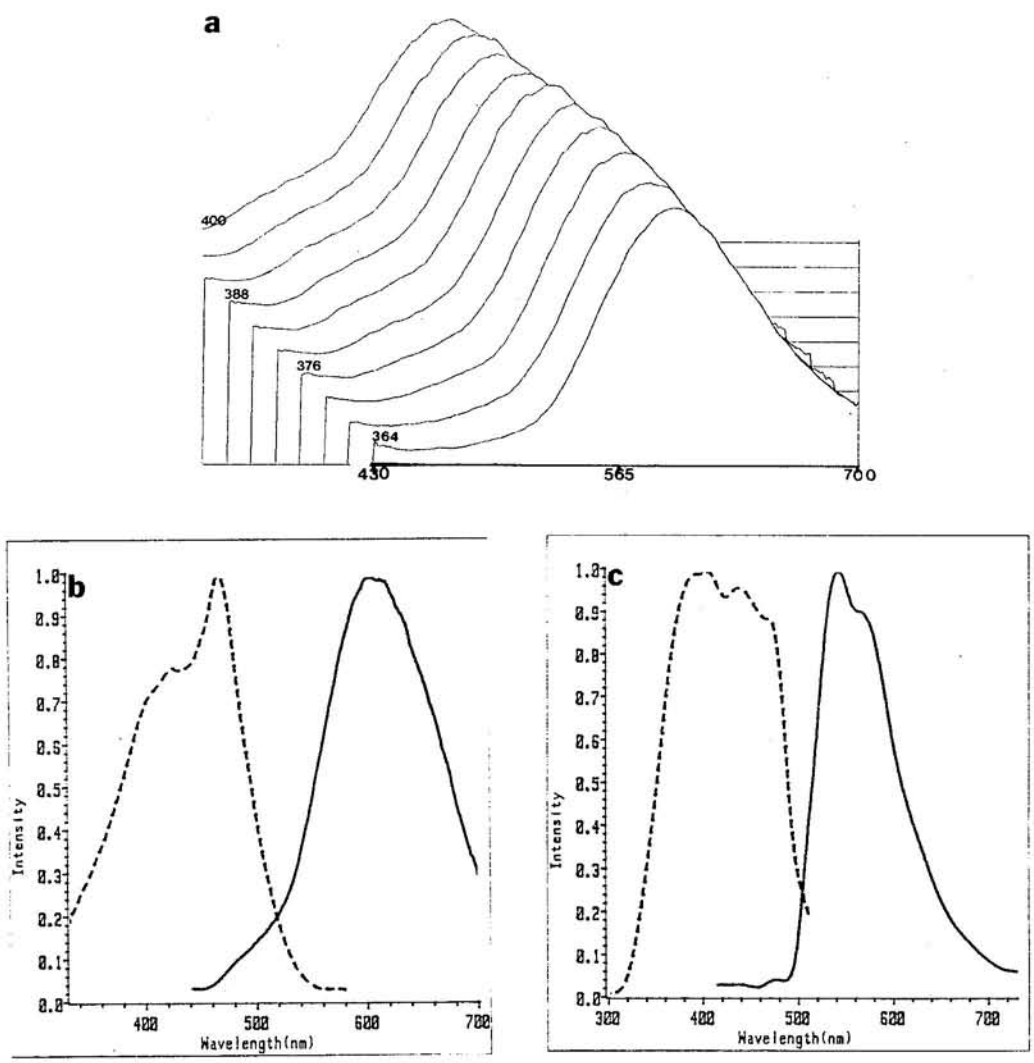

FIGURE 5.4.6:

Emission spectra for $[Ir(bpy\text{-}C^3,N')(bpy\text{-}N,N')Cl]_2Cl_2$ in EtOH:MeOH (0.1 M NaOH)

(a) EEI stack plots, λexcit = 364-404 nm, λemis = 430-700 nm
(b) R.T. ; ————emission, --------excitation,
(c) 77 K ; ————emission, --------excitation.

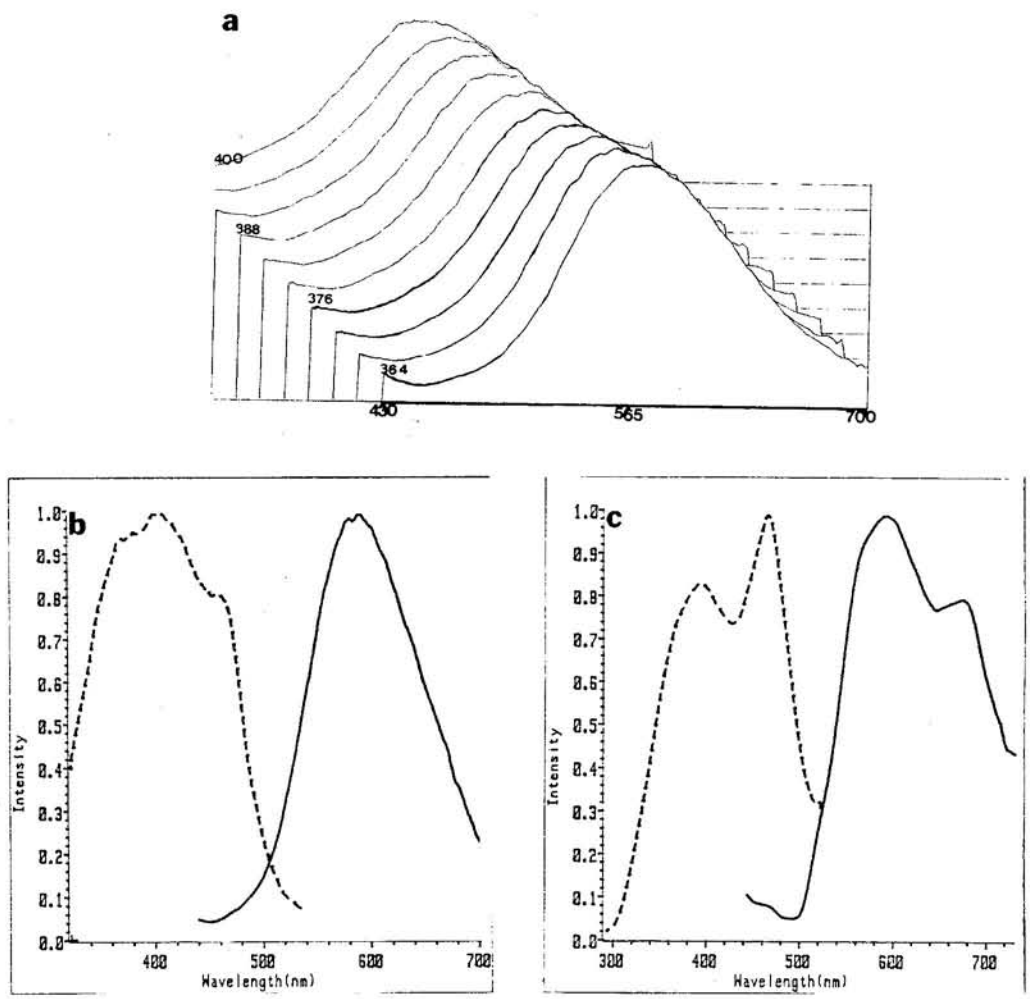

FIGURE 5.4.7:

Emission spectra for $[Ir(bpy\text{-}C^3,N')(bpy\text{-}N,N')Cl]_2Cl_2$ in (aq)EtOH

(a) EEI stack plots, λexcit = 364-404 nm, λemis = 430-700 nm
(b) R.T. ; ————emission, --------excitation,
(c) 77 K ; ————emission, --------excitation.

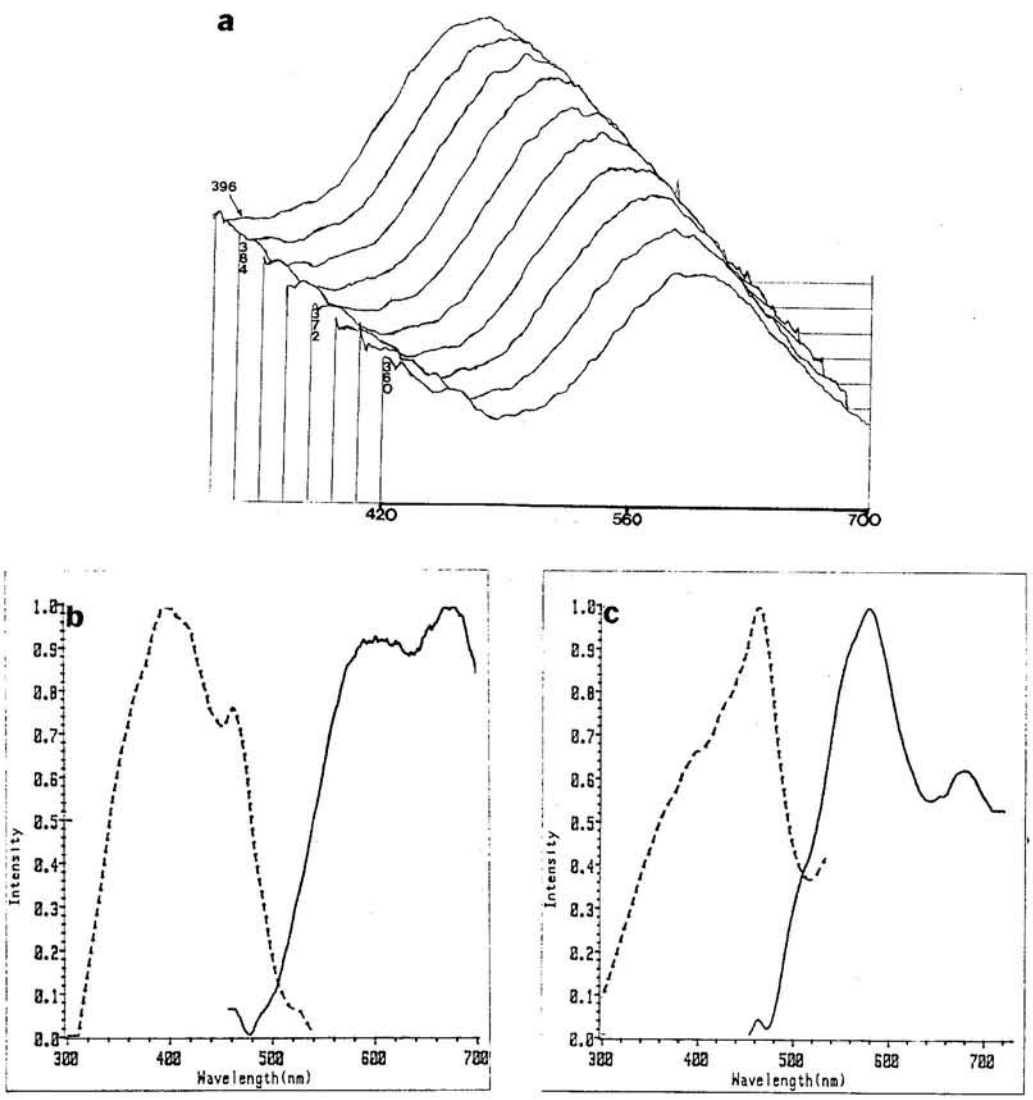

FIGURE 5.4.8:

Emission spectra for $[Ir(bpy\text{-}C^3,N')(bpy\text{-}N,N')Cl]_2Cl_2$ in neat DMF

(a) EEI stack plots, λexcit = 364-404 nm, λemis = 430-700 nm
(b) R.T. ; ————emission, --------excitation,
(c) 77 K ; ————emission, --------excitation.

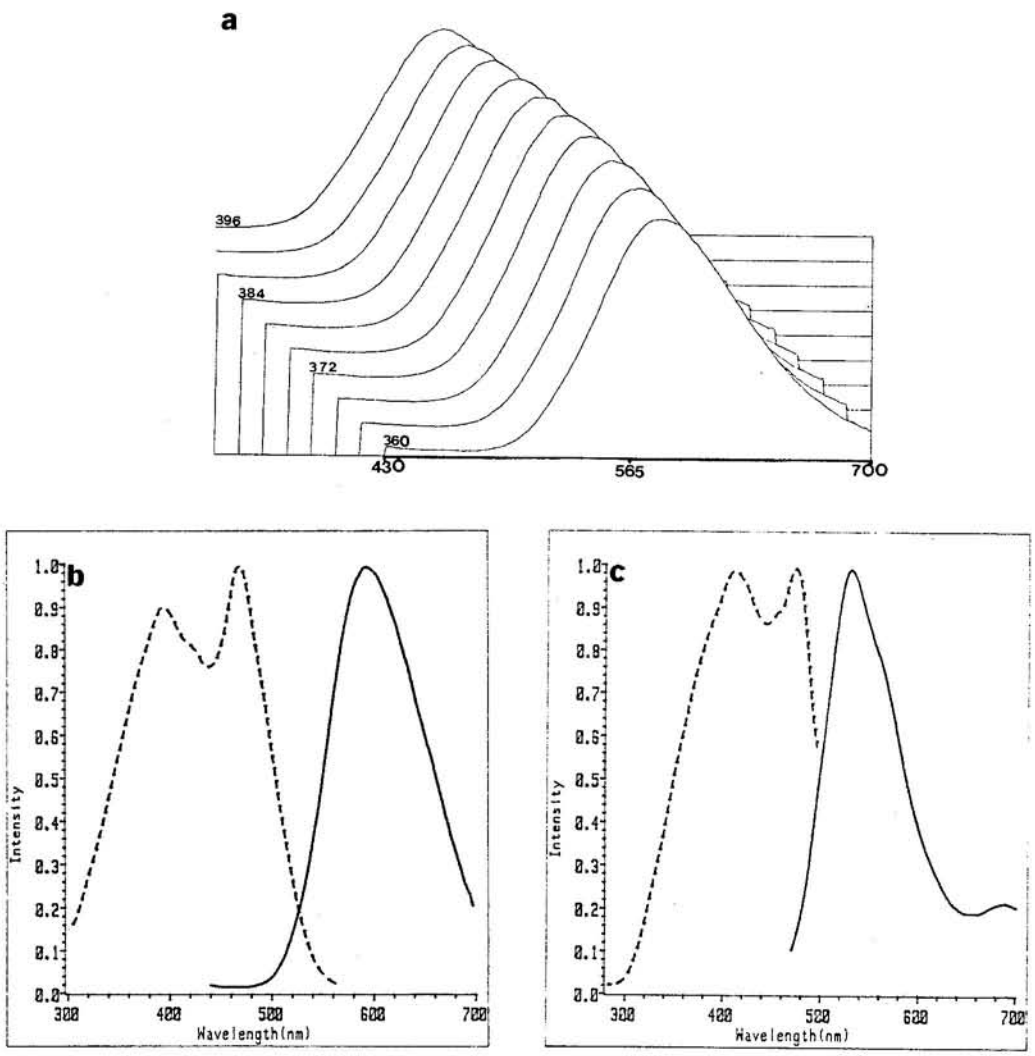

FIGURE 5.4.9:

Time resolved emission spectra for $[Ir(bpy\text{-}C^3,N')(bpy\text{-}N,N')Cl]_2Cl_2$ in EtOH:MeOH at 77 K with (A) 100 ns delay and (B) 25μs delay.

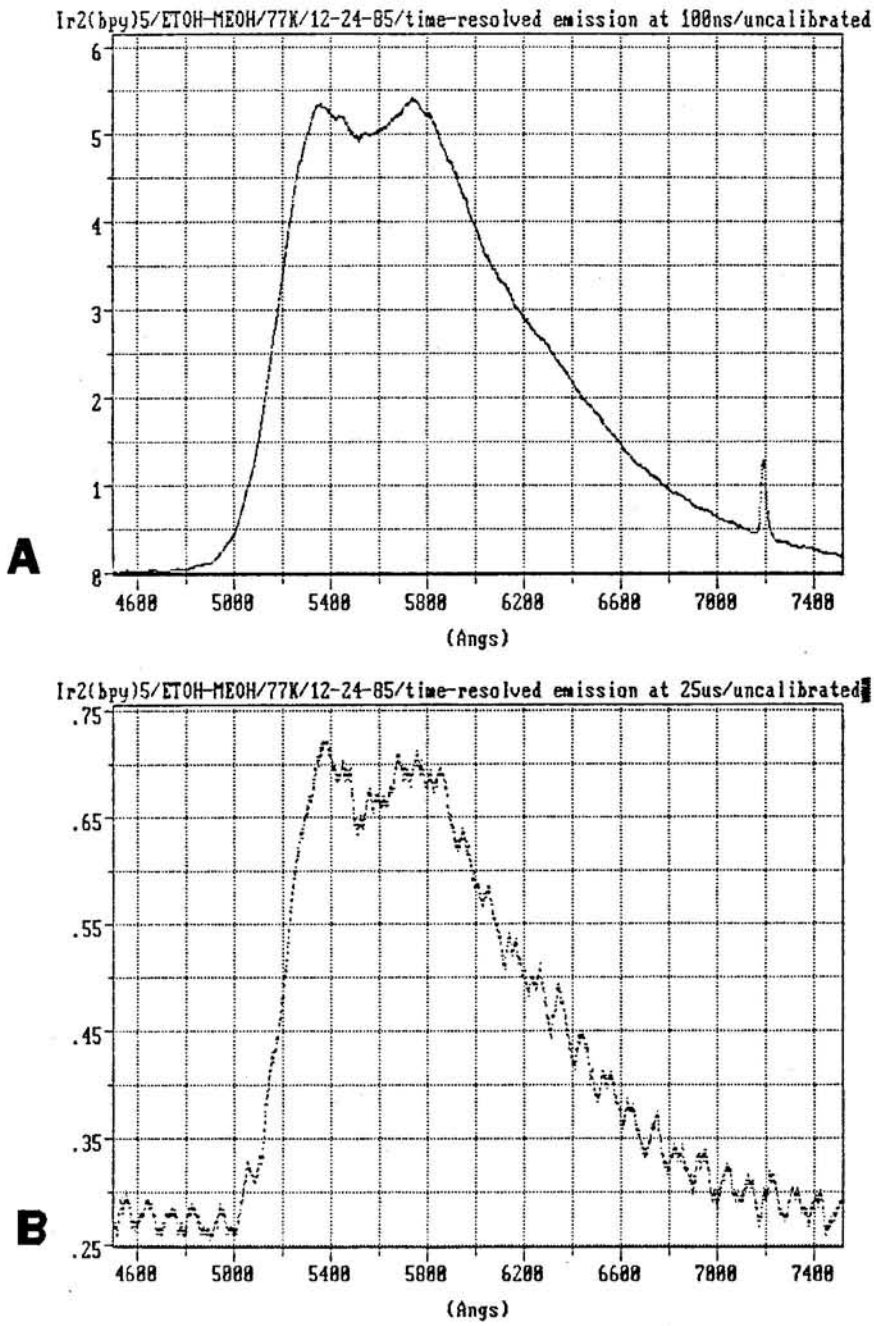

CHAPTER 6

STRUCTURAL CHARACTERIZATION OF BIPYRIDYL IRIDIUM COMPLEXES;
1. EVIDENCE FOR AN ORTHO-METALATED IRIDIUM (III) ION PAIR
2. EVIDENCE FOR AN IRIDIUM (IV) BIPYRIDYL COMPLEX.
3. EVIDENCE FOR A TRANS-IRIDIUM BIPYRIDYL COMPLEX.

All our knowledge has its origins in our perceptions.

-Leonardo da Vinci (1452-1519)

Preparation of $[Ir(bpy\text{-}C^3,N')(bpy\text{-}N,N')Cl]_2Cl_2$ produces many side products of which three have been isolated (II, III and IV). The characterization of these three side products is the subject of this chapter.

The structure (and in some cases, photophysical properties) of these three bipyridyl iridium complexes is consistent with the structural claim for I in Chapter 5. This is especially true of II, which upon recrystallization in DMSO and hot (aq)ETOH, yields yellow crystalline needles of I from solution. Crystallographic analysis indicates that II exists as $[Ir(Hbpy\text{-}C^3,N')(bpy\text{-}N,N')Cl_2]^+$ cation and an $[IrCl_4(bpy)]^-$ anion in an ion pair arrangement. Although there are some ambiguities concerning the $(Hbpy\text{-}C_3,N')$ ortho-metalating bpy in the cationic moiety, an anomalously high electron density about one of the bpy's periphery sites suggests that water may be bound to the protonated nitrogen of the ortho-metalated bipyridine. Furthermore, its ^1H and ^{13}C NMR spectra and its

acid/base luminescence properties, resembles those of I and [Ir(bpy-C^3,N)(bpy-N,N')$_2$]$^{2+}$, strongly suggesting a basic nitrogen site in II. An ortho-metalated bpy in the cation moiety would be consistent with these findings.

Product III is the final material isolated from the preparation of I. Spectroscopic evidence is inconsistent for an [$Ir^{III}bpy_2Cl_2$]$^+$ yet all our evidence suggest a bis bipyridyl dichloro iridium complex! Based on a recent article on several Ir(IV) complexes[39] and the elemental analysis, we propose an Ir(IV), [Ir^{IV}(bpy-N,N')$_2Cl_2$]$^{+2}$ species for product III. Bill Harrison (UCSB) is working on the crystal structure of this material at this writing (see Appendix E).

If Ir(IV) is used to prepare I, a yellow amorphous material is isolated. ^{1}H NMR analysis suggests that this species is the long sought-after trans-Ir(bpy)$_2Cl_2^+$ complex, IV. III is also produced from this synthesis.

Iridium (IV) seems to be a key ingredient in the preparation of novel iridium bipyridyl complexes. So far, four new complexes have been isolated using Ir(IV) as the starting material, but there are still many products (difficult to isolate) left in the reaction mixture. The identification and eventual isolation of these other species (including the complexes described in this chapter), may prove essential in understanding the formation of Ir-C σ-bonds of bpy ligands such as in I and in [Ir(bpy-C^3,N)(bpy-N,N')$_2$]$^{2+}$.

I. SYNTHESES

1. $[Ir(Hbpy\text{-}C^3,N')(bpy\text{-}N,N')Cl_2]^+$ $[IrCl_4(bpy)]^-$; An ion pair (II).

The filtrate collected from the synthesis of I in Chapter 5, is stored for several months at which time orange crystalline material precipitates from solution. The solution is filtered (filtrate is stored for work up of III) and the precipitate washed with hot (aq) EtOH and vacuum dried to yield the product, formulated as an ion pair $[Ir(Hbpy\text{-}C^3,N')(bpy\text{-}N,N')Cl_2]^+$ $[IrCl_4(bpy)]^-$, **II.**

2. $[Ir^{IV}(bpy\text{-}N,N')_2Cl_2]Cl_2$; an Ir(IV), d^5 species? (III)

The filtrate from the above procedure is stored to yield a red, crystalline material. The crystals are collected by filtration, washed with ether and vacuum dried to yield the desired product, formulated as $[Ir^{IV}(bpy\text{-}N,N')_2Cl_2]Cl_2$, **III.** Calculated for $IrC_{20}H_{16}Cl_4 \cdot 1/2\ (H_2O)$ Analysis: C, 36.61%; H, 2.59%; N, 8.54%; Cl, 21.63%. Found: C, 36.60%; H, 2.71%; N, 8.54%; Cl, 21.48%.

3. Trans-$[Ir(bpy)_2Cl_2]$CL; the long elusive trans complex. (IV)

Potassium hexachloroiridate (IV) (.15 g, 0.31 mmol) is combined with 2,2'bipyridine (.289 g, 1.85 mmol) in (aq)ETOH (80 ml) and refluxed in the presence of air for an hour. This solution is rotary evaporated to 20 ml volume and vacuum filtered. The precipitate is worked up to afford I, and the solution is stored. Eventually, after a month, a yellow amorphous material precipitates from the stored solution. This material is filtered, washed with hexanes and ether to afford the trans-$[Ir(bpy)_2Cl_2]^+$, **IV.**

II. MEASUREMENTS

Fast atom bombardment (FAB) was used for the mass spec analysis of **II** with ionization potential of 300 mV in an NBA matrix. Desorption chemical ionization (DCI) was used in methane for **III** with ionization potentials of 189 mV at 250°C.

NMR analysis for **II** and **III** include ^{1}H, ^{13}C, APT and COSY and are described in Appendix A. CPMAS NMR techniques were used to analyze solid samples of **II**, but were inconclusive.

The absorption measurements were obtained from a Hewlett-Packard diode array absorption spectrophotometer, described in Appendix C. Solvent for analysis included EtOH-HCl, (aq)EtOH and neat DMSO.

Emission measurements were obtained in EtOH-MeOH, EtOH-MeOH (HCl) and EtOH-MeOH(NaOH) in 77 K glass matrices with a Spex Fluorolog 2 series spectrophotometer described in Appendix C.

Single X-ray structure was determined for **II** (and **III** see Appendix E); crystallographic procedures and instrumental description are similar to those in Chapter 4.

III RESULTS AND DISCUSSION

1. Mass Spectroscopy

A. $[Ir(Hbpy\text{-}C^3,N')(bpy\text{-}N,N')Cl_2]^+$ $[IrCl_4(bpy)]^-$ The mass spectrum for II, Figure 6.1.1a, shows m/e signals at 594, 576, 557, 548, 528, 504, 461, and clusters of signals between 289 and 461 ppm. Signals between m/e 27 and 154 are almost entirely from the NBA matrix which includes peaks at m/e 289 and 307 (matrix dimer) and 461 (matrix trimer). Peaks above 500 m/e have been magnified 50 times.

The 594 m/e, $[Ir(Hbpy\text{-}C^3,N')(bpy\text{-}N,N')Cl_2]^+ + H_2O$; 576, $Ir(Hbpy\text{-}C^3,N')(bpy\text{-}N,N')Cl_2^+$; 540, $Ir(Hbpy\text{-}C^3,N')(bpy\text{-}N,N')Cl^+$; and 504 m/e, $Ir(Hbpy\text{-}C^3,N')(bpy\text{-}N,N')^+$ series are consistent with the cationic fragment of the ion pair formulated for II, and are summarized in Table 6.1a. The anionic moiety (negative ions) of II can not be detected by the mass spec technique we used.

The mass spectrum was also obtained with ionization potential at 1.6 V, Figure 6.1.1b, showing additional signals at m/e = 507, 546 and 581; residual peaks are observed at m/e = 562 and 595. Possible fragmentations are summarized in Table 6.1b.

B. $[Ir^{IV}(bpy\text{-}N,N')_2Cl_2]Cl_2$ The desorption chemical ionization mass spectrum with I = 189 mV in CH_4 at 250°C for III, shows signals at m/e = 575, 539, 185 and 157. The origin of the peaks at 185 and 157 has already been discussed in Chapter 5. However, the m/e signals at 575 and 539 peaks do suggest $Ir(bpy\text{-}N,N')_2Cl_2^+$ and $Ir(bpy\text{-}N,N')_2Cl^+$ fragments. No signals occur between 185 - 537 m/e.

TABLE 6.1

Mass Spectrum for $[Ir(Hbpy\text{-}C^3,N')(bpy\text{-}N,N')Cl_2][IrCl_4(bpy)]$.

Mass/Charge (m/e)	Intensity (%)	Ion Fragment
(a) I = 299 mV		
504	9.5	$Ir(Hbpy\text{-}C^3,N')(bpy\text{-}N,N')^+$
540	13.5	$Ir(Hbpy\text{-}C^3,N')(bpy\text{-}N,N')Cl^+$
576	34.5	$Ir(Hbpy\text{-}C^3,N')(bpy\text{-}N,N')Cl_2^+$
594	9.5	$[Ir(Hbpy\text{-}C^3,N')(bpy\text{-}N,N')Cl_2]^+ + H_2O$
(a) I = 1.6 eV		
504 - 509	30	$Ir(Hbpy\text{-}C^3,N')(bpy\text{-}N,N')^+$
543 - 549	53	$Ir(Hbpy\text{-}C^3,N')(bpy\text{-}N,N')Cl^+$
561 - 563	< 5	-
579 - 584	100	$Ir(Hbpy\text{-}C^3,N')(bpy\text{-}N,N')Cl_2^+ + 5$ m/e
593 - 597	< 5	$[Ir(Hbpy\text{-}C^3,N')(bpy\text{-}N,N')Cl_2]^+ + H_2O$

FIGURE 6.1.1:

Mass spectra of $[Ir(Hbpy\text{-}C^3,N')(bpy\text{-}N,N')Cl_2]^+[IrCl_4(bpy)]^-$.
(a) I = 0.299 mV (b) I = 1.6 eV.

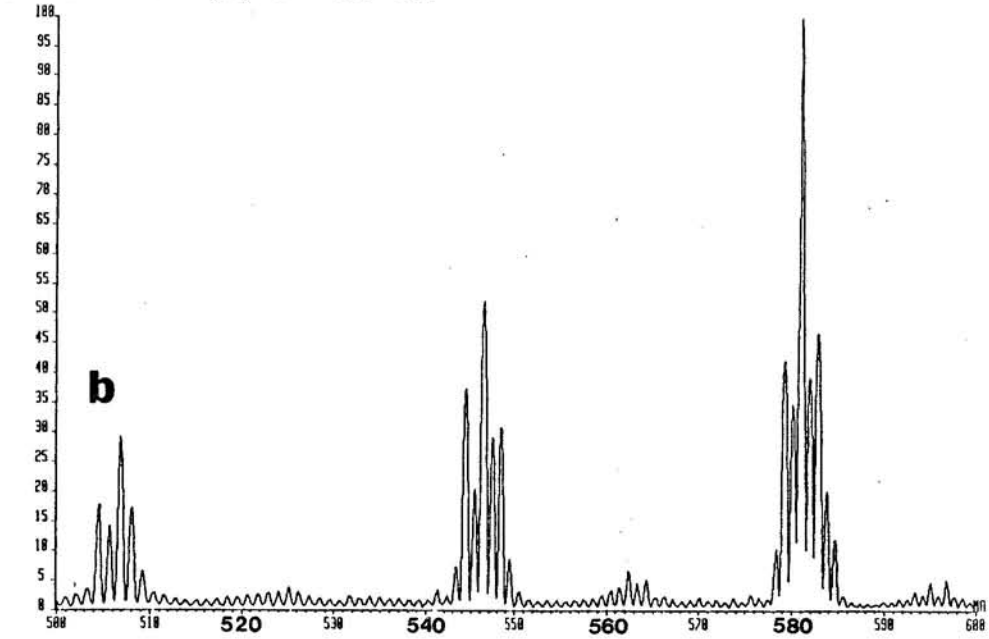

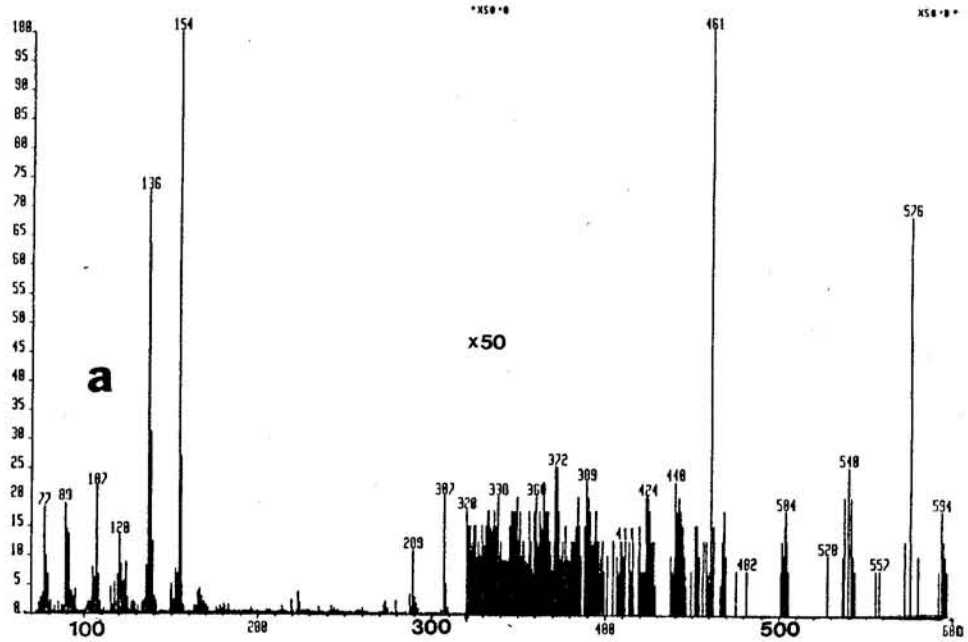

2. NMR Analysis

A. $[Ir(bpy\text{-}C^3,N')(bpy\text{-}N,N')Cl_2]^+$ $[IrCl_4(bpy)]^-$ The ^1H NMR spectrum, Figure 6.2.1b, shows 14 resonances between 9.8 and 7.0 ppm integrating for 23 protons with the 9.73, 8.54, 7.96 and 7.70 accounting for 2, 2, 4 and 4 protons, respectively (see proton count on baseline). These resonances are assigned to the protons in the $[IrCl_4(bpy)]^-$ anion because the bpy ligands possess equivalent pyridyl halves and are expected to show only four type of resonances integrating for two protons each. The four proton integration for the resonances at 7.96 and 7.70 ppm is probably a consequence of overlapping signals from protons in near degenerate environments from the $[Ir(Hbpy\text{-}C^3,N')(bpy\text{-}N,N')Cl_2]^+$ cationic moiety. Based on the multiplicity of the resonances in the ^1H NMR spectrum for II and the proton assignments of 2,2'-bipyridine (Appendix A, Table A.5) the following protons in the anionic $[IrCl_4(bpy)]^-$ moiety are assigned: E_3, 9.73; E_6, 8.54; E_4, 7.96; and E_5, 7.70 ppm.

The other fifteen resonances are assigned to the $[Ir(Hbpy\text{-}C^3,N')(bpy\text{-}N,N')Cl_2]^+$ cation; one of the bpy is protonated (thereby accounting for the +1 charge of the cationic moiety). The acidic proton in $Hbpy\text{-}C_3,N'$ is probably not observed under our NMR experimental conditions because of dynamic exchange with the solvent. The integration of 15 protons (disregarding the 8 protons already accounted for in the E rings of the anionic moiety), is consistent with four nondegenerate pyridyl rings in two bpy ligands;

one pyridyl ring possessing only three observable ^{1}H resonance. Surprisingly enough, these resonances almost coincide with the proton resonances of I, Figure 6.2.6. Furthermore, there are residual peaks in the baseline showing trace amounts of I. Comparing the ^{1}H NMR spectrum of II to that of I (Figure 5.3.2 and Figure 6.2.6), and using the multiplicity of the resonances from the latter, we make the following assignments for the protons in the cationic moiety of II; D_6,9.60; D_3,8.85; C_3,8.68; D_4/A_6,8.4; D_5,8.1; C_5,7.30; and B_5,7.25 ppm. Broad signals at 9.0 and 8.65 ppm are most likely from the β positions from the A and B rings as a result of dynamic exchange of these acidic protons with the environment.[40,41] No other assignments are made (Table 6.2).

The ^{13}C NMR spectra for II, Figure 6.2.2, shows 21 resonances scattered between 122 and 161 ppm. Five of these, δ = 123.6, 126.3, 138.6, 152.3 and 160.3, have intense signals and are assigned to the bpy ligand in the $[IrCl_4(bpy)]^-$ anion. The other sixteen resonances are assigned to the bpys of the $[Ir(Hbpy\text{-}C^3,N')(bpy\text{-}N,N')Cl_2]^+$ cation. Four of the expected twenty resonances for $[Ir(Hbpy\text{-}C^3,N')(bpy\text{-}N,N')Cl_2]^+$, are missing in this spectra. There are however, residual carbon resonances (near the noise level) at 125.5, 129.2, 139.0, and 151.5 ppm (marked by *) which may account for the missing resonances.

Comparison of the ^{13}C NMR spectra to the ^{13}C NMR spectra of I, Figure 5.3.3, shows clusters of resonances in similar chemical shifts. The group of resonances at 122 - 129, 138 - 140, 147 - 160

ppm have similarities to the 5-/ 3-; 4-; and 6- carbon resonances of I. Absolute assignments are difficult because NMR correlation data is lacking, moreover, the poor signal to noise makes these resonances difficult to observe in the spectrum.

In summary the NMR results here suggest an ion pair structure for II. The anionic moiety, $[IrCl_4(bpy)]^-$, shows four distinct proton resonances because each half of the E bpy rings are equivalent. On the other hand, the cationic $[Ir(Hbpy\text{-}C^3,N')(bpy\text{-}N,N')Cl_2]^+$ moiety, shows fifteen proton resonances that can be deciphered to the four pyridyl rings, A,B,C and D in the two nondegenerate bpy ligands.

B. $[Ir(bpy\text{-}N,N')_2Cl_2]Cl_2$ The ^1H NMR spectrum taken in DMSO-d_6 for III, Figure 6.2.3, shows 8 resonances between 10 - 7.5 ppm, with residual signals indicating impurities in the sample (which probably accounts for the poor elemental analysis fit for H). From the 2D COSY stack plots, Figure 6.2.4, spin systems can be deciphered, each possessing four resonances. In order to apply J-connectivity analysis on the COSY spectrum, the A_6 and B_6 protons are assigned to the 9.7 and 8.8 ppm resonance.[30] J-connectivity produces the following assignment: B_6, 9.7; B_5, 7.68; B_4, 7.95; B_3, 8.55; A_3, 8.82; A_5, 7.72; A_4, 8.25; A_6, 8.55, Table 6.2.

The ^{13}C NMR spectrum, Figure 6.2.5, is consistent with the ^1H NMR results showing 10 carbon resonances between 120 - 160 ppm. Comparing this ^{13}C NMR spectrum with that for I and II, suggests

assignments of the four resonances at 123.2, 123.6, 126.5 and 126.8 ppm to the B_3, A_3, B_5 and A_5 carbons (no absolute assignments).

The first structure that comes to mind from the NMR spectra, is $[Ir(bpy\text{-}N,N')_2Cl_2]^+$. Drago[42] et al., and later DeArmond[43] et al., assigned ^1H NMR spectrum for $[Ir(bpy\text{-}N,N')_2Cl_2]^+$; B_6,9.65; B_3,8.91; B_4,8.50; B_5,8.15; A_3,8.82; A_4,8.20; A_6,7.85; and A_5,7.51. Our results are inconsistent with theirs as shown by the ^1H NMR spectra of $[Ir^{III}(bpy\text{-}N,N')_2Cl_2]Cl$ and **III** in Figure 6.2.7b. All our NMR evidence to this point suggest a cis bis bipyridyl dichloro iridium complex—but not the cis-$Ir^{III}(bpy)_2Cl_2^+$ complex. An $Ir^{IV}(bpy)_2Cl_2^+$ however, would settle this puzzle. This complex is a d^5 species and as a paramagnetic complex it inherently has lower field chemical shifts and substantially broader lines.[44] The former effect is demonstrated in Figure 6.2.7, where the ^1H chemical shifts of **III** are generally 0.25 ppm lower field than those of $[Ir(bpy)_2Cl_2]^+$. Conversely, the latter effect may not occur because of the field strength of the spectrometer (11.7 Tesla).[40] In light of the elemental analysis and the mass spec already discussed, an Ir(IV), cis-$Ir^{IV}(bpy)_2Cl_2^{2+}$ species is a strong candidate for **III**.

C. Trans-$[Ir(bpy)_2Cl_2]Cl$ The two bpy ligands in a trans-$[M(bpy)_2Cl_2]$ species would occupy degenerate sites. For **IV**, the ^1H NMR spectrum, Figure 6.2.8, is very much like the free bpy ligand which is expected because in both compounds both halves in the bipyridyl ligands are equivalent resulting in four lines in the ^1H

NMR spectrum. In DMSO-d_6 the ^1H NMR spectrum for the bpy free ligand shows four resonances, squeezed between 7.5 and 8.8 ppm.[43] Upon coordination of the bpy free ligand to a transition metal, however, the ^1H chemical shift of the free ligand usually moves lower field.[34,45] This is observed in Figure 6.2.8 in which the ^1H NMR spectra for **IV** show four resonances downfield between 7.9 - 9.5 ppm. Trans-$[Ru(bpy)_2(CH_3CN)_2]$ in DMSO-d_6 shows the exact same ^1H NMR splitting pattern as that for **IV**, in the range of 7.8 - 9.5 ppm.[46,47] Recently Ford et al. reported partial isomerization of cis-$Rh(bpy)_2(H_2O)Cl^{+2}$ to trans-$Rh(bpy)_2(H_2O)Cl^{+2}$.[48] In that study, the ^1H NMR spectrum of the trans-Rh complex showed proton resonances between 9.5 and 8.0 ppm. Based on the ^1H assignment of the 2,2' bipyridine and trans-$[Ru(bpy)_2(CH_3CN)_2]$ the proton assignments for **IV** are as follow: 4/4', 7.88; 5/5', 8.30; 6/6', 8.72; and 3,3', 9.43 ppm.

Pending other evidence, our NMR results strongly support a trans-$[Ir(bpy)_2Cl_2]^{2+}$ bequeathing some truth to Gillards' original claim.[19]

TABLE 6.2

^{1}H and ^{13}C NMR resonances (and partial assignments) of $[Ir(bpy\text{-}C^{3},N')(bpy\text{-}N,N')Cl_2][IrCl_4(bpy)]$ and $[Ir(bpy\text{-}N,N')_2Cl_2]Cl_2$

$[Ir(Hbpy\text{-}C^{3},N')(bpy\text{-}N,N')Cl_2][IrCl_4(bpy)]$		$[Ir(bpy\text{-}N,N')_2H_2]Cl_2$	
^{1}H (δ)	^{13}C (δ)	^{1}H (δ)	^{13}C (δ)
9.73(E_3)	160.3	9.70(B_6)	160.5
9.60(D_6)	158.5	8.82(A_3)	152.3
9.00	156.1	8.55(A_6/B_3)	150.8
8.85(D_3)	154.2	8.25(A_4)	148.0
8.65	152.1	7.95(B_4)	141.5
8.54(E_6)	149.0	7.72(A_5)	138.5
8.41(D_4/A_6)	147.6	7.68(B_5)	126.8
8.10	140.5		126.5
7.96(E_4)	139.6		123.6
7.80	139.2		123.2
7.70(E_5)	138.6		
7.30(C_5)	128.5		
7.25(B_5)	128.2		
	122.3		
	126.3		
	126.1		
	125.0		
	124.8		
	123.6		
	122.6		

FIGURE 6.2.1:

^1H NMR spectra for $[Ir(Hbpy\text{-}C^3,N')(bpy\text{-}N,N')Cl_2]^+[IrCl_4(bpy)]^-$ in DMSO-d_6 vs. TMS. (a) 10 - 0 ppm (b) 10 - 7.0 ppm.

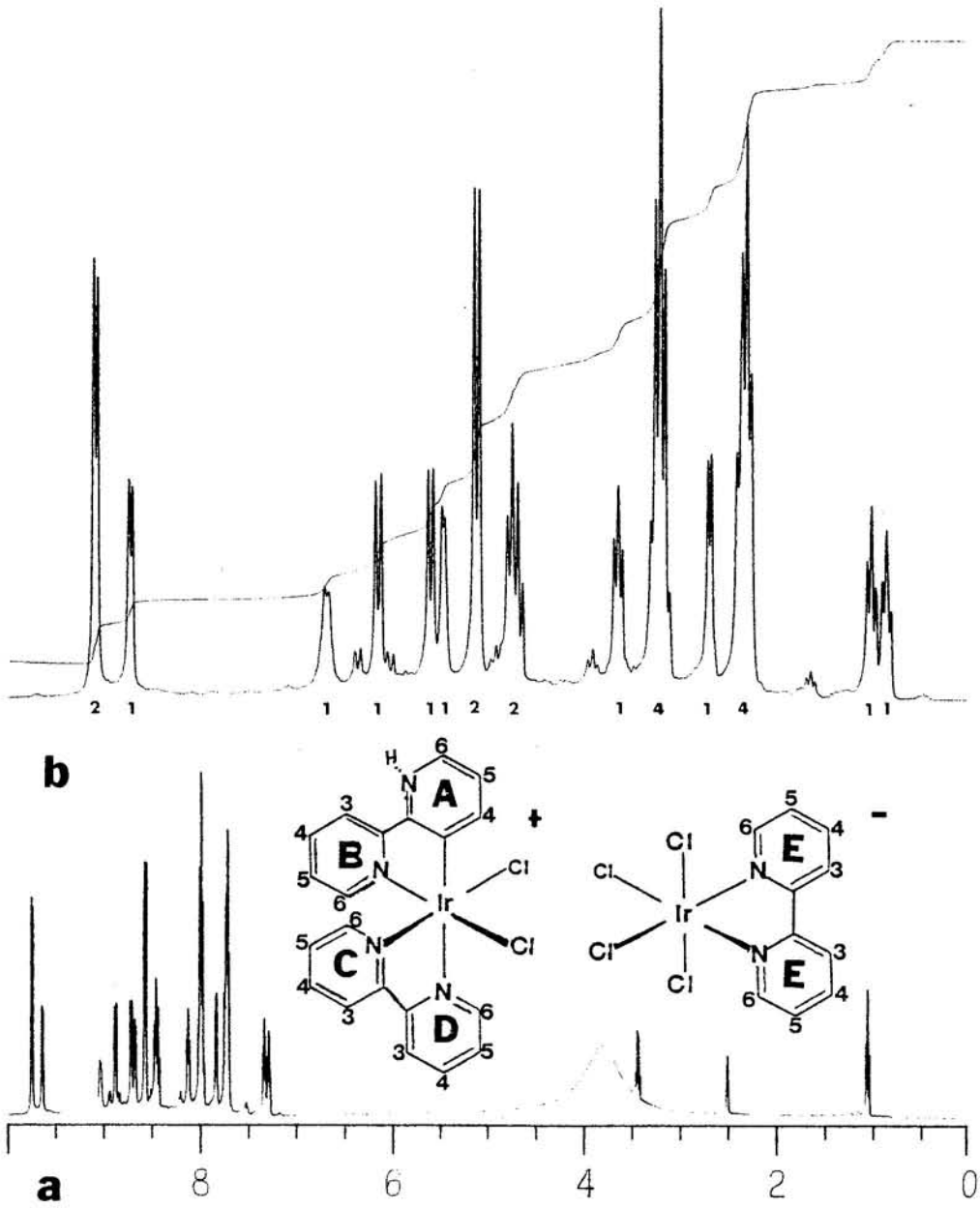

FIGURE 6.2.2:

^{13}C NMR spectra for $[Ir(Hbpy\text{-}C^3,N')(bpy\text{-}N,N')Cl_2]^+[IrCl_4(bpy)]^-$ in DMSO-d_6 vs. TMS. (a) 200 - 0 ppm (b) 161 - 120 ppm.

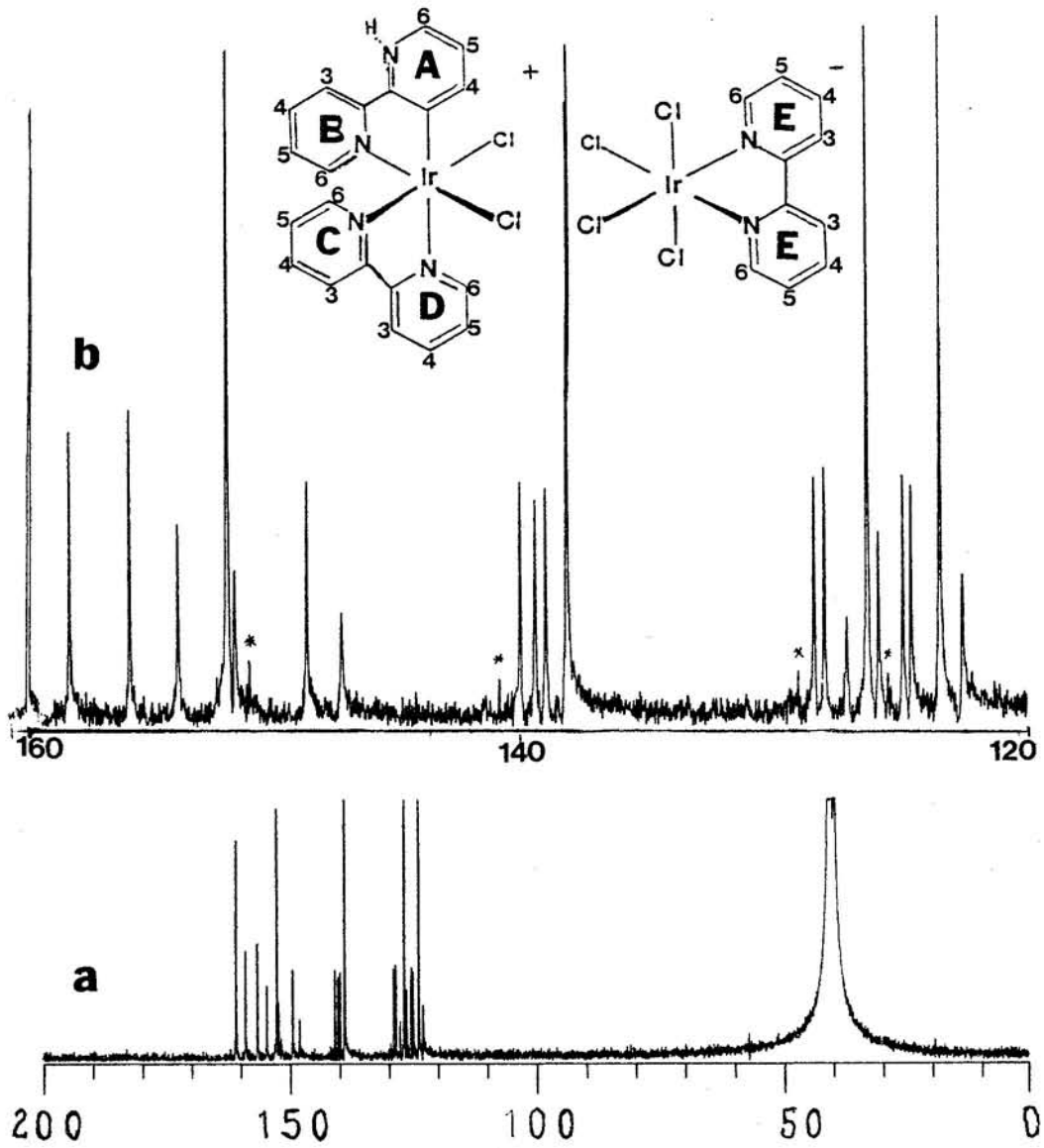

FIGURE 6.2.3:

^1H NMR spectra for $[Ir^{IV}(bpy\text{-}N,N')_2Cl_2]Cl_2$ in DMSO-d_6 vs. TMS. (a) 10 - 0 ppm (b) 10 - 7.0 ppm.

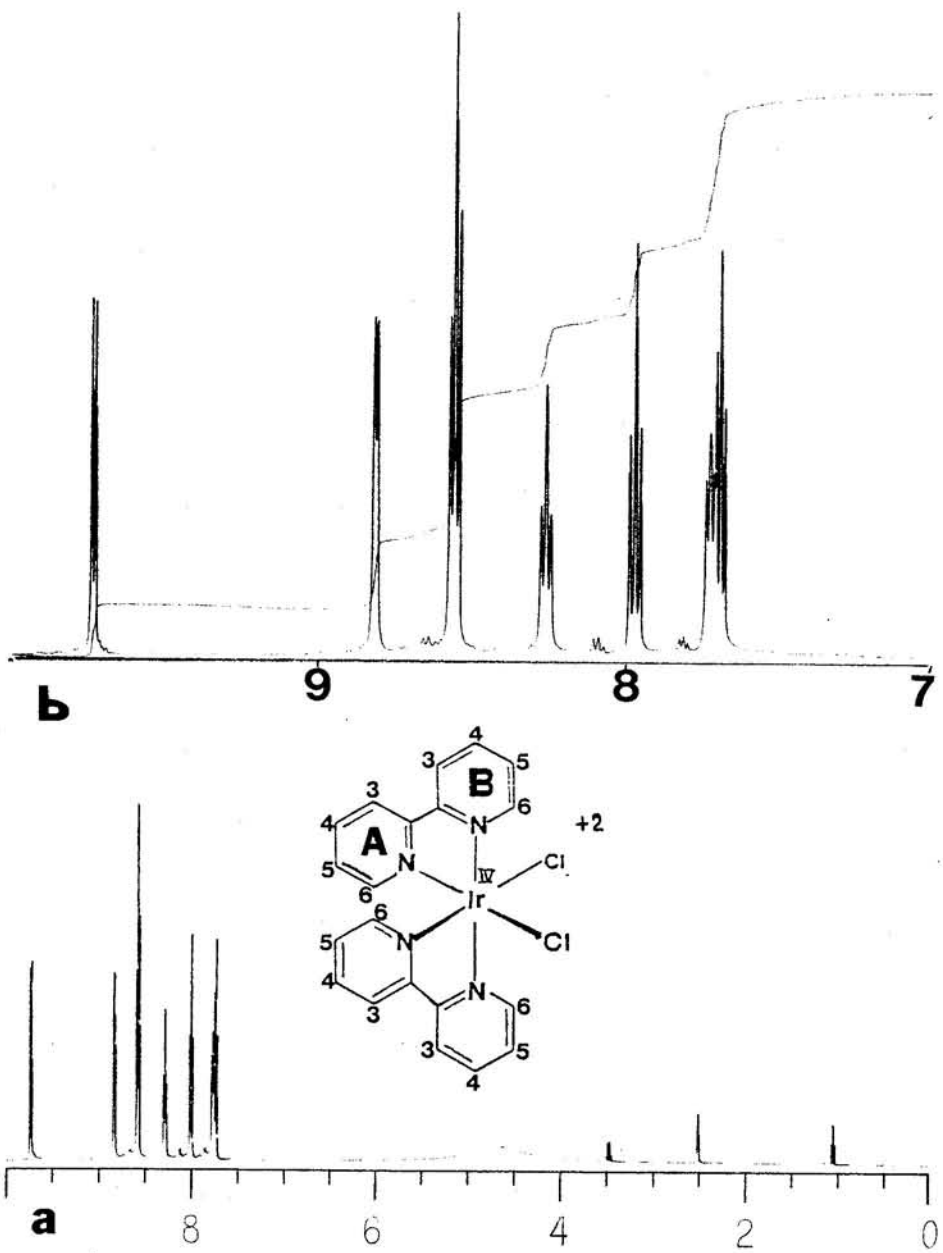

FIGURE 6.2.4:

^{1}H 2D COSY stack plots for $[Ir^{IV}(bpy\text{-}N,N')_2Cl_2]Cl_2$ in DMSO-d_6.

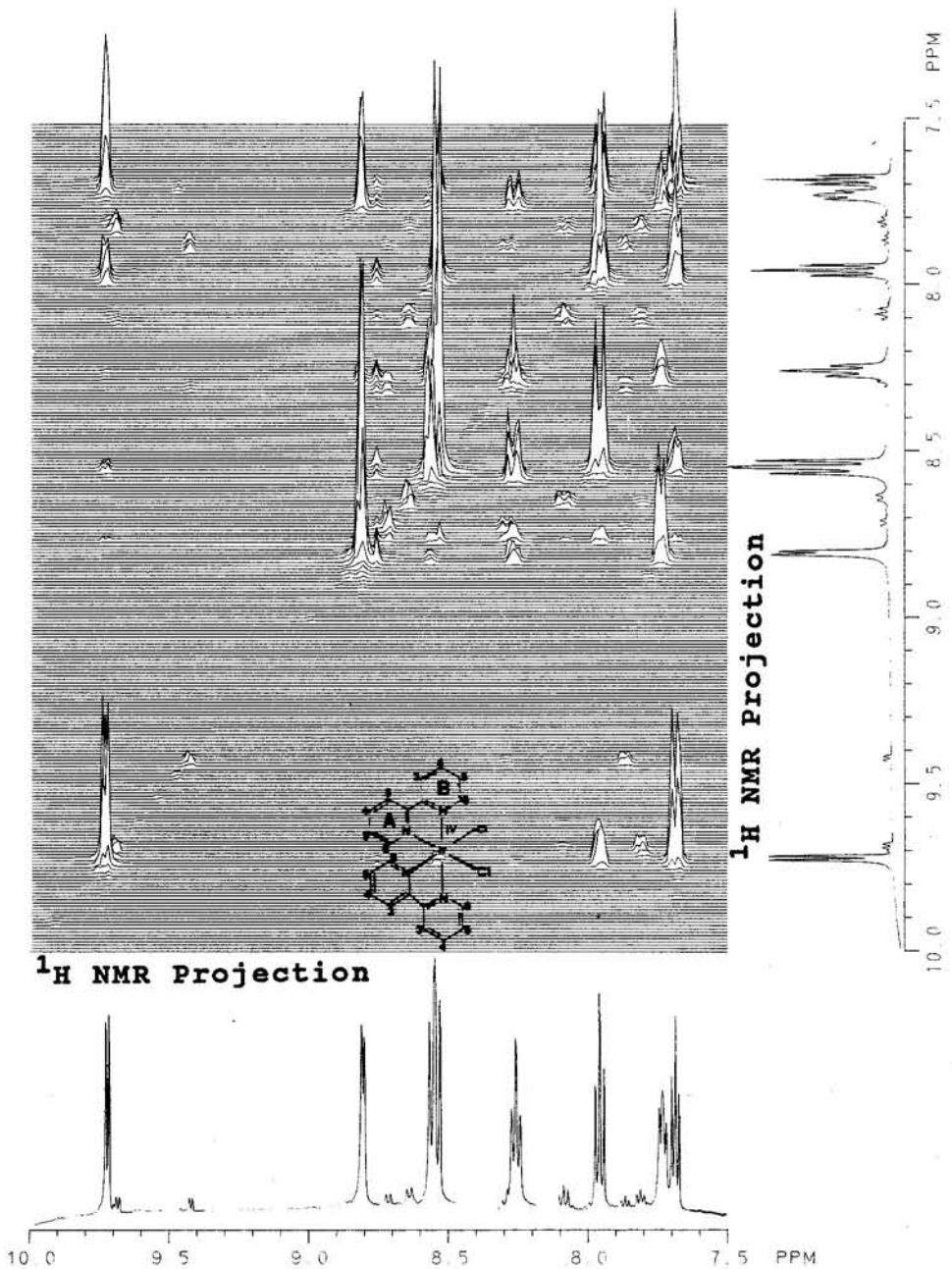

FIGURE 6.2.5:

^{13}C NMR spectra for $[Ir^{IV}(bpy\text{-}N,N')_2Cl_2]Cl_2$ in DMSO-d_6 vs. TMS.
(a) 200 - 0 ppm (b) 161 - 120 ppm.

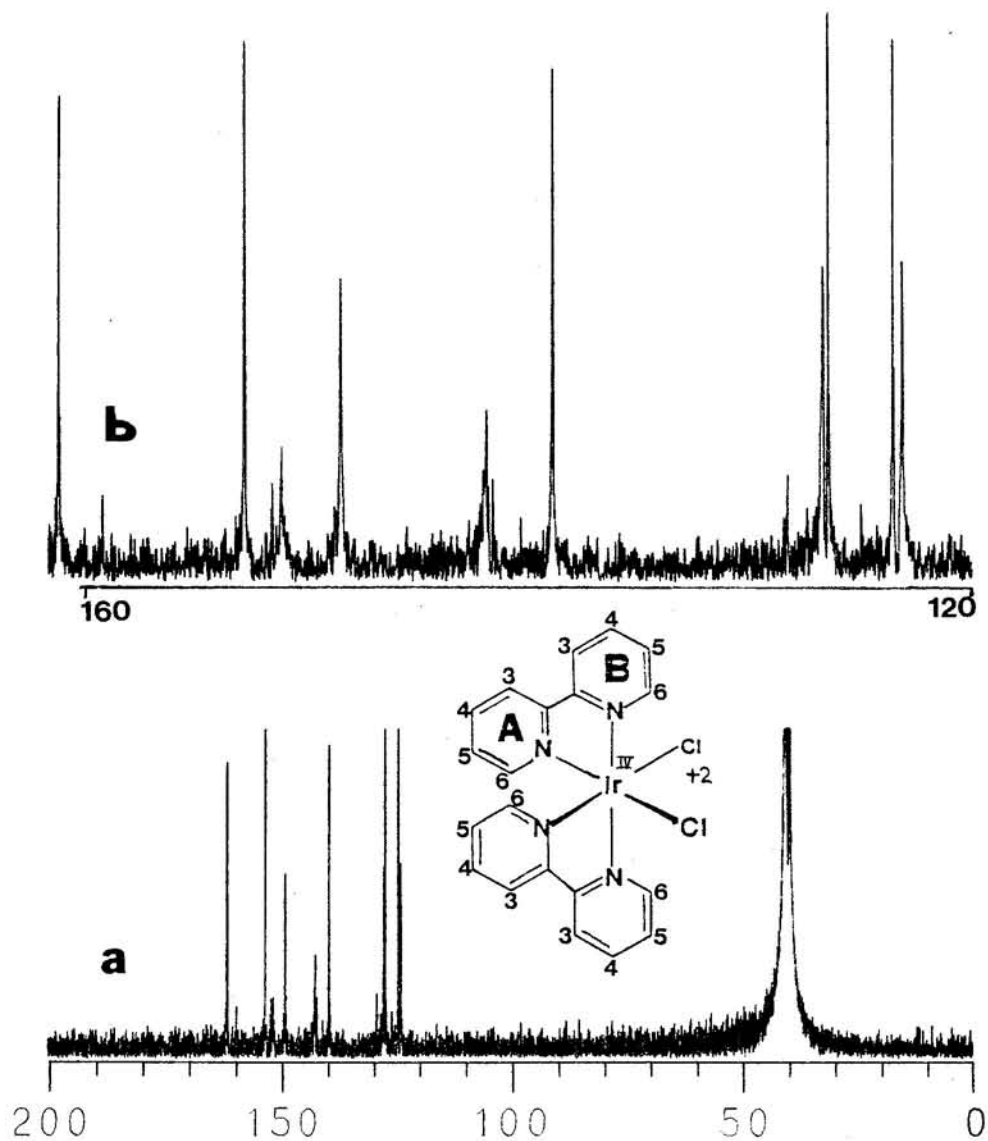

FIGURE 6.2.6:

^{1}H NMR spectra for (a) I (b) II and (c) III (10 - 7 ppm).

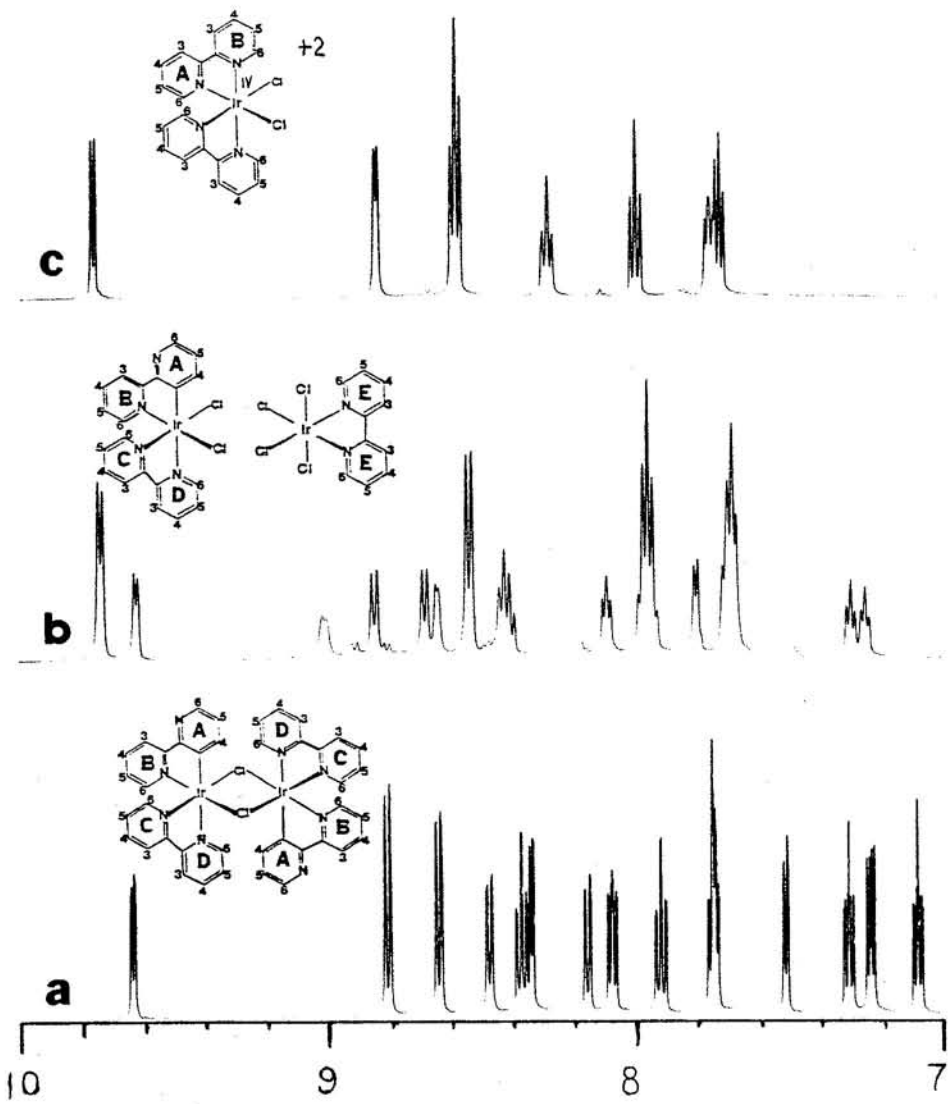

FIGURE 6.2.7:

^1H NMR spectra for (a) $[Ir(bpy\text{-}N,N')_2Cl_2]Cl_2$ and (b) $[Ir(bpy\text{-}N,N')_2Cl_2]Cl$ (10 - 7 ppm).

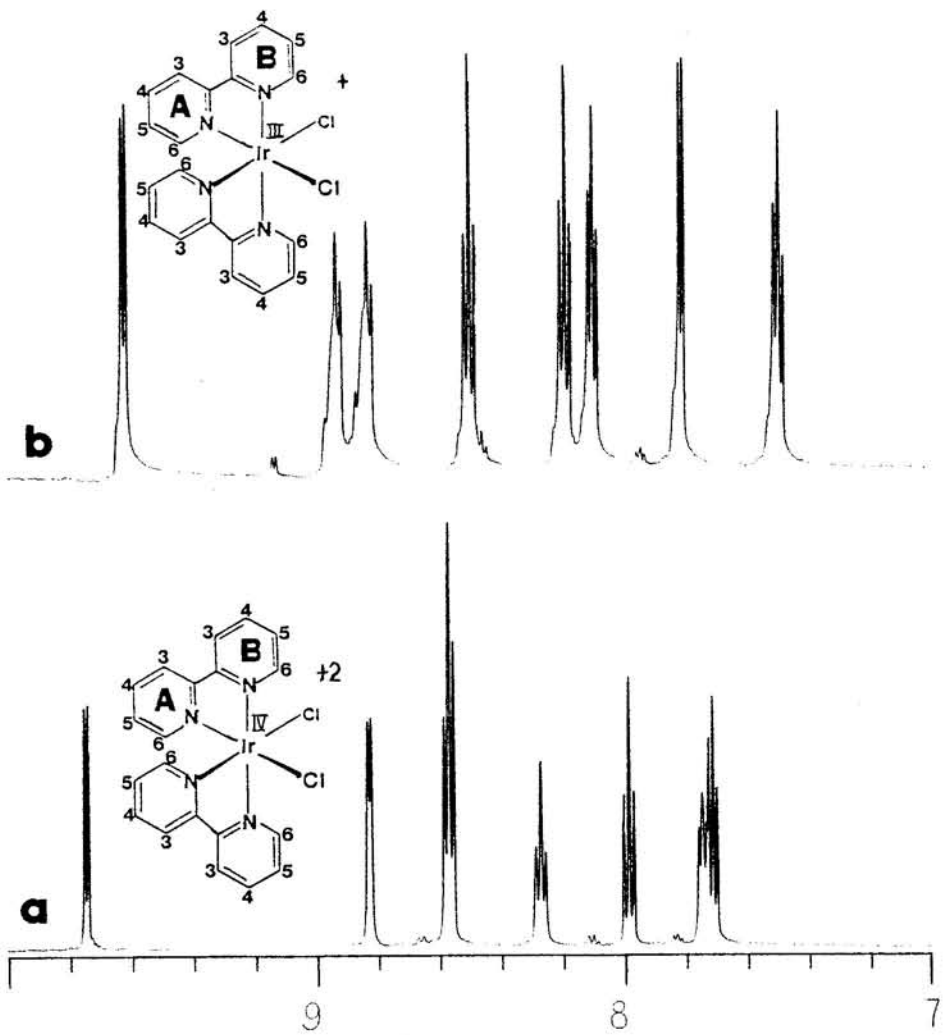

FIGURE 6.2.8

^{1}H NMR spectra for trans-[Ir(bpy)$_2$Cl$_2$]Cl in DMSO-d$_6$ vs. TMS.
(a) 10 - 0 ppm (b) 10 -7 ppm.

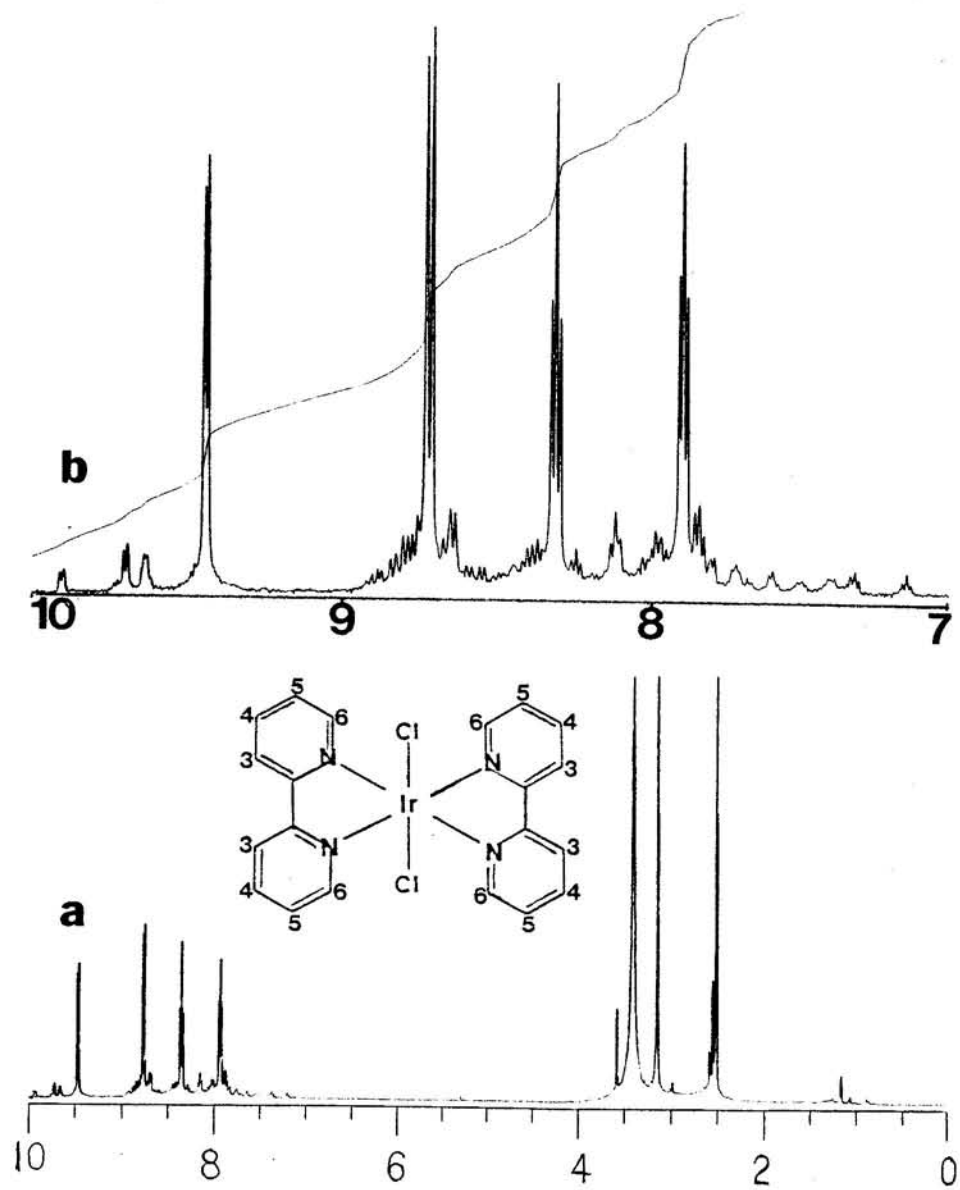

3. **Absorption and Emission; acid /base luminescence.**

A $[Ir(Hbpy\text{-}C^3,N')(bpy\text{-}N,N')Cl_2][IrCl_4(bpy)]$ Absorption spectra of II in (aq)EtOH, EtOH-HCl and DMSO at room temperature are shown in Figure 6.3.1a, b, c respectively. These spectra show band maxima in the visible region between 340 and 600 nm and in the UV region between 260 - 300 nm. These spectra also show some acid/base dependence especially for the the maxima located between 275 - 295 nm; in (aq)EtOH, λ = 276; in EtOH-HCl, λ = 292; and in DMSO, λ = 290 nm. Band maxima are summarize in Table 6.3.

The low temperature (77 K) emission spectra (corrected) in EtOH-MeOH(HCl), EtOH-MeOH(NaOH), and EtOH-MeOH are shown in Figure 6.3.2a,b and c respectively. Under neutral and basic conditions, the spectra show similar, two band maxima, structured emission profiles with λ max = 520 and 551 nm. Under acidic conditions, the profiles are less structured, and the emission maxima red-shift to 535 and 581 nm.

The photophysical properties for II show dependence in acid/base solvents. This is supportive of an ortho-metalated bipyridyl complex, analogous to $[Ir(bpy\text{-}C^3,N')(bpy\text{-}N,N')_2]^{2+}$ and $[Ir(bpy\text{-}C^3,N')(bpy\text{-}N,N')Cl]_2Cl_2$ (I) in which the external nitrogens provide a site for protonation.

B. $[Ir^{IV}(bpy)_2Cl_2]Cl_2$ The room temperature absorption spectra for III, Figure 6.3.3, in (aq)EtOH, EtOH-HCl, and DMSO show large solvent dependence; the band maxima are summarized in Table 6.5.

The absorption profiles in (aq) EtOH are blue-shifted compared to those taken in EtOH-HCl but towards the visible region the absorption profiles become identical. In DMSO however, the absorption profile in the visible region becomes structured with band maxima at 358, 382, 418, 442, 490, 521 and 562 nm. Comparison of the absorption spectra of **III** to those of an Ir^{IV} species, $[Ir^{IV}(bpy)Cl_4]$[39] show striking similarities, the latter shows band maxima at 620, 520, 420 and 380 nm. A d^5 low spin species would have low energy bands originating from d-d, $t_{2g} \longrightarrow e_g$ transitions. This is consistent with the absorption spectra for **III**.

The first vibrational band maximum for cis-$[Ir^{III}(bpy)_2Cl_2]Cl$ in EtOH-MeOH 77 K, occurs at 473 nm.[42] **III** does not emit in room temperature fluid solutions. The low temperature (77 K) excitation and emission spectra in ETOH-MeOH (1:1 v/v) are shown in Figure 6.2.4. The emission shows a structured profile with band maxima at 454, 488, 529, and 558 nm; the excitation profile shows band maxima at 377, 422 and 466 nm.

TABLE 6.3

Absorption band maxima for II and III in various solvents.

(aq)EtOH

A. $[Ir(Hbpy\text{-}C^3,N')(bpy\text{-}N,N')Cl_2]^+$ $[IrCl_4(bpy)]^-$:

276, 296, 316(sh), 354, 418, 443 nm

B. $[Ir^{IV}(bpy\text{-}N,N')_2Cl_2]Cl_2$:

214, 236, 282, 310(sh), 356, 385, 409, 447, 495 nm

EtOH-HCl

A. $[Ir(Hbpy\text{-}C^3,N')(bpy\text{-}N,N')Cl_2]^+$ $[IrCl_4(bpy)]^-$:

292, 315, 352, 410, 445 nm

B. $[Ir^{IV}(bpy\text{-}N,N')_2Cl_2]Cl_2$:

216, 242, 296, 315(sh), 356, 385, 410, 447, 495 nm

DMSO.

A. $[Ir(Hbpy\text{-}C^3,N')(bpy\text{-}N,N')Cl_2]^+$ $[IrCl_4(bpy)]^-$:

292, 350, 420, 442, 478, 560 nm

B. $[Ir^{IV}(bpy\text{-}N,N')_2Cl_2]Cl_2$:

288, 358, 382, 418, 442, 490, 521, 562 nm.

FIGURE 6.3.1:

Absorption spectra for $[Ir(Hbpy\text{-}C^3,N')(bpy\text{-}N,N')Cl_2]^+[IrCl_4(bpy)]^-$, in (a) --------(aq)EtOH; (b) ····· EtOH-HCl; and (c) ————DMSO.

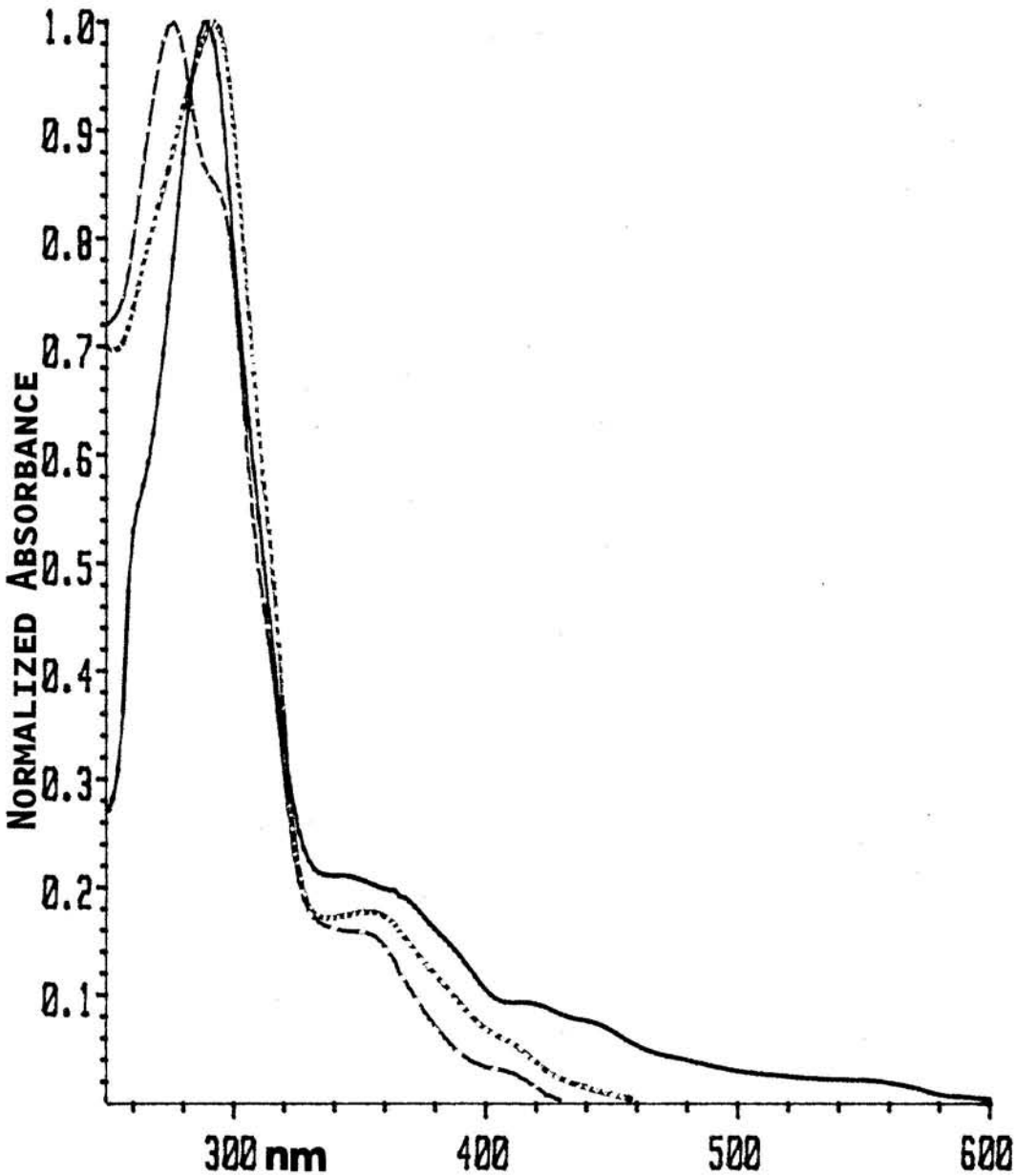

FIGURE 6.3.2:

Low temperature (77 K) emission spectra for $[Ir(Hbpy\text{-}C^3,N')(bpy\text{-}N,N')Cl_2]^+[IrCl_4(bpy)]^-$ at taken in (a) ·····EtOH-MeOH (HCl); (b) -------EtOH-MeOH (NaOH); and (c) ————EtOH-MeOH.

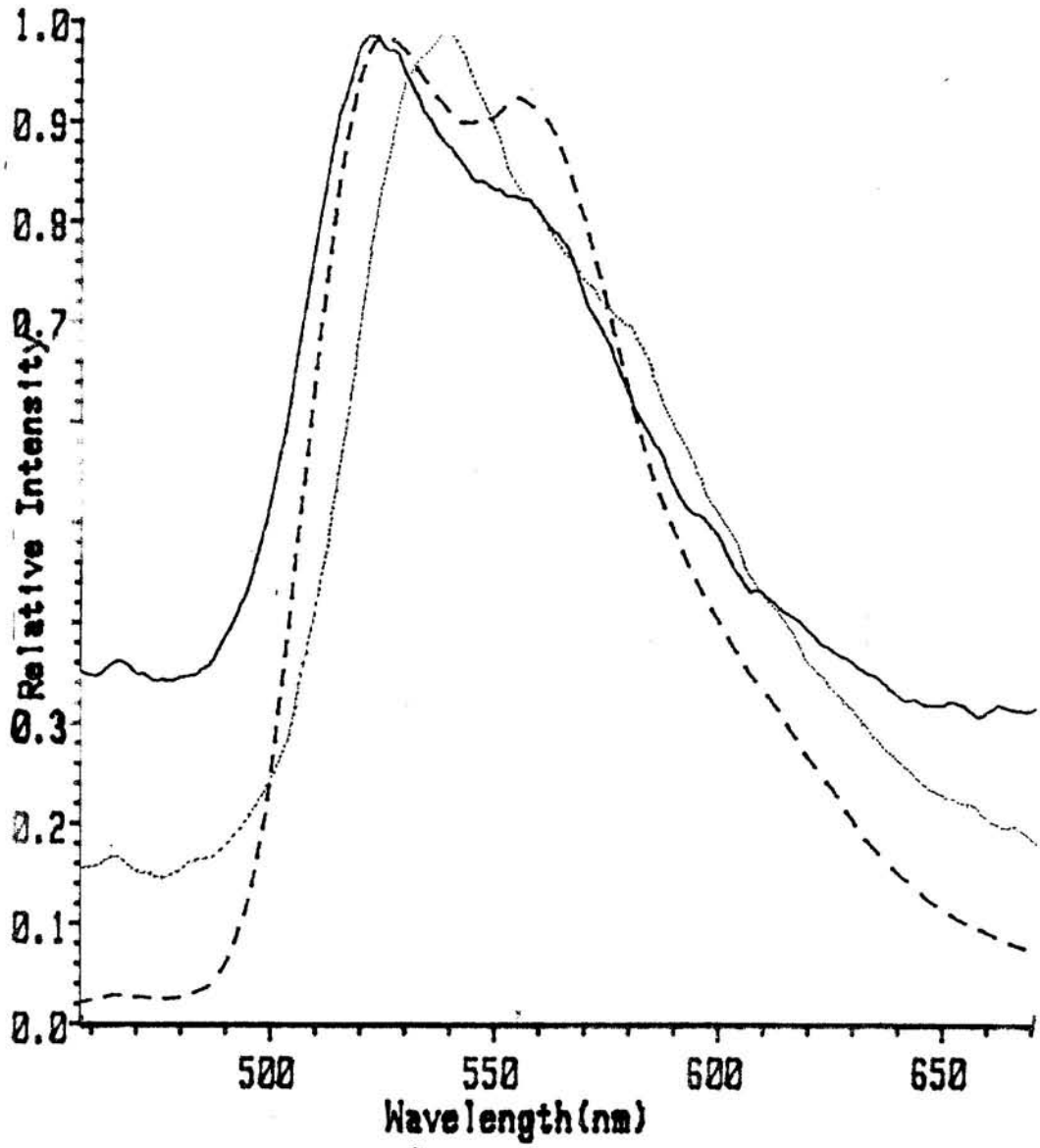

FIGURE 6.3.3:

Absorption spectra for $[Ir^{IV}(bpy)_2Cl_2]Cl_2$ in (a) ------- (aq)EtOH; (b) ····· EtOH-HCl; and (c) ———— DMSO.

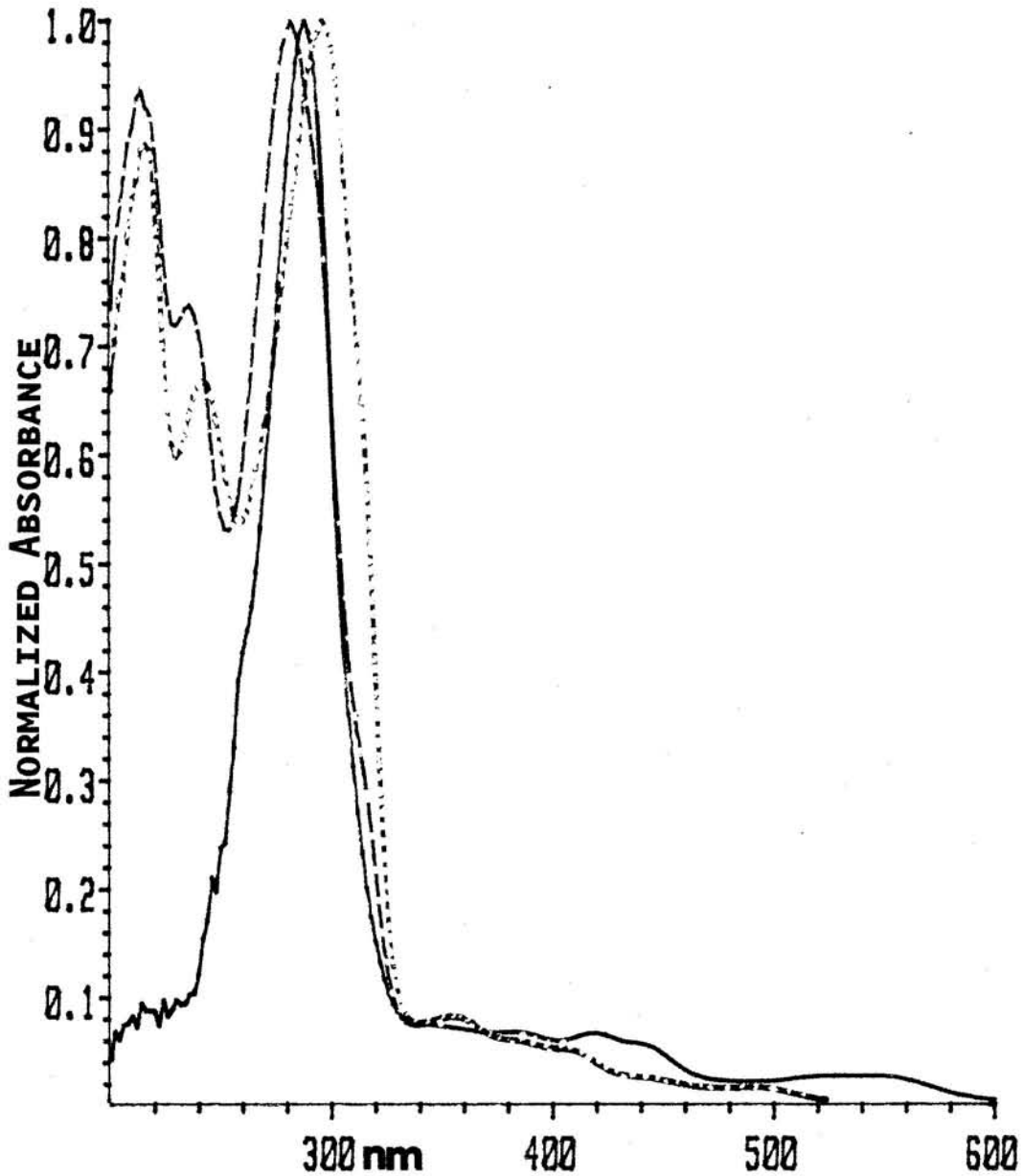

FIGURE 6.3.4:

Low temperature (77 K) emission and excitation spectra for $[Ir^{IV}(bpy)_2Cl_2]Cl_2$ in EtOH-MeOH; ————Emission, ---------Excitation.

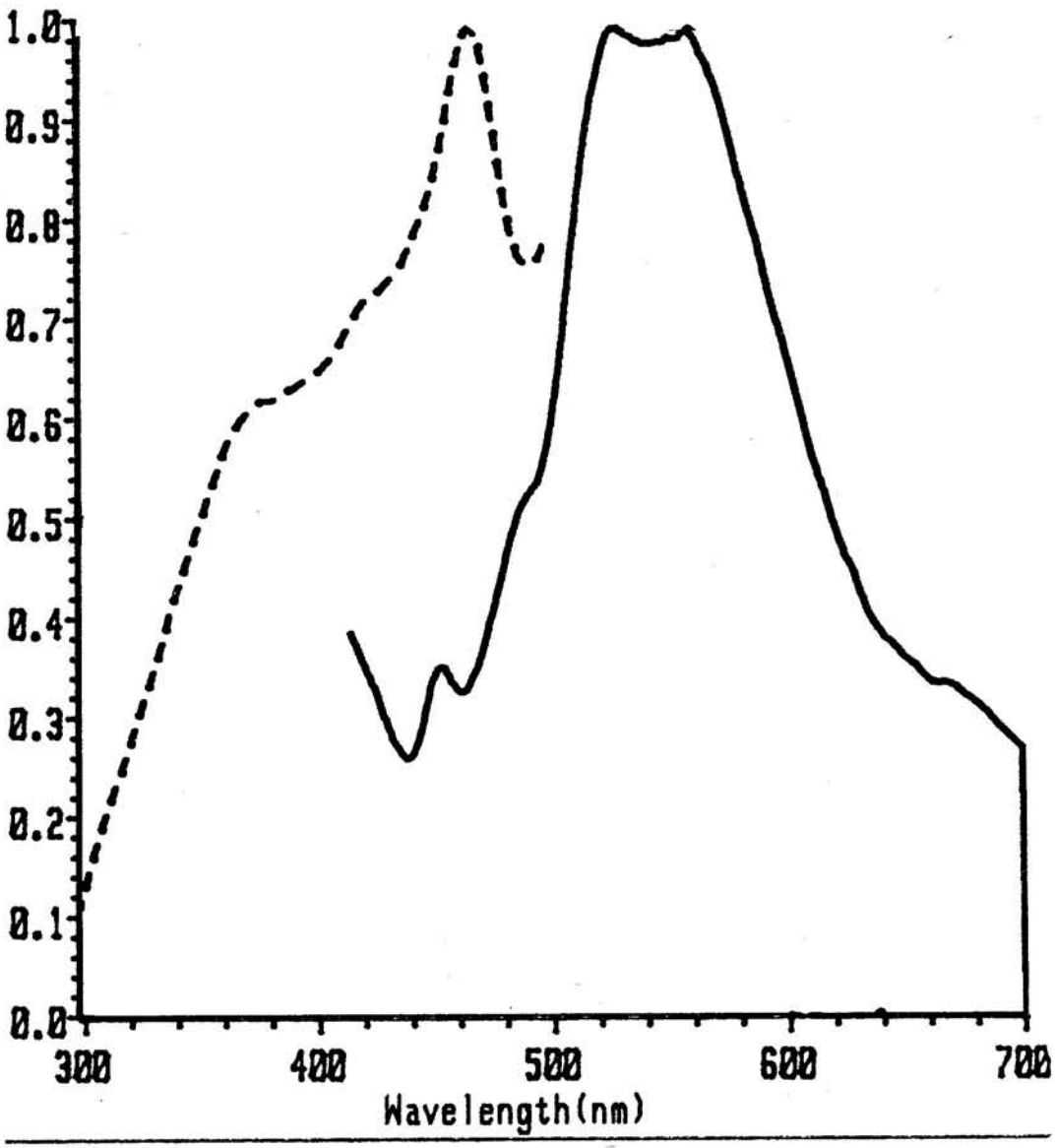

4. Crystallographic analysis

The crystallographic results in this section are provided largely through the efforts of Nancy Keder who unselfishly collected the data set and refined the crystal structure of II.

The experimental procedure for the X-ray data collection and structural refinement is similar to that described in Chapter 4. Systematic absences of h00, h=2n+1; 0k0, k=2n+1; h0ℓ, h=2n+1 are supportive of the space group $P12_1/a1$. The unit cell volume of 3567 $Å^3$ contains four molecules, Figure 6.4.1. The Ir and Cl atoms were located by direct methods; C and N atoms were located by least-squares refinement and difference Fourier syntheses; and hydrogen atom positions were calculated (C-H = 0.95 Å) and included as fixed contributors with a thermal parameter of 3.0 $Å^2$. Positions of all non-hydrogen atoms were refined. Thermal parameters for Ir and Cl atoms were refined anisotropically, while those for N and C atoms were refined isotropically. The final cycle gave an R-factor of 6.8% and an R_w of 8.7%; the error of fit was 2.3.

The cell constants and other crystallographic data for II are summarized in Table 6.4; assorted bond length, bond angles, atomic position in Tables 6.5 - 6.7; anisotropic and isothermal temperature factors in Tables 6.8 and 6.9; the packing diagram for the unit cell are shown in Figure 6.4.1; the labeling scheme and the ORTEP diagram are shown in Figure 6.4.2 and 6.4.3, respectively.

X-ray structural analysis of II reveals two types of iridium center in an ion pair arrangement in the unit cell. The cation contains two bipyridyl and two chloro ligands bound to an iridium (III), while the anion contains one bipyridyl and four chloro ligands bound to the another iridium (III), Figure 6.4.2.

Although the refinement converged at R = 6.8%, there are a couple of anomalies in the structure. First, the 50/60 bipyridyl ligand (50/60 refers to the labeling scheme, Figure 6.4.2) possesses anomalously high electron density about the H(63) and H(64) atoms. Second, this bipyridyl ligand has excessively large thermal parameters suggesting a distorted ring; in particular, the C(53) and C(64) atoms. The other bipyridyl ligands in the cation and in the anion possess normal thermal parameters.

These anomalies suggest that the 50/60 bpy could be ortho-metalated, with the external N-atom protonated and hydrogen bonded to water.[13-15] Mass spec and elemental analysis is supportive of this hypothesis. To test this hypothesis, the N(60) and C(63) atoms were exchanged (ortho-metalation) and the data set refined. This gave no significant difference in the R-factor, however. In addition, an attempt was made to refine the electron density near H(63) as an anisotropic oxygen—on the theory that water may be bonded to the protonated nitrogen of the ortho-metalated bpy. Unfortunately, the refinement yielded only a big smear of electron density that made no chemical sense; i.e., no reasonable H-N, or H-O

bond distances were found.

The disordered bipyridyl ligand did not refine well in either the chelated (N,N′ coordinated) or the ortho-metalated (C^3,N′ metalated) case; this does not confirm or exclude the possibility of ortho-metalation in the 50/60 bpy ring, however. As mentioned in Chapter 4, N and C atoms have nearly identical scattering factors, making it difficult to distinguish them apart. We conclude that the data set obtained for this structure is not good enough to warrant definite structural conclusions on the ortho-metalated nature of II. The interpretation of ortho-metalation must be based on other spectroscopic evidence, i.e., ^1H NMR and acid/base photophysical properties. It is interesting to note however, that our theory concerning ortho-metalation at the N(60) and C(63) ring positions is consistent with II being a precursor for I, and supports the structural configuration of mutually cis Ir-C and Ir-Cl bonds.

TABLE 6.4

Cell and data collection parameters for $[Ir(Hbpy\text{-}C^3,N')(bpy\text{-}N,N')Cl_2]^+[IrCl_4(bpy)]^-$.

Compound	$[Ir(Hbpy\text{-}C^3,N')(bpy\text{-}N,N')Cl_2]^+[IrCl_4(bpy)]^-$
Formula Wt.	1066.7
Xtal dim. (mm)	rectangular needle 0.1 x 0.1 x 0.30
Crystal system	Monoclinic
Space group	$P2_1/a$
Z	4
a,(Å)	12.7201(7)
b,(Å)	18.980 (1)
c,(Å)	15.721 (1)
α, β, γ (°)	90, 70.358(2), 90
Volume ($Å^3$)	3567.0
ρ calc, (g/cc)	1.98
Rad. and λ	Mo Kα (.7107 Å)
Monochrom.	graphite
Temp. (K)	298
Scan range,	
below Kα1	1.3
above Kα2	1.6
Scan rate, (°/min)	4.5
Scan mode	$\theta - 2\theta$.
2θ max	40
Octants collect	+h,+k,$\pm$l
Tot. # refl.	5087
# unique refl.	-
# of ref. obs. $I>3\sigma(I)$	2927
Abs coef, (cm^{-1})	79.1
Abs. correction	empirical
Transmission factor	-
Extinction Parameter	-
R	6.8
Rw	8.7
EOF	2.3
# param refined	217
Data/param.	13.5

TABLE 6.5

Selected bond lengths (Å) for $[Ir(Hbpy\text{-}C^3,N')(bpy\text{-}N,N')Cl_2]^+[IrCl_4(bpy)]^-$.

From	To	Distance
IR(01)	N(10)	2.04(2)
IR(01)	N(60)	2.05(3)
IR(01)	N(50)	2.05(2)
IR(01)	N(20)	2.05(2)
IR(01)	CL(11)	2.34(1)
IR(01)	CL(10)	2.35(1)
N(10)	C(16)	1.40(3)
N(10)	C(12)	1.41(3)
N(20)	C(26)	1.34(3)
N(20)	C(22)	1.35(3)
C(12)	C(13)	1.31(3)
C(12)	C(22)	1.42(3)
C(13)	C(14)	1.30(3)
C(14)	C(15)	1.39(4)
C(15)	C(16)	1.41(4)
C(22)	C(23)	1.37(4)
C(23)	C(24)	1.39(4)
C(24)	C(25)	1.32(4)
C(25)	C(26)	1.40(4)
N(50)	C(56)	1.35(3)
N(50)	C(52)	1.35(4)
N(60)	C(62)	1.32(4)
N(60)	C(66)	1.44(4)
C(52)	C(62)	1.35(4)
C(52)	C(53)	1.43(5)
C(53)	C(54)	1.32(5)
C(54)	C(56)	2.35(5)
C(62)	C(63)	1.53(5)
C(63)	H(63)	1.01
C(63)	C(64)	1.28(5)
C(64)	H(64)	1.00
C(64)	C(65)	1.30(5)
C(65)	C(66)	1.42(5)
IR(02)	N(30)	1.98(2)
IR(02)	N(40)	2.02(2)
IR(02)	CL(21)	2.34(1)
IR(02)	CL(23)	2.36(1)
IR(02)	CL(22)	2.37(1)
IR(02)	CL(20)	2.37(1)
N(30)	C(36)	1.39(3)
N(30)	C(32)	1.39(3)
N(30)	H(36)	2.06
N(30)	C(35)	2.39(4)
N(40)	C(46)	1.36(3)
N(40)	C(42)	1.37(3)
C(32)	C(33)	1.38(3)
C(32)	C(42)	1.46(3)
C(33)	C(34)	1.37(4)
C(34)	C(35)	1.33(4)
C(35)	C(36)	1.32(3)
C(42)	C(43)	1.36(3)
C(43)	C(44)	1.41(4)
C(44)	C(45)	1.33(4)
C(45)	C(46)	1.42(4)

TABLE 6.6

Selected bond angles (°) for $[Ir(Hbpy\text{-}C^3,N')(bpy\text{-}N,N')Cl_2]^+[IrCl_4(bpy)]^-$.

From	Thru	To	Angle
N(10)	IR(01)	N(60)	176.4(10)
N(10)	IR(01)	N(50)	101.1(9)
N(10)	IR(01)	N(20)	78.7(9)
N(10)	IR(01)	CL(11)	96.0(7)
N(10)	IR(01)	CL(10)	85.7(7)
N(60)	IR(01)	N(50)	77.1(10)
N(60)	IR(01)	N(20)	98.2(9)
N(60)	IR(01)	CL(11)	87.1(7)
N(60)	IR(01)	CL(10)	96.2(8)
N(50)	IR(01)	N(20)	94.1(9)
N(50)	IR(01)	CL(11)	86.4(7)
N(50)	IR(01)	CL(10)	172.8(7)
N(20)	IR(01)	CL(11)	174.7(6)
N(20)	IR(01)	CL(10)	89.4(6)
CL(11)	IR(01)	CL(10)	90.7(3)
C(16)	N(10)	C(12)	118.0(22)
C(16)	N(10)	IR(01)	127.7(18)
C(12)	N(10)	IR(01)	114.1(17)
C(26)	N(20)	C(22)	121.5(24)
C(26)	N(20)	IR(01)	122.9(19)
C(22)	N(20)	IR(01)	115.6(18)
C(13)	C(12)	N(10)	122.8(24)
C(13)	C(12)	C(22)	122.3(25)
N(10)	C(12)	C(22)	114.7(23)
C(14)	C(13)	C(12)	119.1(26)
C(13)	C(14)	C(15)	124.5(29)
C(14)	C(15)	C(16)	117.2(26)
N(10)	C(16)	C(15)	118.2(25)
N(20)	C(22)	C(23)	118.8(25)
N(20)	C(22)	C(12)	115.7(24)
C(23)	C(22)	C(12)	125.5(25)
C(22)	C(23)	C(24)	119.5(28)
C(25)	C(24)	C(23)	121.4(31)
C(24)	C(25)	C(26)	118.7(29)
N(20)	C(26)	C(25)	120.0(26)
C(56)	N(50)	C(52)	126.4(28)
C(56)	N(50)	IR(01)	119.8(20)
C(52)	N(50)	IR(01)	113.7(22)
C(62)	N(60)	C(66)	118.7(29)
C(62)	N(60)	IR(01)	115.4(23)
C(66)	N(60)	IR(01)	125.8(23)
C(62)	C(52)	N(50)	117.1(34)
C(62)	C(52)	C(53)	126.2(39)
N(50)	C(52)	C(53)	115.6(35)
N(40)	IR(02)	CL(20)	96.1(6)
CL(21)	IR(02)	CL(23)	91.8(3)
CL(21)	IR(02)	CL(22)	175.8(3)
CL(21)	IR(02)	CL(20)	91.6(3)
CL(23)	IR(02)	CL(22)	90.9(3)
CL(23)	IR(02)	CL(20)	87.9(3)
CL(22)	IR(02)	CL(20)	91.7(3)
C(36)	N(30)	C(32)	115.0(22)
C(36)	N(30)	IR(02)	130.0(18)
C(32)	N(30)	IR(02)	115.1(17)
C(46)	N(40)	C(42)	119.2(23)
C(46)	N(40)	IR(02)	123.2(18)
C(46)	N(40)	C(32)	154.9(19)
C(42)	N(40)	IR(02)	117.3(17)
C(33)	C(32)	N(30)	121.9(23)
C(33)	C(32)	C(42)	121.7(24)
N(30)	C(32)	C(42)	116.4(22)
C(34)	C(33)	C(32)	117.7(25)
C(35)	C(34)	C(33)	121.6(27)
C(36)	C(35)	C(34)	120.0(29)
C(35)	C(36)	N(30)	123.8(27)
C(43)	C(42)	N(40)	123.4(24)
C(43)	C(42)	C(32)	125.8(24)
N(40)	C(42)	C(32)	110.8(22)
C(42)	C(43)	C(44)	116.6(26)
C(45)	C(44)	C(43)	122.2(30)
C(44)	C(45)	C(46)	119.7(29)
N(40)	C(46)	C(45)	119.0(25)
C(54)	C(53)	C(52)	116.9(44)
C(53)	C(54)	C(55)	129.5(43)
C(54)	C(55)	C(56)	112.3(34)
N(60)	C(62)	C(52)	116.4(34)
N(60)	C(62)	C(63)	118.4(33)
C(52)	C(62)	C(63)	124.8(36)
C(64)	C(63)	C(62)	118.3(39)
C(63)	C(64)	C(65)	125.6(46)
C(64)	C(65)	C(66)	119.1(41)
C(65)	C(66)	C(60)	119.6(33)
N(30)	IR(02)	N(40)	79.8(9)
N(30)	IR(02)	CL(21)	89.3(7)
N(30)	IR(02)	CL(23)	96.1(7)
N(30)	IR(02)	CL(22)	87.2(7)
N(30)	IR(02)	CL(20)	175.9(7)
N(40)	IR(02)	CL(21)	88.9(6)
N(40)	IR(02)	CL(23)	175.9(6)
N(40)	IR(02)	CL(22)	88.1(6)

TABLE 6.7

Positional parameters for $[Ir(Hbpy\text{-}C^3,N')(bpy\text{-}N,N')Cl_2]^+[IrCl_4(bpy)]^-$.

Atom	X	Y	Z
IR(01)	0.5235(1)	0.1675(1)	0.9645(1)
CL(10)	0.5010(7)	0.0608(4)	0.8961(5)
CL(11)	0.3971(6)	0.2237(4)	0.9077(5)
N(10)	0.6604(19)	0.1825(12)	0.8526(15)
N(20)	0.6459(18)	0.1211(11)	1.0036(14)
C(12)	0.7557(21)	0.1455(13)	0.8539(16)
C(13)	0.8492(20)	0.1444(13)	0.7849(16)
C(14)	0.8534(25)	0.1765(16)	0.7108(20)
C(15)	0.7666(24)	0.2160(15)	0.7000(19)
C(16)	0.6672(22)	0.2205(14)	0.7748(17)
C(22)	0.7465(22)	0.1149(14)	0.9385(17)
C(23)	0.8298(24)	0.0797(15)	0.9578(19)
C(24)	0.8112(27)	0.0554(17)	1.0449(22)
C(25)	0.7135(25)	0.0629(16)	1.1087(20)
C(26)	0.6280(23)	0.0974(15)	1.0878(19)
N(50)	0.5226(20)	0.2591(13)	1.0341(16)
N(60)	0.3924(22)	0.1529(14)	1.0817(17)
C(52)	0.4435(30)	0.2606(19)	1.1171(24)
C(53)	0.4321(41)	0.3261(27)	1.1643(33)
C(54)	0.5082(35)	0.3749(21)	1.1282(27)
C(55)	0.5948(32)	0.3745(21)	1.0469(26)
C(56)	0.6003(26)	0.3092(17)	0.9978(21)
C(62)	0.3718(29)	0.2060(19)	1.1395(24)
C(63)	0.2778(32)	0.1979(21)	1.2299(25)
C(64)	0.2196(38)	0.1415(26)	1.2442(30)
C(65)	0.2390(33)	0.0867(22)	1.1915(28)
C(66)	0.3265(30)	0.0896(19)	1.1072(24)
IR(02)	0.1849(1)	0.0482(1)	0.6384(1)
CL(20)	0.1004(7)	0.0747(5)	0.7942(5)
CL(21)	0.2426(6)	-0.0625(4)	0.6714(5)
CL(22)	0.1390(7)	0.1611(4)	0.5962(7)
CL(23)	0.0111(6)	0.0027(5)	0.6408(6)
N(30)	0.2643(18)	0.0306(11)	0.5087(14)
N(40)	0.3372(18)	0.0867(11)	0.6265(14)
C(32)	0.3724(20)	0.0570(13)	0.4756(16)
C(33)	0.4381(23)	0.0496(14)	0.3859(18)
C(34)	0.3926(23)	0.0156(15)	0.3295(18)
C(35)	0.2897(26)	-0.0104(16)	0.3595(20)
C(36)	0.2284(23)	-0.0036(15)	0.4453(19)
C(42)	0.4142(21)	0.0910(13)	0.5411(17)
C(43)	0.5166(24)	0.1204(15)	0.5229(18)
C(44)	0.5417(27)	0.1480(16)	0.5969(22)
C(45)	0.4694(25)	0.1457(15)	0.6805(20)
C(46)	0.3632(24)	0.1134(15)	0.6972(19)

TABLE 6.8

Temperature factors for the non-hydrogen atoms of $[Ir(Hbpy\text{-}C^3,N')(bpy\text{-}N,N')Cl_2]^+[IrCl_4(bpy)]^-$.

A. Anisotropic Temp. Factors. B. Isotropic Temp. Factors.

A.

Atom	$U_{11}10^3$	$U_{22}10^3$	$U_{33}10^3$	$U_{12}*10^3$	$U_{13}10^3$	$U_{23}10^3$
IR(01)	52(1)	54(1)	53(1)	5(1)	-19(1)	-2(1)
CL(10)	102(6)	59(5)	85(6)	-13(4)	-45(5)	-1(4)
CL(11)	63(5)	95(6)	78(5)	25(4)	-30(4)	4(5)
IR(02)	46(1)	72(1)	55(1)	-3(1)	-12(1)	-9(1)
CL(20)	71(5)	133(8)	59(5)	-11(5)	1(4)	-27(5)
CL(21)	69(5)	87(6)	69(5)	-11(4)	-14(4)	15(4)
CL(22)	66(5)	77(6)	133(7)	22(4)	-41(5)	-29(5)
CL(23)	53(5)	116(7)	98(6)	-15(5)	-21(4)	-21(5)

The complete temperature factor is:

$$\exp[-\pi^2(a^2U_{11}h^2 + b^2U_{22}k^2 + c^2U_{33}l^2 + 2abU_{12}hk + 2acU_{13}hl + 2bcU_{23}kl)].$$

B.

Atom	$U*10^3$	Atom	$U*10^3$	Atom	$U*10^3$
N(10)	67(7)	C(63)	102(12)	H(23)	12
N(20)	62(6)	C(64)	130(15)	H(24)	12
C(12)	51(7)	C(65)	113(13)	H(25)	12
C(13)	48(6)	C(66)	96(11)	H(26)	12
C(14)	72(8)	N(30)	58(6)	H(53)	12
C(15)	69(8)	N(40)	57(6)	H(54)	12
C(16)	57(7)	C(32)	49(6)	H(55)	12
C(22)	58(7)	C(33)	62(8)	H(56)	12
C(23)	67(8)	C(34)	63(8)	H(63)	12
C(24)	81(9)	C(35)	73(9)	H(64)	12
C(25)	73(9)	C(36)	63(8)	H(65)	12
C(26)	64(8)	C(42)	52(7)	H(66)	12
N(50)	70(7)	C(43)	64(8)	H(33)	12
N(60)	84(8)	C(44)	80(9)	H(34)	12
C(52)	91(10)	C(45)	69(8)	H(35)	12
C(53)	146(17)	C(46)	65(8)	H(36)	12
C(54)	107(12)	H(13)	12	H(43)	12
C(55)	107(12)	H(14)	12	H(44)	12
C(56)	78(9)	H(15)	12	H(45)	12
C(62)	92(11)	H(16)	12	H(46)	12

The complete temperature factor is:

$$\text{Exp}\left[\frac{-U8\pi^2\sin^2\theta}{\lambda^2}\right] \quad \text{or} \quad \text{Exp}\left[\frac{-B\sin^2\theta}{\lambda^2}\right] \quad \text{where } B = U8\pi^2.$$

FIGURE 6.4.1:

Packing diagram for the unit cell of $[Ir(Hbpy\text{-}C^3,N')(bpy\text{-}N,N')Cl_2]^+$ $[IrCl_4(bpy)]^-$ down the (a) A-axis, (b) B-axis, and (c) C-axis.

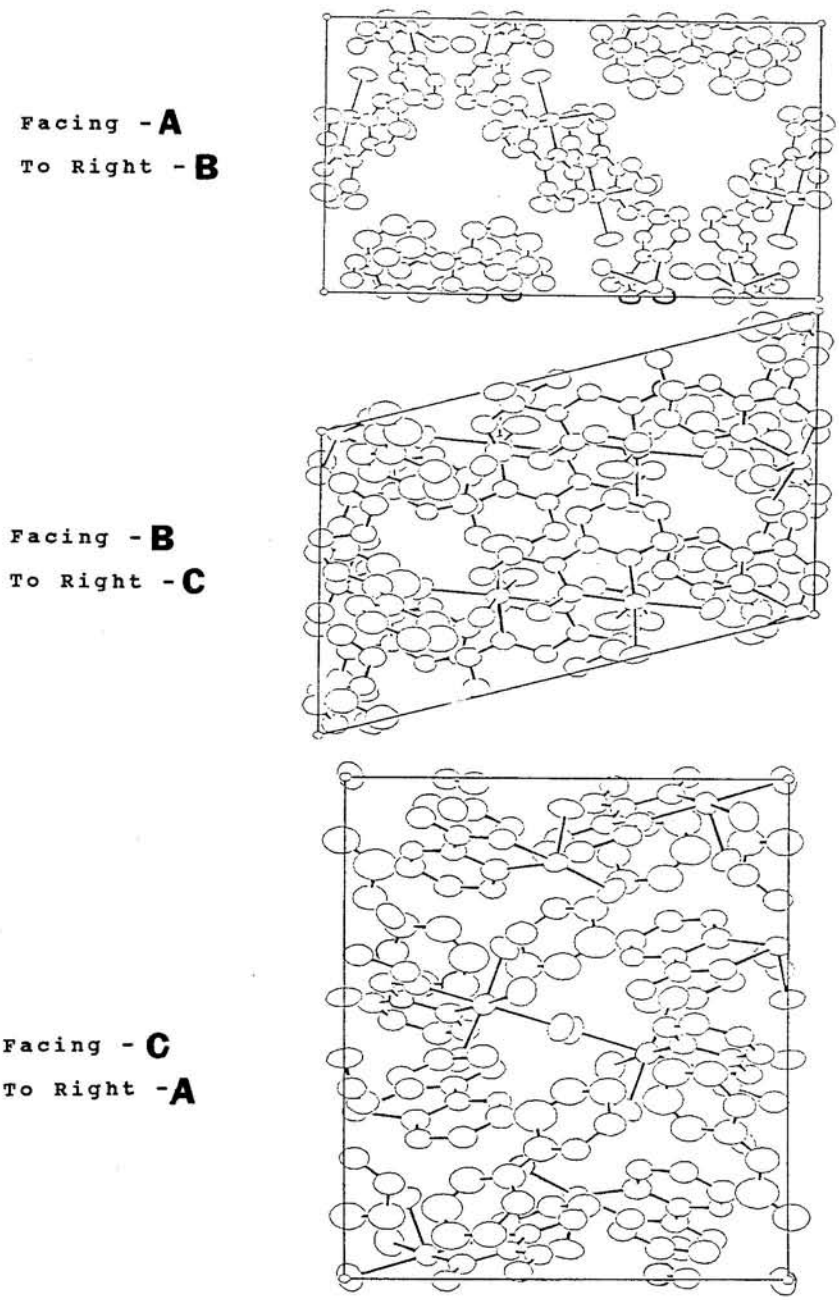

FIGURE 6.4.2:
Labeling Scheme for $[Ir(Hbpy\text{-}C^3,N')(bpy\text{-}N,N')Cl_2]^+[IrCl_4(bpy)]^-$
rotated at (X Y Z = 15, 180 , 0)

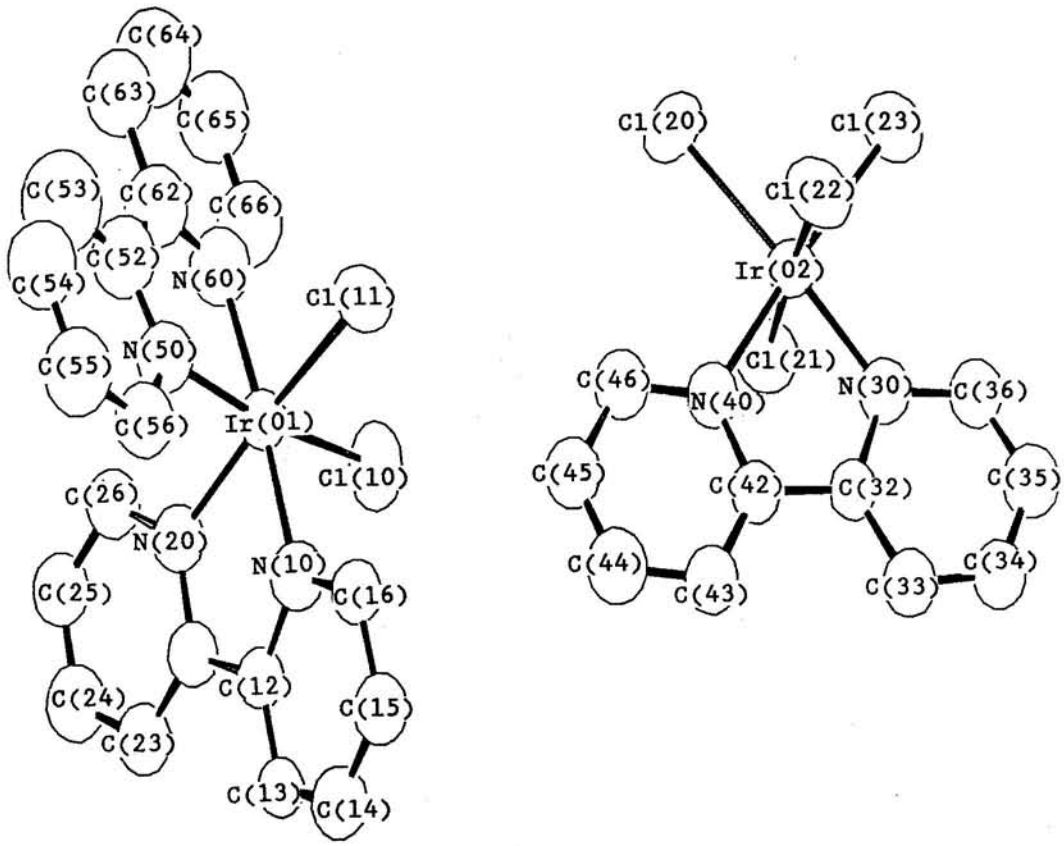

FIGURE 6.4.3:

ORTEP diagram for $[Ir(Hbpy\text{-}C^3,N')(bpy\text{-}N,N')Cl_2]^+[IrCl_4(bpy)]^-$ at rotation (X Y Z = 15, 180, -15)

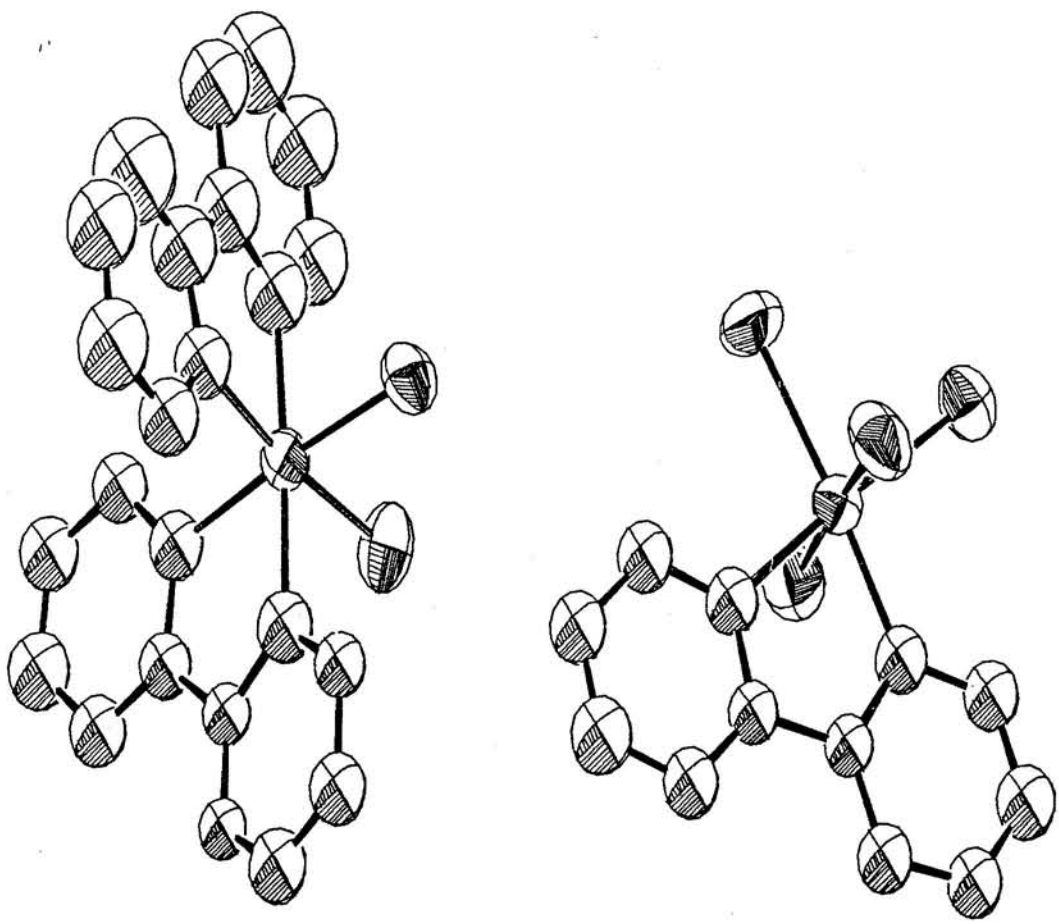

PART II: SUMMARY

The evidences for I in Chapter 5 strongly suggest an ortho-metalated bipyridyl dichloro-bridged complex of Ir (III). Elemental analysis, molecular weight determination, and mass spectroscopy indicate that there are two iridiums, four bipyridines, and four chlorides while the two reversible oxidative waves in the CV suggest a dinuclear complex. Furthermore, the CV redox waves for I indicate the metal center possesses electron density between that of an ortho-metalated Ir center as in $[Ir(ppy)_2Cl]_2$ and that of a chelated Ir center as in $Ir(bpy)_2Cl_2^+$. The ^1H NMR spectra strongly suggest two types of bipyridyl ligands in a "4", "4", "4" and "3" spin system with the 144.7 ppm resonance in the ^{13}C NMR spectrum suggestive of an ortho-metalated carbon. Finally, the acid/base luminescence dependence of I suggest there is a site for protonation analogous to that in $[Ir(bpy\text{-}C^3,N')(bpy\text{-}N,N')_2]^{2+}$.

I is easily made from II by recrystallization of the latter in DMSO/(aq)EtOH. Based on the evidence presented in Chapter 6, complex II is the third example of an ortho-metalated bpy iridium complex. Crystallographic analysis shows the unit cell for II contains two types of Ir center in an ion pair arrangement. From the NMR analysis and acid/base luminescence measurements, we propose that one of the bpy ligands in the cation is bonded to the iridium in an ortho-metalated fashion. The electron density map about the perimeter on one of the bpy rings (50/60) is consistent with this assertion in which the external N-atom of the ortho-metalated bpy is

protonated and hydrogen bonded to water. Although the crystallographic analysis does not give absolute confirmation of our contention, it does not rule it out.

The simplicity of the ^1H NMR spectra for **III** supports a cis-bpy complex. The mass spectrum, elemental analysis and NMR measurements are consistent with a cis-$[Ir^{IV}(bpy)_2Cl_2]Cl_2$ species; a d^5 low spin complex! In light of the reaction conditions, and some luminescence properties, the +4 oxidation state for **III** is not improbable, see Appendix E. In any event we do have crystals of this material; the structural analysis may provide some insight on this molecule.

Product **IV** is proposed as the trans-$[Ir(bpy)_2Cl_2]^+$. Our only evidence for this structure is the ^1H NMR spectra. The resemblance of this spectrum to that of trans-$[Ru(bpy)_2(CH_3CN)_2]$ and trans-$Rh(bpy)_2(H_2O)Cl^{+2}$ strongly advocates a trans complex, however.

The complexes presented in Part 2 were all prepared from a one pot synthesis. Although there are many products from this synthesis, selective precipitation using DMSO/(aq)ETOH proved useful in isolating **I**, **II**, **III** and **IV**. Iridium (IV) has a profound role in favoring ortho-metalated products as demonstrated by **I** and **II**; perhaps the preparation of the triply ortho-metalated complex starting with Ir(IV) and NC may be realized. Whatever role Ir(IV) plays in ortho-metalation reactions, it has nevertheless opened new synthetic doors towards novel iridium bipyridyl complexes.

LITERATURE CITED:

1. King,K.A.; Garces,F.O.; Sprouse,S.; Watts,R.J. in "Proceedings of the Seventh International Symposium on the Photochemistry and Photophysics of Coordination Compounds"; Yersin,H. and Volger,A. Ed., Springer-Verlag, Berlin, 1987; p.141.

2. Craig,C.A.; Garces,F.; Watts,R.J. Ibid.

3. Balzani,V.; Maestri,M.; Melandri,A.; Sandrini,D.; Chassot,L.; Deuschel-Cornioley,C.; Maeder,U.; Von Zelewsky,A. Ibid.

4. Ohsawa,Y.; Sprouse,S.D.; King,K.A.; DeArmond,M.K.; Hanck,K.W.; Watts,R.J. J. Phys. Chem. **1987** 91 1047

5. King, K.A.; Finlayson M.F.; Spellane,P.J.; Watts R.J. Sci. Pap. Inst. Phys. Chem. Res. **1984** 78 97

6. King,K.A.; Spellane,P.J.; Watts,R.J. J.Am. Chem. Soc. **1985** 107 1431.

7. Sprouse,S.D.; King,K.A.; Spellane,P.J.; Watts,R.J. J. Am. Chem.Soc. **1984** 106 6647

8. Maestri,M.; Sandrini,D.; Balzani,V.; Chassot,L.; Von Zelewsky,A. J. Am. Chem. Soc. **1987** 109 7720, and ref. therein.

9. Maestri,M.; Sandrini,D.; Balzani,V.; Chassot,L.; Von Zelewsky,A.; Jolliet,P. Helv. Chim. Acta. **1988** 71 134.

10. Maestri,M.; Sandrini,D.; Balzani,V.; Chassot,L.; Von Zelewsky,A.; Deuschel-Cornioley,C.; Jolliet,P. Helv. Chim. Acta. **1988** 71 1053, and ref. therein.

11. Watts, R.J.; Harrington, J.S.; Van Houten, J. J. Am. Chem. Soc. **1977** 99 2179.

12. Watts, R.J.; Harrington, J.S.; Van Houten, J. J. Adv. Chem. Ser. **1978** 168 157.

13. Wickramashinghe, W.A.; Bird, P.H.; Serpone, N. J. Chem. Soc. Chem. Commun. **1981** 1284.

14. Nord, G.; Hazell, A.; Hazell, E.; Wernberg, O. Inogr. Chem. **1983** 22 3429.

15. Spellane, P.J.; Watts, R.J.; Curtis, C.J. Inorg. Chem. **1983** 22 4060.

16. Kutal,C. Adv. Chem. Ser. **1978** 168 158

17. Grutsch,P.A.; Kutal,C. J. Am. Chem. Soc. **1986** 108 3108

18. Slama-Schwok,A.;Gershuni,S.; Rabani,J.; Cohen,H.; Meyerstein,D. J. Phys. Chem. **1985** 89:12 2460

19. Gillard, R.D.; Heaton, B.T.; Chem Comm., **1968** 75

20. Nonoyama,M. Bull.Chem.Soc.Jpn. **1974** 47 767

21. Nonoyama,M. J. Organomet. Chem. **1974** 82 271

22. Nonoyama,M. J. Organomet. Chem. **1975** 86 263

23. Nonoyama,M. J. Organomet. Chem. **1975** 92 89

24. Nanoyama,M. Bull. Chem. Soc. Jpn. **1979** 52:12 3749

25. Selbin,J.; Gutierrez,M.A. J. Organomet. Chem. **1981** 214 253

26. Parshall,G.W.; Chem. Comm. **1979** 139

27. Olah,G.A.; Chem. Comm. **1971** 240

28. Cerny,R.L; Sullivan,B.P.; Bursey,M.M; Meyer,T.J. Inorg. Chem. **1985** 24 397

29. Nicholson,R.S. Anal. Chem. **1965** 37:11 1351

30. Garces,F.O.; King,K.A.; Watts,R.J.; Inorg. Chem. **1988** 27 3464.

31. Kahl,J.L.; Hanck,K.; DeArmond,K. J. Phys. Chem. **1978** 82 540

32. Roffia,S.; Ciano,M.; J. Electroanal. Chem. **1978** 87 267

33. Spellane,P.J. "Ph.D.Thesis" University of California, Santa Barbara, 1985

34. Orellana,G.; Ibarra,C.A.; Santoro, J. Inorg. Chem. **1988** 27 1025

35. Reveco,P.; Medley,J.; Garber,A.R.; Bhacca,N.S.; Selbin,J. Inorg. Chem. **1985** 24 1096

36. Mader,U.; Jenny,T.; Zelewsky,A.-V. Helv. Chim. Acta **1986** 69 1085

37. Steel,P.J.; LaHousse,F.; Lerner,D.; Marzin,C. Inorg. Chem. 1983 22 1488

38. Cook,M.J.; Lewis,A.P.; McAuliffe,G.S.G.; Thomson,A.J. Inorg. Chim. Acta. 1982 64 25

39. Derome,A.E. "Modern NMR Techniques for Chemistry Research"; Balwin,J.E. ed., Pergamon Press: Oxford, U.K. 1986

40. Sanders,J.K.M.; Hunter,B.K.; "Modern NMR Spectroscopy, A Guide for Chemist"; Oxford University Press: Oxford, U.K. 1987

41. DeSimone,R.E.; Drago,R.S. Inorg.Chem. 1969 8:11 2517

42. Kahl,J.L.; Hanck,K.; DeArmond,K. J. Inorg. Chem. 1979 41 495

43. Sullivan,B.P.; Meyer,T.J. J.Chem. Soc. Chem. Comm. 1984 403

44. Harris R.K.; "Nuclear Magnetic Resonances Spectroscopy"; Pitman: Marshfield, Mass. 1983.

45. Lavallee,D.K.; Baughman,M.D.; Phillips,M.P. J. Am. Chem. Soc. 1977 99:3 718

46. Wash,J.L.; Durham,B.; Inorg. Chem. 1982 21 329

47. Durham,B.; Wilson,S.R.; Hodgson,D.J.; Meyer,T.J. J. Am. Chem. Soc. 1980 102:2 600

48. Wieland,S.; DiBenedetto,J.; Van Eldik,R.; Ford,P.C. J. Am. Chem. Soc. 1986 25 4893

CHAPTER 7

MISCELLANEOUS ORTHO-METALATED Ir(III) COMPLEXES

The most beautiful thing we can experience is the mysterious.
It is the source of all true art and science.

-Albert Einstein.

This chapter describes new iridium complexes that were prepared by the synthetic techniques described in Chapters 2 and 3. The preparation of the dimers described in Chapter 2 results in the formation of small amounts (<5%) of the triply ortho-metalated complex, $Ir(NC)_3$. One of these complexes, $Ir(mppy)_3$, will be discussed in this chapter.

Monomeric ortho-metalated derivatives are prepared by thermal bridge cleavage substitution of the dimers, Chapter 3. Two complexes, $[Ir(mppy)_2phen]^+$ and $[Ir(mppy)_2pic]$, where phen is 1,10-phenanthroline and pic is picolinic acid, are described here.

Finally, Professor Kazuhiko Mizuno prepared $[M(2\text{-}stpy)_2Cl]_2$, where M = Rh, Ir, and 2-stpy = 2-styrylpyridine (among others); the iridium dimer will be discussed here.

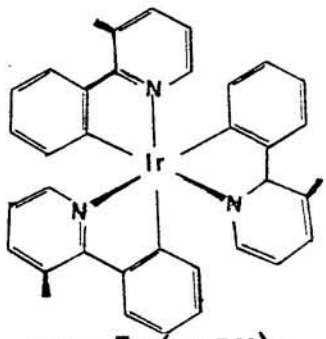

FAC-IR(MPPY)$_3$

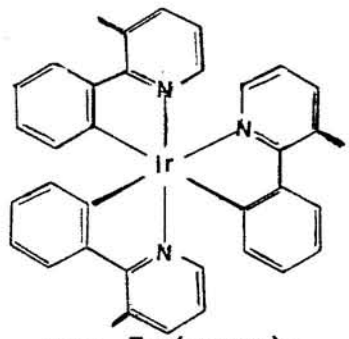

MER-IR(MPPY)$_3$

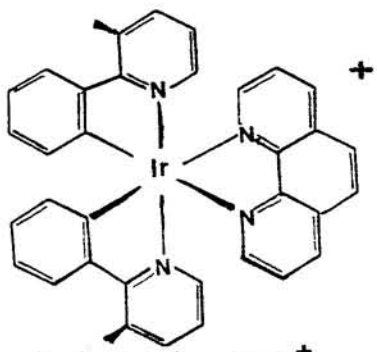

IR(MPPY)$_2$PHEN$^+$

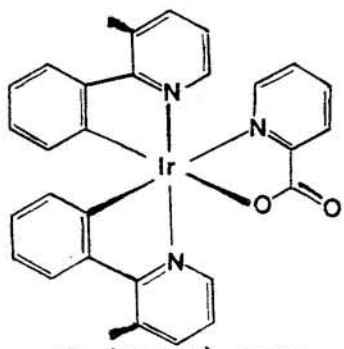

IR(MPPY)$_2$PIC

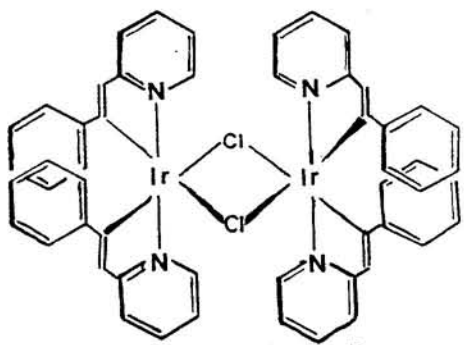

[IR(STPYY)$_2$CL]$_2$

I. Tris(3-methyl-2-phenylpyridine)Iridium (III), $Ir(mppy)_3$.

One of the side products from the preparation of $[Ir(NC)_2Cl]_2$, is the triply ortho-metalated $Ir(NC)_3$ complex; $Ir(ppy)_3$ was previously isolated by King[1]. We reasoned that the methyl-substituted derivatives would be more potent photo-reducing agents than $Ir(ppy)_3$ from our findings for the methyl-substituted dimer derivatives described in Part I, Table I and in Chapter 2. An undertaking to isolate and characterize the methyl substituted analogue, $Ir(mppy)_3$, was attempted and is described here.

Iridium (IV) chloride[2] (.500 mg, 1.5 mmol) was combined with 3-methyl-2-phenylpyridine (0.95 ml, 6.0 mmol) in 50 ml 2-ethoxy ethanol and 13 ml water and refluxed under a blanket of nitrogen for 24 hours at 135°C. After reflux, the solution was cooled to room temperature and the yellow precipitate collected via gravimetric filtration with the filtrate saved. The precipitate was washed with 60 ml (aq) EtOH 50%, and 60 ml acetone. The washings were combined with the filtrate, then rotary evaporated to dryness. A yellow-orange residue was left which was dissolved in 20 ml dichloromethane and washed three times with 5 ml aliquot, of 1 M HCl in a separatory funnel. The dichloromethane layer was extracted and washed with 6 ml of water to yield a bright yellow solution which was dried with anhydrous magnesium sulfate and filtered. Evaporating the solution to dryness by nitrogen purge, gave a faint green residue that emitted green under UV irradiation.

Preparative TLC was used to purify $Ir(mppy)_3$ using 1 mm thick silica plates. The plates were first pre-eluted to deactivate using 2:1:1 hexanes-dichloromethane-acetone elutant. We discovered that the best resolution in separating the "top green" band, $Ir(mppy)_3$, from all other components in the TLC plates, was by using an elutant composed of toluene-acetone-dichloromethane (1:2:1). More than 50 TLC plates were developed in the first isolation cycle by scrapping off the top green band of these plates and collecting the scrapings in a beaker. The scrapings were dissolved in dichloromethane, stirred overnight and vacuum filtered. Irradiation under short UV of the dichloromethane solution showed a more intense green emission than before; we proceeded to further purify this product in the dichloromethane solution by repeating the TLC procedure.

In the course of purifying $Ir(mppy)_3$ by repetitive TLC, we discovered that the product decomposed (as shown by ^1H NMR) by reacting with atmospheric oxygen or with the elutant. This is not surprising since these methyl-substituted analogues are expected to be potent photo-reductants; repetitive TLC results in reaction of the complex with oxygen or dichloromethane.

The ^1H NMR analysis $Ir(mppy)_3$ shows complicated resonances between 10.0 - 5.5 ppm, Figure 7.1.1a. There are ten resonances which can be fitted to 21 protons in the integration. This is reasonable for a mer-$Ir(mppy)_3$ complex, in which none of the ligands occupy equivalent sites. The overlapping signals are a consequence of protons in near degenerate environments in the complex.

The ^1H NMR spectrum of $Ir(mppy)_3$, after more TLC, Figure, 7.1.1b showed a forest of complicated resonances between 8.2 - 6.0 ppm. This is similar to that of fac-$Ir(ppy)_3$ which shows resonances between 8.0 and 6.5 ppm.[3,4] Although the ^1H NMR spectrum for $Ir(mppy)_3$ indicates significant decomposition of our product the solution continued to emit a green luminescence upon UV irradiation. The photophysical properties of $Ir(mppy)_3$ alone, warrant a few paragraphs in this chapter, albeit the product was never purified. The following photophysical results are from the $Ir(mppy)_3$ material with the ^1H NMR spectrum shown in Figure 7.1.1a

The absorption profile, shown in Figure 7.1.2a, consists of band maxima at 235, 258, 320, 450, 660 nm. The 660 nm band is shown as a broad feature that starts at 520 nm and extends to 780 nm.

The room temperature luminescence spectrum, Figure 7.1.2b, shows invariant emission band maximum at 513 nm upon excitation of 330 to 390 nm and an excitation spectrum showing band maxima at 371, 392, 429 and 455 when monitored at 520 nm.

Time resolved emission at 77 K with time delays at 0.05, 0.1, 0.5, 1.0, 5.0, 10.0, 15.0 and 20.0 μs are shown in Figure 7.1.3. At short times, the emission has a structured profile with band maxima at 486, 500 and 516 nm. Towards longer delay, the emission blue shifts and becomes poorly resolved. The lifetime in ETOH-MeOH is 120 ns at room temperature and 5 μs at 77 K.

Based on the initial properties described here, $Ir(mppy)_3$ is a more potent photo-reducing agent than $Ir(ppy)_3$; it is this attribute which also makes it difficult to isolate. The possible future success of isolating these methyl-substituted triply ortho-metalated derivatives might be improved with glove box techniques.

FIGURE 7.1.1:

^1H NMR spectra for $Ir(mppy)_3$ in dichloromethane-d_2. (a) mer-$Ir(mppy)_3$ (b) $Ir(mppy)_3$ after subsequent TLC.

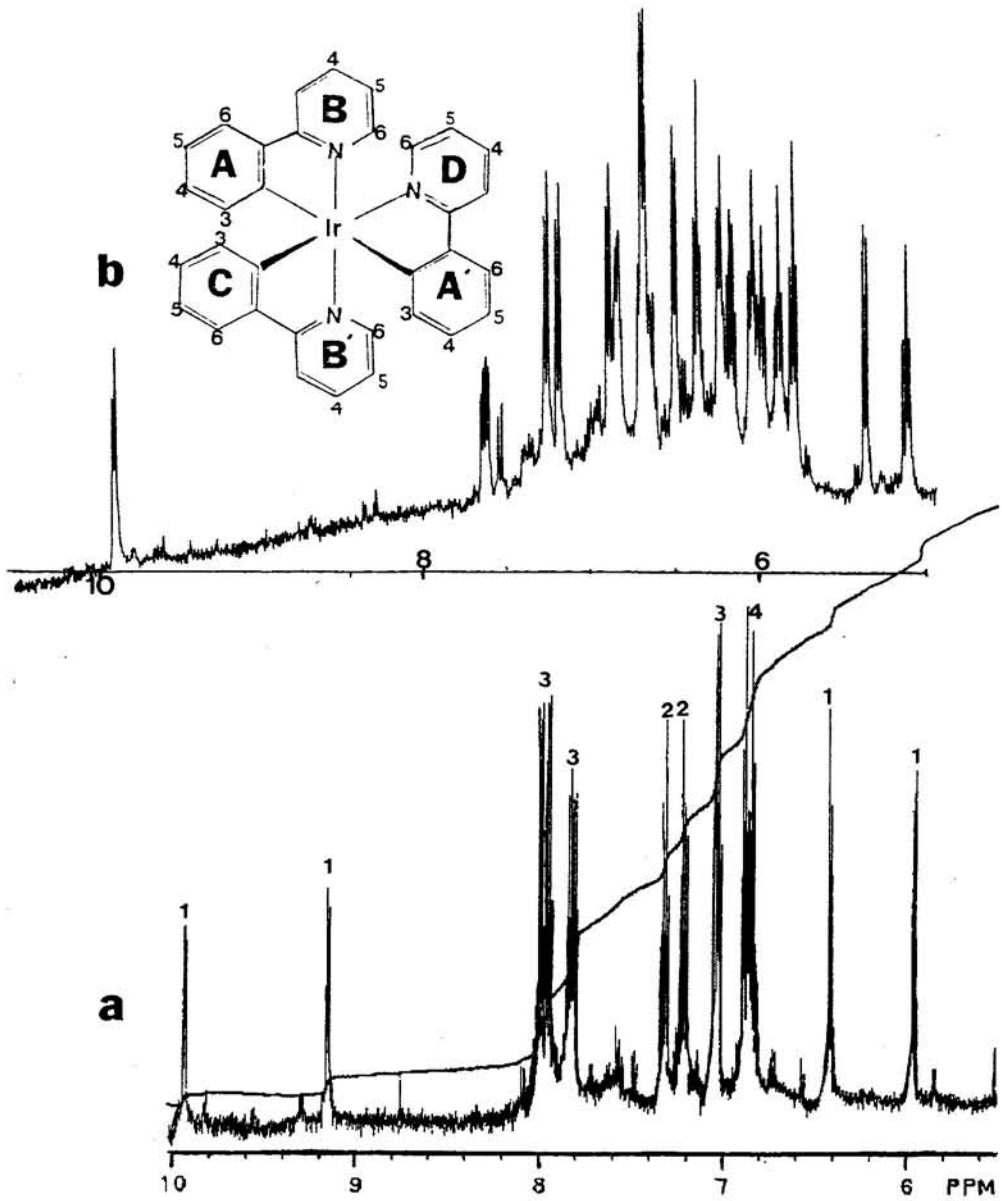

FIGURE 7.1.2:

Room temperature absorption and emission spectra for $Ir(mppy)_3$ in dichloromethane. (a) Absorption (b)---------excitation spectra monitored at 520 nm, ———————— emission spectra excited at 340,360,370,380,390 and 400 nm.

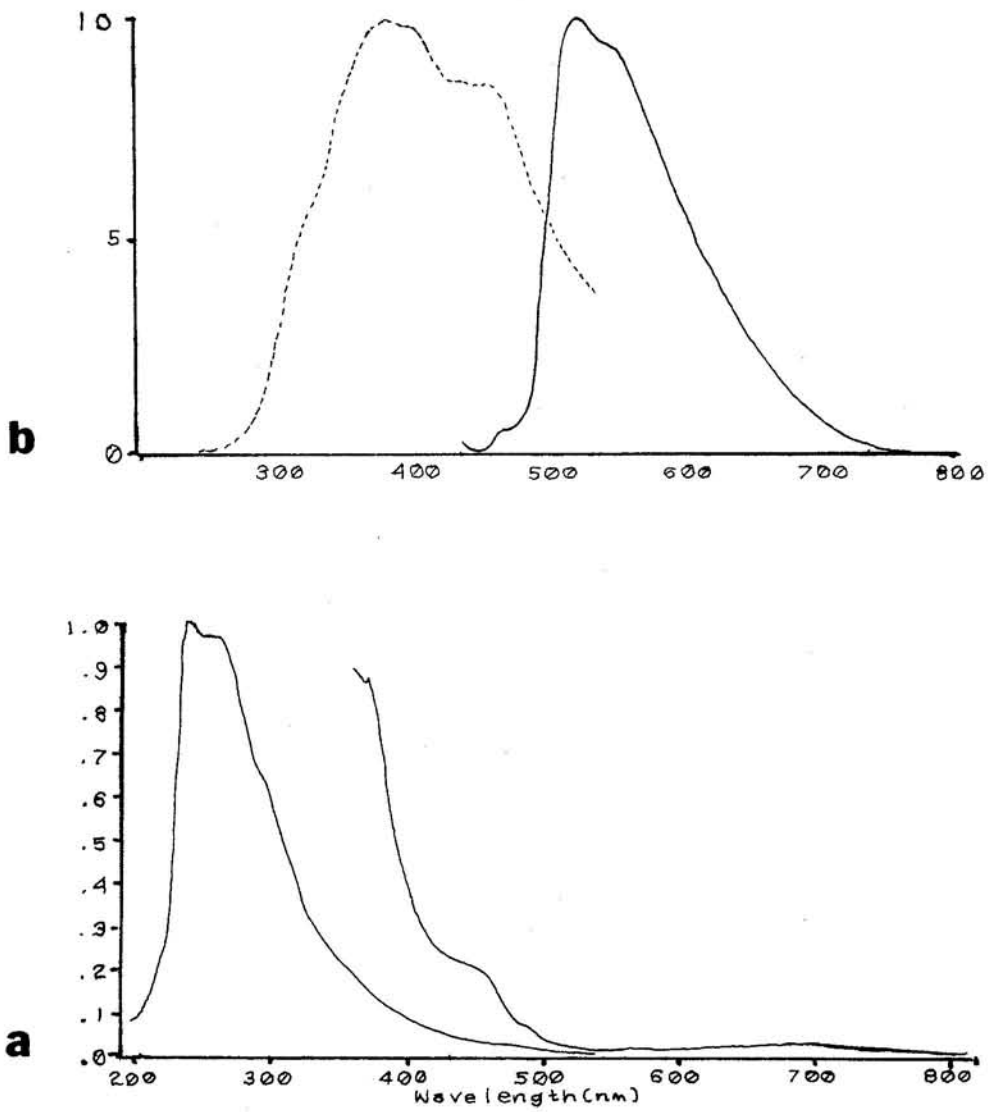

FIGURE 7.1.3:

Time-resolved-emission for $Ir(mppy)_3$ at 77 K, EtOH-MeOH (4:1 v/v) at 0.05, 0.1, .5, 1.0, 5.0, 10.0, 15.0, 20.0 μs delays.

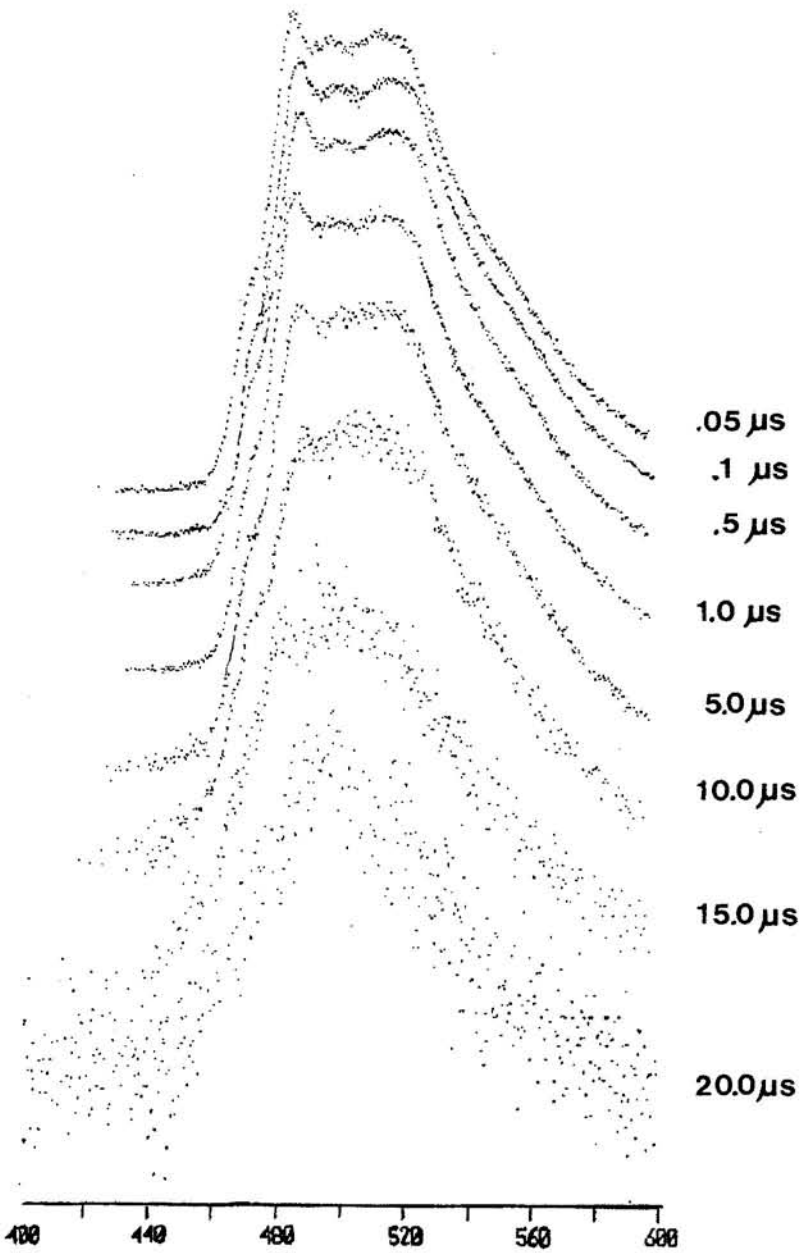

II. 1,10-Phenanthroline bis(3-methyl-2-phenylpyridine) Iridium (III), $[Ir(mppy)_2phen]^+$.

The $[Ir(mppy)_2phen]^+$ monomer is prepared in the analogous manner as the monomeric ortho-metalated bpy derivatives described in Chapter 3.[4-6] The ^1H NMR spectrum of $[Ir(mppy)_2phen]^+$ in dichloromethane-d_2, Figure 7.2.1b, shows eleven resonances between 6.0 to 9.0 ppm. The ^1H 2D COSY spectrum, Figure 7.2.2, separates the contours to four distinct spin systems containing one, three, three and four resonances. J-correlation connectivity of these resonances provide the assignments of the protons in the A, B, C and D rings in the complex. Carbon resonances are assigned in the ^{13}C NMR spectrum by mapping the contours in the CSCM via J_{C-H} coupling, Figure 7.2.3. Proton and carbon assignments for $[Ir(mppy)_2phen]^+$ are summarized in Table 7.1.

The absorption spectra for $[Ir(mppy)_2phen]^+$ in dichloromethane, Figure 7.2.4, shows absorption maxima at 232, 264, 286(sh), 308(sh), 336, 382, 414, and 464 nm. The visible bands are assigned to charge transfer transitions analogous to those of the $[Ir(NC)_2bpy]^+$ monomers described in Chapter 3. The room temperature luminescence in dichloromethane shows a structureless broad maximum at 585 nm.

FIGURE 7.2.1:

^{1}H NMR spectra for $[Ir(mppy)_2phen]^+$ in dichloromethane-d_2.
(a) 10 - 0 (b) 9 - 6 ppm.

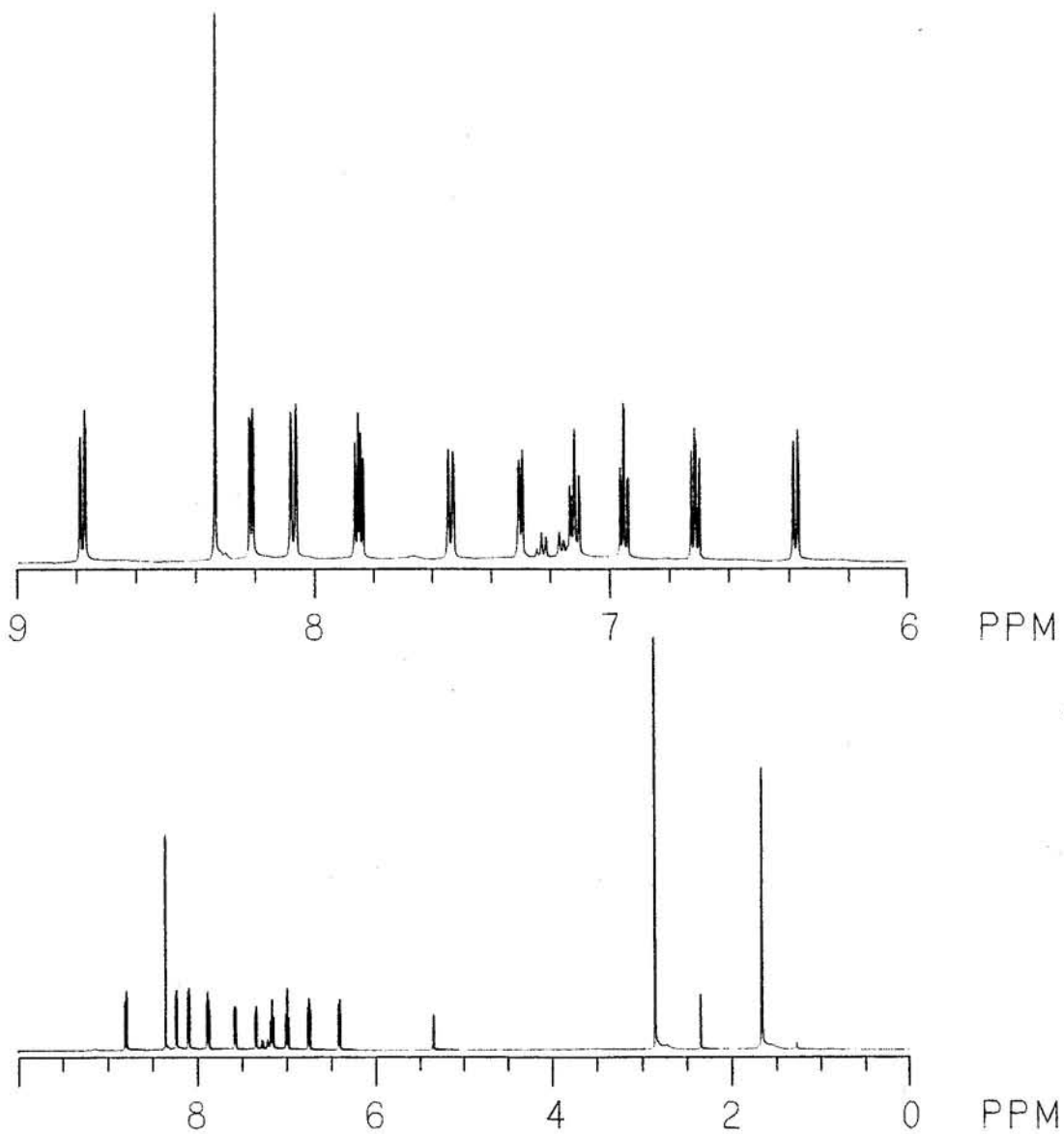

FIGURE 7.2.2:

^{1}H 2D COSY spectrum for $[Ir(mppy)_2phen]^+$ in dichloromethane-d_2.

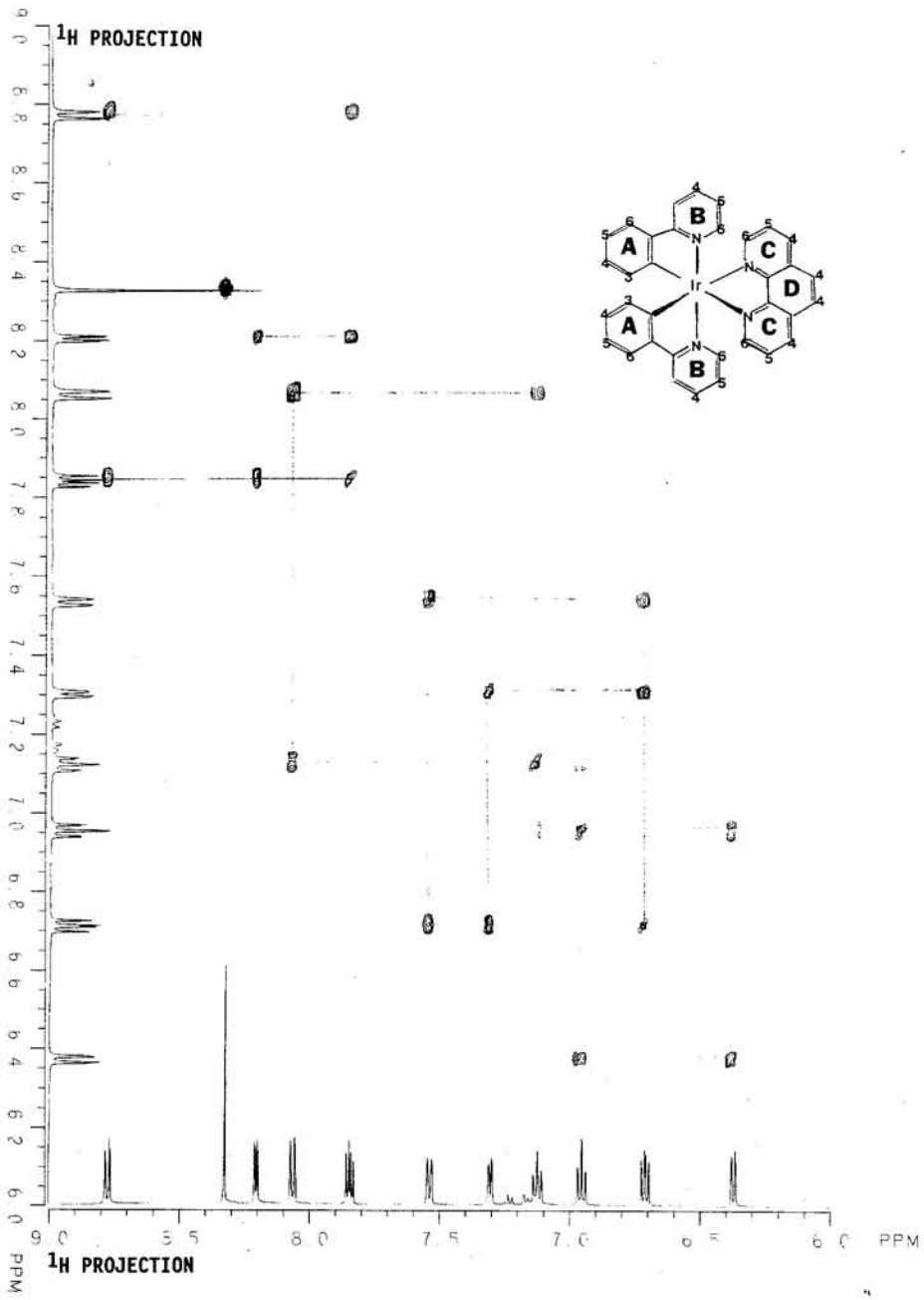

FIGURE 7.2.3:

CSCM spectrum for $[Ir(mppy)_2phen]^+$ in dichloromethane-d_2.

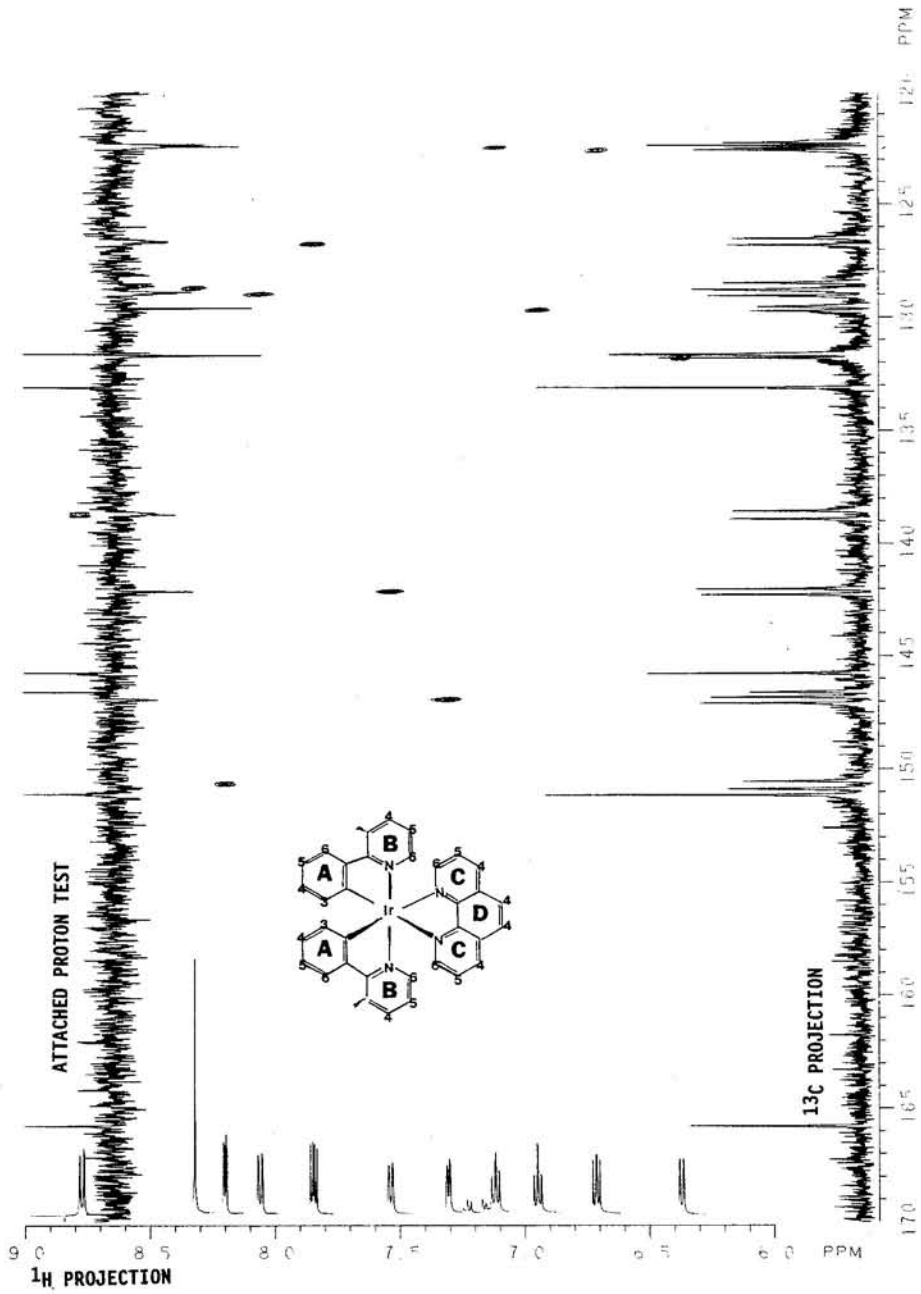

FIGURE 7.2.4:

Absorption spectra for $[Ir(mppy)_2phen]^+$ in dichloromethane.

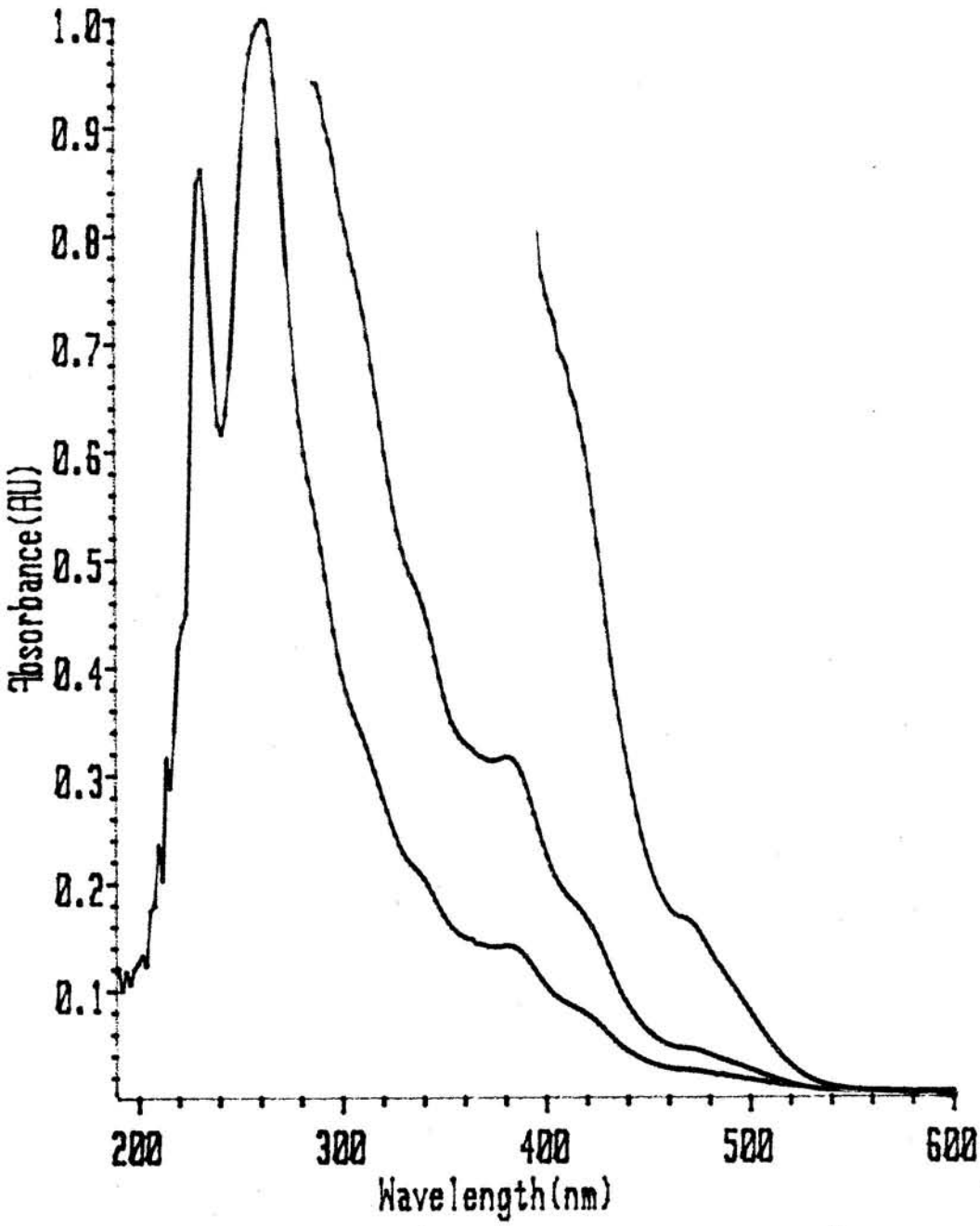

III. Picolinate bis(3-methyl-2-phenylpyridine) Iridium (III), [Ir(mppy)$_2$pic]

In the same manner that [Ir(mppy)$_2$phen]$^+$ was prepared, combination of picolinic acid,(7.4 mg, 60.05 mmol) with [Ir(mppy)$_2$Cl]$_2$, (33.9 mg, 30.05 mmol) results in green crystals of [Ir(mppy)$_2$pic] (39.07 mg, 16%) suitable for X-ray analysis.

The complexity of the ^{1}H NMR spectrum for Ir(mppy)$_2$pic, Figure 7.3.1, results from the loss of symmetry in the molecule because of the asymmetric picolinic ligand. Although there are five type of rings in Ir(mppy)$_2$pic, some protons in the A, A′ and B, B′ rings (see inset) are in near degenerate environments. The ^{1}H NMR spectrum shows fourteen resonances between 8.8 - 6.0 ppm, integrating for seventeen protons which is consistent with an asymmetric complex. Using the initial assignments of the two high field doublets (δ = 6.15, 6.39) to the A$_3$, A′$_3$ protons respectively, and comparing the ^{1}H assignments from [Ir(mppy)$_2$bpy]$^+$ and [Ir(mppy)$_2$phen]$^+$, the protons in Ir(mppy)$_2$pic are assigned by J-connectivity of the COSY spectrum, Figure 7.3.2. The proton assignments, Table 7.1, indicate that the A$_6$, A′$_6$; A$_5$, A′$_5$; and A$_4$, A′$_4$ are in near degenerate environments with the proton resonances in the prime (′) spin system at higher field relative the unprime A spin system because the latter A′ ring is trans to the π-acceptor pyridyl ring of the picolinic ligand while the former A ring is trans to the σ-donor oxygen.

Owing to the complexity and poor resolution of the ^{13}C NMR spectrum, Figure 7.3.3, the carbon resonances are not assigned.

Room temperature UV irradiation of $Ir(mppy)_2pic$ in dichloromethane results in a bright green glow. The absorption spectra, Figure 7.3.4, shows band maxima at 230, 260, 312, 354, 402 and 446 nm with epsilon on the order of 10^{-4} M^{-1} cm^{-1} in the visible region.

Recently, a series of trans-ruthenium picolinate derivatives were reported in which the complexes undergoes reversible pH-dependent oxidation and reduction processes.[7] Although not investigated, $Ir(mppy)_2pic$ does possess the potential to exhibit similar properties. In this way, this complex may provide means of "tuning" the excited state redox potential by adjusting the pH.

FIGURE 7.3.1:

^1H NMR spectra for $Ir(mppy)_2pic$ in dichloromethane-d_2.
(a) 10 - 0 (b) 9 - 6 ppm.

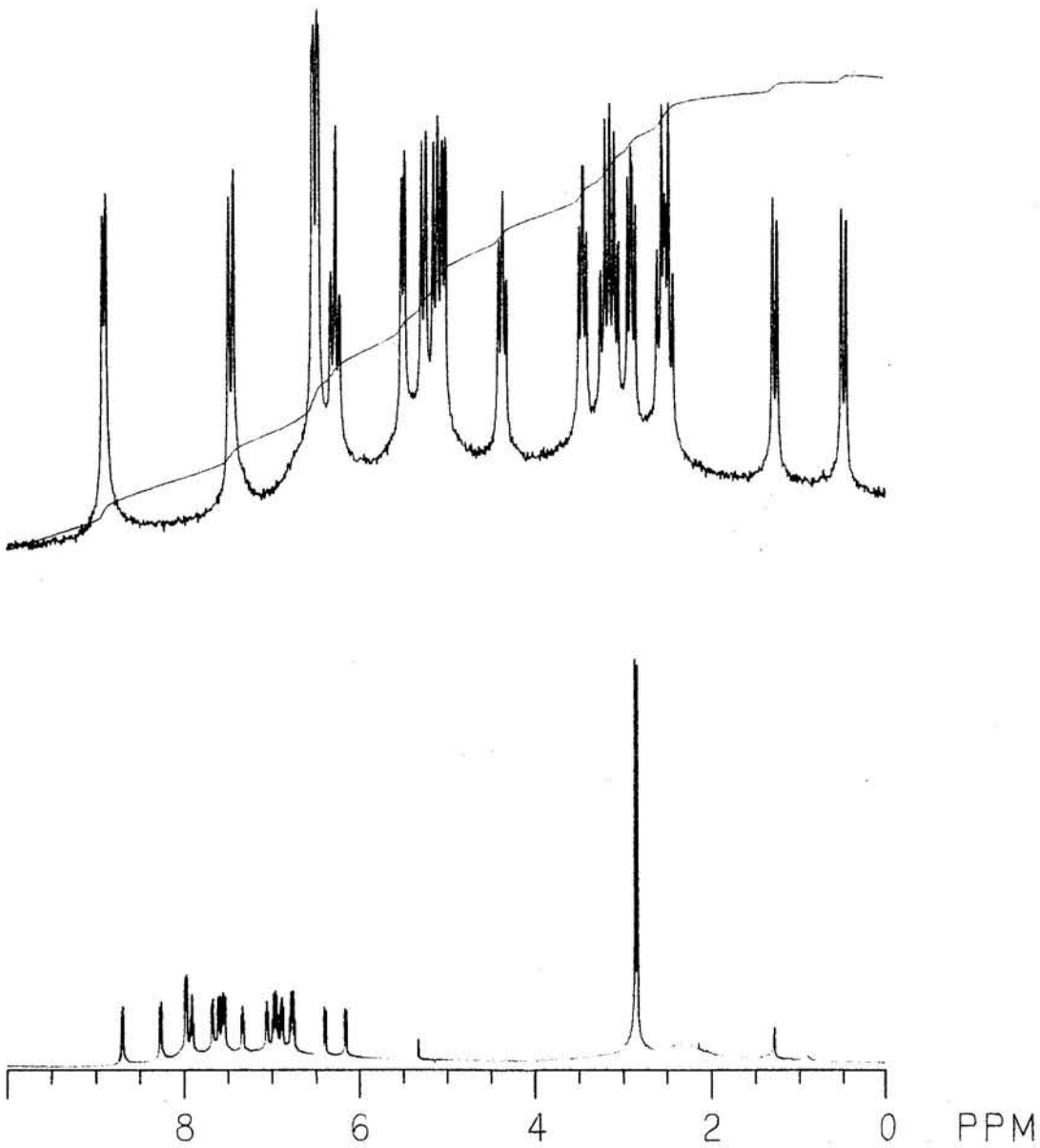

FIGURE 7.3.2:

^1H 2D COSY spectrum for $Ir(mppy)_2pic$ in dichloromethane-d_2.

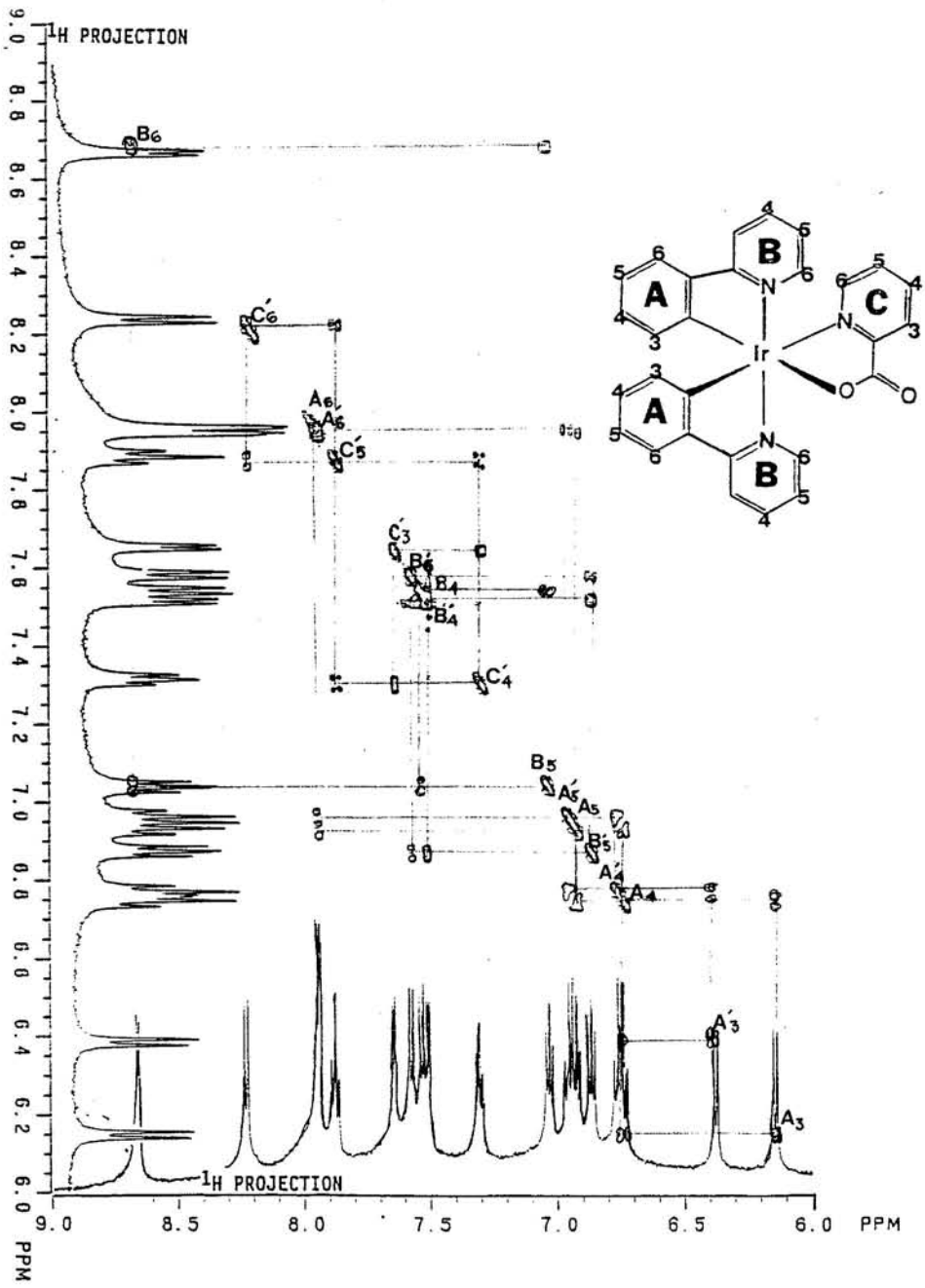

FIGURE 7.3.3:

^{13}C NMR spectra for $Ir(mppy)_2pic$ in dichloromethane-d_2.
(a) 200 - 0 (b) 170 - 110 ppm.

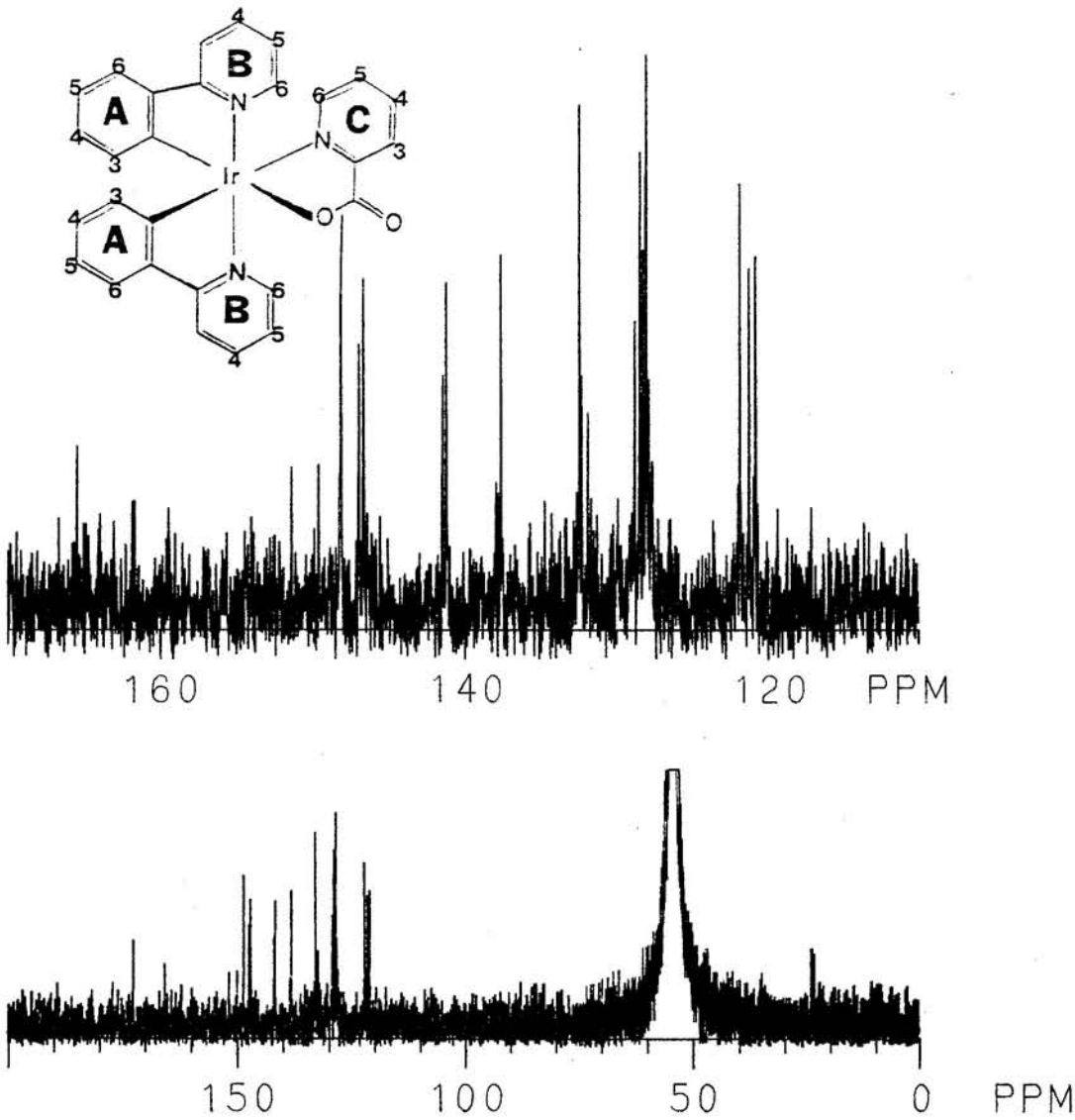

FIGURE 7.3.4:

Absorption spectra for $Ir(mppy)_2pic$ in dichloromethane.

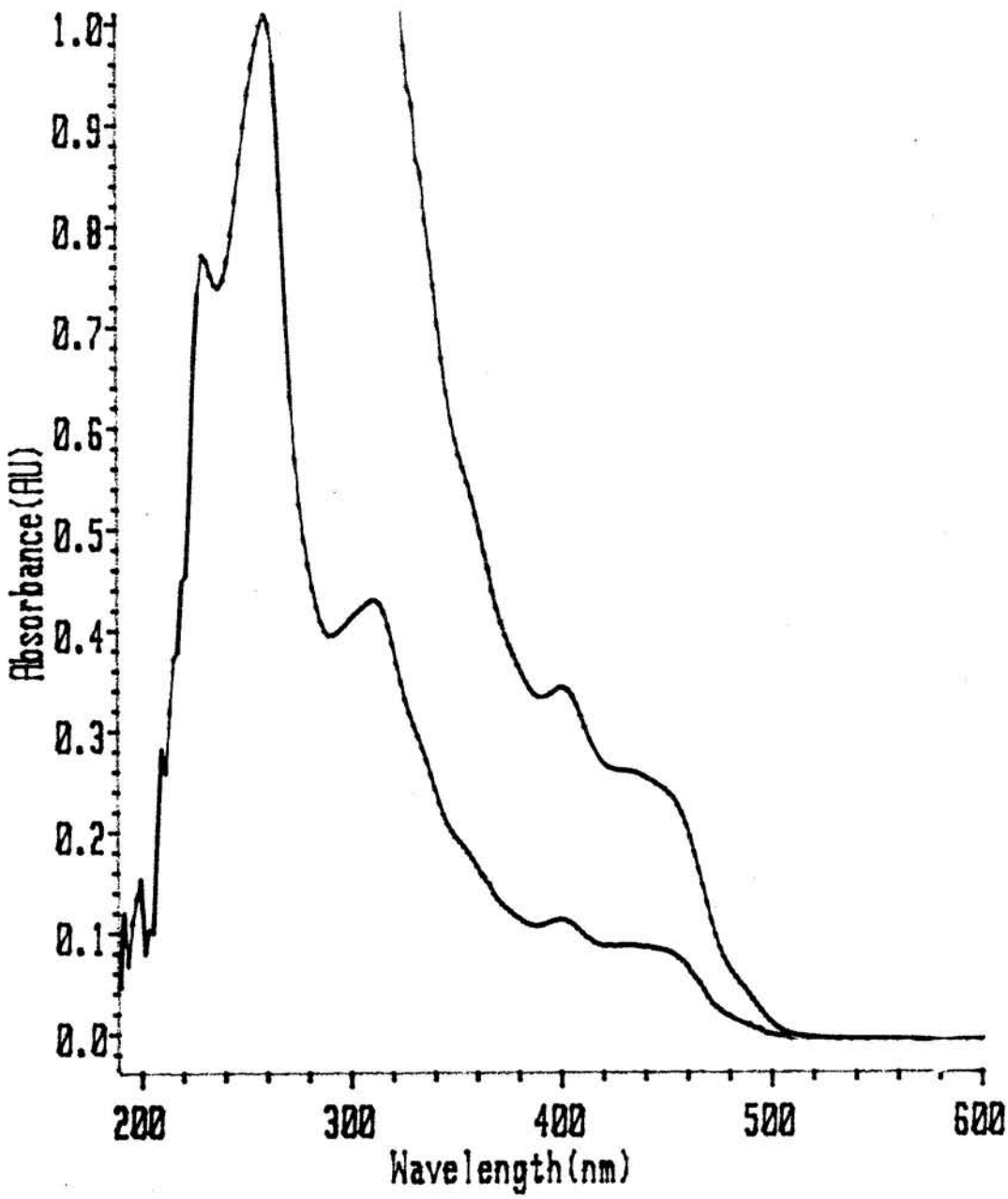

IV. Tetrakis (2-styrylpyridine)-μ-Dichlorodiiridium, $[Ir(stpy)_2Cl]_2$.

Our lab was privileged to host a visiting Professor from the University of Osaka Prefecture in the winter of 87-88. Professor Kazuhiko Mizuno synthesized a number of ortho-metalated complexes using both iridium and rhodium. One of these complexes, $[Ir(stpy)_2Cl]_2$ where stpy is 2-styrylpyridine, is described here.

The synthesis and work-up of this product is analogous to that of the dimers in which combination of iridium trichloride hydrate (146 mg) and 2-styrylpyridine (285 mg) yields $[Ir(stpy)_2Cl]_2$ as a pale orange powder (203 mg). The melting point is in excess of 300°C, but noticeable decomposition occurs at 250°C. Mass spectroscopy is consistent with a dichloro-bridged ortho-metalated species giving the following m/e analysis: 588 (4.5%), 553 (3.2%), 210 (23.8%), 182 (100% base peak), and 180 (94%).

The complete NMR analysis (^1H, ^{13}C, APT, COSY and CSCM) was realized, Table 7.1 summarizes the carbon and proton assignments.

The absorption spectrum for $[Ir(stpy)Cl]_2$ in dichloromethane, Figure 7.4.1a, shows band maxima at 198, 266, 310, 386 and 456 nm. These band maxima are higher energy that that of $[Ir(ptpy)_2Cl]_2$ and $[Ir(mppy)_2Cl]_2$. The low temperature (77 K) emission spectrum in EtOH-MeOH (4:1 v/v), Figure 7.4.1b (inset), shows band maxima at 591 and 637 nm. The large differences in the 460 nm absorption maximum and the 591 nm emission maximum suggest that $[Ir(stpy)_2Cl]_2$ possesses large nuclear distortion in the excited state.

FIGURE 7.4.1:

Absorption/Emission spectra for $[Ir(stpy)_2Cl]_2$.
(a) Room temperature absorption in dichloromethane
(b) Low temperature (77 K) in EtOH-MeOH (4:1 v/v) excit at 380 nm.

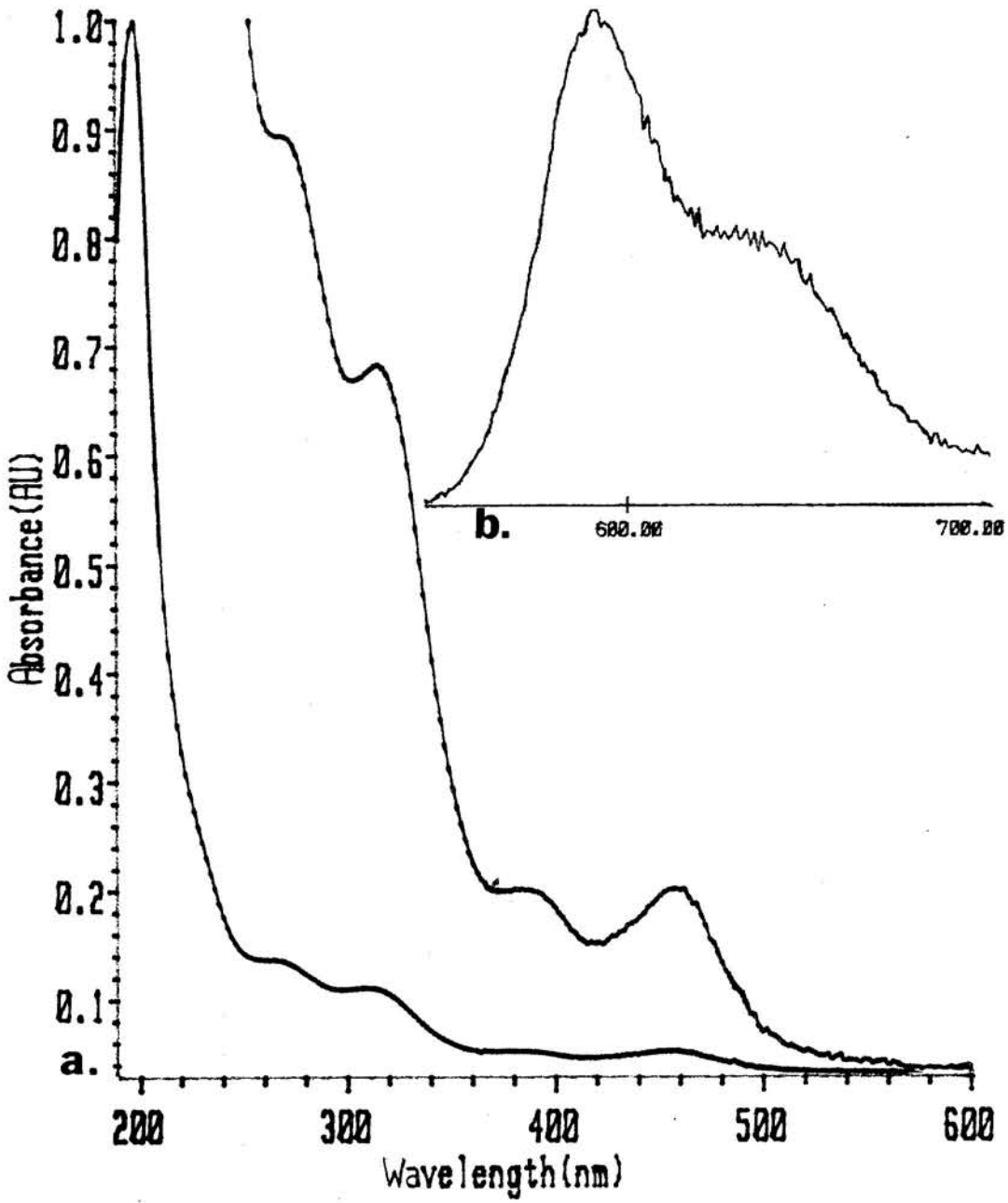

TABLE 7.1

^{1}H and ^{13}C NMR assignment for $[Ir(mppy)_2phen]^+$, $Ir(mppy)_2pic$, and $[Ir(stpy)_2Cl]_2$ in dichloromethane-d_2 (vs. TMS)

A. $^{1}H/^{13}C$ - $[Ir(mppy)_2phen]^+$:

A_1 (-/146.6); A_2 (-/145.8); A_3 (6.70/131.8); A_4 (6.95/129.5); A_5 (7.13/122.3); A_6 (8.06/129.0); B_2 (-/151.2); B_3 (-/133.0); B_4 (7.30/147.0); B_5 (6.71/122.4); B_6 (7.55/142.2); C-D_2 (-/165.8); C-D_3 (-/131.6); C_4 (8.20/150.8); C_5 (7.85/126.5); C_6 (8.78/138.7); D_4 (8.33/128.8).

B. ^{1}H - $Ir(mppy)_2pic$:

A_3 (6.15); A'_3 (6.39); A_4 (6.75); A'_4 (6.75); A_5 (6.95); A'_5 (6.95); A_6, (7.97); A'_6 (7.99); B_4 (7.54); B'_4 (7.52); B_5 (7.04); B'_5 (6.87); B_6 (8.67); B'_6 (7.59); C_3 (7.65); C_4 (7.32); C_5 (7.90); C_6 (8.24).

C. $^{1}H/^{13}C$ - $[Ir(stpy)_2Cl]_2$

A_1 (-/169.68); A_2,A_6 (6.67/124.63); A_3,A_5 (6.78/127.00); A_4 (6.86/125.06); B_2 (-/170.07); B_3(7.09/119.20); B_4 (7.17/135.29); B_5 (5.87/118.21); B_6 (7.96/150.47); α (6.55/129.55); β (-/147.41).

LITERATURE CITED:

1. King,K.A.; Spellane,P.J.; Watts,R.J. J.Am. Chem. Soc. **1985** 107 1431.

2. Based on the success of ortho-metalating bpy ligands using Ir(IV) (chp 5), we rationalized that the yield of the triply ortho-metalated specie may be increased if we start with Ir(IV).

3. Spellane,P.J. "Ph.D.Thesis" University of California, Santa Barbara, 1985

4. King,K.A. "Ph.D.Thesis"; University of California, Santa Barbara, 1986

5. Ohsawa,Y.; Sprouse,S.D.; King,K.A.; DeArmond,M.K.; Hanck,K.W.; Watts,R.J. J. Phys. Chem. **1987** 91 1047

6. King, K.A.; Finlayson M.F.; Spellane,P.J.; Watts R.J. Sci. Pap. Inst. Phys. Chem. Res. **1984** 78 97

7. Llobet, A.; Doppelt,P.; Meyer,T.J. Inorg. Chem. **1988** 27 514

APPENDIX A

NMR SPECTROSCOPY

1. NMR Measurements

We use NMR spectroscopy primarily to answer questions concerning the purity and structure of complexes prepared in our lab. Classical methods of analysis such as melting point, elemental analysis, and TLC do not always give unambiguous results. NMR spectroscopy offers a convenient technique that provides fast reliable answers to these questions. Free ligand contamination, for example, can easily be detected because proton resonances from the ligand occur in a different spectral region than those of the chelated form. Moreover, a mixture of products can be confirmed because of its complicated spectrum in contrast to the simpler ^{1}H NMR spectrum from a sample containing only a single species. Furthermore, geometric isomers can be assessed because a ^{1}H or ^{13}C NMR spectrum of isomers will detect nonequivalent ligands from the unusual chemical shifts which can diagnose structural configurations of the ligands i.e., cis, trans configuration. For our purpose, NMR spectroscopy provides information on the reaction products, dynamic processes, and structural properties of molecules which in turn may offer insights into the luminescence properties of complexes prepared in this lab.

The development of high resolution NMR spectrometers and ingenious pulse sequences, has accessed a wealth of structural information that otherwise may not have been obtained from other spectroscopic techniques. The NMR literature has seen an explosion of reviews in recent years demonstrating the popularity of this utilitarian spectroscopic technique. In particular, the development of two dimensional pulse sequences has revolutionized the field of NMR. It is not my intention to provide a comprehensive discussion on these pulse sequences or to review the recent methods available in NMR spectroscopy. There are many articles, reviews and texts available that would provide clearer explanations.[1-4] Rather, I will attempt to explain enough about selected pulse sequences so that you will know what type of information may be obtained from these NMR experiments. Through the work covered in this dissertation, I hope that you will appreciate the viability of these NMR experiments to simplify complicated NMR spectra and provide structural information especially for organometallic compounds.

The six major pulse sequences we used to simplify ^{1}H and ^{13}C NMR spectra are selective decoupling (SD), nuclear Overhauser enhancement (nOe), two dimensional homonuclear shift correlation spectroscopy (COSY), single frequency off-resonance decoupling (SFORD), attached proton test (APT), and $^{1}H/^{13}C$ heteronuclear correlation spectroscopy (CSCM). The first three were used to elucidate ^{1}H NMR spectra and provide structural information based on

^{1}H chemical shifts. The last three were used to clarify the ^{13}C NMR spectra and to afford carbon resonance assignments; the SFORD technique will not be reviewed here.

There are other pulse sequences available that may be more appropriate to a particular problem. Two excellent texts providing a practical review of these experiments are: *Modern NMR Spectroscopy: A Guide for chemist* by J.K.M. Sanders and B. Hunter[3]; and *Modern NMR Techniques for Chemistry Research* by A.E. Derome[4]. The five experiments mentioned above were selected, however, for their simplicity and their capacity to provide maximum information with little set-up effort. Historically, the SFORD was an important technique, but because it is time consuming and suffers from poor resolution, it has been replaced by more elaborate pulse sequence experiments such as DEPT, INEPT and APT or heteronuclear two-dimensional correlation experiments.[5,6] All of the experiments described here can be found in the "Library of Standard Pulse Sequence" in Appendix A of the GN-500 spectrometer software manual.

^{1}H, ^{13}C, APT, nOe, COSY and CSCM experiments were executed on a General Electric GN-500 FT-NMR spectrometer. The SD experiment was done on a Nicolet NT-300 FT NMR spectrometer. T_1 relaxation was measured by inversion recovery. A 90° pulse widths of 30 and 8μs, spectral windows of 7500 and 15000 Hz, recycled delays of 1.5 and 3.0 s were used for the ^{1}H and ^{13}C NMR measurements, respectively. For both types of experiments, 16 K data points were used.

i. Selective decoupling[3,4,7] or double resonance may be illustrated by considering an AB spin system. In this spin system there are two orientations for each nuclei, α and β. In a double resonance experiment, nucleus A is observed with the normal RF field (observe frequency) while simultaneously irradiating nucleus B with a second, much stronger RF field (decoupling frequency). Saturation at B induces rapid transition between the α and β states such that nucleus A can not distinguish the separate orientation, but only experiences the average orientation of B. In effect, the coupling (J_{A-B}) between the two nuclei disappears and the A-doublet collapses into a singlet. For a more complicated first order spin system, SD can simplify the NMR spectrum by eliminating unwanted, complicated coupling which enables one to identify nuclei mutually coupled. If, however, the spectrum contains complicated overlapping resonances, then 2D pulse techniques become more advantageous.

The selective decoupling experiment for $[Ir(ptpy)_2Cl]_2$, Figure A.1 **a-c**, demonstrates the J-coupling relationship between mutually coupled nuclei. Spectrum **a** shows the nondecoupled spectrum, while spectra **b** and **c** show selected resonance stimulated (↓), and resonances affected (*). In spectrum **b**, saturation of the B_6 resonance at 9.21 ppm causes the 6.79 ppm B_5 triplet to collapse into a doublet. Similarly in spectrum **c**, saturation of the 6.67 ppm A_5 resonance results in the collapse of the 7.44 ppm, A_6 doublet into a singlet.

Figure A.1

Selective Decoupling ^{1}H NMR spectrum for $[Ir(ptpy)_2Cl]_2$; 9.5-5.5ppm (a) Normal ^{1}H spectrum, (b) excitation at 9.21 ppm, (c) excitation at 6.67 ppm.

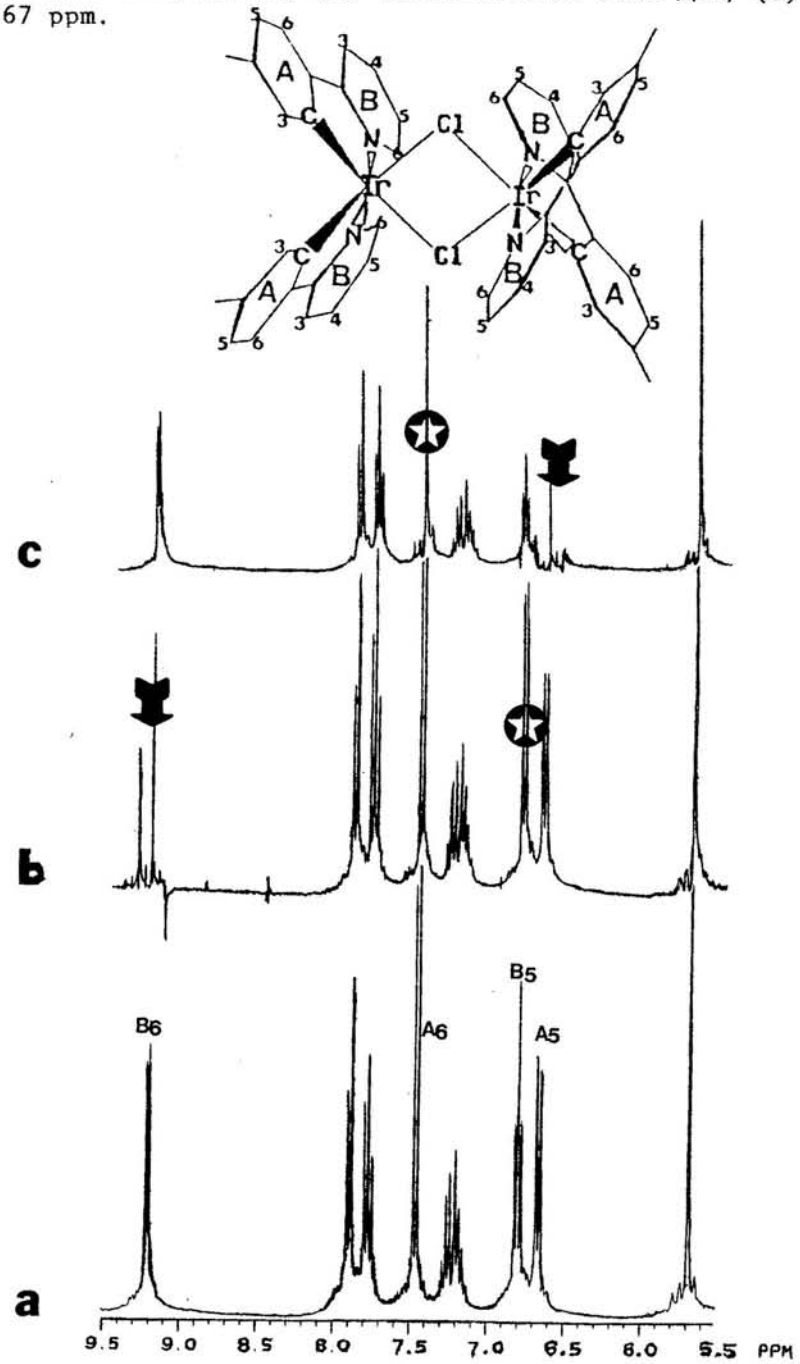

ii. **Nuclear Overhauser effect**[3,4,7,8] exploits the dipolar coupling to increase the populations between energy levels connected by transitions of a low magnetogyric-ratio nucleus. The basic idea behind the nOe is to couple the large ΔE of one spin, i.e., ^{1}H, to the smaller ΔE of another, i.e., ^{13}C. By doing so, the less sensitive nucleus (^{13}C) gains an enhancement of intensity proportional to the magnetogyric ratio of the sensitive nucleus (^{1}H), as shown in equation A.1.

(A.1) $$I(s) = I_o\ (1 + \eta)$$

Here η is the nOe factor and is equal to $0.5(\gamma_s/\gamma_i)$, γ is the magnetogyric ratio, **s** is the nucleus being saturated (usually ^{1}H), and **i** is the nucleus being observed (usually ^{13}C). It can be shown that the nOe factor, η, is inversely proportional to the sixth power of the distance between the two nuclei.[4]

(A.2) $$\eta = (\tau/\rho)r^{-6}$$

Where τ is the dipolar coupling to longitudinal relaxation, and ρ is the extra relaxation term for the nucleus arising from other dipolar interactions. For similar molecules, τ/ρ is assumed constant so that measured nOe's are directly proportional to r^{-6}. In theory nOe experiments may be used to determine atomic distances. When combined with difference spectroscopy and/or two-dimensional methods, it provides one of the most powerful and most easily exploited methods of structural elucidation technique available.

Internuclear distances from nOe are best used **qualitatively**, attempts to quantify nOe can be realized by using calibration

curves.[9-11] The important feature of nOe is its ability to differentiate signals that have identical appearance in the spectrum. These signals differ in their spatial positions, and it is this property that is exploited.

The nOe experiment described in Chapter 5, used difference spectroscopy to detect the nOe relationship between nuclei of interest. This "difference spectroscopy" is particularly valuable, if up to .1% enhancement is to be detected behind complicated multiplets. In our structural analysis of **I** in Chapter 5, nOe was utilized to solve the structural riddle. The nOe spectra in Figure 5.3.5, suggest that the D_3 protons and the C_3 protons are spacially "near" each other, spectra **d** and **e**. On the other hand, because excitation of the B_3 resonances produced no nOe to any A spin resonances, we conclude that the B_3 protons are spacially "far" from any A spin protons. Similarly, no nOe could be detected for any B spin resonances, upon excitation of A_6 or A_4 resonances. The nOe for D_5 in spectrum **e** is 7.4%, similarly for D_3 and C_4, spectrum **d**, it is 5.7% and 10.3%; the maximum theoretical nOe is 50% according to equations (A.1). The structure we proposed for **I** in Chapter 5, is consistent with these nOe findings.

In order to obtain the largest possible useful nOe, the contribution of intramolecular dipole-dipole relaxation should be maximized. This can be achieved by eliminating other pathways for relaxation by filtering paramagnetic particles, using dilute

TABLE A.1

NOE experimental parameters for $[Ir(bpy\text{-}C^3,N')(bpy\text{-}N,N')Cl]_2Cl_2$ from the GN-500 spectrometer.

```
IBYNOE   .001
FOGGER   23MAY87

IR(BPY)2CL/2 IN DMSO F-P-T SAMP
NOE EXPT 1H NMR

ONE PULSE WITH DEC
PRESATURATION

P2        =    30.00 USEC
D5        =     9.00  SEC
D10       =     5.00  SEC
D12       =   100.00 USEC
L1        =   30
NA        =        40
SIZE      =    16384
ADC       =       12
RG        =       10
PA        =    152.1
PB        =     -1.7
LOCK      =     7.24
T(C)      =     25.0
OF        =  4250.99
SW        =  +/- 750.750  HZ
DW        =   666 USEC
DE/DW     =   .60
AT        =     5.46  SEC
SF      =  500.1267536
F2      =  500.1267536
```

```
DECOUPLER OFFSET LIST ON
DECOUPLER OFFSET LIST
#    1=      355.8
#    2=      565.4
#    3=      151.4
#    4=      355.8
#    5=       68.4
#    6=       -2.9
#    7=      355.8
#    8=      -52.4
#    9=      -83.2
#   10=      355.8
#   11=     -168.4
#   12=     -361.4
#   13=      355.8
#   14=     -390.4
#   15=     -490.8
#   16=      355.8
#   17=         .0
```

solutions, using non viscous solvents, and removing dissolved oxygen by freeze-pump-thaw techniques.

Samples in the nOe experiments described in Chapter 5 were dissolved in 99.9 atom % DMSO-d_6 and filtered through glass wool. Freezed-pump-thawing was used to remove dissolved oxygen. The pulse sequenced used from the GN-500 spectrometer library, #4, was modified for ^1H homonuclear nOe. Experimental conditions are summarized in Table A.1 and consist of a 30.0 μs 90° pulse width and a 16dB decoupler lever (L1). Quadrature detection (QDP) was turned on with N = 4, and automatic baseline (AP) applied. The EF routine

was used to create a list of frequencies to be excited, a total of 13 resonances were investigated for their nOe. Sixteen interferograms (NA = 16) were recorded for each nOe spectra.

iii. 2D homonuclear shift correlation spectroscopy,[1-4,7,8] is the most reliable and most frequently used of all two-dimensional experiments. It can be thought of as a set of n decoupling experiments in which the decoupling frequency is incremented systematically across the spectral region after each n_i spectrum. At the end, all the decoupling spectra are presented together in a two dimensional array to show relationships between mutually J-coupled nuclei. The problem with the experiment just described is that it is inefficient because the measurement is being made in the frequency domain, a sort of CW-FT 2D spectrum (continuous wave). The COSY experiment introduces the FT advantage into the second dimension.

FIGURE A.2

Vector model for COSY pulse sequence.[4]

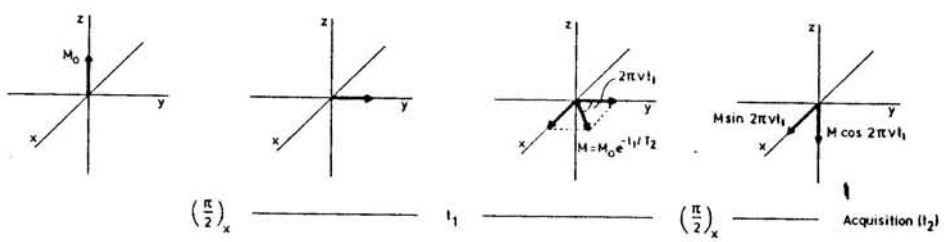

The basic COSY pulse sequence involves a preparation period, a 90° pulse, an evolution period, another 90° pulse and finally the acquisition; $(\pi/2)_x$ - τ_1 - $(\pi/2)_x$ - Acquire(τ_2).[12,13] Figure A.2 shows a vector model of this pulse sequence. The first $\pi/2$ pulse tips the magnetization vector (M_o) in the xy plane at which time, the vector evolves through an angle $2\pi\nu t_1$. If another $(\pi/2)_x$ pulse is applied, the y component of the vector is directed down the z

FIGURE A.3

Result of the COSY pulse sequence for variable t_1, see text for description.[4]

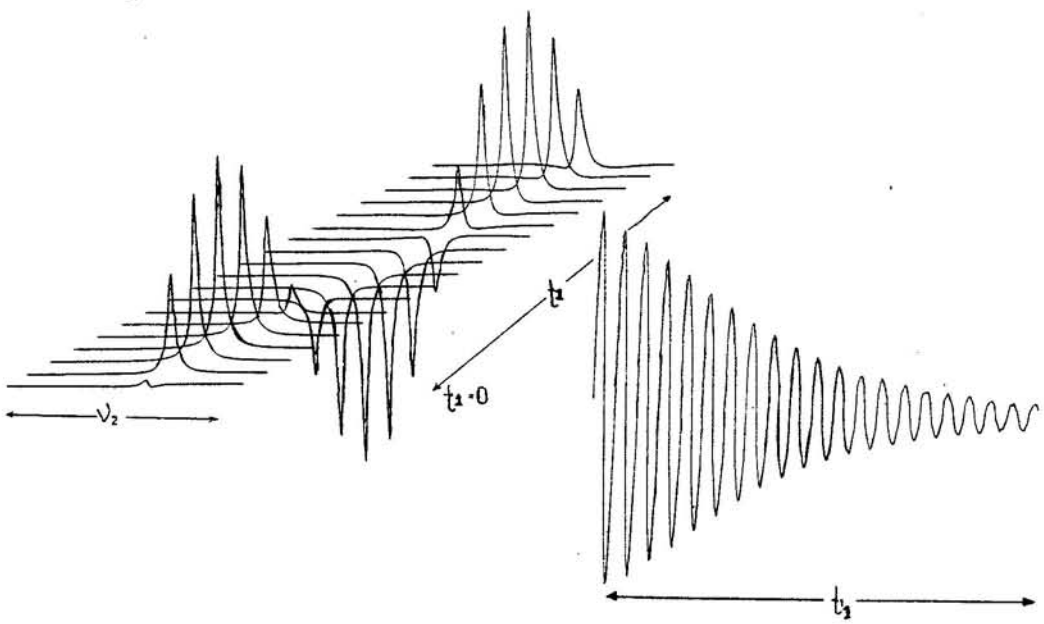

axis, leaving the x-component unchanged. At this point, the NMR spectrum is perfectly normal apart from the change in amplitude. If this sequence is performed for a series of t_1s, and the maxima from each t_1 spectrum is plotted, Figure A.3a, a sinusoidal exponentially decaying graph, Figure A.3b, is generated; an FID! The mixing

FIGURE A.4

J-correlation on COSY of $[Ir(bpy\text{-}C^3,N')(bpy\text{-}N,N')Cl]_2Cl_2$ isolation of spin systems A, B, C and D.

1

Isolate the indiviudal spin systems as shown below.

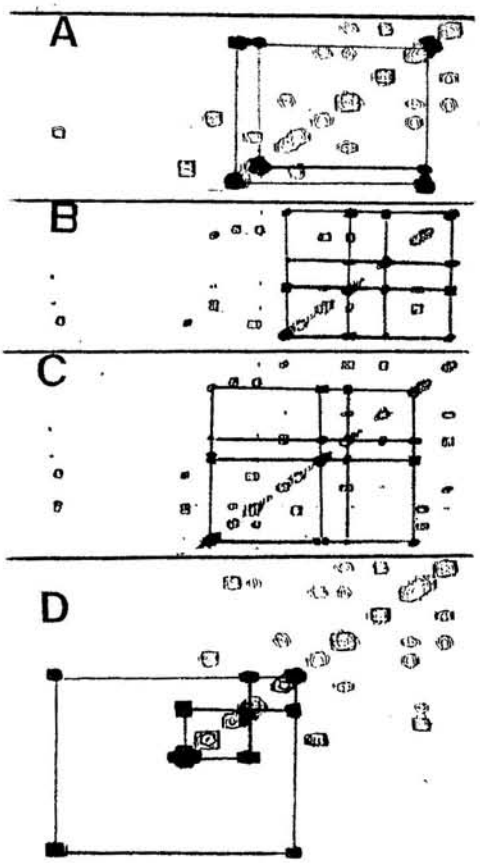

2

Start with a logical assignment for at least one signal of each spin system.

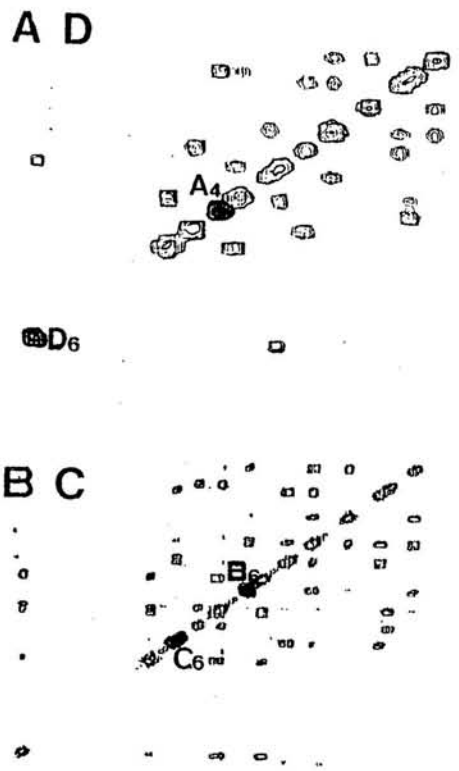

effect from the second $\pi/2$ pulse ensures that the populations of all of the transitions for all the other coupled protons are perturbed. Fourier transformation of these interferograms generates the two-dimensional data set as a function of two time domains; t_1 and t_2. The normal spectrum is along the diagonal because the intensity of

each transition oscillates at ν_1 at t_1 and because its detected frequency in t_2 is also ν_1.[3] The off-diagonal "cross peaks" are indicators of signals coupled to each other because the intensity of the ν_1 transition is modulated during τ_1 by all the transitions to which it is connected.

As you undoubtedly notice, this dissertation is full of COSY experiments. The COSY spectrum for $[Ir(bpy\text{-}C^3,N')(bpy\text{-}N,N')Cl]_2Cl_2$, from Chapter 5, Figure 5.3.4 is reproduced again in Figure A.4,5 to demonstrate the process of COSY J-correlation analysis. In these spectra, the $J_{H\text{-}H}$ coupling are represented as contours; spectra **A** and **D** show contour level five and spectra **B** and **C** shows contour level 13. The first step in decoding a COSY spectrum is to isolate the individual spin system, as shown in Figure A.4 **A-D**. Then for each isolated spin system, at least one of the resonances is assigned, Figure A.4(**AD,BC**); In our example, resonances A_6, D_6, B_6 and C_6 are assigned. Finally, for one of the spin system, the contours are traced through by J-correlation connectivity, Figure A.5. In our example, the D_6 contour is J-correlated to the contour at 8.10 ppm (step 1), thus identifying the D_5 resonance. A vertical projection of the D_5 resonance to the diagonal contour and then a horizontal projection, identifies the D_4 resonance (step 2). Connectivity of the D_4 to the D_3 is performed in the same manner (step 3). The result is the complete assignment of each resonance in the D spin system (step 4). The rest of the resonances from the

remaining spin systems A, B, and C are assigned in this same manner. The COSY experiment, # 19 in the GN-500 software library, consists of a 2000 Hz spectral window and time domain matrices of 512 * 512. Quadrature detection (QDP) was turned on with N = 0, and automatic baseline correction (AB) applied. Before Fourier transformation(FT), baseline correction (BC), exponential multiplication (EM) and zero filling (ZF) was used in the t_1 dimension. The final 2D spectrum was developed in 512 * 512 data matrices with digital resolution of 1.2-2.0 Hz which was further improved by symmetrization. Table A.2 summarizes the parameters used in this experiment.

TABLE A.2

^{1}H COSY experimental parameters for $[Ir(bpy\text{-}C^3,N')(bpy\text{-}N,N')Cl]_2Cl_2$ from the GN-500 spectrometer.

2D HOMONUCLEAR J-CORRELATION		
P2	=	30.00 USEC
D5	=	100.00 MSEC
D8	=	666.00 USEC
T8	=	666.00 USEC
	=	128
ZE	=	512
DC	=	16
RG	=	10
PA	=	42.6
PB	=	90.4
LOCK	=	2.49
T(C)	=	25.0
OF	=	4250.99
VOF	=	4250.99
F1SW	=	1501.50
F2SW	=	1501.50
F1DW	=	666
F2DW	=	666
F1 ORIG SIZE	=	256
F2 ORIG SIZE	=	256
F1 FINAL SIZE	=	256
F2 FINAL SIZE	=	256
F1SF	=	500.1267536
F2SF	=	500.126756

FIGURE A.5

^{1}H 2D COSY for $[Ir(bpy\text{-}C^{3},N')(bpy\text{-}N,N')Cl]_2Cl_2$, J-connectivity.

3 Trace through the COSY spectrum using J-correlation connective analysis. Use the vertical and horizontal projections together with the diagonal (normal 1D ^{1}H spectrum) as guides. Below is an example of the proton assignment for the D rings of the titled complex.

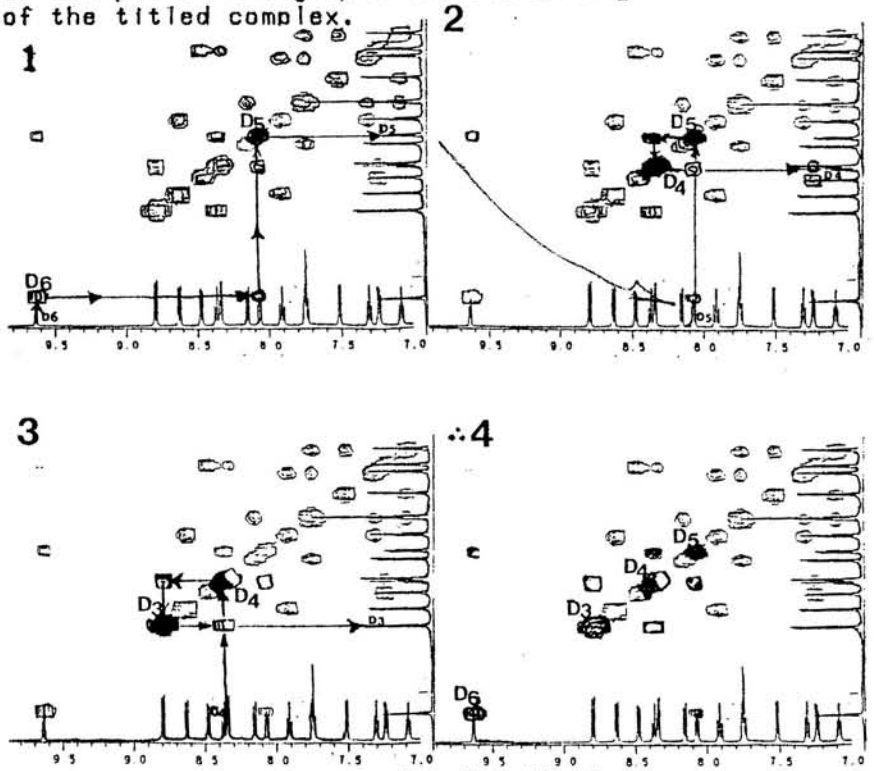

iv. Attached proton test[3,4,7,8,14,15] or J-modulated spin echo is an editing polarization transfer technique which takes advantage of ^{1}H nucleus to enhance the sensitivity of ^{13}C nucleus. It is designed to differentiate carbons on the basis of the number of attached protons. For this experiment the basic spin echo pulse sequence is modified by varying the time in which the proton decoupler is turned on during the second delay. This in effect produces a spectrum where the amplitude of the carbon signal depends

on the delay during acquisition. The time dependent amplitude, or amplitude modulation, is a function only of J_{C-H} and the number of attached protons.

A recycle delay (delay after first $\pi/2$ pulse) of 5.0 s and a second delay (delay after π pulse) of 7.0 ms phases quaternary and methylene carbon resonances to positive signals and methyl and methine carbon resonances to negative signals. Number 13 in the GN-500 software library, the experimental parameters for this experiment are summarized in Table A.3.

TABLE A.3

APT experimental parameters for $[Ir(ptpy)_2bpy]^+$ from the GN-500 spectrometer.

```
IR(BPY)2CL/2
APT 13C NMR

ATTACHED PROTON TEST

P4          =    22.50 USEC
P6          =     8.00 USEC
D5          =     5.00  SEC
D10         =   200.00 USEC
L2          =   63
NA          =     9528
SIZE        =    65536
ADC         =       12
AI          =       10
RG          =       10
EM          =     1.00
PA          =    249.1
PB          =    101.9
LOCK        =     2.04
OF          =  14843.42
SW          =  +/- 16129.0   HZ
DW          =     31 USEC
DE/DW       =    .60
AT          =     1.02  SEC
SF      =  125.7707368
F2      =  500.1212880

PARAMETER LISTS

D0 DELAY LIST
 #    1=     7.00 MSEC
 #    2=      .00 USEC
```

The APT spectrum for $[Ir(ptpy)_2bpy]^+$, shown in Figure 3.1.8, was from 10,000 interferograms. This spectrum shows eleven negative signals, and four positive signals, the inset shows that the signal at 141.41 ppm, is actually the superposition of the A_1 and A_4 carbon resonances. Interpretation of the spectrum is straightforward, the positive signals are assigned to the five quaternary carbons, and the negative signals are assigned to the eleven methine carbons in $[Ir(ptpy)_2bpy]^+$.

v. X-H shift correlation[3-6,8,16-18] or CSCM is similar to the COSY experiment because both provide J-connectivity. The difference is that in the CSCM pulse sequence, coherence transfer processes of the second $\pi/2$ pulse have been extended to another nucleus, by providing a simultaneous pulse at another frequency. In this way, the chemical shifts of an X-nuclei (usually ^{13}C) is correlated to the chemical shifts of the proton nuclei it is J_{X-H} coupled to.

In a CSCM experiment, J_{C-H} coupling is observed as modulation in the 2D spectrum. Proton assignments from the COSY spectrum lead directly to the ^{13}C assignments. Mapping the contours, protons are assigned directly to the carbons they are attached to and vice versa. The experiment can be "tuned" to show connections between directly attached pairs, or to reveal longer-range couplings.[6] If proton resonances can not be unambiguously assigned, CSCM may be used to provide the assignment of the ^1H nuclei by working from the ^{13}C assignment.

The CSCM contour plot of $[Ir(bpy\text{-}C^3,N')(bpy\text{-}N,N')Cl]_2Cl_2$ is

shown in Figure A.6. There are 14 ^{1}H resonances integrating for 15 proton and 20 carbon resonances of which 15 are protonated as show in the APT spectrum projection. The ^{1}H spectrum has already been assigned and so assignment of the ^{13}C spectra becomes a trivial exercise. Figure A.6 shows the connectivity of the ^{1}H to the ^{13}C resonances.

The 2D carbon-proton shift correlation experiment, #26 in the GN-500 Library, uses a 38 μs decoupler pulse width for a power level of (OC) 61. Time domain matrices of 2 K * 128 covered a spectral width of 2200 * 6300 Hz. The t_1 dimension was apodize by double exponential multiplication (EM) before fourier transformation (FT). The final 1024 * 512 data matrices were apodized by double exponential multiplication (EM), zero filled (ZF), fourier transformed (FT) and magnitude calculated (MC). The parameters are given in Table A.4.

TABLE A.4

CSCM experimental parameters for $[Ir(bpy\text{-}C^3,N')(bpy\text{-}N,N')Cl]_2Cl_2$ from the GN-500 spectrometer.

```
IBY       .DAT
FOGGER    06APR87

IRBPY CSCM 13C NMR ZOOM 170 120
13C NMR
P2          =     8.00 USEC
P4          =    16.00 USEC
D2          =    38.00 USEC
D5          =     2.00  SEC
D8          =    21.00 USEC
D10         =     3.50 MSEC
D12         =     2.50 MSEC
I8          =   221.00 USEC
L1          =   71
L2          =   71

NA          =      112
SIZE        =     2048
ADC         =       16
RG          =       10
LOCK        =     7.24
T(C)        =     25.0
OF          =  18236.24
VOF         =   4126.06
F1SW        =   6329.11
F2SW=       2262.44
F1DW=        158
F2DW=        442
F1 ORIG SIZE=      1024
F2 ORIG SIZE=       128
F1SF        =  125.7741340
F2SF        =  500.126630
```

FIGURE A.6

CSCM contour spectrum for $[Ir(bpy\text{-}C^3,N')(bpy\text{-}N,N')Cl]_2Cl_2$.

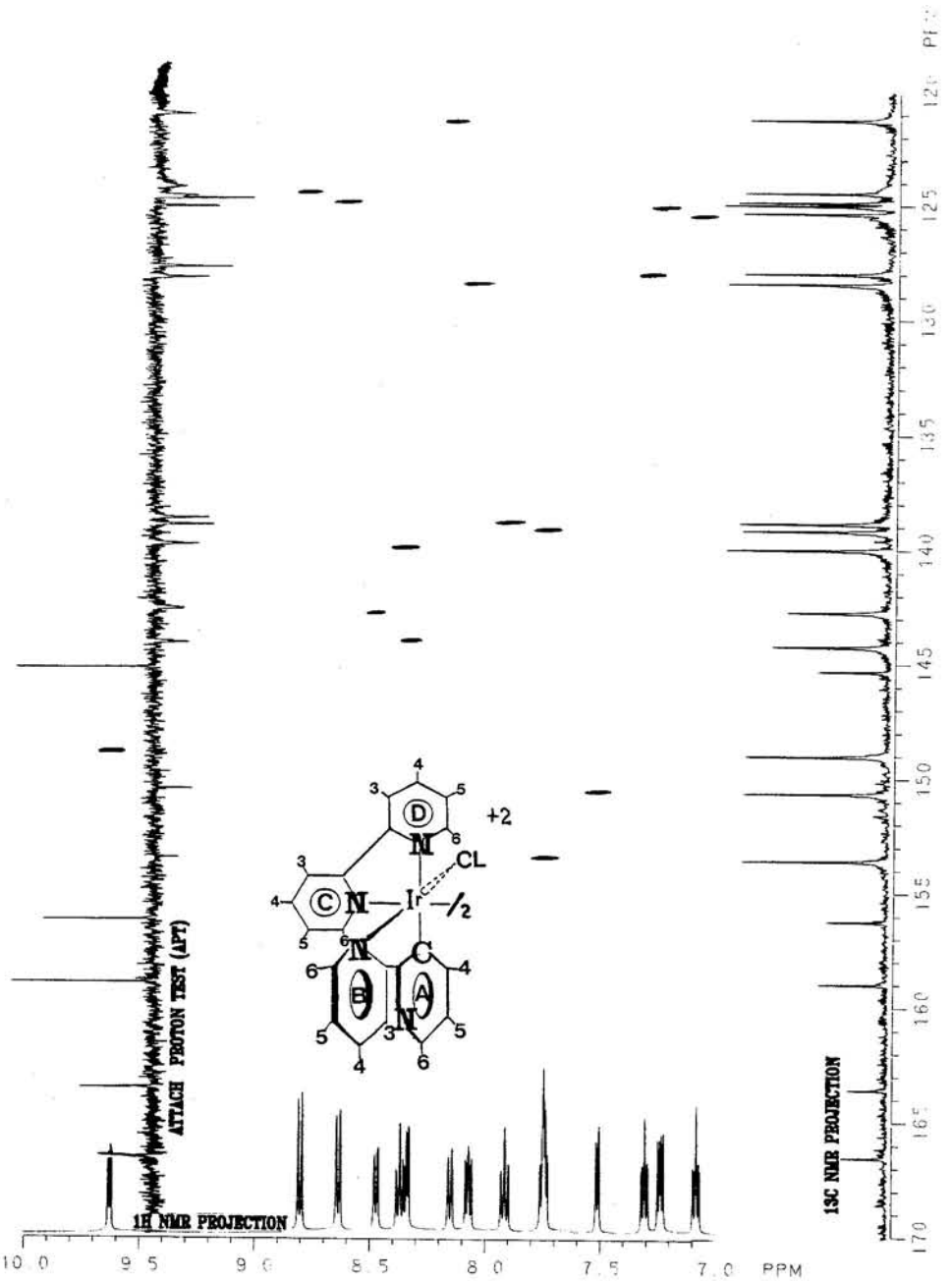

2. ^{1}H and ^{13}C Assignment

The following is a compilation of ^{1}H and ^{13}C assignments for ligands, and iridium complexes discussed in this dissertation.

TABLE A.5

^{1}H and ^{13}C NMR Assignments for PTPY, MPPY and BPY Free Ligands in $CDCl_3$ (vs. TMS)

Assig.	PTPY	MPPY	BPY
A_1	- / 140.5	- / 138.8	- / -
A_2	7.78 / 129.0	7.04 / 129.5	- / -
A_3	7.70 / 128.1	7.80 / 126.8	- / -
A_4	- / 130.9	7.40 / 119.9	- / -
A_5	7.70 / 128.1	7.80 / 126.8	- / -
A_6	7.78 / 129.0	7.04 / 129.5	- / -
B_2	- / 158.3	- / 157.1	- / -
B_3	7.83 / 138.6	- / 135.5	- / -
B_4	7.65 / 127.9	7.36 / 135.6	- / -
B_5	7.41 / 122.2	6.83 / 121.8	- / -
B_6	8.79 / 146.9	8.53 / 149.4	- / -
C_2	- / -	- / -	- / 157.0
C_3	- / -	- / -	8.40 / 137.3
C_4	- / -	- / -	7.84 / 121.4
C_5	- / -	- / -	7.30 / 149.3
C_6			8.70 / 123.9
Me	2.49 / 20.0	2.40/22.0	- / -

TABLE A.6

^{1}H and ^{13}C NMR Assignments for PTPY And MPPY Ir (III) Dimeric and Monomeric Complexes in CD_2Cl_2 (vs. TMS)

Assig.	$[Ir(ptpy)_2Cl]_2$	$[Ir(mppy)_2Cl]_2$	$[Ir(ptpy)_2bpy]^+$	$[Ir(mppy)_2bpy]^+$
A_1	/145.4	/147.4	/150.8	/152.3
A_2	/141.8	/146.6	/141.4	/145.9
A_3	5.68/131.5	5.84/131.0	6.03/126.6	6.39/132.0
A_4	- /139.6	6.54/128.4	- /118.8	6.87/129.9
A_5	6.67/122.7	6.80/121.4	6.84/124.0	7.07/122.5
A_6	7.44/123.9	7.85/128.2	7.36/125.1	8.00/129.2
B_2	/168.4	/166.4	/156.4	/156.2
B_3	7.87/118.6	- /132.1	7.80/118.7	- /133.4
B_4	7.76/136.8	7.61/141.3	7.66/138.3	7.57/142.4
B_5	6.79/122.4	6.70/122.6	6.84/123.0	6.87/122.9
B_6	9.21/151.8	9.29/151.0	7.53/148.7	7.50/147.3
C_2	-	-	/168.2	/166.1
C_3	-	-	9.25/132.7	9.19/126.5
C_4	-	-	8.13/140.0	8.22/140.0
C_5	-	-	7.36/128.4	7.42/128.3
C_6	-	-	7.90/150.6	7.86/150.3
Me	1.97/21.7	2.87/23.8	2.06/21.8	2.84/23.9

TABLE A.7

^{1}H and ^{13}C NMR assignments for
$[Ir(bpy\text{-}C^{3},N')(bpy\text{-}N,N')Cl]_2Cl_2$ in DMSO-d_6 (vs. TMS)

Position	^{1}H (δ) PPM	^{13}C (δ) PPM
A_2	-	155.62
A_3	-	144.70
A_4	8.50	142.32
A_5	7.26	124.50
A_6	8.37	143.65
B_2	-	162.97
B_3	8.18	120.77
B_4	7.76	138.68
B_5	7.12	124.86
B_6	7.54	150.15
C_2	-	165.97
C_3	8.66	124.35
C_4	7.95	138.35
C_5	7.34	127.44
C_6	7.78	153.06
D_2	-	152.90
D_3	8.83	123.92
D_4	8.41	139.50
D_5	8.10	127.89
D_6	9.67	148.51

TABLE A.8

^{1}H and ^{13}C NMR resonances of $[Ir(bpy\text{-}C^{3},N')(bpy\text{-}N,N')Cl_2][IrCl_4(bpy)]$ and $[Ir(bpy\text{-}N,N')_2Cl_2]Cl_2$

$[Ir(bpy\text{-}C^{3},N')(bpy\text{-}N,N')Cl_2][IrCl_4(bpy)]$		$[Ir(bpy\text{-}N,N')_2Cl_2]Cl_2$	
$^{1}H(\delta)$	$^{13}C(\delta)$	$^{1}H(\delta)$	$^{13}C(\delta)$
$9.73(E_3)$	160.3	$9.70(B_6)$	160.5
$9.60(D_6)$	158.5	$8.82(A_3)$	152.3
9.00	156.1	$8.55(A_6/B_3)$	150.8
$8.85(D_3)$	154.2	$8.25(A_4)$	148.0
8.65	152.1	$7.95(B_4)$	141.5
$8.54(E_6)$	149.0	$7.72(A_5)$	138.5
$8.41(D_4/A_6)$	147.6	$7.68(B_5)$	126.8
8.10	140.5		126.5
$7.96(E_4)$	139.6		123.6
7.80	139.2		123.2
$7.70(E_5)$	138.6		
$7.30(C_5)$	128.5		
$7.25(B_5)$	128.2		
	122.3		
	126.3		
	126.1		
	125.0		
	124.8		
	123.6		
	122.6		

TABLE A.9

^{1}H and ^{13}C NMR assignment for $[Ir(mppy)_2phen]^+$, $Ir(mppy)_2pic$, and $[Ir(stpy)_2Cl]_2$ in CD_2Cl_2 (vs. TMS)

A. $^{1}H/^{13}C$ - $[Ir(mppy)_2phen]^+$:

A_1 (-/146.6); A_2 (-/145.8); A_3 (6.70/131.8); A_4 (6.95/129.5); A_5 (7.13/122.3); A_6 (8.06/129.0); B_2 (-/151.2); B_3 (-/133.0); B_4 (7.30/147.0); B_5 (6.71/122.4); B_6 (7.55/142.2); C-D_2 (-/165.8); C-D_3 (-/131.6); C_4 (8.20/150.8); C_5 (7.85/126.5); C_6 (8.78/138.7); D_4 (8.33/128.8).

B. ^{1}H - $Ir(mppy)_2pic$:

A_3 (6.15); A'_3 (6.39); A_4 (6.75); A'_4 (6.75); A_5 (6.95); A'_5 (6.95); A_6, (7.97); A'_6 (7.99); B_4 (7.54); B'_4 (7.52); B_5 (7.04); B'_5 (6.87); B_6 (8.67); B'_6 (7.59); C_3 (7.65); C_4 (7.32); C_5 (7.90); C_6 (8.24).

C. $^{1}H/^{13}C$ - $[Ir(stpy)_2Cl]_2$

A_1 (-/169.68); A_2,A_6 (6.67/124.63); A_3,A_5 (6.78/127.00); A_4 (6.86/125.06); B_2 (-/170.07); B_3(7.09/119.20); B_4 (7.17/135.29); B_5 (5.87/118.21); B_6 (7.96/150.47); α (6.55/129.55); β (-/147.41).

APPENDIX B

CYCLIC VOLTAMMETRY (CV)

CV has been claimed to be the most versatile electroanalytical technique for the study of electroactive species.[19] Its versatility combined with ease of measurement, has resulted in its extensive use in almost every field of chemistry. CV spectroscopy can provide information about reaction kinetics and electron transfer mechanisms;[20-22] we use this technique mostly to measure ground state redox potentials, however.[19,23-25]

An IBM EC-225 voltammetric analyzer was used to obtained cyclic voltammogram measurements, plots were provided from an IBM 7424 MT X-Y-T recorder. A three compartment cell was used together with a platinum disk working electrode, a platinum wire auxiliary electrode and a general purpose AgCl reference electrode. Room temperature measurements were obtained in a degassed (dry dinitrogen) electrolyte solution consisting of a saturated solution of tetraethylammonium hexafluorophosphate (TEAH) and alumina in 50 ml solvent (solvents used were described for each complex). Low temperature measurements (-77°C) required a dry-ice acetone bath to house the CV cell.

Background voltammograms were first determined for each complex by running CV's of the electrolyte solution, after which approximately 2 mg of the complex was added to the working cell chamber and the CV recorded. In some instances, current sensitivity

and switching potentials were varied to elucidate wave patterns in the voltammograms. After measuring the voltammograms for each complex, voltammograms were measured for ferrocene (5.0mg). Since the half-wave potential $E_{1/2}$, for $Fc^{+/0}$ is insensitive to solvent and temperature, this redox potential is ideal as an internal reference. All CVs were monitored at scan rates of 1.0 V/s.

The nomenclature for the CV results are illustrated and described in Figure B.1.[19]

FIGURE B.1

Cyclic voltammogram nomenclature description.[19]

E_{pa} = CV wave max for anodic sweep.

E_{pc} = CV wave max for cathodic sweep.

$E_{pa/2}$ = CV wave max for anodic @ 1/2 width.

$E_{pc/2}$ = CV wave max for cath. @ 1/2 width.

ΔE_{p-p} = diff. between E_{pa} and E_{pc}.

$E_{1/2}$ = arithmetic avg of $E_{pa/2}$ and $E_{pc/2}$.

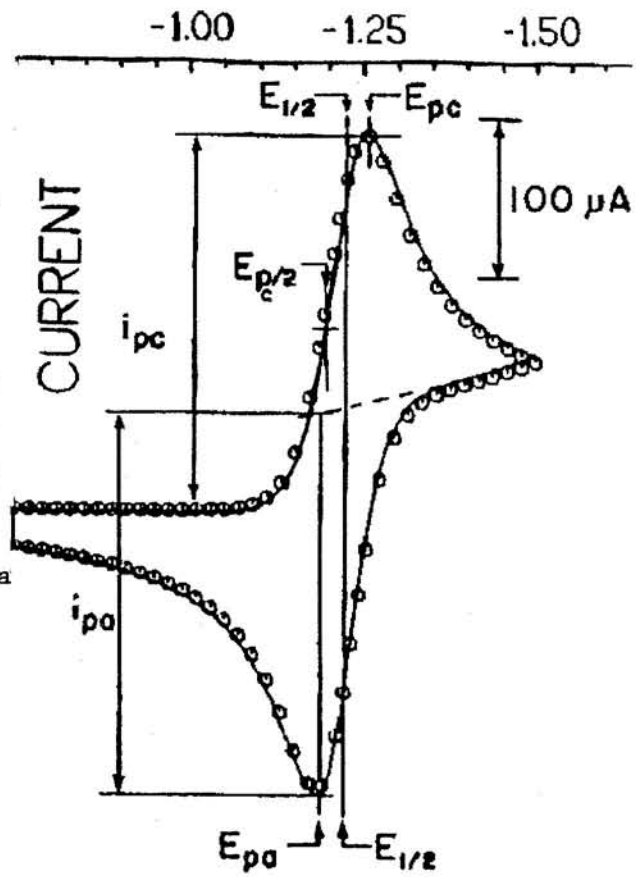

TABLE B.1

Cyclic Voltammetric Potentials for Ir(III) Complexes (V vs. SCE)

COMPLEX	Epa	Epc	Epa/2	Epc/2	ΔEp-p	$E_{1/2}$
$[Ir(ppy)_2Cl]_2$ [a]						
Ox-scan 1st [b]	0.96	0.83	0.90	0.95	.13	0.93 (0.51) [c]
Ox-scan 2nd	1.20	1.08	1.15	1.15	.12	1.15 (0.73)
Re-scan	*NO OBSERVABLE REDUCTION WAVES*					
$Fc^{+/0}$	0.65	0.20	0.46	0.38	.45	0.42
$[Ir(ptpy)_2Cl]_2$ [a]						
Ox-scan 1st	0.90	0.80	0.84	0.85	.10	0.85 (0.39)
Ox-scan 2nd	1.18	1.08	1.10	1.13	.10	1.12 (0.66)
Re-scan 1st	-0.88	-1.00	-0.93	-0.90	.12	-0.92 (-1.38)
$Fc^{+/0}$	0.70	0.24	0.58	0.34	.46	0.46
$[Ir(mppy)_2Cl]_2$ [a]						
Ox-scan 1st	0.90	0.83	0.85	0.85	.07	0.85 (0.41)
Ox-scan 2nd	1.15	1.08	1.10	1.10	.07	1.10 (0.66)
Re-scan 1st	-	-1.13	-	-1.00	-	-
$Fc^{+/0}$	0.60	0.28	0.45	0.43	.32	0.44
$[Ir(ppy)_2bpy]^+$ [d]						
Ox-scan 1st	1.32	1.24	1.12	1.20	.08	1.28 (0.88)
Re-scan 1st	-1.34	-1.42	-1.37	-1.35	.08	-1.38 (-1.78)
$[Ir(ptpy)_2bpy]^+$ [d]						
Ox-scan 1st	0.95	-	-	-	-	-
Ox-scan 2nd	1.20	1.18	1.15	1.20	.02	1.18 (0.79)
Re-scan 1st	-1.40	-1.45	-1.43	-1.41	.05	-1.42 (-1.81)
$Fc^{+/0}$	0.51	0.28	0.40	0.38	.23	0.39
$[Ir(mppy)_2bpy]^+$ [d]						
Ox-scan 1st	1.05	-	1.01	-	-	-
Ox-scan 2nd	1.25	1.18	1.19	1.23	.07	1.21 (0.81)
Re-scan 1st	-1.36	-1.45	-1.41	-1.40	.09	-1.41 (-1.81)
$Fc^{+/0}$	0.50	0.29	0.40	0.40	.21	0.40
$[Ir(bpy\text{-}C^3,N')(bpy\text{-}N,N')Cl]_2Cl_2$ [e]						
Ox-scan 1st [f,g]	1.25	1.13	1.17	1.18	.12	1.17 (0.60)
Ox-scan 2nd	1.58	1.46	1.50	1.15	.12	1.52 (0.95)
Re-scan 1st	-0.17	-0.25	-	-0.15	.08	-
Re-scan 2nd	-0.54	-0.72	-0.70	-0.65	.18	-0.68 (-1.25)
Re-scan 3rd	-	-1.00	-.99	-	-	
Re-scan 4th	-	-1.33	-	-	-	-
Re-scan 5th	-1.30	-1.21	-1.28	-1.22	.05	-1.25 (-1.82)
$Fc^{+/0}$	0.78	0.50	0.53	0.60	.25	0.57

a) Solvent; dichloromethane

b) 1st (2nd) wave of oxidative or reductive scan

c) Values in parenthesis are $E_{1/2}$ vs. $Fc^{+/0}$

d) Solvent; acetonitrile

e) Solvent; N,N'-Dimethylformamide

f) A minor reversible wave at $E_{1/2}$ = 0.60 V is assigned to chloride oxidation.

g) reversible only at switching potential of 1.5 V.

APPENDIX C

ABSORPTION AND LUMINESCENCE

1. Absorption Measurement

Two types of spectrometer were used for absorption measurements. The first was a CARY 15 spectrometer. The second was a Hewlett Packard 8552A Diode array spectrophotometer interfaced to an HP 9000/300 work station with spectra provided by an HP 7475A plotter.

2. Luminescence

Samples for room temperature excitation and emission (corrected/uncorrected) measurements were generally degassed with dinitrogen or by freeze-pump-thaw cycles. For 77 K rigid matrices, capillary samples or freeze-pump-thaw samples were prepared, measurements were made by submersion of these samples in a finger quartz optical dewar filled with liquid nitrogen. Room temperature and low temperature (77 K) measurements were obtained either from a Perkin-Elmer MPF-3 spectrophotofluorimeter or a Spex Fluorolog 2 series spectrophotometer. The latter instrument is equipped with single monochromators with a 150 watt xenon lamp set perpendicular to the sample with a Hamamatsu R928 photomultiplier tube (thermostatically cooled) configured for photon counting. Emission measurements were digitized and worked up using a Spex Datamate computer. Three dimensional emission intensity / emission

wavelength / excitation wavelength stacked plots were automatically accumulated with a Spex Datamate under control by an excitation-emission matrix program supplied by Spex Industries. Spectra were plotted on a Houston Instruments Hiplots DMP-3 digital plotter. Correction factors from a standard quartz-halogen lamp were applied to correct for wavelength dependencies of the photomultiplier and optical response on the emission intensities.

Lifetimes and time-resolved-emission spectra were measured with an AVCO-Everett C-950 nitrogen laser with 337 nm pulses. Luminescence were measured perpendicular to the laser pulses with a Fastie-Ebert 0.8 m scanning grating monochromator with 1 nm optical resolution. The emitted signal was detected by an RCA 8852 photomultiplier whose output was applied to either a PAR 4422 gated integrator with a model 4420 boxcar averager and 4402 signal processor or a Stanford Research Systems SR250 gated integrator with SR280 power supply. The latter system was interfaced to an IBM PC computer through a SR245 interface using the SR265 data acquisition software. Lifetimes were measured using waveform mode and time-resolved-emissions were measured using static gate mode for both boxcar averagers.

i. Quantum yields for luminescence were measured by optically dilute methods. The experimental technique transcribed here was described by Dr. King;[25,26] the theoretical background is described in a review article by Demas and Crosby[27].

Absorption measurements of a stock solution of fluorescein in

0.1 M NaOH are recorded in a 10 cm quartz cell; the concentration of the fluorescein is kept below 10^{-6} M. An excitation wavelength is selected in which the lumiphore and fluorescein have mutual absorption maxima. If the same excitation wavelength is used for the fluorescein and the lumiphore then the term $[I_{(\lambda r}/I_{(\lambda r)}][I_{(\lambda r}/I_{(\lambda r)}]$ in equation C.1 goes to one. The emission spectrum is recorded for both the fluorescein and the lumiphore with the area under the emission curve calculated and used in equation C.1. This equation calculates the quantum yield for optically dilute samples.

(C.1) $$\Phi = \Phi_r \, [(A_{r(\lambda r)}/A_{x(\lambda x)}][I_{(\lambda r)}/I_{(\lambda r)}][\eta_x{}^2/\eta_r{}^2][D_x/D_r]$$

where, Φ_r = 0.9 for fluorescein.

$A_{r(\lambda r)}$ = absorbance of fluorescein at λ.

$A_{x(\lambda x)}$ = absorbance of lumiphore at λ.

$I_{(\lambda r)}$ = Excitation wavelength for fluorescein.

$I_{(\lambda x)}$ = Excitation wavelength for lumiphore.

η_x = refractive index for solvent (ACN).

η_r = refractive index for NaOH solution.

D_x = area of emission for lumiphore.

D_r = area of emission for fluorescein.

ii. Stern-Volmer quenching studies may be used to determine the electron transfer rates, kq. Chapter 1 already discussed the

relationship between the rate of electron transfer and the excited state redox potential of a complex. In this section, the preparation and calculation necessary for Stern-Volmer quenching analysis will be discussed.

For the quenching study described in Chapter 3, at least two sets of four different concentration (total of eight) were prepared per quencher for each monomer. Each sample contained the monomer complex and the quencher of interest in acetonitrile solvent (Burdrick and Jackson, used without further purification). Freeze-pump-thaw cycles were carried out for each sample and each vacuum sealed after the fifth freeze-pump-thaw cycle. With 14 quenchers (Table 1.2) necessary to cover the oxidative and reductive range (Figure 3.4.11), and two complexes to analyzed, a total of 224 samples were prepared and analyzed!

Eight lifetimes were determined per quencher per lumiphore. These lifetimes were fitted in equation 1.4 to give the electron transfer rate kq for the quencher of interest. Next, a plot of log kq verses E° (quencher's redox potential) is generated, Figure 3.4.11, to provide an estimate of the excited state redox potential of the lumiphore. In Figure 3.4.11, the breaking point of the graph gives an estimate of the monomer excited state redox potential. In our example, we estimated the excited state oxidation potential as 0.80 and 0.55 V (vs. NHE) for $[Ir(ptpy)_2bpy]^+$ and $[Ir(mppy)_2bpy]^+$ respectively, see Table I.

APPENDIX D

EXCITED STATE ABSORPTION

The following is the experimental procedure taken from a recent publication on the excited state absorption of $[Ir(ppy)_2bpy]^+$.[28] Excited state absorption measurements were obtained at the University of Tokyo with instrumentations described in a previous publication.[29] Acetonitrile samples of the monomer and the benzophenone reference in 3 mm quartz cell, were excited at 266 nm with 5 ns, 1.7 mJ fourth-harmonic pulses from a Quanta Ray DCR Nd:YAG laser. Concentrations for samples and reference solution were adjusted to identical absorbance values at 266 nm. The analyzing probe light was generated by 250 nm pulses from a xenon flash lamp produced with a Sugawara nanosecond pulser. The timing of the laser and probe pulses were adjusted to produce a laser pulse at the time of maximum intensity of the probe pulse and at one-half the repetition rate of the probe. Probe lamp profiles with and without excitation by the pump were detected with a Unisoku USP450 photodiode array and digitized with an Iwatsu DM 901 transient digitizer. Data analysis was performed with a NEC PC-9801 VM microcomputer. Typically, results were collected and averaged over 1000 probe lamp pulses with and without the laser pump in order to generate excited-state difference spectra. The absolute values of molar extinction coefficients from these difference absorption profiles were obtained by comparison to the known excited-state

extinction coefficients of benzophenone and were corrected for effects due to ground-state absorption in the region from 340 to 540 nm by using the known extinction coefficients of the ground-state species. Quantum yield for formation of the lowest excited state following pulsed excitation at 266 nm was assumed to be unity in estimations of excited-state extinction coefficients.

APPENDIX E

STRUCTURAL CONCLUSIONS ON III; Is it really an Ir(IV) complex.

Some famous last words about this product. During and after my dissertation defense, my committee convinced me that although the evidence presented in Chapter 6 supports a cis-bis bipyridyl dichloro iridium complex, and although the elemental analysis shows four chlorides per iridium, the fact that an NMR signal is obtained for this product (with pretty good resolutions too) strongly suggests that III can not be an Ir(IV),d^5, paramagnetic species.

Several possibilities were offered in light of these paradoxical results. The first was offered by our group. We proposed a doubly protonated bis bipyridyl ortho-metalated species. In this structure, iridium has a +3 oxidation state with each external nitrogen protonated, accounting for eight types of protons in the complex.

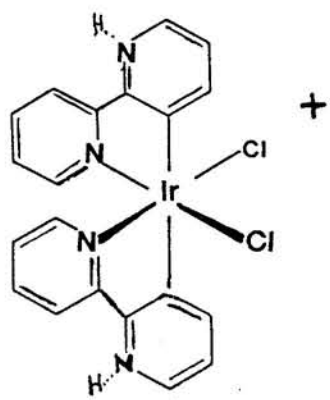

The problem with this structural proposal, however, is that there is no precedent in the literature for a proton resonance from an acidic proton on a nitrogen atom of a bipyridyl ligand. At the very least, a proton of this type would have broad signals because of its acidic nature. Furthermore, an elemental analysis for this proposed structure would analyze for three chlorides per iridium metal. This is an unlikely structure for III.

As I have mentioned throughout Chapter 6, Dr. Bill Harrison did work on the crystallographic structure of III. Unfortunately the structure he solved was that of the ion pair, product II. I am certain that I provided Dr. Harrison the correct vial containing product III (same batch I sent off for elemental analysis). The fact that he solved the ion pair (II) structure has bewildered all of us. I offer three scenarios. First, I gave Harrison the wrong sample, in which case he resolved the crystal structure of product II. (I might add that Harrison's structural solution gave the same anomalous i.e., high electron density about the 50/60 ring, as that solved by Dr. Keder.) Second, I provided Bill the correct sample, product III, but the product co-crystallizes in both the II and III forms. Bill, like winning the lottery, selected the one ion pair single crystal in the batch. Third, product III is actually some type of ion pair structure (Harrison solved the correct structure), in which only one of the moieties in the ion pair is observed on the NMR time scale. This is a strong possibility especially if the phantom moiety contains an Ir^{IV} center. Considering the

superposition of ^{1}H resonances between product II and III in the ^{1}H NMR spectra, Figure 6.2.6, this scenario is a good possibility. The mass spec would also be consistent with such a structure. Doubt arises however because an elemental analysis of such this structure calculates for six chlorides and two bipyridine for every two iridiums. I get migraines trying to make this analysis agree with that found for III in Chapter 6.

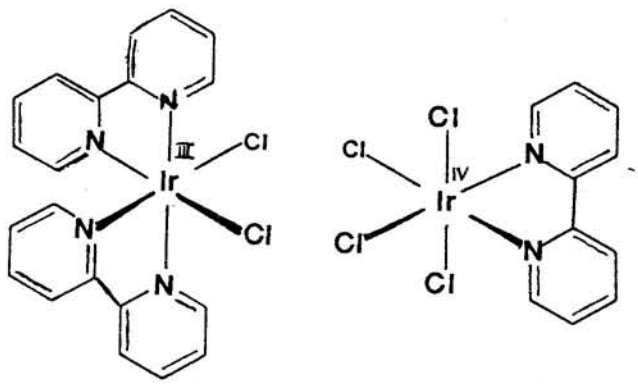

Another possible structure was offered by Professor Butler and reiterated by Professor Ford. They proposed that product III may be some dimeric unit in which there are two d^5 iridium centers undergoing "superexchange".[30] More specifically a dimeric $[Ir^{IV}(bpy)_2Cl]_2Cl_6$ was proposed. In this dimer, the coupling between the individual magnetic moments of the paramagnetic d^5 species cause spontaneous dipolar coupling through the electrons of

intervening nonmetal atoms, i.e., chloride bridge. In this way, the paramagnetism relaxation mechanism for the ^{1}H nucleus are suppressed or eliminated resulting in observable NMR signals. For this proposed structure, the elemental analysis, mass spec and ^{1}H NMR spectrum (if observable) would be in agreement with those found in Chapter 6.

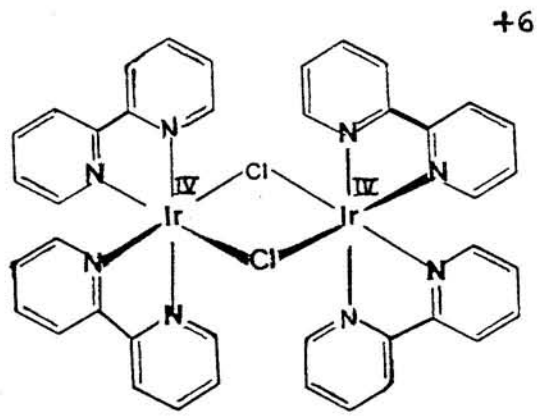

Finally a combination of the first and third structures proposed above would also be consistent with the our experimental result for III. A dimeric Ir(IV) doubly protonated ortho-metalated bipyridyl dichloro-bridged structure, $[Ir(Hbpy\text{-}C^{3},N')_2Cl]_2Cl_6$ is proposed. In this structure, we **speculate** that there is superexchange between the two Ir(IV) centers and that the protons on the N-H moieties are observable in the NMR time scale. We justify the latter to the poor acidity of the N-H moiety as a result of the electropositive Ir(IV) metal centers.

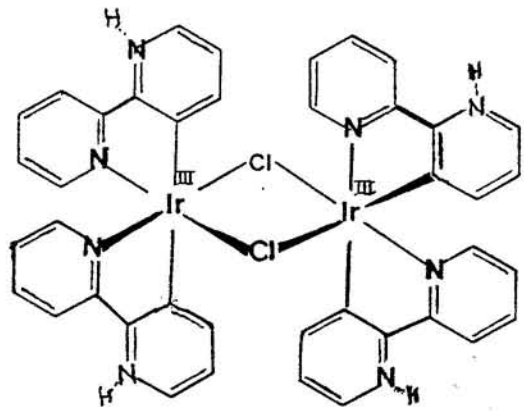

Whatever the structure for III turns out to be, there are several facts that must not be overlooked. First, there are definitely four chlorides and two bipyridyls per iridium. Second, the two bipyridyl ligands must be in degenerate environments in order to accounts for eight proton signals in the ^1H NMR spectrum. Third, in agreement with the ^1H NMR spectrum, the proposed structure must account for an $Ir(bpy)_2Cl_2$ fragment in the mass spec. And, finally, the structural assignment must take into account the low-energy metal-centered (d-d) transition observed in the absorption spectrum, Figure 6.3.3. Good luck!

APPENDIX F

I believe that we cannot live better
than in seeking to become still better
than we are.
-Socates

We've come to my favorite section of this dissertation. I just completed the dedication page found at the beginning (p iii). I feel that there are still many others I need to acknowledge. I know this section may seem unorthodox, but it is my thesis and I feel that this work would be incomplete without this last acknowledgment. (Besides, I do owe someone a pigeon section). These individuals are very much a part of this work because each has touched my life and in that way have contributed to this work.

I read somewhere (Trina Paulus, "Hope for the Flowers", — thanks for the book Pia) that someone once asked an artist how long it took him to make a certain picture. *"Five minutes and my whole lifetime,"* he responded. This dissertation is like that. I want to sincerely thank each who has given either to this work itself or to the lifetime that made it possible.

To my family (again)—Nieves, Joe, Noel, Lelian, Grace and Will. Thanks for always standing by my side, especially in difficult moments.

To three great senior members of the Watts' Institute —PJS, KAK, and CAC (Ondine who once said to me "Fogger you've got to learn how to control your "s#!t".") Thanks for being a great inspiration. You guys are all great protege of S.C. KTFWF!!

To other members of the WIW—Ashley (So when fo' we goin' rubah neck at Sam's n' throw back some brewskies?), Pete, Christine, Ken, Greg, Hector and Mizuno (Mr. V-ball ringer-san). It was great keeping TFWF with all of you. (P.S. Don't let Ali down.)

To the undergraduates I've had a pleasure working with. In the GRMP program; Selmira Tellechea, Maryann Torres and Mae Libunao (Stern Volmer quenching study, Chapter 3) SARI program Joe Escobar (FTG, Top Green, Chapter 7)and Debbie Rashe (Acid\base luminescence, Chapter 5). To the graduate division who provided funding for these undergraduates to work with me. Thanks Christine Iriart, and Dorothy Nagaran.

To my relatives in Fairfield, CA who believed in me and my abilities enough to sponsor me in my senior year in high school. Thanks uncle Bert, auntie Lydia, cousins Steve (Nilda), Darryl, Eric and Clifford Valmores. I also like to thank the Topacios—especially Hilda (Mark).

To the individuals in Guam and S.B. who always knew some how this day was coming— Mr Piel, Mrs. Lawrence, Isidro Yatar, Greg (Julie and family) and Mike Cruz and Stanley Aki.

To my buddies Dan and Dave. We've come a long ways from our hoodlum days back in Agat.

To Pia, hey look it finally happened! You know though Pia, it doesn't feel any different.

To Gloria George, my landlord at Santa Barbara while attending UCSB. Thank you for being so generously hospitable with your home for these past four years.

To members of my dissertation committee--Professor Ford, Professor Offen and Professor Stucky. Thanks for your time and effort in serving in this committee. I am most grateful and honored.

To Dr. Ata Shirazi, Dr. J.T. Gerig and Dr. H. Eckert, thanks for assistance and helpful discussion on the NMR work.

To my beach and intramural volleyball partners—you know who you are. Thanks for the great games!!

To Dr. Mike Eddy (aka dad-Mr) folks, he is possibly the greatest sport legend (not a bad crystallographer either) in his own mind.

To Dr. Bill Harrison, Dr. Hermann Mayer and D. Gregory—Crystals, NMRs and computers- deadly combo da one.

To Sue Yamagata, thanks for the late night company. We've got to do mud pies again one of these days.

To the Department of Energy, Campus fellowship, President Dissertation Year Fellowship and the Chemistry Department for providing financial support.

To da **Foxxy Babes** of Santa Barbara:

Dawn (aka mom-lady, its a long story folks), in your own way you've always been special. Thanks for watching out fo' your trouble-maker son, 'specially when he no can keep his "s#!+".

Margi (Jim), thanks for making the third floor a pleasant place to work. Your Big smile always somehow bring out the sunshine—even in foggy days. Thanks also fo'— you know what fo'.

Dukie (Delphine), thanks for late-nite company on the NMR spectrometer. The androstan collaboration taught me a lot, we got a lot of mileage from it. Hang in there and don't let me down.
X's & O's.

Ty (Sui), a very special ski bunny (sorry Sui). Thanks for being my first friend at UCSB, for that you'll always be special. Most of all, thanks for the great memories at UCSB. Finally, thanks for at least trying to make me keep in control em $#!+, even though I lose em.

Killer (Kathy), thanks for making me lose control of my "$#!+". (Just kidding). Thanks for the fun and the good times, I will miss you dearly.

And to others I fear I forgot, sorry 'ey?

A special thank you to Dr. Nancy Keder (Bill). Thanks for countless proof reading of the crystal section, for being a great crystallography teacher, for being a true friend. At least for now you won't have any more miserable iridium structure to solve. (Notice I said "for now".) Chapter 4 is dedicate to you in your honor. You're awesome!!!

Finally a special acknowledgment goes to Dr. Big Kahuna, Da boss 4-U and 4-me, Professor R.J. Watts. I will always be indebt to you. I don't think I can put into words the gratitude I owe you. (Knowing me it'll probably come out in pigeon any wayz.) It was a **great pleasure** working for you and in your lab. You've taught me much, but most of all, you've taught me how to lose my s#!+ !!. The memories will linger (kinda scary hu?).

A SCIENTIST CREED

Relying upon a faith that our
universe is not a chaos
but an ordered cosmos.

I believe that through sincere
and courageous efforts
man can learn what is true

I believe that inherent is what
is true is that which
will serve creation in its
highest form, which is Humanity.

I believe that truth shall
make man free—free from the
ills of the flesh and the spirit.

I rely upon an unfolding
knowledge of the truth to
provide a solution for the
problems and conflicts that
vex humanity.

I therefore dedicate
myself to the task
of seeking the truth
fearlessly and zealously,
and to the application
of what knowledge I
may gain for the
establishment of a
peaceful, just and
orderly civilization on
earth.

——Arthur H. Compton

LITERATURE CITED:

1. Freeman,R.; Morris,G.A. Bull. Magn. Reson. **1979** 1 5.

2. Kessler,H.; Gehrke,M.; Griesinger,C. Angew.Chem.Int.Ed. Engl. **1988** 27 490, and references therein.

3. Sanders,J.K.M.; Hunter, B. "Modern NMR Spectroscopy: A Guide for chemist"; Oxford University Press, Oxford, U.K. 1988

4. Derome,A.E. "Modern NMR Techniques for Chemistry Research"; Baldwin,J.E. ed., Pergamon Press, Oxford, U.K. 1988

5. Budddrus,J.; Bauer,H. Angew.Chem.Int.Ed. Engl. **1987** 26 625, and references therein.

6. Martin,G.E.; Zektzer,A.S.; Magn. Reson. Chem. **1988** 26 631, and references therein.

7. Abraham,R.J.; Loftus,P. "Proton and Carbon-13 NMR Spectroscopy"; Heyden; London, U.K. 1978

8. Ernst,R.R.; Bodenhausen,G.; Wokaun, A. "Principles of Nuclear Magnetic Resonance in One and Two dimensions"; Oxford University Press, Oxford, U.K. 1987

9. Sanders,J.K.M.; Mersh,J.D. Prog. NMR Spectros. **1982** 15 353

10. McFarlane,H.C.E.; McFarlane,W. "Specialist periodical reports on NMR spectroscopy"; Royal Society of Chemistry, Vol 13 and 14, London, 1984, 1985.

11. Neuhaus,D.; Williamson,M.P. "the nuclear Overhauser effect in structural and conformational analysis"; Verlag Chemie, New York, 1988.

12. Jeener.J.; Ampere International Summer School, Basko Polje, Yugoslavia (1971).

13. Bax,A.; Freeman,R.; Morris,G. J. Magn. Reson., **1981** 42 164

14. Breitmaier,E.; Bauer,G.; "^{13}C NMR Spectroscopy; A working manual with exercises.2 Vol 3"; Elias, H-G, ed., Harwood Academic Publishers, Chur, Switz. 1984

15. Patt,S.L.; Shoolery,J.N J. Magn. Reson., **1982** 46 535.

16. Freeman,R.; Morris,G.A. J. Chem Soc. Chem Commun., **1978** 684

17. Bodenhausen,G.; Freeman,R. J. Am. Chem. Soc., **1978** 100 320

18. Bax,A; Morris,G.A. J. Magn. Reson. **1981** 42 501

19. Evans,D.H.; O'Connel,K.M.; Petersen,R.A.; Kelly,M.J. J. Chem. Educ. **1983** 60:4 290, and references therein.

20. Nicholson,R.S.; Shain,I. Anal. Chem. **1964** 36:4 706

21. Nicholson,R.S. Anal. Chem. **1965** 37:11 1351

22. DeArmond K., etal., J. Phy. Chem. **1978** 82:5 540

23. Headridge,J.B. "Electrochemical Techniques for Inorganic Chemist"; Academic Press, London, 1969.

24. Brown,E.R.; Large,R.F.; "Physical Methods of Chemistry. PartIIA: Electrochemical Methods"; Wiley-Interscience, New York, 1971.

25. Ohsawa,Y.; Sprouse,S.D.; King,K.A.; DeArmond,M.K.; Hanck,K.W.; Watts,R.J. J.Phys.Chem. **1987** 91 1047

26. King,K.A. "Ph.D. Thesis"; University of California, Santa Barbara, 1986

27. Demas,J.N.; Crosby,G.A.; J. Phys. Chem. **1971** 75 991

28. Ichimura,T.K.; Kobayashi,T.; King,K.A.; Watts,R.J. J. Phys. Chem. **1987** 91 6104

29. Kobayashi,T.; Yasufuku,K.; Iwai,J.; Yesaka,H.; Noda,H.; Ohtani,H. Coord. Chem. Rev **1985** 64 1

30. Jolly,W.L. "Modern Inorganic Chemistry"; McGraw Hill, New York, N.Y., 1984, p 429.

INDEX

WILFRED OMEGA GARCES
CDL . PERM. 132597-6
431 CAMINO LAGUNA VISTA 967-5497
P.O. BOX 2644
GOLETA, CA 93118

1165

12.6 1988

16-66/1220

Pay to the order of VC Regents $ 98 50

ninety eight 50/100

Bank of America NT&SA
Hollister-Storke Road Branch 0780
P.O. Box 1048
Goleta, CA 93116

For

Wilfred

⑈122000661⑈1165⑈ 07806⑈09238⑈ ⑈00

UCSB
CASHIERS OFFICE
12/06/88

NONBRC	120 #
REFRNC	0 #
ADD AMNT	98.50
CHECK	98.50

THANK YOU
#198157 C00# R03 T14:57

Phinally Done!
UNIVERSITY OF CALIFORNIA, SANTA BARBARA

CERTIFICATE OF COPYRIGHT REGISTRATION

FORM TX
UNITED STATES COPYRIGHT OFFICE

REGISTRATION NUMBER

TX 2 790 317
TX TXU

EFFECTIVE DATE OF REGISTRATION

4 Month 2 Day 90 Year

This certificate, issued under the seal of the Copyright Office in accordance with the provisions of section 410(a) of title 17, United States Code, attests that copyright registration has been made for the work identified below. The information in this certificate has been made a part of the Copyright Office records.

OFFICIAL SEAL

REGISTER OF COPYRIGHTS
United States of America

89-16,344

DO NOT WRITE ABOVE THIS LINE. IF YOU NEED MORE SPACE, USE A SEPARATE CONTINUATION SHEET.

1 TITLE OF THIS WORK ▼ STRUCTURAL CHARACTERIZATION AND PHOTOPHYSICAL INVESTIGATION OF IRIDIUM-CARBON SIGMA BONDED COMPLEXES

PREVIOUS OR ALTERNATIVE TITLES ▼

PUBLICATION AS A CONTRIBUTION If this work was published as a contribution to a periodical, serial, or collection, give information about the collective work in which the contribution appeared. Title of Collective Work ▼

If published in a periodical or serial give: Volume ▼ Number ▼ Issue Date ▼ On Pages ▼

2 NAME OF AUTHOR ▼

a GARCES, FRED OMEGA

DATES OF BIRTH AND DEATH
Year Born ▼ 1960 Year Died ▼

Was this contribution to the work a "work made for hire"?
☐ Yes
☒ No

AUTHOR'S NATIONALITY OR DOMICILE
Name of Country
OR Citizen of ▶ UNITED STATES
Domiciled in ▶

WAS THIS AUTHOR'S CONTRIBUTION TO THE WORK
Anonymous? ☐ Yes ☒ No
Pseudonymous? ☐ Yes ☒ No
If the answer to either of these questions is "Yes", see detailed instructions.

NATURE OF AUTHORSHIP Briefly describe nature of the material created by this author in which copyright is claimed. ▼
ENTIRE TEXT

NOTE
Under the law, th... h... n... s...

AME OF AUTHOR ▼

DATES OF BIRTH AND DEATH
Year Born ▼ Year Died ▼

s this contribution to the work a "work made for hire"?
] Yes
] No

AUTHOR'S NATIONALITY OR DOMICILE
Name of Country
OR Citizen of ▶
Domiciled in ▶

WAS THIS AUTHOR'S CONTRIBUTION TO THE WORK
Anonymous? ☐ Yes ☐ No
Pseudonymous? ☐ Yes ☐ No
If the answer to either of these questions is "Yes", see detailed instructions.

ATURE OF AUTHORSHIP Briefly describe nature of the material created by this author in which copyright is claimed. ▼

AME OF AUTHOR ▼

DATES OF BIRTH AND DEATH
Year Born ▼ Year Died ▼

as this contribution to the work a "work made for hire"?
☐ Yes
☐ No

AUTHOR'S NATIONALITY OR DOMICILE
Name of Country
OR Citizen of ▶
Domiciled in ▶

WAS THIS AUTHOR'S CONTRIBUTION TO THE WORK
Anonymous? ☐ Yes ☐ No
Pseudonymous? ☐ Yes ☐ No
If the answer to either of these questions is "Yes", see detailed instructions.

NATURE OF AUTHORSHIP Briefly describe nature of the material created by this author in which copyright is claimed. ▼

0335204 80
033520480

3 YEAR IN WHICH CREATION OF THIS WORK WAS COMPLETED This information must be given in all cases.
1988 ◀YEAR

DATE AND NATION OF FIRST PUBLICATION OF THIS PARTICULAR WORK
Complete this information ONLY if the work has been published.
MONTH ▶ NOVEMBER DAY ▶ 15 YEAR ▶ 1989
U.S.A. ◀NATION

4 COPYRIGHT CLAIMANT(S) Name and address must be given even if the claimant is the same as the author given in space 2. ▼
GARCES, FRED OMEGA
C/O CHEMISTRY DEPT., COLUMBIA UNIVERSITY
NEW YORK, NY 10065

See instructions before completing this space.

APPLICATION RECEIVED
APR 02 1990
ONE DEPOSIT RECEIVED
APR 02 1990
TWO DEPOSITS RECEIVED
REMITTANCE NUMBER AND DATE

DO NOT WRITE HERE OFFICE USE ONLY

TRANSFER If the claimant(s) named here in space 4 are different from the author(s) named in space 2, give a brief statement of how the claimant(s) obtained ownership of the copyright. ▼

MORE ON BACK ▶
- Complete all applicable spaces (numbers 5-11) on the reverse side of this page.
- See detailed instructions.
- Sign the form at line 10.

DO NOT WRITE HERE
Page 1 of 2 pages

*YEAR DATE IN NOTICE: 1988

*Special relief granted under 202.20(d) of the C. O. reg.

TX 2 790 317

EXAMINED BY

CHECKED BY

FORM TX

☐ CORRESPONDENCE Yes

☐ DEPOSIT ACCOUNT FUNDS USED

FOR COPYRIGHT OFFICE USE ONLY

DO NOT WRITE ABOVE THIS LINE. IF YOU NEED MORE SPACE, USE A SEPARATE CONTINUATION SHEET.

PREVIOUS REGISTRATION Has registration for this work, or for an earlier version of this work, already been made in the Copyright office? 5

☐ Yes ☒ No If your answer is "Yes," why is another registration being sought? (Check appropriate box) ▼

☐ This is the first published edition of a work previously registered in unpublished form.

☐ This is the first application submitted by this author as copyright claimant.

☐ This is a changed version of the work, as shown by space 6 on this application.

If your answer is "Yes," give: Previous Registration Number ▼ Year of Registration ▼

DERIVATIVE WORK OR COMPILATION Complete both space 6a & 6b for a derivative work; complete only 6b for a compilation. 6

a. Preexisting Material Identify any preexisting work or works that this work is based on or incorporates. ▼

b. Material Added to This Work Give a brief, general statement of the material that has been added to this work and in which copyright is claimed. ▼

See instructions before completing this space.

MANUFACTURERS AND LOCATIONS If this is a published work consisting preponderantly of nondramatic literary material in English, the law may require that the copies be manufactured in the United States or Canada for full protection. If so, the names of the manufacturers who performed certain processes, and the places where these processes were performed must be given. See instructions for details. 7

Names of Manufacturers ▼	Places of Manufacture ▼
UNIVERSITY MICROFILMS INC.	ANN ARBOR, MICHIGAN 48106

REPRODUCTION FOR USE OF BLIND OR PHYSICALLY HANDICAPPED INDIVIDUALS A signature on this form at space 10, and a check in one of the boxes here in space 8, constitutes a non-exclusive grant of permission to the library of Congress to reproduce and distribute solely for the blind and physically handicapped and under the conditions and limitations prescribed by the regulations of the Copyright Office: (1)copies of the work identified in space 1 of this application in Braille(or similar tactile symbols); or (2)phonorecords embodying a fixation of a reading of that work; or (3)both. 8

a ☐ Copies and Phonorecords b ☒ Copies Only c ☐ Phonorecords Only

See instructions.

DEPOSIT ACCOUNT If the registration fee is to be charged to a Deposit Account established in the Copyright Office, give name and number of Account. 9

Name ▼ UNIVERSITY MICROFILMS INC. Account Number ▼ DAO 64793

CORRESPONDENCE Give name and address to which correspondence about this application should be sent. Name/Address/Apt/City/State/Zip ▼

UNIVERSITY MICROFILMS INC.
300 NORTH ZEEB RD.
ANN ARBOR MICHIGAN 48106

Area Code & Telephone Number ▶ 313-761-4700

Be sure to give your daytime phone number. ◀

CERTIFICATION I, the undersigned, hereby certify that I am the 10

Check one ▶
☐ author
☐ other copyright claimant
☐ owner of exclusive right(s)
☒ authorized agent of GARCES, FRED OMEGA

of the work identified in this application and that the statements made by me in this application are correct to the best of my knowledge.

Name of author or other copyright claimant, or owner of exclusive right(s) ▲

Typed or printed name and date ▼ If this is a published work, this date must be the same as or later than the date of publication given in space 3.

PATRICIA L. MARTELL date ▶ 11/21/89

Handwritten signature (X) ▼

Patricia L. Martell

MAIL CERTIFICATE TO

Name ▼
GARCES, FRED OMEGA

Number/Street/Apartment Number ▼
c/o CHEMISTRY DEPT., COLUMBIA UNIVERSITY

City/State/Zip ▼
NEW YORK, NY 10065

Certificate will be mailed in window envelope

11

Have you:
- Completed all necessary spaces?
- Signed your application in space 10?
- Enclosed check or money order for $10 payable to Register of Copyrights?
- Enclosed your deposit material with the application and fee?

MAIL TO: Register of Copyrights, Library of Congress, Washington, D.C. 20559

*17U.S.C. 506(e): Any person who knowingly makes a false representation of a material fact in the application for copyright registration provided for by section 409, or in any written statement filed in connection with the application, shall be fined not more than $2,500.

U.S. GOVERNMENT PRINTING OFFICE: 1987-181-531/40,016

January 1987-145,000